

INITIAL IMPERFECTIONS OF HIGH STRENGTH UOE MANUFACTURED
STEEL PIPES AND THEIR EFFECTS ON PIPE BUCKLING

by

Muntaseer Sarwar-E-Kainat

A thesis submitted in partial fulfillment of the requirements for the degree of

Doctor of Philosophy

in

STRUCTURAL ENGINEERING

Department of Civil and Environmental Engineering
University of Alberta

© Muntaseer Sarwar-E-Kainat, 2014

ABSTRACT

The use of high strength steel pipes in the pipeline industry is increasing due to its cost reduction benefits. The development of high steel grades has enabled the manufacturing of line pipes with large diameter to thickness ratios. The high strength large diameter pipes are commonly manufactured by the UOE forming process, during which, thin steel plates are deformed using mechanical presses and expansion. The plastic deformation of pipe material induced during the UOE forming process is likely to result in initial geometric imperfections in the manufactured pipes.

This research introduces a new imperfection measurement technique that employs a high resolution surface profiler for geometric data acquisition, and a reverse engineering software for the geometric analysis of line pipes. The measurements reveal that the geometric imperfections in UOE pipes follow certain patterns in terms of outside radii and pipe wall thickness deviations with respect to the location of the longitudinal seam weld. The outside radii are less than the nominal value at locations opposite to the longitudinal seam weld in a pipe cross section. The pipe wall thickness values are lower at locations near the longitudinal seam weld compared to the thickness at locations opposite to the longitudinal seam weld. These patterns can be expressed in a cylindrical coordinate system with respect to the longitudinal seam weld's location. The sources of the observed patterns can be traced back to the UOE manufacturing process itself.

A finite element analysis further confirms that the thickness deviation imperfection observed in the scanned pipes has significant effects on the buckling capacity of line pipes. Critical buckling capacity was reduced up to 27% in unpressurized pipes modelled with the observed thickness deviation compared to the ideal case. This reduction occurred for the case when compressive strain develops in the regions near the location of the longitudinal seam weld. Similarly, for pressurized pipes, the thickness deviation imperfection observed in the scanned pipes reduced the peak moment compared to the ideal pipe by up to 20%. The dimensional tolerances for wall thickness specified in the ASTM codes may not be reliable in this regard. These tolerances need to be revisited for the cases where the critical strain capacity governs the design of pipeline. A higher quality control for UOE manufacturing process is required. The observed imperfection patterns will aid towards improving the quality control of UOE manufactured pipes.

ACKNOWLEDGEMENTS

I would like to acknowledge the Natural Sciences and Engineering Research Council and TransCanada PipeLines Ltd. for their financial support. The pipe specimens used for this research were supplied by TransCanada PipeLines Ltd., and the data collection was carried out in their Spruce Grove storage facility. I would like to thank all the TransCanada employees in the Spruce Grove Facility for their technical support and cooperation.

I would like to thank Jonathon Schofield, Dr. Amin Komeili, Behzad Vafaeian, Sunil Neupane, Celal Cakiroglu, Meng lin, and the rest of the former and current members of our research group for lending a hand when I needed. Special thanks to Dr. J. J. Roger Cheng for his valuable advice and directions throughout this research work. His guidance and suggestions improved my overall understanding of the research topic.

I would like to express my utmost gratitude to my supervisor Dr. Samer Adeeb. He has been supportive and helpful during each and every step. He never lost his patience with me the numerous times I failed to meet deadlines. It is amazing how he managed to guide me to the right direction while letting me work freely on my own. I truly have learned a lot from him, which expands beyond “Engineering” and “Pipelines”.

The support and encouragement of my friends and family are deeply appreciated. I am grateful to my parents, my grandmother, and my wife for their kindness, inspiration, and prayers. I hope I made them proud.

TABLE OF CONTENTS

CHAPTER 1: INTRODUCTION	1
1.1 Background	1
1.2 Problem Statement.....	4
1.3 Research Objective and Scope	6
1.3.1 Quantifying the initial geometric imperfections.....	6
1.3.1.1 <i>Devising an accurate and time efficient measurement technique</i> 6	
1.3.1.2 <i>Validating the accuracy of the technique</i>	7
1.3.1.3 <i>Applying the technique to the measurement of imperfections</i>	7
1.3.1.4 <i>Developing initial geometric imperfection models</i>	8
1.3.2 Quantifying the effects of the geometric imperfections.....	8
1.3.2.1 <i>Investigating the individual and combined effects</i>	8
1.3.2.2 <i>Investigating the sensitivity of buckling to the geometric imperfections of pipes:</i>	8
1.4 Outline of the Thesis.....	9
CHAPTER 2: LITERATURE REVIEW	10
2.1 Introduction	10
2.2 Types of Imperfections	10
2.3 Codes and Standards on Imperfection (CSA Z662-11 and ASME B31.8)	
13	
2.4 Research on Measurements of Imperfections.....	15
2.5 Research on Initial or Pre-existing Imperfections.....	17
2.6 UOE Forming Process and the Mechanical Behaviour of UOE Pipes..	19
2.7 Research on Operational Damages.....	21
2.8 Conclusion	28
CHAPTER 3: MEASUREMENT OF GEOMETRIC IMPERFECTION USING 3D LASER SCANNER.....	30
3.1 Introduction	30
3.2 Metrology	31

3.2.1	Basic Concepts	31
3.2.2	3D Metrology.....	32
3.3	An Overview of 3D Optical Sensors.....	33
3.3.1	3D Optical Sensors	33
3.3.2	3D Triangulation Scanner.....	34
3.4	The 3D Scanner	40
3.4.1	Overview	40
3.4.2	Data Acquisition using the 3D Scanner	43
3.4.3	Accuracy Verification of the 3D Scanner	50
3.4.3.1	<i>Comparison with Micrometer Measurements</i>	<i>51</i>
3.4.3.2	<i>Influence of the Photogrammetry Model on the Acquired Data .</i>	<i>57</i>
3.4.3.3	<i>Discussion on Accuracy.....</i>	<i>61</i>
3.5	Geometric Analysis of Pipes, Sleeves, and Elbows	63
3.5.1	Geometric Analysis of UOE Manufactured Pipes.....	63
3.5.1.1	<i>Alignment.....</i>	<i>64</i>
3.5.1.2	<i>Reference Ideal Pipe</i>	<i>67</i>
3.5.1.3	<i>Comparison between Ideal and Actual Pipe.....</i>	<i>68</i>
3.5.1.4	<i>Measuring Ovalization</i>	<i>70</i>
3.5.1.5	<i>Measuring Pipe Wall Thickness.....</i>	<i>71</i>
3.5.1.6	<i>Measuring Seam Weld Geometry.....</i>	<i>72</i>
3.5.2	Geometric Analysis of Fiber Glass Reinforcement Sleeve Fitting .	74
3.5.2.1	<i>Sleeve and Support Details.....</i>	<i>74</i>
3.5.2.2	<i>Sleeve Geometry Measurement.....</i>	<i>76</i>
3.5.3	Pipe Elbow Geometry Analysis.....	76
3.5.3.1	<i>Idealized Geometry.....</i>	<i>78</i>
	<i>Step 1: Planes of Symmetry.....</i>	<i>80</i>
	<i>Step 2: Radius of Curvature of the Outer Curve.....</i>	<i>80</i>
	<i>Step 3: Axis and Centre of Elbow.....</i>	<i>81</i>
	<i>Step 4: Alignment with Coordinate System</i>	<i>82</i>
	<i>Step 5: Radius of Torus Cross-section.....</i>	<i>83</i>

<i>Step 6: Distance of the Centre of the Circle from the Axis of Revolution</i> .	83
<i>Step 7: Comparison with Idealized Geometry</i>	84
<i>Step 8: Ovalization Measurement</i>	84
<i>Step 9: Wall Thickness Measurement</i>	85
3.5.4 Summary of the Geometric Analyses	87
3.6 Conclusion	88
CHAPTER 4: RESULTS OF THE GEOMETRIC ANALYSIS OF UOE MANUFACTURED STRAIGHT PIPES	89
4.1 Introduction	89
4.2 Pipe Specifications	89
4.3 Weld Geometry	89
4.4 Deviation from Ideal Pipe	91
4.5 Ovalization	96
4.6 Pipe Wall Thickness	99
4.7 Discussion on Results	105
4.8 Conclusion	111
CHAPTER 5: RESULTS OF THE GEOMETRIC ANALYSIS OF FRP SLEEVES AND ELBOWS	112
5.1 Introduction	112
5.2 FRP Sleeve Fitting	112
Table 5.1.....	112
5.2.1 Discussion.....	124
5.3 Pipe Elbow Geometry.....	125
5.3.1 Idealized Dimensions:	126
5.3.2 Ovalization Values:.....	126
5.3.3 Wall Thickness Deviation:	127
5.3.4 Discussion.....	131
5.4 Conclusion	132

CHAPTER 6: INITIAL GEOMETRIC IMPERFECTION MODELS FOR UOE MANUFACTURED PIPES	134
6.1 Introduction	134
6.2 Qualitative Characterization of Initial Geometric Imperfection Patterns	134
6.2.1 Outside Radius Deviation Patterns	134
6.2.2 Pipe Wall Thickness Deviation Patterns	142
6.3 Possible Sources of Initial Geometric Imperfection	144
6.4 OR Deviation Model	147
6.4.1 Reference Deviation Data	148
OR Deviation Model 1	150
OR Deviation Model 2	153
6.5 Wall Thickness Deviation Model	157
6.6 Imperfections in the Longitudinal Direction	163
6.7 Conclusion	164
CHAPTER 7: EFFECTS OF INITIAL GEOMETRIC IMPERFECTIONS ON PIPE BUCKLING	166
7.1 Introduction	166
7.2 FEA Model	168
7.2.1 Geometry, Mesh, and Element	168
7.2.2 Anisotropic Material Model	172
7.2.3 Applied Boundary Conditions, Load and Rotation	174
7.3 Buckling Response of an Ideal Pipe	177
7.4 Effects of the Geometric Imperfections on Buckling Response	181
7.4.1 Effects of OR Deviation	181
7.4.2 Effects of Wall Thickness Deviation	184
7.4.3 Combined Effect of OR and Wall Thickness Deviation	186
7.4.4 Discussion on the Effects of the Geometric Imperfection Models	190

7.5	Sensitivity of the OR Deviation Model 2.....	192
7.6	Sensitivity of the Thickness Deviation Model	199
7.6.1	Effects of the Location of the Maximum Wall Thickness	199
7.6.2	Effects of the Extent of Negative Deviation.....	203
7.6.3	Effects of the Relative Magnitudes of the Maximum Deviations..	207
7.6.4	Effects of Longitudinal Variation of the Thickness Deviations	209
7.7	Parametric Study.....	211
7.7.1	NPS 42 inch pipe with 10.312 mm specified wall thickness (D/t = 103.47)	212
7.7.2	NPS 34 inch pipe with 9.525 mm specified wall thickness (D/t = 90.71)	215
7.7.3	NPS 42 inch pipe with 14.275 mm specified wall thickness (D/t = 74.75)	216
7.7.4	Summary of the parametric study.....	218
7.8	General Discussion on Initial Imperfections	220
7.9	Conclusion	222
CHAPTER 8: SUMMARY, CONCLUSIONS, AND RECOMMENDATIONS		224
8.1	Summary.....	224
8.2	Conclusions.....	226
8.3	Recommendations	228
REFERENCES		230

LIST OF FIGURES

Figure 1.1 Imperfection measurement device (Dorey et al., 2006)	3
Figure 2.1 Classification of initial imperfections of line pipes	11
Figure 3.1 Triangulation based laser point and laser line sensors (Jahne et al.)	35
Figure 3.2 Principle of Triangulation for measuring depth	36
Figure 3.3 Calculation of a point coordinate from camera's field of view	37
Figure 3.4 3D measurement by stereo vision sensors (Chen S. et al., 2008)	38
Figure 3.5 Different types of artificial targets (Jahne et al., 2000)	38
Figure 3.6 Use of reference targets on the background and surface of an object (Jahne et al., 2000)	39
Figure 3.7 Optimum method of applying targets to enable the accurate self- positioning of the scanner (Creaform Handyscan Manual)	41
Figure 3.8 Tolerance stacking phenomenon (Creaform Handyscan Manual)	41
Figure 3.9 Reference cross, scale bars, and coded targets (Creaform Handyscan Manual)	42
Figure 3.10 Unstructured triangulated surface generation during scanning (Creaform Handyscan Manual)	43
Figure 3.11 Acquired noise due to bright light exposure	44
Figure 3.12 Improvement in captured surface after sheltering with a tent	44
Figure 3.13 Reflective targets applied on pipe surface	45
Figure 3.14 Complete pipe setup with reference cross, bars, and coded targets	46
Figure 3.15 Paths followed while taking pictures for the photogrammetry model	46
Figure 3.16 Capturing the targets on the inside surface of the pipe	47
Figure 3.17 Photogrammetry model of the targets on the pipe	48
Figure 3.18 Configuration of laser power and shutter speed (Creaform Handyscan Manual)	48
Figure 3.19 Laser paths recorded by the scanner during scanning (Creaform Handyscan Manual)	49
Figure 3.20 a) Outside surface of pipe, b) Outside and inside surface near pipe edge, c) Weld surface	50
Figure 3.21 NPS 30 inch pipe clamp set up with reflective targets	52

Figure 3.22	STL surface imported in Geomagic®	52
Figure 3.23	Cross section of clamp and reference lines for measuring wall thickness	53
Figure 3.24	Measuring grid on the pipe clamp	54
Figure 3.25	Wall thickness measurement using the micrometer	54
Figure 3.26	Micrometer and Geomagic® measurements plotted against each other	56
Figure 3.27	Scanned surface of the NPS 12 inch pipe segment	57
Figure 3.28	Cross sectional deviation of pipe surfaces scanned with and without the photogrammetry model	58
Figure 3.29	Comparison of the cross sections of girth weld surfaces scanned with and without a photogrammetry model	59
Figure 3.30	Comparison of the two scanned surfaces with a reference cylinder of fixed radius	59
Figure 3.31	Longitudinal axis of a pipe extracted from best fit cylinder	64
Figure 3.32	Extracted point at pipe end to be used as coordinate origin	64
Figure 3.33	Separating the weld surface with trimming planes	65
Figure 3.34	Centroid of weld surface	65
Figure 3.35	Plane bisecting the weld surface	66
Figure 3.36	Pairing the point, line and plane features with the global coordinate system	66
Figure 3.37	Pipe surface after alignment	67
Figure 3.38	Best fit cylinder modified with the specified OD of the scanned pipe	67
Figure 3.39	Deviation of the scanned pipe surface from the ideal cylinder	68
Figure 3.40	3D deviation spectrum	68
Figure 3.41	2D cross sectional deviation spectrum	69
Figure 3.42	Minimum and maximum diameter measuring process at a cross section of a pipe	71
Figure 3.43	Planes through and normal to pipe axis for thickness measurement	71
Figure 3.44	Thickness measurement scheme	72
Figure 3.45	Cross section of pipe wall thickness with measured dimensions	72
Figure 3.46	Representation of idealized weld dimensions	73

Figure 3.47	Measuring the seam weld thickness in Geomagic©	74
Figure 3.48	Support Specifications	75
Figure 3.49	a) The centre, axis and radius of revolution, and cross section of an ideal torus, b) Vertical and horizontal planes of symmetry of an ideal torus	78
Figure 3.50	Planes of Symmetry	80
Figure 3.51	Radius of Curvature of the outer curve of the elbow	80
Figure 3.52	a) Trimmed elbow slice, b) Cylinder, and c) Trimmed CAD object	81
Figure 3.53	Axis of revolution of the pipe elbow	82
Figure 3.54	Alignment of elbow with the coordinate system	82
Figure 3.55	Average radius of elbow to be used to define the ideal torus	83
Figure 3.56	Distance of the centre of the circle from the axis of revolution of the ideal torus	83
Figure 3.57	Repositioning of the idealized torus with respect to the actual pipe elbow	84
Figure 3.58	a) Plane through Z axis for taking cross section, b) Schematics of wall thickness measurement	85
Figure 3.59	a) Method 1, and b) Method 2 for elbow wall thickness measurement	86
Figure 3.60	Comparison between the two methods of wall thickness measurement	86
Figure 4.1	2D deviation spectrum, NPS 20 A ($D/t = 64.10$), 2200 mm from edge	92
Figure 4.2	2D deviation spectrum, NPS 34 A ($D/t = 90.71$), 400 mm from edge	92
Figure 4.3	2D deviation spectrum, NPS 42 D ($D/t = 74.75$), 1200 mm from edge	93
Figure 4.4	2D deviation spectrum, NPS 42 B ($D/t = 103.47$), 300 mm from edge	93
Figure 4.5	Deviation distribution histogram of NPS 34 A	95
Figure 4.6	Thickness variation (%) of NPS 20 A (wall thickness = 7.925 mm) at a section 200 mm from pipe edge	100
Figure 4.7	Thickness variation (%) of NPS 20 B (wall thickness = 7.925 mm) at a section 250 mm from pipe edge	100
Figure 4.8	Thickness variation (%) of NPS 34 A (wall thickness = 9.525 mm) at a section 250 mm from pipe edge	101

Figure 4.9 Thickness variation (%) of NPS 34 B (wall thickness = 9.525 mm) at a section 250 mm from pipe edge	102
Figure 4.10 Thickness variation (%) of NPS 42 A (wall thickness = 10.312 mm) at a section 300 mm from pipe edge	103
Figure 4.11 Thickness variation (%) of NPS 42 B (wall thickness = 10.312 mm) at a section 250 mm from pipe edge	103
Figure 4.12 Thickness variation (%) of NPS 42 E (wall thickness = 14.275 mm) at a section 200 mm from pipe edge	104
Figure 4.13 Thickness variation (%) of NPS 42 F (wall thickness = 14.275 mm) at a section 250 mm from pipe edge	104
Figure 4.14 Average ovalization values of each pipe group with increasing D/t Ratio	108
Figure 4.15 Measured wall thickness variations of all eight specimens in a single plot	110
Figure 5.1 Thickness of Sleeve	113
Figure 5.2 Topography of Sleeve Outer Surface	113
Figure 5.3 Deviation Spectrum for Pipe 1	114
Figure 5.4 Deviation Spectrum for Pipe 2	114
Figure 5.5 Deviation Spectrum for Pipe 3	115
Figure 5.6 Deviation Spectrum for Pipe 4	115
Figure 5.7 Deviation Spectrum for Pipe 5	115
Figure 5.8 Deviation Spectrum for Pipe 6	116
Figure 5.9 Wall thickness deviation of elbow 12inch_GR359_1	128
Figure 5.10 Wall thickness deviation of elbow 12inch_GR359_2	129
Figure 5.11 Wall thickness deviation of elbow 24inch_GR359_2	130
Figure 5.12 Two different patterns of deviation from perfect torus observed through 3D comparison of two elbows a) 24inch_GR359_2, and b) 12inch_GR359_2	131
Figure 6.1 OR deviation pattern in NPS 20 pipe	135
Figure 6.2 OR deviation pattern of NPS 34 A, D/t = 90.71, average ovalization 0.0092, manufactured by Sumitomo	136
Figure 6.3 OR deviation pattern of NPS 34 B, D/t = 90.71, average ovalization 0.0089, manufactured by Sumitomo	136

Figure 6.4 OR deviation pattern of NPS 42 A, D/t = 103.47, average ovalization 0.0049, manufactured by Sumitomo	137
Figure 6.5 OR deviation pattern of NPS 42 B, D/t = 103.47, average ovalization 0.0150, manufactured by Sumitomo	137
Figure 6.6 OR deviation pattern of NPS 42 C, D/t = 74.75, average ovalization 0.0067, manufactured by Nippon	138
Figure 6.7 OR deviation pattern of NPS 42 D, D/t = 74.75, average ovalization 0.0117, manufactured by Nippon	138
Figure 6.8 OR deviation pattern of NPS 42 E, D/t = 74.75, average ovalization 0.0099, manufactured by Nippon	139
Figure 6.9 OR deviation pattern of NPS 42 F, D/t = 74.75, average ovalization 0.0073, manufactured by Nippon	139
Figure 6.10 Angle subtended by the OR deviation waves of NPS 42 B to its centre	140
Figure 6.11 Angle subtended by the OR deviation waves of NPS 34 A to its centre	140
Figure 6.12 Angle subtended by the OR deviation waves of NPS 42 E to its centre	141
Figure 6.13 Ellipse or ovalization approximation of the OD deviations	142
Figure 6.14 Typical wall thickness deviation pattern in the UOE manufactured pipes	143
Figure 6.15 Schematic representation of the typical thickness deviation pattern of UOE manufactured pipes	144
Figure 6.16 The four stages of the UOE manufacturing process: a) Crimping, b) U-punch, c) O-press, and d) Expansion (Herynk et al., 2007)	145
Figure 6.17 Extraction of points from the reference cross section	148
Figure 6.18 Measured OR values at the reference cross section	149
Figure 6.19 Modified radii values expressed as percentage deviation from nominal OR	150
Figure 6.20 OR Deviation Model 1	151
Figure 6.21 OR Deviation Model 1 fitted to the measured OR deviation of NPS 34 A at a cross section 600 mm from edge	152
Figure 6.22 OR Deviation Model 1 fitted to the measured OR deviation of NPS 34 B at a cross section 400 mm from edge	152

Figure 6.23	OR Deviation Model 1 fitted to the measured OR deviation of NPS 42 C at a cross section 600 mm from edge	153
Figure 6.24	OR Deviation Model 2	154
Figure 6.25	OR Deviation Model 2 fitted to the measured OR deviation of NPS 34 A at a cross section 600 mm from edge	155
Figure 6.26	OR Deviation Model 2 fitted to the measured OR deviation of NPS 34 B at a cross section 400 mm from edge	155
Figure 6.27	OR Deviation Model 2 fitted to the measured OR deviation of NPS 42 C at a cross section 600 mm from edge	156
Figure 6.28	Qualitative comparison between the reference cross section and the two OR deviation models	156
Figure 6.29	Measured deviation of wall thickness of NPS 42 E, 1067 mm nominal OD and 14.275 mm specified wall thickness	157
Figure 6.30	Thickness Deviation Model fitted to the measured deviation through regression analysis	158
Figure 6.31	Thickness Deviation Model manually fitted to the measured deviation	159
Figure 6.32	Thickness Deviation Model fitted to the measured deviation of NPS 34 A at a section 250 mm from edge	160
Figure 6.33	Thickness Deviation Model fitted to the measured deviation of NPS 34 B at a section 250 mm from edge	161
Figure 6.34	Thickness Deviation Model fitted to the measured deviation of NPS 42 F at a section 300 mm from edge	161
Figure 6.35	Sample plots of deviation from Equation 6-3 with different magnitudes and extents of deviation	162
Figure 6.36	Assumed types of longitudinal variation of pipe wall thickness deviation	164
Figure 7.1	Organization of FEA models	167
Figure 7.2	Orientation of pipe cross section with respect to the Cartesian Coordinate system	169
Figure 7.3	Mesh generated in ABAQUS corresponding to an NPS 42 inch pipe model 170	
Figure 7.4	Cylindrical Coordinate system adopted for assigning the thickness deviation model	171

Figure 7.5 Shell thickness deviation spectrum and its orientation	172
Figure 7.6 Plastic Anisotropy in HSS UOE pipe material (Neupane et al., 2012)	173
Figure 7.7 Stress Strain responses along the longitudinal and circumferential directions obtained from tension coupon test and FEA	174
Figure 7.8 Idealized representation of symmetry boundary condition	175
Figure 7.9 Von Mises stress distribution after applying internal pressure and the location of buckle after applying rotation using a) Rigid Body Constraint, and b) Kinematic Coupling Constraint	178
Figure 7.10 Buckled shape of an ideal pipe with and without internal pressure	179
Figure 7.11 Moment-Rotation response of an NPS 42 inch ideal pipe with 14.275 mm specified wall thickness	180
Figure 7.12 M-R responses of unpressurized pipe with OR Deviation Model 1	181
Figure 7.13 M-R responses of pressurized pipe with OR Deviation Model 1	182
Figure 7.14 M-R responses of unpressurized pipe with OR Deviation Model 2	182
Figure 7.15 M-R responses of pressurized pipe with OR Deviation Model 2	183
Figure 7.16 M-R responses of unpressurized pipe with Thickness Deviation	184
Figure 7.17 M-R responses of pressurized pipe with Thickness Deviation	185
Figure 7.18 M-R responses of unpressurized pipe with Thickness Deviation and OR Deviation Model 1	186
Figure 7.19 M-R responses of pressurized pipe with Thickness Deviation and OR Deviation Model 1	187
Figure 7.20 M-R responses of unpressurized pipe with Thickness Deviation and OR Deviation Model 2	187
Figure 7.21 M-R responses of pressurized pipe with Thickness Deviation and OR Deviation Model 2	188
Figure 7.22 Variations of peak moments with increasing ovalization for the three combinations of D_{max} and D_{min}	194
Figure 7.23 Deformation (scaled by a factor of 20) due to pressurization of an ideal and an ovalized pipe cross section at mid length	195

Figure 7.24	Variations of critical end rotations with increasing ovalization for the three combinations of D_{max} and D_{min}	196
Figure 7.25	Deformed shapes of pipes corresponding to the three combinations of ovalization (full lengths of pipes are shown for visual clarity)	196
Figure 7.26	Longitudinal cross section of the pipe with Combination 3, ovalization of 0.03, and at 37% of CER	198
Figure 7.27	Moment Rotation responses of the half pipe model with symmetry boundary condition and the full pipe model	198
Figure 7.28	The thickness deviation model used in the buckling analysis	199
Figure 7.29	Thickness deviation models for investigating the sensitivity of the location of maximum thickness	200
Figure 7.30	Buckling responses of unpressurized pipe with varying locations of maximum wall thickness	201
Figure 7.31	Buckling responses of pressurized and pressurized pipes with varying locations of maximum wall thickness	201
Figure 7.32	Variations in peak moment and CER with changes in the location of maximum thickness	202
Figure 7.33	Thickness deviation models with $\theta_{neg dev}$ increasing from 120 degrees to 200 degrees	203
Figure 7.34	Variations in peak moment and CER with $\theta_{neg dev}$ increasing from 120 degrees to 200 degrees	204
Figure 7.35	Change in shape of the thickness deviation models with $\theta_{neg dev}$ increasing from 120 degrees to 200 degrees	205
Figure 7.36	Buckling responses of unpressurized and pressurized pipes with the original and the symmetric ($\theta_{neg dev} = 180$ degrees) thickness deviation models	206
Figure 7.37	Thickness deviation models with maximum positive deviation decreasing from 30% to 15%	207
Figure 7.38	Buckling responses of unpressurized and pressurized pipes with the maximum thickness deviation decreasing from 30% to 15%	208
Figure 7.39	Three types of longitudinal variations of the cross sectional thickness deviations	209
Figure 7.40	Buckling responses of unpressurized pipes with longitudinal variations	210

Figure 7.41	Buckling responses of pressurized pipes with longitudinal variations	210
Figure 7.42	Moment-Rotation responses of unpressurized pipe with $D/t = 103.47$	213
Figure 7.43	Moment-Rotation responses of pressurized pipe with $D/t = 103.47$	214
Figure 7.44	longitudinal cross section of the buckled shape of pipes with the thickness deviation ranges of -10% to +20% and -15% to +30%	214
Figure 7.45	Moment-Rotation responses of unpressurized pipe with $D/t = 90.71$	216
Figure 7.46	Moment-Rotation responses of pressurized pipe with $D/t = 90.71$	216
Figure 7.47	Moment-Rotation responses of unpressurized pipe with $D/t = 74.75$	217
Figure 7.48	Moment-Rotation responses of pressurized pipe with $D/t = 74.75$	218
Figure 7.49	Changes in peak moments of unpressurized and pressurized pipes with increasing thickness deviation amplitudes	218
Figure 7.50	Changes in CER of unpressurized and pressurized pipes with increasing thickness deviation amplitudes	219

LIST OF TABLES

Table 3.1	Comparison between micrometer and Geomagic® measurements	55
Table 3.2	Maximum OD, Minimum OD, and Ovalization values calculated from the two scans	60
Table 3.3	Expected values of error in pipe wall thickness measurement	62
Table 3.4	Specifications of the scanned pipes	63
Table 3.5	Pipe and Sleeve Description	74
Table 3.6	Elbow Specifications	77
Table 4.1	Specifications of the scanned pipes	89
Table 4.2	Weld thickness of NPS 34 A, B and NPS 42 A, B	90
Table 4.3	Idealized Weld width and thickness values of NPS 42 D, E, and F	91
Table 4.4	Maximum and Average deviation from nominal OD	94
Table 4.5	Deviation Range with maximum percentage of surface points	96
Table 4.6	Ovalization Values at different sections	97
Table 4.7	Summary of Ovalization	99
Table 4.8	Average ovalization of each pipe group	108
Table 4.9	Wall Thickness deviation ranges	109
Table 5.1	Pipe and Sleeve Description:	112
Table 5.2	Best Fit Geometry of Sleeves	112
Table 5.3	Pipe 1: 3D Comparison Results	117
Table 5.4	Pipe 2: 3D Comparison Results	118
Table 5.5	Pipe 3: 3D Comparison Results	119
Table 5.6	Pipe 4: 3D Comparison Results	120
Table 5.7	Pipe 5: 3D Comparison Results	121
Table 5.8	Pipe 6: 3D Comparison Results	122
Table 5.9	Maximum, Average, and Standard Deviations of Data Points	123
Table 5.10	Summary of Deviation Distribution	123
Table 5.11	Elbow Specifications	125
Table 5.12	Idealized geometry of the elbows	126
Table 5.13	Ovalization values of the scanned elbows	127
Table 7.1	Peak Moment and CER values corresponding to the OR deviation models	183
Table 7.2	Peak Moment and CER values corresponding to the thickness deviation model	185

Table 7.3 Peak Moment and CER values corresponding to the combination of the thickness and OR deviation models	189
Table 7.4 Combinations of D_{\max} and D_{\min} for the sensitivity investigation	193
Table 7.5 Peak Moment and CER values corresponding to increasing values of $\theta_{\text{neg dev}}$	205

LIST OF NOTATIONS

UOE	Pipe Manufacturing Process
ASTM	American Society for Testing and Materials
HSS	High Strength Steel
SMYS	Specified Minimum Yield Strength
LVDT	Linear Variable Differential Transducer
FEA	Finite Element Analysis
OD	Outside Diameter
ID	Inside Diameter
OR	Outside Radius
CSA	Canadian Standard Association
ASME	American Society of Mechanical Engineers
DNV	Det Norske Veritas
CAD	Computer Aided Design
CMM	Coordinate Measuring Machine
ISO	International Organization for Standardization
W	Weld Width
t	Weld Thickness
NPS	Nominal Pipe Size
CV	Coefficient of Variation

St. Dev	Standard Deviation
D/t	Diameter to Thickness Ratio
PCC	Pearson Product-Moment Correlation Coefficient
CER	Critical End Rotation
M-R	Moment Versus Rotation
$\theta_{\text{neg dev}}$	Extent of Negative Deviation

CHAPTER 1: INTRODUCTION

1.1 Background

The price of fossil fuel has increased with the increase in their demand in the last decade. As a result, the exploration of energy reserves in the sub-Arctic regions of North America has become an economically beneficial option. Consequently, the oil and gas industry is now an influential part of the Canadian economy. The industry accounts for exploration, extraction and transportation of oil and gas. Buried pipelines are considered to be a cost effective and efficient form of transportation from the source to the point of consumption. Due to the harsh environmental conditions in the sub-Arctic regions, buried pipelines have to pass through regions of discontinuous permafrost. The pipelines are subjected to differential settlements due to seasonal freeze-thaw cycles. The differential settlements impose bending stresses on pipe segments in addition to the stresses induced by internal and external pressure and differential temperature. These stresses are often responsible for the failure of a pipeline.

In recent years, the use of high strength steel (HSS) pipes has increased due to its cost reduction benefits. Manufacturers are able to produce grades as high as X100 which has a Specified Minimum Yield Strength (SMYS) of 690 MPa (100 ksi). The advantages of HSS are high yield strength and toughness. The use of higher steel grades has resulted in the manufacturing of lighter pipe segments with higher diameter to thickness (D/t) ratio as compared to normal grade steel pipes. The high strength large diameter pipes are generally manufactured by the UOE manufacturing process (U-ing, O-ing, and Expansion). UOE is a cold forming process, where thin steel plates are deformed and made into slender pipes with high D/t ratio through mechanical presses, longitudinal seam welding and expansion. The details of the different stages of the UOE manufacturing process is presented in Chapter 6 (section 6.3). It has been revealed through experiments that the stress strain responses of HSS pipes are different for specimens obtained from the longitudinal and circumferential directions. The anisotropic behavior results from the imposed deformations during the UOE manufacturing process. It is also very likely that the final product of the exhaustive manufacturing process will deviate from the ideal pipe geometry in

terms of radii and pipe wall thickness. In other words, initial geometric imperfection can be a very probable feature in the UOE manufactured pipes.

Imperfections can be defined as any physical attribute in an element that can prevent it from performing in its most idealistic state. For pipelines, imperfections can have a negative effect on their structural capacity due to the increased risk for global buckling or the formation of local buckles. Imperfections may develop at any stage between pipe manufacturing and putting them into service. Common types of geometric imperfections are: ovalization, non-uniformity of the pipe wall thickness, and dents. It is to be noted that the failure of pipeline is not necessarily solely due to the deterioration in their structural health, but can be extended to describe the incidents when the allowance for proper flow is hindered. The restriction of the flow can often be considered an initiation point at which catastrophic failures may occur (Dorey et al., 2001). Geometric imperfection can be pre-existing since the manufacturing process, or may be inflicted upon during installation and operation. Ovalization, non-uniformity of wall thickness in the circumferential direction, and misalignment of plate edge at seam weld location are some of the imperfections that are difficult to identify visually. They can be categorized as initial or pre-existing imperfections, and can be measured, repaired and/or considered in the design prior to installation.

Measurement of initial imperfections has been a major focus of research in energy pipelines. Bailey et al. (1984), Chen et al. (1993), DeCol et al. (1998) carried out some of the most impressive research works in this area that improved the knowledge of initial geometric imperfections of line pipes. Their devised methods of imperfection measurements typically involved locating the pipe axis and taking physical measurements on a cylindrical grid using dial gauges or Linear Variable Differential Transducers (LVDT) (Figure 1.1). The axis worked as a reference for the measurement grid and a mechanism allowed for the gauges to reach the grid points from the axis. Thus the set up was able to locate each grid point in terms of the distance travelled along the axis and the angle rotated around it. The gauges measured the distances of the grid points from the axis, resulting in a measurement matrix on a regular cylindrical grid.

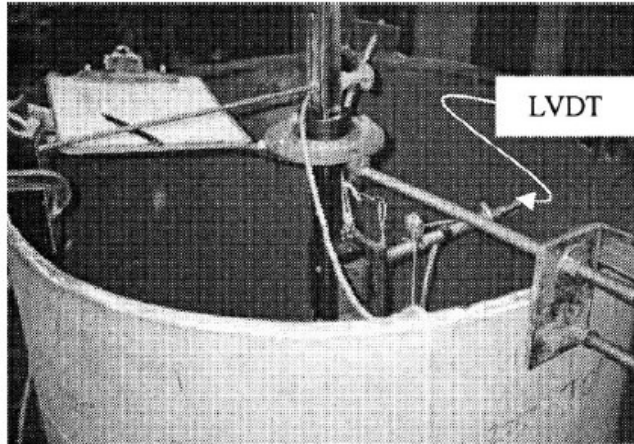


Figure 1.1 Imperfection measurement device (Dorey et al., 2006)

The investigation of the effects of measured geometric imperfections has also been the focus of numerous research works. Chen et al. (1993) examined the effects of three types of initial imperfections on the buckling response of stiffened cylinders. They were able to compare the behaviour of the perfect and imperfect specimens, and concluded that the bending moment was reduced between 1% and 7% due to the presence of the imperfections. DelCol et al. (1998) studied the behaviour of large pipelines under combined application of internal pressure, axial compression, temperature variation, and forces from deformations typically imposed on pipelines in the arctic regions. Their experimental results indicated that imperfections reduce the buckling capacity of a pipeline, causing it to fail at lower compressive strains. The numerical models analysed in their study also demonstrated minor effect of imperfection on peak moment capacity but substantial effect on ductility after failure. Thus, DelCol et al. (1998) were able to validate that only a minor imperfection can reduce the ductility of a pipeline, making it fail after a small amount of deflection. Dorey et al. (2006) performed detailed measurements on initial imperfections. Their study focused on developing a simple idealized model that could summarize the imperfections in a pipe. Their study showed that, neglecting imperfections would drastically overestimate both the peak global end moment and the degree of global curvature in a line pipe subjected to buckling (Dorey et al., 2006).

Adeeb et al. (2006) and Fatemi et al. (2008) have shown that HSS pipes demonstrate anisotropic behavior to a greater extent compared to normal strength pipes. The specimens taken from longitudinal direction show different

stress strain response compared to those taken from the circumferential direction. The yield stress in the circumferential direction is higher than that in the longitudinal direction. The circumferential stress strain curve shows a distinct yield point, while the longitudinal stress strain curve has a more round shape and generally lies below the circumferential stress strain curve. Neupane et al. (2012) were able to demonstrate that anisotropic behavior of HSS pipes can be modeled using a yield surface translation in the stress space. They were successful in developing a combined isotropic / nonlinear kinematic hardening model that can accurately capture the plastic anisotropy of HSS pipes. Their developed material model can be incorporated into Finite Element Analysis (FEA) software such as ABAQUS.

1.2 Problem Statement

The geometric measurement studies that have been carried out previously were primarily intended to measure the imperfection magnitudes that were specific to selected specimens. The developed measurement technique using an assumed axis and linear distance measuring devices was both effective and appropriate for the purpose of these studies. The results of these imperfection measurements led to detailed numerical models for pipe buckling analysis, which further culminated in important findings regarding the effects of imperfections on the critical buckling strength of line pipes.

Despite the large amount of research on geometric imperfections of pipeline, there is still a lack of knowledge regarding the initial or pre-existing geometric imperfections of UOE manufactured HSS pipes. In order to investigate the systematic imperfections arising from the manufacturing process, a measurement technique is needed that satisfies a number of requirements. Without any prior knowledge of the types of imperfections that may exist initially in a UOE manufactured pipe, the measurements need to be performed on a large data set corresponding to each pipe specimen. The large data set will enable an exhaustive investigation of unknown initial imperfections. Therefore a data acquisition system is needed that can fulfill this requirement. In order to investigate the existence of recurring systematic imperfections across specimens, the data acquisition has to be performed on a number of pipe segments from different sources and with varying dimensions. It will not be

feasible to transport large diameter pipe segments to the laboratory and set up the measurement devices for each specimen. Therefore the acquisition method has to be portable, fast, and must have acceptable measurement accuracy.

In this regard, the previous measurement method is not suitable for the investigation of initial geometric imperfections of large diameter UOE manufactured pipes. The setup of the measurement device will take days of preparation for each specimen. There are always difficulties in locating the pipe axis accurately. The out of straightness of a pipe specimen as well as the failure to maintain the measurement mechanism aligned and centered to the pipe axis add up to measurement errors. The position of the gauge or LVDT at the time a measurement is recorded is very challenging to control accurately. The angle of the instrument is the most difficult degree of freedom to control. It is possible to overlook imperfections such as small dents which may be positioned between the measuring grid points. These methods can only be applied to specimens that are short enough to be positioned vertically and the measuring points have to be accessible by the operator from the outside of the pipe.

The geometric imperfection models previously developed are in most cases idealizations of the combinations of different measured imperfections. The studies confirmed the adverse effects of the imperfections on the buckling response of pipes. Therefore it is necessary to further the research on UOE manufactured pipes to understand the effects of initial imperfections on their buckling response. It is unwise to employ the previously developed imperfection models in the study of UOE manufactured pipes without the knowledge of the types of initial geometric imperfections typically present in such pipes.

While the knowledge of material anisotropy in HSS UOE formed pipes are at a very advanced level, the investigation of initial geometric imperfections is still at an early stage. The measurement of initial imperfections of HSS UOE manufactured pipes through a reliable and accurate method is required to quantify initial imperfection on the inside and outside surfaces of a line-pipe. Investigating the effects of these imperfections in combination with anisotropic material is also necessary to understand the buckling behaviour of HSS UOE manufactured pipes.

1.3 Research Objective and Scope

The objectives of this research are to:

1. Quantify the initial geometric imperfections in HSS UOE manufactured pipes.
2. Quantify the effects of the geometric imperfections combined with material anisotropy on the buckling resistance of HSS UOE manufactured pipes

To quantify the initial geometric imperfections in HSS UOE manufactured pipes, the following tasks are performed:

- a. Devise an accurate and time efficient measurement technique
- b. Validate the accuracy of the technique
- c. Apply the technique to the measurement of straight pipe segments, pipe sleeve fitting, and ninety degree elbows
- d. Develop initial geometric imperfection models for straight pipe segments based on measurement results

To quantify the effects of the geometric imperfections combined with material anisotropy on the buckling response of pipes, the following tasks are performed:

- a. Investigate the effects of the geometric imperfections combined with material anisotropy on the buckling response of pipes through finite element analysis
- b. Investigate the sensitivity of the buckling response to the geometric imperfections of pipes through finite element analysis

The methods for achieving each objective are discussed below:

1.3.1 Quantifying the initial geometric imperfections

1.3.1.1 *Devising an accurate and time efficient measurement technique*

A new imperfection measurement technique with high accuracy, large data size, and fast acquisition of data, and which overcomes the problem of locating the pipe axis and eliminates the complications related to maintaining the exact position of LVDT and dial gauges is devised. In addition, this method is applicable to pipe segments of large diameter and length, either in the laboratory

or in field. This new imperfection measurement technique involves the use of a high resolution surface profiling device for data acquisition. In addition, reverse engineering software is used for the analysis of the acquired data. The surface profiling device is a handheld non-contact three dimensional (3D) laser scanner, which has a volumetric accuracy of $20 \mu\text{m} + 25 \mu\text{m}/\text{m}$ and is able to scan pipe surfaces at a maximum resolution of 0.1 mm. The scanner uses positioning features (reflective targets) on the pipe surface, creates a 3D map of the features through a photogrammetry model, and finally acquires surface profile of the pipe through laser scanning. The details of the 3D scanner will be discussed in Chapter 3. The scanner is used to obtain the outside and inside surface profile of HSS UOE manufactured pipes with different D/t ratios. The acquired data is analysed in Geomagic®, a 3D reverse engineering and inspection software. The scanned pipe surfaces are compared to a perfect cylinder with specified dimensions corresponding to each pipe in order to measure their radii variation and ovalization imperfections. The distance between the inside and the outside surfaces of the pipes at different cross sections are measured to find the pipe wall thickness deviation patterns.

1.3.1.2 Validating the accuracy of the technique

The scanner is able to create a 3D map of the positioning features (reflective targets) on the pipe surface through a photogrammetry model to minimize measurement errors. The validation of the scanner accuracy is performed in two stages. The outside surface of a pipe is scanned with and without the photogrammetry model. The surfaces acquired from the scans are compared to find the error induced by not using the photogrammetry model. In the next stage, a micrometer is used to measure the pipe wall thickness. The result is then compared with those obtained by scanning and analysing the inside and outside surfaces of the pipes.

1.3.1.3 Applying the technique to the measurement of imperfections

The measurement technique is employed to the measurement of the initial geometric imperfections in straight pipe segments. A total of ten straight pipes are measured and analyzed, eight of which are known to be UOE manufactured. The technique is also applied to the geometric measurements of protective sleeves on straight pipe segment. The dimensional compatibility between the

protective sleeves and the shoes designed to accommodate them are investigated. The measurement technique is further applied to the measurement of initial geometric imperfections of ninety degree pipe elbows. The measurements of the elbows are performed with the intention of providing geometric information to researchers involved in the investigation of Bourdon Effect. The application of the measurement technique to straight pipes, pipe sleeves, and pipe elbows will be elaborated in Chapter 3.

1.3.1.4 Developing initial geometric imperfection models

The measurement results of the straight pipe segments are analysed to detect any recurring pattern of radii deviation, ovalization, and pipe wall thickness deviation. The patterns are expressed numerically through parametric equations as imperfection models, which can be adopted into Finite Element Analysis (FEA) software.

1.3.2 Quantifying the effects of the geometric imperfections

1.3.2.1 Investigating the individual and combined effects

The effects of the geometric imperfections combined with material anisotropy on the buckling response of pipes are investigated through Finite Element Analysis. The developed geometric imperfection models are incorporated into the FEA model of a pipe along with an anisotropic material model previously developed by Neupane et al., (2012). The most severe cases of imperfections observed from measurements are used in the FEA model. Outside Diameter (OD) and pipe wall thickness deviation is incorporated into the FEA model individually and in combination. The imperfect pipe models are analyzed under pure bending with and without internal pressure. The buckling response corresponding to different directions of applied end rotation are studied.

1.3.2.2 Investigating the sensitivity of buckling to the geometric imperfections of pipes:

The sensitivity of the buckling response to the geometric imperfections of pipes is investigated through parametric Finite Element Analysis. The D/t ratios of the pipes and the extents of the observed imperfection magnitudes are considered as the input parameters. The changes in the buckling response of the pipes with changes in the input parameters are studied.

1.4 Outline of the Thesis

The thesis is organized into eight chapters. Chapter 2 provides a literature review on the imperfections of pipes. This includes the studies carried out on geometric and material imperfections. The different types of imperfections and their effects are presented based on previous research works. The guidelines specified by design standards and codes are also discussed. Chapter 3 elaborates the new technique that has been devised for the measurement of initial geometric imperfections. The details of the data acquisition using 3D laser scanner, and the measurement techniques through reverse engineering software are discussed in this chapter. The application of the new technique of measurement on straight pipe segments is presented. The technique is also applied in the acquisition and analysis of protective pipe sleeves and ninety degree pipe elbows, which are included in this chapter. Chapters 4 and 5 introduce the results of the measurements performed previously. Chapter 6 addresses the characterization and development of initial geometric imperfection models for UOE manufactured pipes. In Chapters 7, the effects of these developed imperfection models on pipe buckling are studied through finite element analysis. Chapter 7 focuses on identifying the imperfections that are most influential to the changes in buckling behaviour, and presents the results of a parametric study that displays the sensitivity of the buckling responses to the varying magnitudes of imperfections. Chapter 8 is the conclusion that summarises all the findings of this work, its limitations, and future recommendations.

CHAPTER 2: LITERATURE REVIEW

2.1 Introduction

As technology continues to advance and as the understanding of structural concepts continue to improve, there has been an increased attention towards understanding the effects of how imperfections can influence the structural behaviour of steel pipes. This chapter will focus on the different types of imperfections, the methods previously developed to measure these imperfections, and their effects on the buckling capacity of pipes. Imperfections may develop at any stage between manufacturing, transportation, construction or while in service. Any type of irregularity that results in the discontinuity of a perfect cylindrical cross section of a pipe and hinders the serviceability is considered as a pipeline imperfection. This includes pre-existing imperfections such as ovalization, non-uniformity of the pipe wall thickness, dents, misalignment of pipe cross section at girth weld, etc. Experiments have been performed to validate the use of computer aided numerical analysis, which has vastly improved the quality and quantity of research that can be performed. This chapter will discuss the definition and types of imperfections, the acceptance criteria currently employed by design codes and standards, an overview of the imperfection measurement methods used in different studies, review of literature on different types of imperfections, and conclusion based on the reviewed literature.

2.2 Types of Imperfections

Imperfections can be defined as any physical attribute in an element that can prevent it from performing in its most idealistic state. For pipelines, imperfections can have a negative effect on their structural capacity due to the increased risk for global buckling or the formation of local buckles. Imperfections may develop at any stage between pipe manufacturing and putting them into service. Common types of imperfections are: ovalization, non-uniformity of the pipe wall thickness, and dents. It is to be noted that the failure of pipeline is not necessarily solely due to the deterioration in their structural health, but can be extended to describe the incidents when the allowance for proper flow is hindered. The restriction of the flow can often be considered as an initiation point at which catastrophic failures may occur (Dorey et al., 2001). Initial geometric imperfections are typically

classified as out of straightness, radii variation, and out of roundness of cross section as shown in Figure 2.1:

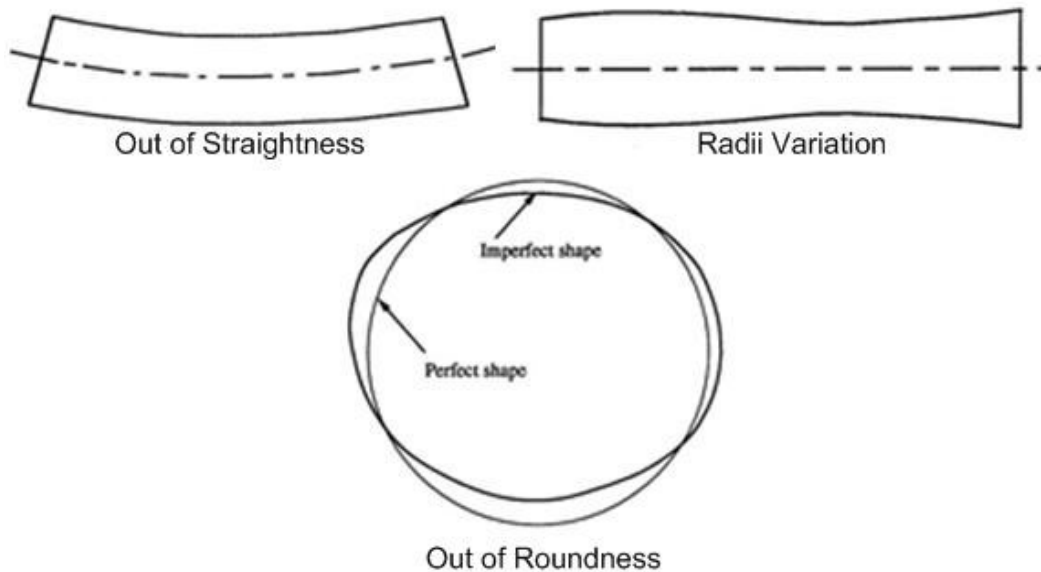


Figure 2.1 Classification of initial imperfections of line pipes

The ovalization imperfection has been referenced as “out of roundness” by some authors. Ovalization is the case where a pipe loses its circular form and begins to resemble an elliptical shape. This type of imperfection can lead to a reduction in the moment capacity (Dorey et al., 2010). Ovalization may occur during the manufacturing phase or may start to develop while the pipe is in service. In case of elevated pipelines, if the design does not provide enough vertical support and the pipe begins to sag, the pipe will start to lose its circular form. In other words, this type of imperfection is dependent on the length of the pipe. Pipes with closer supports will have end conditions that will help restrain and maintain a circular cross section (Houliara et al., 2011). Pipes with a bend due to distant supports can also be said to have an “out of straightness” imperfection (Chen et al., 1993). A pipe can develop non-uniform radius due to shrinkage that occurs from the circumferential welds (Chen et al., 1993). This problem with the pipe can lead to variability in the pipe capacity due to the changes in the cross section as well as possible residual stresses due to the shrinkage. Typically a cylinder that begins to develop an elliptical cross section will become more flexible due to applied bending around the major axis of the ellipse, since the distance between the

tension and compression faces decreases. For thin walled cylinders, the increase in the longitudinal stress can lead to the formation of transverse wrinkles and reduction of the moment resistance of the pipe (Houliara et al., 2011).

The most challenging imperfection to assess is the inconsistency of a pipe wall thickness. Issues regarding the non-uniformity of wall thickness commonly develop during the manufacturing process of a pipe. Cold formed pipes are commonly manufactured using steel plates, which are deformed and bent in a particular manner to produce the final product. The deformations and bending are typically applied through mechanical presses, compressions and expansions. The process also includes bringing the two ends of the plate together and joining them through welding. During the manufacturing process, it is possible that the bending of the cross section of the steel plate fails to maintain a uniform thickness. The two edges that meet to close the pipe may also have different thicknesses. Any axial loading on such section will be eccentric to the true centroid of the cross section (Luzzi and Marcello, 2011). In cold bends and cold formed pipe elbows, thinning of a pipe section also occurs when pipes have relatively sharp bending radii. The outside edge of the pipe tends to thin out due to the much longer arc length compared to the inside of the bend (Luzzi and Marcello, 2011).

Inconsistent pipe wall cross sections in the axial direction of a pipe are also a type of imperfection. Discontinuities of wall thickness in a pipeline system may arise if the pipe segments are assembled with girth welds. Dorey et al. (2010) observed that circumferential girth welds can influence the location of a local buckle. Souza and Murray (1999) also observed that buckling typically occurred directly at circumferential girth weld locations. Yoosef-Ghodsi et al. (1994) observed that girth welded pipes have reduced buckling capacity compared to plain pipes.

The presence of different combinations of imperfections in line pipe can be even more detrimental. Pipes that require any type of welding should be considered for the possibility of having a misalignment imperfection. Misalignments can occur at the location of longitudinal seam weld in UOE manufactured pipes if the two ends are not lined up correctly, or at the location of circumferential girth weld, if the two

pipe ends do not match perfectly. It can be more damaging at locations of girth welds when combined with ovalization imperfection. Pipes with sharp bends causing thinning, in addition to the presence of girth welds can pose the risk of developing wrinkle, a common type of local buckle, which drastically reduces the moment capacity of a pipe (Dorey et al., 2001).

From the above discussion it can be summarized that, an imperfection can be pre-existing since the manufacturing process, or may be inflicted upon during installation and operation. Ovalization, non-uniformity of wall thickness in the circumferential direction, and misalignment of plate edge at seam weld location can be categorized as initial or pre-existing imperfections, and can be measured, repaired and/or considered in the design prior to installation. Dents, gouges, grooves and corrosion can appear during installation, operation, and due to environmental effects, and should be determined through inspection. Thinning of pipe wall in the longitudinal direction at sharp bends, ovalization and out of straightness due to insufficient support, and misalignment due to inconsistent pipe cross sections at girth weld locations can also be classified as operational damages and may lead to other type of imperfections such as wrinkles.

2.3 Codes and Standards on Imperfection (CSA Z662-11 and ASME B31.8)

Canadian Standards Association (CSA) standards are developed through a consensus standards development process approved by the Standards Council of Canada. CSA Z662-11 is the standard for oil and gas pipeline systems. The American Society of Mechanical Engineers (ASME) code is developed under procedures accredited as meeting the criteria for American National Standards. ASME B31.8 is the code for pressure piping.

There are three possible sources of pipeline imperfections: manufacturing of the pipe segments, installation of the pipeline, and finally operational damages. Operational damages are usually attributed to ground movements, environmental effects and/or third party induced mechanical damages. There are different types of imperfections that can be caused by the above sources, that include ovalization, dents, gouges, cracks and corrosion. According to CSA Z662-11, ovalization is the change in pipe cross section from a circular to an elliptical shape and is measured by the difference between the maximum and minimum

outside diameters divided by the average outside diameter, all measured at a particular cross section. CSA Z662-11 considers ovalization to be induced as a result of fabrication, installation and repair. According to CSA Z662-11, a dent can be defined as a depression caused by mechanical damage that produces visible disturbance in the curvature of the pipe wall, without affecting the thickness. CSA Z662-11 quantifies a dent as the measured distance between the lowest point of the pipe wall to the prolongation of the original contour. This is consistent with the ASME B31.8 definition of a dent as a permanent deformation of the circular cross section of the pipe that produces a decrease in the diameter and is concave inward. Gouges are defined by CSA Z662-11 as surface imperfections caused by mechanical removal or displacement of metal that reduces the wall thickness of the pipe. Again, this definition is consistent with ASME B31.8 definition as a mechanically induced metal loss. In general, the ovalization deformation can be considered as an imperfection due to manufacturing and/or installation, while dents, gouges, cracks and corrosion can be considered as operational damages.

Both the CSA Z662-11 and the ASME B31.8 suggest limits on the different imperfections, beyond which a pipe segment is needed to be repaired or rejected. ASME B31.8 does not provide any limit for ovalization. Regarding ovalization, CSA Z662-11 suggests that the critical value should be determined by valid analysis methods or physical tests and also provides a limit of 0.03 in the absence of detailed information. The limits for dents, however, are fairly consistent in CSA Z662-11 and ASME B31.8. In CSA Z662-11, the limit for an acceptable dent depth on the pipe body with a diameter less than 101.5 mm is 6 mm or less. For pipes larger than 101.5 mm, the maximum acceptable dent depth is 6% of the pipe outside diameter. This particular limit does differ from ASME B31.8, however, the CSA code does address that the designer should consider limiting the depth of plain dents to 2% of the outer diameter, which happens to be the ASME B31.8 limit. For pipes that have dents located on a mill or field weld, CSA Z662-11 specified limit of a dent depth beyond which the dent has to be repaired is 2% for pipe sizes larger than 323.9 mm, and 6mm otherwise. For pipes larger than 323.9 mm, the limit in CSA Z662-11 follows the ASME B31.8 limit of only allowing 2% of outer diameter as a dent depth.

According to CSA Z662-11, if any dent is outside the suggested boundaries, or contains stress concentrators such as gouges, grooves or cracks, the pipe is required to be repaired by either grinding or full replacement of the pipe section unless determined by an engineering assessment to be acceptable. ASME B31.8 also suggests that dents containing stress concentrators should be removed.

The current standards and codes provide clear guideline on the acceptance criteria for operational damages such as dents, gouges, grooves, and corrosion, and their repairing methods. Guidelines on pre-existing imperfections such as ovalization are, however, not very elaborate. ASME B31.8 does not provide any limit for ovalization. CSA Z662-11 proposes that the critical ovalization value should be determined by valid analysis and/or physical tests, and suggests a limit of 0.03 in the absence of detailed information. The codes also fail to consider the different imperfections as design parameters in their design equations.

2.4 Research on Measurements of Imperfections

A pipeline is a cylindrical element and it is very challenging to measure its different geometric features. Pre-existing or initial imperfections such as ovalization or non-uniform wall thickness are impossible to identify visually. Initial imperfections can be identified in laboratory by measuring the distances of predefined points on the pipe surface using dial gauges and linear variable differential transducers (LVDT). Operational damages, such as dents, gouges, grooves, corrosion, etc. can be identified visually, and have to be measured in the field using mechanical measurement methods. Real time monitoring of pipe pressure can be employed as an indicator of the development of pipe leaks while in service.

Measurement of initial imperfections has been a major focus of research in energy pipelines. Bailey et al. (1984) used a series of dial gauges mounted along an aluminum channel. This device measured the distances of selected points on the inner wall surface of the pipe to an assumed longitudinal axis. They also devised a method to measure the imperfections externally for pipes with small diameter. Chen et al. (1993) and DeIcol et al. (1998) used similar apparatus for measuring initial imperfections from the inside of the pipe. Their apparatus consisted of an aluminum tube placed along the center of the specimen and

secured to the ends. The whole setup was in a vertical position to avoid sagging of both the pipe and the tube under self-weight. An aluminum track, a carriage, and an LVDT were mounted to the tube. The aluminum tube was able to rotate about its longitudinal axis and the carriage moved along the track. Thus the LVDT was able to measure distances of inner surface of pipe wall with respect to the tube. Dorey et al. (2001) further refined the measuring apparatus with high precision machined rail.

The above mentioned methods need days of preparation and have multiple sources of error that can hardly be eliminated. There are always errors due to the out of straightness of the rail and its misalignment to the center of the pipe specimen. The position of the LVDT at the time a measurement is recorded cannot be controlled accurately. The angle of the instrument is the most difficult degree of freedom to control. It is possible to overlook imperfections such as small dents which may be positioned between measuring grids. These methods can only be applied to specimens that are short enough to be positioned vertically and the measuring points have to be accessible by the operator from the outside of the pipe.

It is possible to identify operational damages such as leaks, that develop while the pipe is in service, but very difficult to locate precisely. Abnormal pressure fluctuation is an indicator to leaks in the system. Intelligent pigs are also used for this purpose. The term pigs or intelligent pigs refer to the use of robotic vehicles that carry measurement equipment down a pipeline to gather data on the health and status of the pipe. The pigs can be categorized as a Metal Loss Pig, Leakage Pig or Pipe Geometry Pig (Reed et al. 2004). Chou (2010) developed a method to monitor the health of buried pipelines continuously by using distributed strain sensory systems and a trained Artificial Neural Network (ANN). This system can provide a significant monetary gain to the corporations owning a pipeline by allowing them to not require a total shut down of a pipeline in order to determine the condition of a pipe. It also provides safety to the general public by reducing the risk of a sudden failure in between inspection cycles.

Imperfection measurement is a substantial field of research with good prospect. Initial imperfections are relatively easy to measure compared to operational

damages. Knowledge on initial imperfection is necessary for designing safe and durable transmission systems. Operational damages, on the other hand, are more challenging to assess and restore, and have pronounced economic effects. Therefore, initial and operational imperfections are equally important to evaluate.

2.5 Research on Initial or Pre-existing Imperfections

Initial imperfections are inflicted upon pipelines during the manufacturing process. A number of studies have been carried out to identify the geometric and material imperfections that arise during the manufacturing of pipelines and their effects on the structural behaviour of the pipelines. The experimental and analytical studies carried out on initial imperfections typically comprises of taking physical measurements, developing idealized imperfection models, incorporating the actual and/or idealized imperfections in numerical analysis, and comparing them with experimental results. The material imperfections developed during pipe manufacturing have also been studied by several researchers.

Chen et al. (1993) examined the effects of three types of initial imperfections on the buckling response of stiffened cylinders. Both the experimental and numerical tests were modeled from existing pipes with 3 mm and 5 mm thickness and measured for imperfections using the mechanical measurement methods described in the previous section. The measured pipe imperfections were classified as: Out-Of-Straightness, Variation of Radii, and Out-Of-Roundness. Since the pipes had existing imperfections, Chen et al. (1993) incorporated them in their numerical model but did not perform a parametric study. They were unable to quantify the negative effect of each individual type of imperfection, as the three different types of imperfections were present altogether with relatively similar magnitudes and on cylinders with two different thicknesses. However, Chen et al. (1993) had experimental results of eight other cylinders without any initial imperfections present and were able to compare between the perfect and imperfect specimens. It was noted that the bending behaviour and failure mode of the perfect cylinders were similar to the cylinders with imperfections. Furthermore, Chen et al. (1993) observed that the bending moment was reduced between 1% and 7% due to the presence of the imperfections. Although Chen et al. (1993) were able to effectively measure the initial imperfections and model the buckling behaviour of stiffened cylinders, the initial imperfections were

considered moderate and it was difficult to quantify their effect on pipeline buckling behaviour. It should also be noted that the outside diameters of these pipes ranged from 2.5 meters to 4.0 meters, and cannot be representative of oil and gas pipes.

DelCol et al. (1998) studied the behaviour of large pipelines with a diameter to thickness ratio of 92 under the combined application of internal pressure, axial compression, temperature variation, and imposed forces from deformations typically imposed on pipelines in the arctic regions. They performed full scale buckling tests on four pipelines with existing measured imperfections and then simulated the results through numerical models. DelCol et al. (1998) used the mechanical measuring devices described previously to determine the maximum and minimum initial imperfections. The measured imperfections were the difference in the measured radius to the nominal radius of the pipe. Their way of defining imperfections did not differentiate between out of straightness, out of roundness or deviation in radius. The results from DelCol et al. (1998) illustrated that the size of imperfection had negligible effect on the peak moment capacity of the pipeline. However, the specimens with the largest imperfections displayed significant reduction in the critical strain and curvature. Hence, their experimental results indicated that imperfections reduce the ductility of a pipeline, causing it to fail at lower deflections. The numerical models analysed in their study also demonstrated minor effects of imperfection on peak moment capacity, but substantial effects on their behaviour in the post buckling stage. Thus, DelCol et al. (1998) were able to validate that only a minor imperfection can reduce the buckling capacity of a pipeline, making it susceptible to failure after a small amount of deformation. Furthermore, it was demonstrated numerically that the overall moment capacity is not significantly affected by imperfections.

Dorey et al. (2006) also performed detailed measurements on initial imperfections. Their study focused on developing a simple idealized model that could summarize the imperfections in a pipe. They developed a detailed finite element model using the actual measurements of a pipe surface by methods described in the previous section. The detailed model was able to accurately predict the buckling behaviour recorded during the laboratory experiments. They then developed a simplified finite element model by assuming three types of plain

initial imperfection patterns: the ring, the half-ring, and the blister. The responses of the simplified models were compared to the detailed model and the experimental results. It was observed that the responses of the blister type imperfection closely agreed with both the experimental results and the detailed finite element model. The buckling responses of the three imperfection patterns were also compared to that of a perfect pipe. Their study showed that, neglecting imperfections would drastically overestimate the degree of curvature (Dorey et al., 2006).

2.6 UOE Forming Process and the Mechanical Behaviour of UOE Pipes

Adeeb et al. (2006) investigated the anisotropic material behaviour that the UOE process induces on the longitudinal and circumferential directions. In order to accurately model the UOE process, Adeeb et al. (2006), modeled a flat plate, rolled it around a rigid cylinder, and expanded it by 1%. They were able to demonstrate that the UOE process drastically changed the material properties in both the circumferential and the longitudinal directions compared to the virgin material. The circumferential direction was stiffened while the longitudinal direction was softened, but both directions were still able to reach the same ultimate stress of approximately 650 MPa. Adeeb et al. successfully demonstrated that, modeling a pipeline considering the UOE process stiffens the bending behaviour and causes the pipeline to buckle at a lower rotation and slightly higher moment (Adeeb et al., 2006).

Shinohara et al. (2010) also studied the effects of anisotropic material formation during the UOE process on the buckling response of a pipeline. They conducted a parametric study of the amount of prestraining. Prior to modeling the buckling behaviour of pipeline, Shinohara et al. (2010) developed constitutive equations to replicate laboratory tension tests for different prestraining and directions. They were able to demonstrate that increased prestraining during fabrication or installation drastically alters the bending behaviour. Introducing a 6% prestrain significantly increased the bending resistance but drastically reduced the bending angle at the onset of buckling. They also concluded that the size of imperfection had a negligible reduction in bending resistance and significant reduction in bending angle.

Neupane et al. (2012) were able to demonstrate that anisotropic behavior of HSS pipes can be modeled using a yield surface translation in the stress space. In UOE forming process, a steel plate is first bent into a U shape, and then a press is used to convert the U into an O shape. The plate is then welded in the longitudinal direction, and finally, it is expanded in the circumferential direction. The expansion process induces 2% circumferential plastic strain. The stress strain behavior of the tensile coupons taken from these pipes depends on the history of loading. When a UOE formed HSS pipe is loaded in the circumferential direction, its yield point will be higher than the original plate material. When loaded in the longitudinal direction, its yield point will be lower than that of the original plate material. This is a result of strain hardening and Bauschinger effect, typically exhibited by elastic-plastic material subjected to cyclic loading. During the expansion stage in the manufacturing process, the yield centre moves in the stress space in the direction of increasing stress, i.e., the circumferential direction. Upon unloading and reloading, the yield point is expected to be higher than the original plate material in the circumferential direction, and lower in the longitudinal direction. Neupane et al. (2012) were successful in developing a combined isotropic / nonlinear kinematic hardening model that can capture the plastic anisotropy of HSS pipes accurately. They approximated the virgin material curve from the available experimental stress strain data and calibrated the material parameters for the backstress evolution laws through an optimization scheme. Their developed material model can be incorporated into Finite Element Analysis (FEA) software.

Fathi et al. (2012) also developed material models that are capable of representing the anisotropic behaviour of HSS UOE pipes. Their developed model was a combined hardening material model consisting of a linear isotropic, and Armstrong-Frederick kinematic hardening components. They calibrated the model based on available stress-strain data of HSS pipe material in both the longitudinal and the transverse directions. Their proposed model was able to successfully capture the anisotropic behaviour in the two directions in both tension and compression. Fathi et al. (2012) were able to validate their model by comparing numerical results of pipe buckling with those of full scale test results.

The progress of experimental and numerical studies on initial imperfections during the last few decades has been very promising. New techniques have been developed for detailed and precise measurement of imperfections. Detailed numerical models of pipes with measured imperfections have been developed that are able to predict structural behaviors accurately. The development of idealized imperfection models has resulted in simplified numerical analysis. The studies on material imperfections have revealed the actual material behaviour in different directions. It is now possible to combine the geometric and material imperfections together in one imperfection model and further the study on initial imperfections.

2.7 Research on Operational Damages

Operational damages such as dents, gauges, grooves, corrosion, pipe wall thinning, ovalization, out of straightness, misalignment at girth weld, etc. are inflicted upon pipes during installation and operation. These imperfections may lead to the development of other types of imperfections during service and result in pipe failure.

Souza and Murray (1999) performed a study to simulate the behaviour of girth welded pipes with misalignment imperfections, where finite element models were analyzed and compared with experimental results. In this study, NPS 12 and NPS 20 pipes were physically tested under pressurized and unpressurized conditions. It was found during these tests that for pipes that were pressurized, a bulging buckling mode developed. For unpressurized pipes, a diamond buckling mode formed. Souza and Murray (1999) verified that wrinkling will form at the same moment at which the global curvature of the pipe reaches the softening point, otherwise known as the point where the moment capacity will begin to decrease rapidly with increasing curvature. Two different types of misalignments were considered by Souza and Murray (1999). The first was described as an "Offset Imperfection". The other was called an "Elliptical Imperfection", where two pipes with out-of-roundness imperfections are connected at 90 degrees with each other. The study was able to successfully recreate the physical buckling phenomenon in an analytical setting. When comparing the curve for the average end moment vs. average curvature, it was found that the results were quite acceptable. However, the correlation between the numerical and test results for

the pressurized pipe was not as accurate as the unpressurized pipe (Souza and Murray, 1999).

The misalignment imperfections studied by Souza and Murray (1999) were also used by Torselletti et al. (2005), who compared the analysed bending moment capacity using finite element and the design moment provided by DNV OS-F101. They analysed models with offset misalignment from 0mm to 3mm and ovalization (elliptical) misalignment from 3mm to 8mm. This study analyzed X65, X70 and X80 pipes with a diameter to thickness ratio ranging from 35 to 60. The applied load combinations included pure bending, bending and internal differential pressure. The analysis found that the DNV equations for the limit bending moment should be reduced from 5% to 10% to match the results from the finite element model. The 10% reduction was for the case where the ovalization imperfection was 1.0% of the cross section and a 90 degree ovalization misalignment (Torselletti et al. 2005). The reduction suggested by Torselletti et al. (2005) also depends on the amount of internal pressure. DNV equations for calculating longitudinal strain did not require a reduction when considering girth weld misalignments (Torselletti et al., 2005).

Al-Showaiter et al. (2008) carried out another research considering pipelines with only offset misalignments but with different orientations of 0, 45 and 90 degrees. Within each orientation the amplitude of the misalignment was varied to a maximum of 1.6 mm which is the limit imposed by CSA Z-662 (2011). This study did not consider the ovalization imperfections or nonuniformity of the pipe wall thickness. The parameters investigated in this study were misalignment amplitude, misalignment orientation, internal pressure, axial force and the diameter to wall thickness ratio. The study showed that the curvature limit decreases significantly for only 0.2 mm misalignment amplitude. At the maximum amplitude tested, there is a drop of 10% in the moment capacity and up to 60% drop in curvature limit. It was observed that with increasing internal pressure, the peak moment achieved by a pipe greatly reduces. The study by Al-Showaiter et al. (2008) also concluded that with increasing axial force, the load capacity and curvature limit both decreases. The shape of the buckle achieved in the finite element models agreed with the findings by Souza and Murray (1999). For unpressurized condition, the pipe formed a diamond mode buckle whereas the

pressurized pipe formed a bulge mode buckle. When considering the equations provided by DNV OS-F101 standards, a reduction factor does attempt to reduce the strain capacity due to the presence of a girth weld. Findings by Al-Showaiter et al. (2008) suggest that the equations provided by the standards may not be conservative.

Barrett et al. (2009) conducted research to develop a robust finite element model that can properly represent the behaviour of a true girth welded pipe and studied parametrically the structural behaviour of the pipe due to imperfections of the girth welds. They were able to confirm the findings by Torselletti et al. (2005). In this study, the DNV equations also proved to be unconservative with regards to bending moment. They determined that the strain and moment capacity of the pipeline is greatly affected by the axial load ratio and the pressure effects. The applied pressure reduced the moment capacity and the longitudinal strain calculated using DNV equations by approximately 50%. Barrett et al. (2009) also states that the moment capacity reduces by 50% and strain capacity by 30% due to axial effects. The initial ovality imperfection was tested for 5%, 10% and 15% of the pipe wall thickness. The bending moment capacity reduced up to 10% and strains were reduced up to 35%.

The reviewed literature involving girth weld misalignments show that finite element analysis is an exceptional resource for performing studies on pipelines with girth welds. Souza and Murray (1999) developed an appropriate method to create a model that will behave according to physical specimens. The two different modes of buckling observed by Souza and Murray (1999) were also confirmed by the finite element study performed by Al-Showaiter et al. (2008). Torselletti et al. (2005) studied the accuracy of the DNV OS-F101 equation compared to finite element models. Under this study it was determined that the DNV equations were conservative enough to account for the reduction in moment and strain capacity due to the girth weld. These results do not quite coincide with studies by Al-Showaiter et al. (2008) and Barrett et al. (2009). Both these studies were focused on girth welded pipes and the acceptability of the DNV equations for moment capacity and strain limit. They agreed that the DNV equations are not as conservative as expected.

To ensure that a pipeline remains safe and reliable, Yatabe et al., (2004) studied the effects of geometric imperfections and material properties on pipelines undergoing large deformations. Knowing that a pipe bend is the weakest and is most prone to imperfections, they investigated imperfections in the bent and transition sections for both opening and closing modes. Yatabe et al. (2004) modeled a perfect bent pipe without any imperfections under both Closing and Opening mode. The failure mechanism for a perfect pipe was determined to be different when displaced in the closing mode and opening mode. Ovalization occurred for the closing mode compared to the formation of wrinkles for the opening mode. Furthermore, the opening mode was seen to withstand approximately 40% larger bending moment than the closing mode. Typically, the bent section of a pipe is the most critical due to ovality, varying wall thickness and varying bend radius imperfections which are formed during the bending process (Yatabe et al., 2004). For the finite element model, ovality was set to 2.5%, while the wall thickness distribution varied from 15 to 21 mm. Both an increase and decrease in bend radius of 22 mm was induced at a specific location. Similar to the perfect pipe, the imperfect bent section could withstand significantly more bending moment in the opening mode direction for all three types of imperfections. All three types of imperfections had negligible effect on the closing mode direction. Although the bending response was not altered by the 2.5% ovality, the bending angle was reduced by approximately 30% due to the variation in pipe wall thickness. Yatabe et al., (2004) was able to demonstrate that a bent pipe being displaced in a closing mode direction is not affected by the type of imperfections and can withstand approximately 40% less bending displacement than the opening mode direction. Furthermore, they illustrated that it is important to monitor and determine the variation in pipe thickness and bend radius in the bent section as these imperfections significantly reduce the amount of bend closing displacement it can withstand prior to failure.

Veerappan et al., (2010) developed interaction diagrams from equations to determine the allowable internal pressure accounting for ovality, thinning, pipe diameter and pipe bend radius. The interaction diagrams were modeled and tested against 400 different pipe bends using finite element analysis. Veerappan et al., (2010) took five acceptable criteria equations from ASME 2007 and

modified them into two dimensionless allowable internal pressure ratio criteria. Ovality and pipe wall thinning were varied in their finite element model to develop interaction diagrams. Each individual interaction diagram is for specific bend ratio, bend radius divided by diameter, and thickness ratio, thickness divided by diameter. Unlike traditional pipeline design, these interaction diagrams allow the use of pipe bends with different degree of ovality or thinning instead of having to keep both individually below a tolerance value. The use of such interaction diagrams is a more efficient way to design for pipe bends accounting for ovality and thinning compared to traditional tolerance limits. Unfortunately, the interaction diagrams were only developed for D/t ratio of 1, 10, 15 and 20 while the oil and gas pipelines can be very large. While the interaction diagrams are for small D/t ratio, Veerapan et al. (2010) have demonstrated the type of design tools which could be developed for pipelines accounting for imperfections.

Villarraga et al. (2004) dedicated their research to developing a method for analyzing buried pipelines with initial imperfections. Pipelines in the field are typically far from being straight and have been known to show up to a 25% reduction in the longitudinal stress resulting from hot pressurized fluids. Villarraga et al. (2004) accounted for out of straightness imperfections in their analyses model. The research showed that increasing the imperfection reduced the maximum stress developed below the ASME design code value.

Cumming and Rathbone (2010) investigated the potential to alter Euler's Buckling Equation to determine the critical buckling force in a pipeline segment. They looked at out of straightness geometric imperfections and provided insight into using closed form buckling equations for pipe design. They believed that the critical length for buckling will be the length in which the Euler buckling force and the frictional restraint are both overcome. Their theory came from the idea that if the applied force exceeds the buckling force but not the friction force, the pipe will only displace but not buckle. Cumming and Rathbone (2010) equated the length term in the Euler Buckling Equation and frictional restraint force resulting in a potential perfect pipeline buckling equation. The equation was compared with finite element analysis of pipes having different bend radius in order to validate its accuracy. Using the theory from Euler, Cumming and Rathbone (2010) were able to develop a buckling equation for pipelines without cross sectional imperfections.

The equation can be used to determine what the critical offset angle that can be allowed when laying a pipeline down. This approach allows for the designer to set the critical offset angle allowed during construction to ensure that buckling will not be a concern.

Tianfeng et al. (2010) focused on Pipe-in-pipe (PIP) systems, which are widely used for high temperature pipelines that are most vulnerable to buckling. Their finite element models accounted for out of straightness imperfections in the pipelay but not geometric imperfections in the cross section. The PIP system buckling resistance and post buckling behaviour was investigated for three and four connection segments of pipes. Tianfeng et al. (2010) demonstrated that the postbuckling behaviour could either resist additional axial force or may result in drastic loss of axial resistance depending on the number of pipe segments and the magnitude of out of straightness.

Pipe bending imperfections are unavoidable and their effect on pipelines must be accounted for in proper design. Both Yatabe et al. (2004) and Houliara and Karamanos (2011) were able to illustrate that it is critical to determine the variation in pipe thickness and bend radius as these imperfections significantly reduce the amount of displacement a bend can withstand prior to failure. Yatabe et al. (2004) showed that ovalization imperfections hardly affected the pipe and the maximum bending moment experience negligible change due to any imperfection. Yang et al. (2008) used finite element analysis and the British Standard to determine that a real pipeline imperfection was above the critical flaw size causing the pressure to be reduced 50% to prevent buckling. Acceptable criteria equations from ASME 2007 were modified and tested by Veerappan et al. (2010) to develop very useful interaction diagrams for a more efficient pipe bend design accounting for ovality and thinning. Villarrage et al. (2004) showed that it is critical to know what the soil interaction will be with a curved pipeline in order to accurately determine whether hot pressurized fluids will cause buckling. Using Euler buckling theory, Cumming and Rathbone (2010) developed a new equation to predict buckling of a pipeline taking into account the out of straightness imperfection. Finally, Tianfeng et al. (2010) demonstrated the ability to design for buckling to occur in a pipe-in-pipe system to relieve axial stresses.

Houliara and Karamanos (2011) studied the elastic and inelastic buckling behaviour for varying degree of wrinkle imperfections. They were able to show that at a critical curvature, the effects of ovalization cause a reduction in the resisting moment. The imperfections modeled were waves on the compression face. An extremely small wave imperfection resulted in a catastrophic snap through buckle causing an instant reduction in moment capacity. For a more typical imperfection size, the maximum moment is reduced by 15% but a gradual reduction in moment resistance occurs. Houliara and Karamanos (2011) observed that the more dramatic reduction in moment resistance and curvature occurs for smaller imperfections, while increased imperfections have a larger effect on the amount of curvature the pipe can withstand prior to failure.

Yang et al. (2008) investigated a single offshore pipeline with local buckling imperfection near the girth weld using finite element analysis. They used the results from the finite element model and British Standard BS7910:2005 to plot the actual flaw and critical flaw size respectively. Yang et al. (2008) investigated the condition of a single flaw and determined that its magnitude was outside the critical level using finite element analysis and the British Standard.

Jiao and Kyriakides (2009) investigated the consequences of cyclic loading on perfect pipes. Their experiment intentionally ensured that there were as few imperfections as possible instead of studying the effect of varying imperfection amplitude. The perfect pipe was loaded to its ultimate stress and then unloaded and loaded repeatedly. During loading and unloading the wrinkle growth was measured to observe the concentration and buckling of the originally perfect pipe. Jiao and Kyriakides (2009) collected the laboratory experimental results and compared them to their finite element analytical results. The analytical results slightly exaggerate the deformation but both analytical and experimental data followed a similar curve showing that after a specific number of cycles the pipe buckles. Although Jiao and Kyriakides (2009) investigated a perfect pipe, it is apparent that cyclic loading from temperature and pressure changes can cause accelerated failure for pipelines with imperfections.

2.8 Conclusion

This chapter reviewed the research and findings developed in the areas of imperfections of pipelines. It can be seen that the improvement in computer processing power and the use of numerical analysis has opened the possibility of using computer models to perform research on the effects of imperfections on the structural behaviour of pipelines.

The definitions of different pipeline imperfections have become more detailed as research has discovered that each form of imperfection can affect the structural behaviour of pipes in different ways. There is a gap between the definitions that have been defined through research and what is considered acceptable in the current standards and codes. The CSA and ASME codes acceptance criteria only appear to focus on defects that can be visually detected, such as cracks, gouges or dents. A primary reason for this simplicity may be attributed to the fact that the limits for the other defects such as out-of-roundness (ovality), out-of-straightness, radii variation, and non-uniform wall thickness still have not been clearly defined or researched. Current available measurement methods are also a limiting reason for the standards to not define a proper acceptance criterion for pipes.

The current methods for measuring the structural health of a pipeline are quite time consuming. Mechanical robots such as intelligent pigs are used to travel down pipelines with different measuring devices which can capture certain properties of the pipe. There are other methods such as a pressure system which allows an owner to predict if there is a problem and provide limited information to be able to assess the condition of the pipe.

The studies that focused on pipelines with girth welds found that the DNV OS-F101 equation for critical strain may provide a higher moment and strain limit than the results from finite element models. The equation does allow for a factor for girth welds, but the factor itself is only based on the pipe diameter to wall thickness ratio. This factor needs to be reviewed in further research to include the effects of misalignment as it was determined by the studies that this imperfection combined under certain load combinations can reduce the moment and strain limit up to 50%.

Cross sectional imperfections are considered the most difficult imperfection to design for due to the unpredictable magnitudes, locations and effects. Similar to girth welds, the current equations do not account for all of the possible difficult cross sectional imperfections that can exist. Several researchers were able to demonstrate that a minor imperfection will instantly reduce pipelines ductility but have insignificant effect on the maximum moment capacity, similar to bending imperfections. It was also noted that after the initial reduction in ductility due to a small imperfection, larger imperfections had a smaller reduction in comparison. Therefore, since it is always known that there will be a degree of cross sectional imperfections, modeling at least a minimal amount should account for the effects. Using this theory, a simple idealized blister imperfection was able to summarize the total effect of a complicated measured imperfect surface using finite element analysis. These findings help to provide an understanding of the effect of cross sectional imperfections and ways to simplify these difficult imperfections for a fast and safe design.

The understanding of the anisotropic behaviour of HSS UOE manufactured pipe material is at an advanced stage compared to the understanding of the initial geometric imperfections typically present in them. Idealized imperfections have always been included in numerical models, which were able to predict the buckling behaviour of pipes quite closely. These idealized imperfection models were not developed based on measurements taken on UOE manufactured pipes. Moreover, the individual effects of each type of imperfections are yet to be studied extensively. The type of imperfections typically present in UOE pipes have not been investigated elaborately. Therefore, it is possible that the imperfection models previously used might not be appropriate for UOE manufactured pipes. Accurate anisotropic material models being at our disposal, a comprehensive research on initial geometric imperfections of UOE manufactured pipes is required to understand which imperfections are most influential on the buckling behaviour of pipes.

CHAPTER 3: MEASUREMENT OF GEOMETRIC IMPERFECTION USING 3D LASER SCANNER

3.1 Introduction

Reverse engineering technologies in the field of inspection, quality control, and integrity management of industrial products have evolved and advanced rapidly in the past decades. With little or no additional knowledge about the manufacturing procedures, reverse engineering enables the deduction of the defects and their sources from the end product. In recent years, with the increased processing power and graphic display capabilities of computers, reverse engineering has become a viable method for creating 3D virtual models of physical objects. Reverse engineering, in conjunction with Computer-aided Design (CAD), has become a powerful tool in the creation, analysis, modification, and optimization of industrial products (Varady et al., 1997).

The process of reverse engineering comprises of constructing the 3D model of an object from the data acquired by taking measurements. The methods for acquiring data can be broadly classified as Non-Contact Methods and Tactile Methods. Each method requires a technique or mechanism to interact with the surface of an object in order to acquire physical readings. From the physical readings obtained, a further analysis is necessary to determine the position of points on an object's surface (Varady et al., 1997). Regardless of the method being employed, the acquired data is a point cloud of geometric samples on the surface of the object, which can later be interpolated to reconstruct the object's shape.

Tactile methods include the use of mechanical arms and Coordinate Measuring Machine (CMM), which probe an object through physical touch while collecting surface data. Different robotic devices are available for tactile measurements. These methods are very robust and accurate, although their speed is limited by the slow movements of the articulated arm. The use of CMM is very popular due to its ability to follow paths along a surface and collect accurate and noise free data. Tactile methods are mostly employed in the manufacturing industries (Jahne et al., 2000).

Non-Contact methods commonly use light, sound, or magnetic fields to interact with an object's surface. In an acoustic method, a sound wave is emitted from a source and reflected from the surface of an object. From the known speed of the sound wave, the distance between the source and the surface is determined. The magnetic field measurement method senses the strength of a magnetic field source to determine and record point data within a field. The optical method is by far the fastest method for measuring shape and geometry. Optical methods generally employ the ambient radiation from an object, laser point, laser line, light beam, or structured lighting. The projection of the radiation is commonly sensed by camera(s). Different techniques have been developed and are currently employed to determine the depth of the surface points from the source of illumination and the camera(s).

The cost of 3D optical sensors has decreased dramatically in recent years, and the potential of this technology has expanded beyond the entertainment industry. This chapter focuses on the application of 3D sensors and reverse engineering technologies in the field of pipe inspection and analysis.

3.2 Metrology

The science of measurements is referred to as metrology. "A measurement is a series of manipulations of physical objects or systems according to a defined protocol which results in a number" (Simpson et al., 1981). Technical metrology is a special class of metrology that deals with dimensional compatibility and conformation to design specifications in order to ensure the proper functioning for the intended use of an object (Simpson et al., 1981). Metrology is an integral part of quality control in manufacturing industries. The fundamental concepts in metrology are discussed in the following sections:

3.2.1 Basic Concepts

The three basic concepts to be aware of in metrology are error, accuracy, and precision. The scope of this research only involves linear measurements such as length and thickness. Therefore, the concepts are discussed in that context.

The error of a measurement can be defined as the difference between the indicated value and the true value. The true value of a quantity being measured is in most cases unknown. Total error can be resolved into two types:

Random error: Errors that are accidental in nature, their fluctuation is unpredictable. It is not possible to correct random errors that may arise from various reasons such as a lack of equipment sensitivity or noise in the measurement.

Systematic error: Errors that are not usually detected by the repetition of a measurement operation (Darmody 1967). Systematic error tends to shift all measurements that causes the mean value to vary constantly in a predictable way. It can be corrected only if a true value is known.

Accuracy is the degree of closeness or agreement of a measurement with an accepted reference value (ASTM 1977). Every measurement apparatus has an accuracy specified by its manufacturer that takes into account the errors associated with measurement. For example, if a micrometer has a specified accuracy of ± 0.02 mm, and it measures a particular dimension to be 2.5 mm, the true value of the measurement will be a value between 2.48 mm and 2.52 mm.

Precision is the degree of how well identically performed measurements agree with each other (American Society for Testing and Materials 1977). This concept is applicable to a set of measurements, because individual measurements tend to scatter about their mean value (Borrer et al., 2009). However precision of measurement may also refer to the smallest division of a measuring instrument. For example, a ruler with a 1 mm minimum division has a precision of 1 mm.

3.2.2 3D Metrology

The concepts of applied metrology are not applicable in the field of 3D metrology. As mentioned previously, 3D optical sensor is the widely used tool in 3D metrology. Unlike conventional length measuring apparatuses, 3D sensors produce point clouds, from which, the shape and dimensions of an object is later extracted. The accuracy of 3D sensors is inherent in its capability to calculate the coordinate of a point on an object with respect to a reference 3D coordinate origin. Their accuracy is specified as "Volumetric Accuracy", which takes into account the positioning error in each direction of the coordinate axes, and the angular error about each coordinate axes (Wang et al., 2003). ISO 230-6 (2002), and ASME B5.54 (2005) provide the guidelines for measuring the volumetric accuracy of 3D optical sensors.

3.3 An Overview of 3D Optical Sensors

3.3.1 3D Optical Sensors

3D optical sensors are capable of producing the shape and the complete 3D geometry of an object. A 3D optical sensor may be based on one of three basic principles: a) Triangulation, b) Time of Flight Measurement, and c) Interferometry. Triangulation technique involves determining the depth of an unknown point within a triangle. From the known values of the triangle base and side angles pointing towards the unknown point, the depth information is calculated through trigonometry. Time of Flight technique acquires the depth information by measuring the time of flight of a light signal and based on the known speed of light. Interferometry also employs time of flight, but deduces the surface information from the interference pattern of the emitted and reflected electromagnetic wave.

The depth information, also referred to as the 'Depth Map', acquired by a 3D sensor is basically a spatial point cloud on a regular grid of a preferred coordinate system. The advancement of computer graphics and computational capabilities has enabled the fast visualization and analysis of these point clouds. The measurement uncertainty of depth maps, on the other hand, still has its limitations with regard to the speed of acquisition, the size of an object, and the surrounding environment of the object.

In metrology, the precision or uncertainty of measurement refers to the scattering of the measured values with respect to a true value of the measurand. The accuracy or systematic measuring error, on the other hand, is the degree of closeness of the measured value to the true value. Relative uncertainty is the ratio of the measured uncertainty to the measured value. In case of 3D sensors, the measurement uncertainty can be expressed in terms of the depth measuring range and the depth resolution. Depth measuring range is the range of the distance, between which a 3D sensor is able to acquire point clouds on a target object's surface. Depth resolution is the minimum difference of depth that can be measured by a sensor. Therefore, relative uncertainty for 3D sensors is the ratio of the depth resolution to the distance of the object from the sensor (Jahne et al.,

2000). A measuring system can be very precise but inaccurate, with the degree of inaccuracy being much larger than the precision.

Many research works have been devoted to the comparison of different depth measuring techniques. Jahne et al. (2000) reported that the measuring uncertainties of the three principles of measurement have different correlations with the measurement depth. The uncertainty of triangulation has a quadratic relationship with depth. Uncertainty of time of flight is linearly proportional to the measurement depth, while interferometry shows inversely proportional relationship between uncertainty and depth.

Interferometry has the lowest uncertainty, while its depth range is limited between micrometers to meters. It is best suited for surface topology measurements in industrial manufacturing. Triangulation has a bigger depth range, between millimeters to hundred meters, while its precision is comparatively low. Time of flight has depth range in the order of ten kilometers, with its precision being the lowest among the three.

Each principle has its pros and cons specific to the type of application. Clearly, there is no best method of the three, but should rather be chosen based on the particular requirements of the application. The inspection and measurements of pipelines are in most cases required to be performed onsite. The limitations of 3D sensor application in the inspection and measurement of pipelines are mainly associated with the size of the object, available clearance around the object, and the surrounding environment. Therefore a 3D sensor should be portable, unsusceptible to light exposure, and operable within a minimum clearing around an object, without compromising its accuracy and precision to fulfil the requirements of pipe inspection. Triangulation depth sensors seem to meet these requirements. While its accuracy can be lower than interferometry, significant improvement can be achieved with the help of photogrammetry, which will be discussed in the following sections.

3.3.2 3D Triangulation Scanner

Triangulation scanners can be active or passive. A passive scanner detects the ambient radiation reflecting off of an object and creates points cloud through triangulation. An active scanner on the other hand, requires a structured

illumination. Active triangulation scanners most commonly use laser dot or line to probe an object's surface. When the emitter of the scanner projects a laser dot on the object's surface, it appears in the camera's field of view. The emitter, the laser dot, and the camera form a triangle and from the known angles and distances, the depth of the single point on the surface corresponding to the laser dot is obtained.

Line sensors use similar principle, but project a narrow laser line instead of a single dot. This is known as light sectioning, where the laser light projected onto a surface appears distorted from different perspective views, and the triangulation technique enables the exact reconstruction of the geometric profile of the surface. The two methods are shown in Figure 3.1.

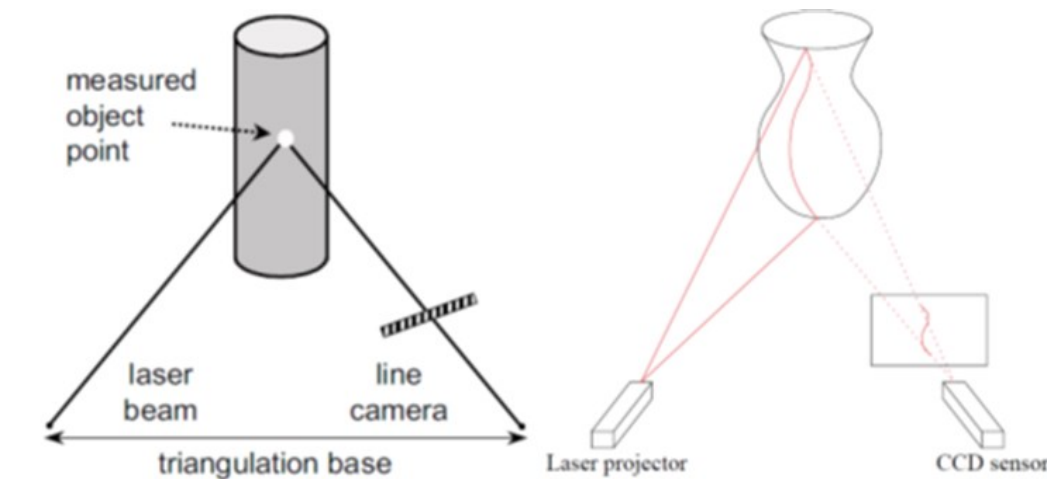


Figure 3.1 Triangulation based laser point and laser line sensors (Jahne et al.)

Depth measurement using triangulation relies on projecting a laser beam onto an object from the emitter (Figure 3.2). The distance of the laser origin and the focal point of the camera's lens is b . The distance of the projected laser dot and the origin of the laser is l . The distance of the laser dot from the camera's focal point is the depth d , which is the measurand. The lengths b , l and d form the three sides of a triangle. 3D optical sensors usually have the camera and the laser emitter integrated in a system where the base length (b) and the two angles θ and φ are known. Therefore the value of the depth (d) can be calculated using

geometry and the law of Sine from Equations 3-1 and 3-2. This is the principle of triangulation in its simplest form.

$$\theta + \varphi + \gamma = 2\pi \quad 3-1$$

$$\frac{b}{\sin \gamma} = \frac{d}{\sin \varphi} = \frac{l}{\sin \theta} \quad 3-2$$

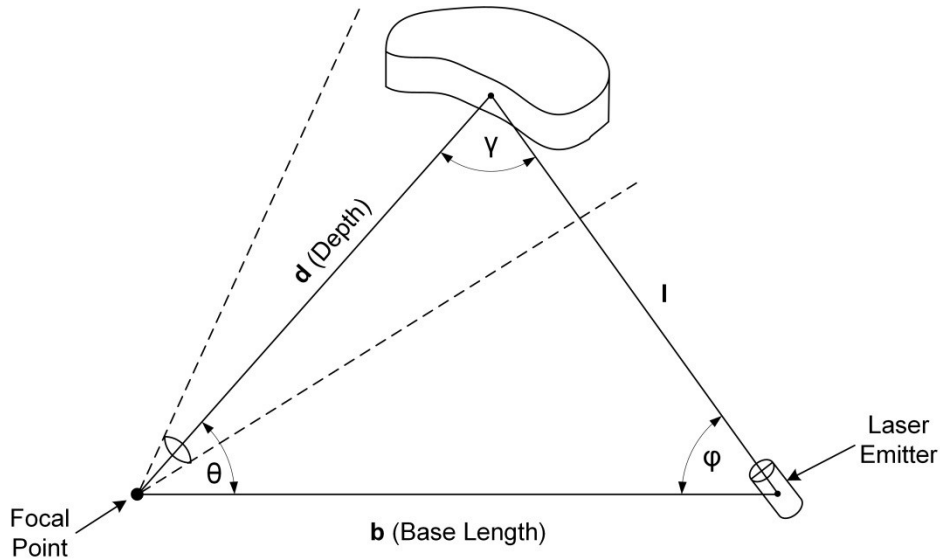


Figure 3.2 Principle of Triangulation for measuring depth

It is more practical to measure the coordinates of the laser dot in a Euclidian or cylindrical coordinate system instead of measuring the depth d alone. This is possible from the known attributes of the camera's field of view and frame resolution (Figure 3.3)

Let us consider the camera's field of view and its focal plane in a Euclidian coordinate system. The laser dot appears at point S on the camera's field of view, and its image appears at s' on the focal plane. Let the coordinates of S in the field of view be (X, Y) and the coordinates of s' on the focal plane be (x, y) . $d\theta$ is the angle between the lines connecting S and s' , and the coordinate origins of the two planes. $d\theta$ can be decomposed about the coordinate axes into $d\theta_x$ and $d\theta_y$. The coordinates of the point s' on the focal plane is known from the known values of the resolution of the camera (h and w). The angles $d\theta_x$ and $d\theta_y$ can be calculated from this known information.

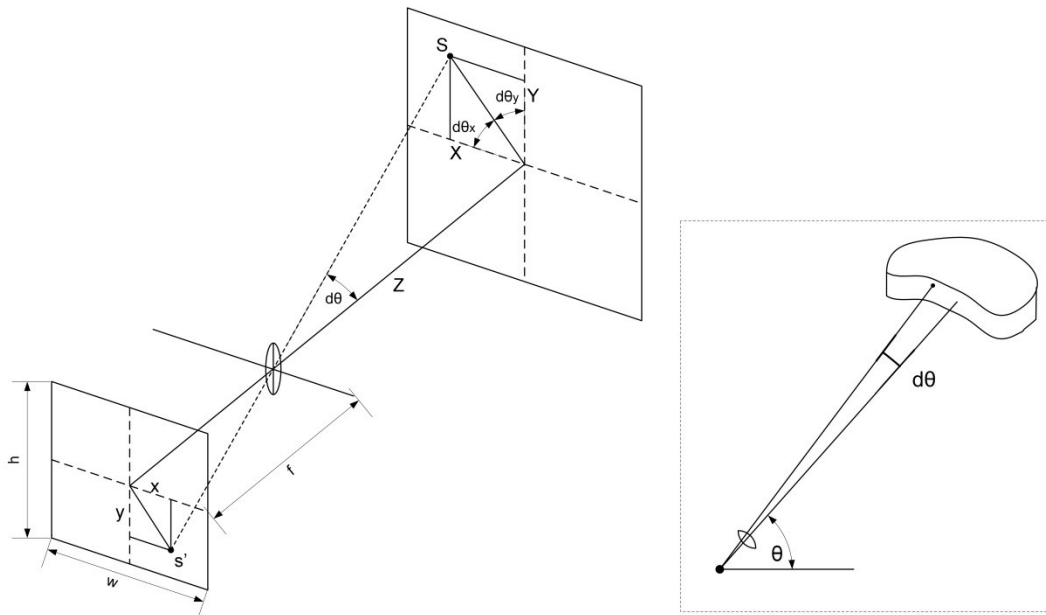


Figure 3.3 Calculation of a point coordinate from camera's field of view

The extraction of the X, Y, Z coordinates of the laser dot is therefore possible through the application of trigonometry and triangulation. The same principle is applicable to a laser line appearing in the camera's field of view instead of a laser dot. Laser line is advantageous in the sense that more information about a surface can be acquired with the same amount of effort.

Some 3D sensors employ the principle of active stereo vision in conjunction with triangulation. In stereo vision, two cameras are used instead of one to extract depth information of a point on an object. The two cameras acquire the depth information by looking at a location from two different viewpoints in space. The distance between the focal points of the two cameras and their angular orientations are known. The laser dot or line appears on the image plane of the cameras. The two cameras have different perspective views of the laser projection, and its coordinates can be calculated through triangulation. From the known geometric attributes (distance and angles) of the stereo vision system, the global coordinate of the point on an object is calculated (Figure 3.4).

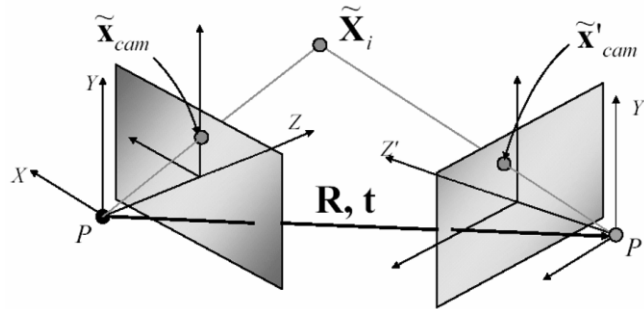


Figure 3.4 3D measurement by stereo vision sensors (Chen S. et al., 2008)

Close range photogrammetry is also known to be used in conjunction with 3D sensors. Photogrammetry is the technique of acquiring measurements from photographs. Stereo-photogrammetry, a more sophisticated form of conventional photogrammetry, is typically employed in stereo vision 3D sensors to achieve higher accuracy. Stereo-photogrammetry involves measuring 3D coordinates of points from two or more pictures taken from different perspectives. After identifying the common points on each picture, the line of sights corresponding to each camera can be determined. The intersecting points of the line of sights can be calculated through triangulation, which describe the 3D location of the points. The overall quality of photogrammetric measurement of a 3D sensor relies on the accuracy of calculating the intersection points (Jahne et al., 2000). The use of artificial target points is known to have significant improvement to this regard. Artificial targets are typically highly reflective and have specific geometry (Figure 3.5). Reflectivity is a requirement for good optical quality of a target, and specific geometry aides to the recognition of targets of a 3D sensor system. These targets can be used not only as a reference background (Figure 3.6), but also on an object to acquire surface information.

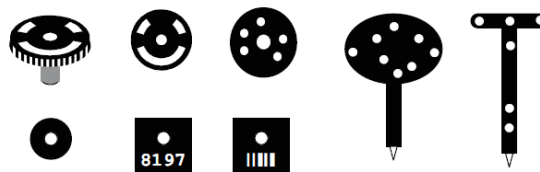


Figure 3.5 Different types of artificial targets (Jahne et al., 2000)

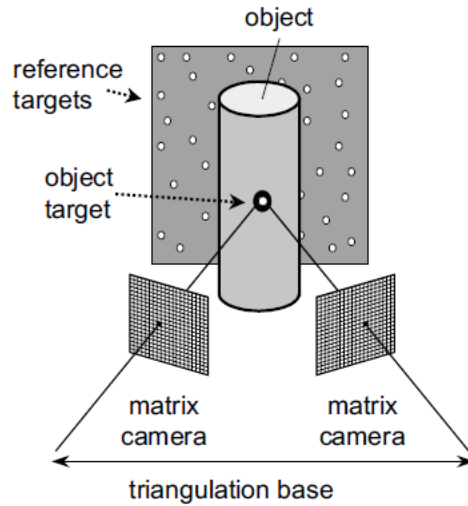


Figure 3.6 Use of reference targets on the background and surface of an object (Jahne et al., 2000)

Stereo vision 3D sensors are able to calculate the coordinates of the artificial targets at high precision and create a target map through photogrammetry prior to measuring point coordinates on an object (Jahne et al., 2000). The known coordinates of the targets assist towards the precise calculation of the surface point coordinates of an object. As a result, the use of artificial targets in conjunction with stereo-photogrammetry results in higher accuracy and faster data acquisition.

In pipeline inspection, the most influential factors for selecting a measurement system are portability, sensitivity to light exposure, and clearance requirements. Many portable 3D triangulation sensors are currently being produced by different manufacturers. Among these, some 3D sensors use laser light to probe an objects surface. Evidently, 3D triangulation sensor would be a good choice in the field of pipe inspection. The downside of triangulation sensors are the lower accuracy compared to interferometry. Interferometry would not be applicable in this case since it has issues with portability and light exposure. On the other hand, the accuracy of triangulation sensors can be improved with the help of artificial targets and photogrammetry. Therefore, a portable 3D triangulation stereo vision sensor which is capable of using artificial targets and photogrammetry model is selected for the research. The sensor will henceforth

be referred to as the “3D Scanner”. The specifics of the 3D scanner are discussed in the following section.

3.4 The 3D Scanner

3.4.1 Overview

The 3D scanner used in this research is a hand held optical 3D sensor named MAXscan which is manufactured by Creaform. The general overview of the 3d Scanner presented in this section is based on the user’s manual provided by the manufacturer. The scanner is designed to scan large parts. It uses a class 2 eye safe laser cross for probing. It has a maximum resolution of 0.1 mm and a maximum accuracy of 0.05 mm. It has a volumetric accuracy of 0.02 mm + 0.025 mm/m. The stand-off distance of the scanner from a surface is 300 mm, with ± 150 mm depth of field. So the 3D scanner is able to capture surface information within a distance range of 150 mm to 450 mm from an object without compromising its accuracy. The laser cross has an area of 210 mm X 210 mm, which enables a very high rate of 18,000 measurements per second. The 3D scanner uses uncoded reflective targets for scanning, which are referred to as “positioning features”, “markers”, or simply as "targets". It uses coded targets for creating the 3D photogrammetry model of the positioning features. Additionally, it uses a coded reference cross to specify the origin of the coordinate system, and two coded reference scale bars to calibrate the coordinate measurement. In order to create the photogrammetry model, pictures need to be taken from a distance of 1.5 meters to 2 meters. The portability of the 3D scanner, its high accuracy and fast measurement rate, and its relatively small clearance requirements make it a viable choice for pipe inspection applications.

The 3D scanner is able to position itself with respect to the targets applied on an object and its surrounding environment. Its position in space is continuously calculated through triangulation by the stereo vision cameras. For this purpose, at least four targets need to appear on the cameras' field of view at all times. The targets have to be placed randomly on surfaces that are relatively plane within a distance of 20 mm to 100 mm from each other (Figure 3.7).

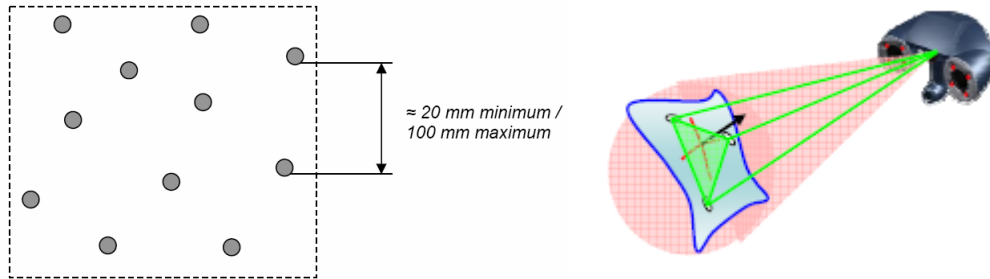


Figure 3.7 Optimum method of applying targets to enable the accurate self-positioning of the scanner (Creaform Handyscan Manual)

The randomness of the targets plays an important role in the continuous self-positioning process. The random patterns formed by the targets are recognized by the scanner and used to triangulate its initial position in space relative to the first four targets that appear in its view. After the initial positioning, each new target that appears in its view is detected and positioned relative to the targets from the previous field of view. The accuracy of a target's position is dependent on the accuracy of the previously detected targets added to its own detection accuracy (Figure 3.8).

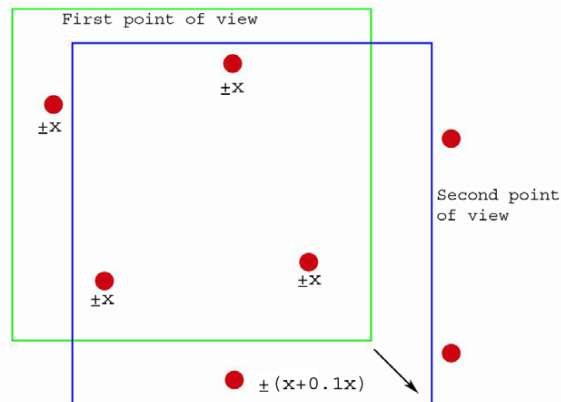


Figure 3.8 Tolerance stacking phenomenon (Creaform Handyscan Manual)

The detection error (x) of the 3D scanner is relatively low, and therefore its overall accuracy for small and medium sized objects is very good. However, as the size of an object increases, the number of targets required for scanning also increase. The error associated with detecting each additional target accumulates and increases to a point when the overall accuracy loss can no longer be considered insignificant. The error accumulation is known as tolerance stacking (Creaform Handyscan Manual). To preserve the 3D scanner's accuracy for large

objects, a regular photogrammetric system can be used. Photogrammetric systems have wider field of view and can capture a large number of targets in each picture at a time, which reduces the tolerance stacking phenomenon. The additional requirements for creating a photogrammetric model of the targets prior to scanning are a reference cross, scale bars, and coded targets (Figure 3.9)



Figure 3.9 Reference cross, scale bars, and coded targets (Creaform Handyscan Manual)

A minimum of four coded targets need to appear in each picture taken from different positions relative to an object. The reference cross specifies the coordinate origin of the photogrammetry model, and the scale bars have standard dimensions for calibrating the model. The cameras of the 3D scanner are used to take the pictures from above, below, left and right at a 30 degree to 45 degree angle relative to the centre of the object. After taking pictures, the quality of the model can be assessed by observing the number of times each coded target has appeared in the pictures.

The photogrammetry model is a very accurate 3D map of all the targets applied on and near the object. When the scanning procedure is started and the scanner is pointed to any region of the object, the cameras see the targets appearing in the view, compares with the 3D map of all the targets to determine the exact region it is looking at, and triangulates its position relative to the targets. The 3D scanner projects a laser cross onto the surface and records its movement relative to the targets. The output of the 3D scanner is an optimized surface rather than a point cloud. The surface information is captured through an automatic surface generation. The data is further converted into stereo lithography or STL format, which is an unstructured triangulated surface with unit normal and vertices (Figure 3.10).

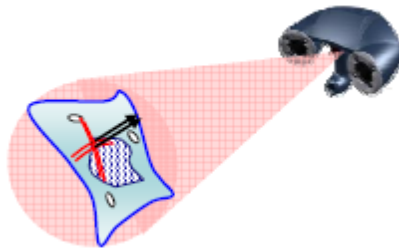


Figure 3.10 Unstructured triangulated surface generation during scanning (Creaform Handyscan Manual)

The 3D scanner uses dedicated data acquisition software "VXelements" while performing the aforementioned tasks. The correspondence between the 3D scanner and the software is ensured through the use of a high speed firewire cable. The user can monitor the data acquisition process on a computer in real-time using the software.

3.4.2 Data Acquisition using the 3D Scanner

The motivation behind using a 3D scanner in pipe inspection is to capture accurate surface information at a very fast rate. The user's manual provided information on the operating procedure of the scanner. Based on the understanding of the scanner's operating procedure, a method for acquiring pipe surface data has been developed. The data acquisition method is an original development of this research, which utilizes the general capabilities of the 3D scanner in order to be applicable to pipe inspection. In this section, the general procedure for capturing pipe surface information using the 3D scanner will be discussed.

The scanning procedure was perfected through multiple test scans performed on a straight pipe segment in a storage facility. The pipe was set up horizontally on two steel beams with approximately 3 feet clearance above ground. The 3 feet height facilitates the scanning of the bottom surface of the pipe, as well as provides easy access to the top surface using a step ladder. The scanner has certain sensitivity to light exposure. The first test scan was attempted outside in an open yard. Due to sunlight exposure, the scanner cameras were unable to detect the targets perfectly while taking pictures in a flatter angle. Therefore, it was not possible to acquire a photogrammetry model of the entire pipe. Getting

the top surface of the pipe in the model required many pictures and took up considerable time. It was observed that bright sunlight exposure results in a significant amount of noise in the acquired data (Figure 3.11) and also slows down the process.

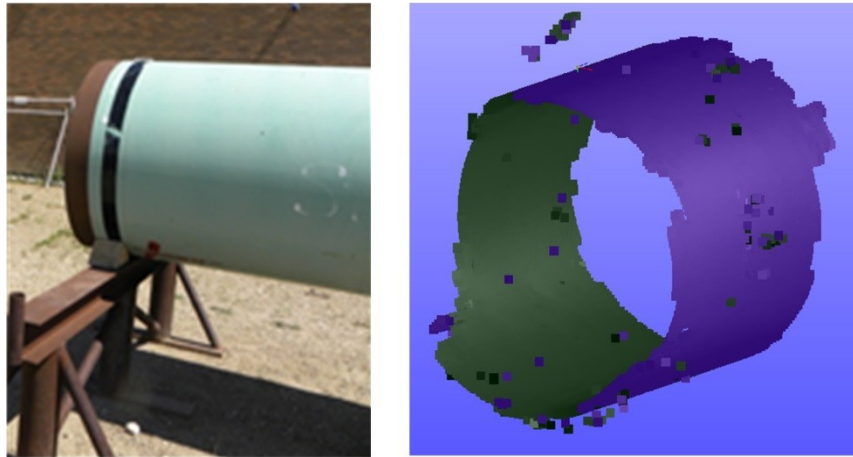


Figure 3.11 Acquired noise due to bright light exposure



Figure 3.12 Improvement in captured surface after sheltering with a tent

In the next attempt, the pipe segment was sheltered using a tarp tent, and good improvement in the quality of acquired data was observed (Figure 3.12). However, a tent cannot shade the entire pipe, especially the edges. Scanning the pipe edge is of major concern, but the tent frame and clamps block part of the pipe edge, resulting in difficulties with scanning. The acquisition software frequently freezes due to the excess temperature, which adds up to the wastage of scanning time.

The scanner performed its best when the pipe was setup indoors in a warehouse, with no sunlight exposure. The scanner cameras are able to detect the reflective targets perfectly while taking pictures at flatter angles, resulting in a good photogrammetry model. The indoor temperature was found to be optimum for the scanner-computer system, and the data acquisition speed was at its highest. The acquired surface data was considerably better compared to the previous attempt with the tent. This indoor setup was used in all subsequent scans.

At the beginning of the procedure, the pipe surface needs to be prepared. This includes scrubbing the surface free of all dirt and debris so that the coated pipe surface is completely exposed. Any undesirable material on the pipe surface will be picked up by the scanner and may appear to be pipe surface imperfection in a post processing stage, and therefore the surface preparation is a very important first step.

After the pipe surface is cleaned off, the reflective targets are placed in a particular way, maintaining a distance of 20 mm to 100 mm between them, while preserving randomness of their pattern. The reflective targets are magnetic, which can be easily attached and taken off of the pipe without tampering its surface (Figure 3.13).

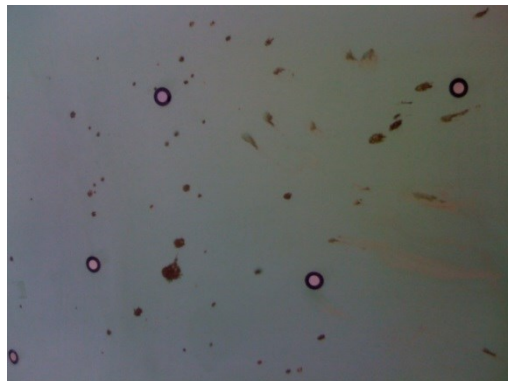


Figure 3.13 Reflective targets applied on pipe surface

The targets are setup to cover the entire outside surface of the pipe and the inside surface near the edge, in order to capture sufficient inside surface data for measuring pipe wall thicknesses. Next, the coded targets are placed between the uncoded targets, covering the entire outside surface and the inside edges, and the reference cross and scale bars are setup (Figure 3.14).



Figure 3.14 Complete pipe setup with reference cross, bars, and coded targets

The next step is to create a photogrammetry model of the uncoded reflective targets by taking pictures. The objective is to capture all the targets on the outside surface a sufficient number of times in the pictures, so that the algorithm is able to create a continuous 3D map of the targets. As mentioned earlier, the photos are required to be taken from a specific distance and approximate angles. The photo capturing process is shown schematically in Figure 3.15:

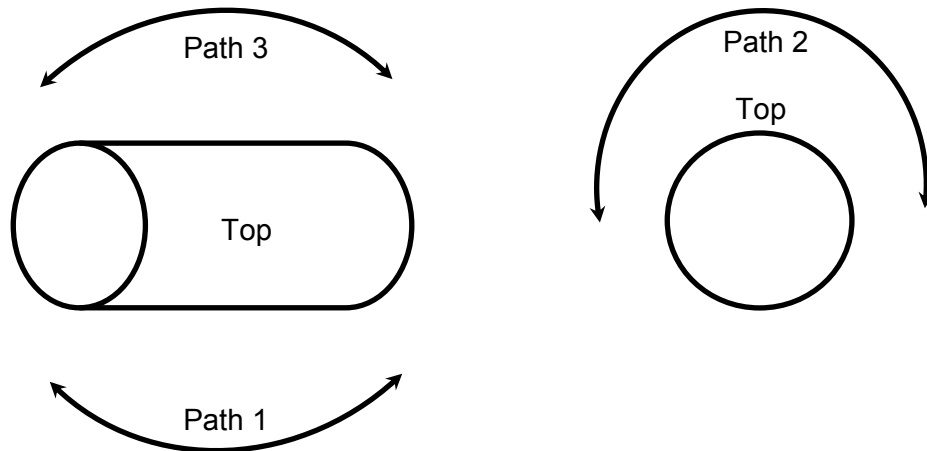


Figure 3.15 Paths followed while taking pictures for the photogrammetry model

In the figure, the paths used to take pictures are shown. In the first path (Path 1), the cameras are pointed towards the side of the pipe, where the reference cross and scale bars are attached. These references are required to appear in the first photo taken. Subsequent photos are taken on different positions on the path, and varying the camera angle within the optimum range mentioned previously. In the next path (Path 2) the camera is pointed towards the top surface of the pipe. This path ensures the continuity of the 3D map by connecting the targets on the top

surface with those on the two sides. Path 2 is repeated to take pictures from both ends of the pipe. Path 3 is a repetition of Path 1 on the other side of the pipe. This procedure results in efficient capturing of all the targets on the pipe surface, except a few on the bottom. The three feet height does not provide sufficient clearance for taking pictures of the bottom of the pipe. However, the 3D scanner is able to detect and add new targets that did not appear in the photogrammetry model initially. Another issue with the photogrammetry model is capturing the targets on the inside surface near the edges. In order to do that, the photos are taken with the camera at a specific position and pointing towards the pipe edge (Figure 3.16).

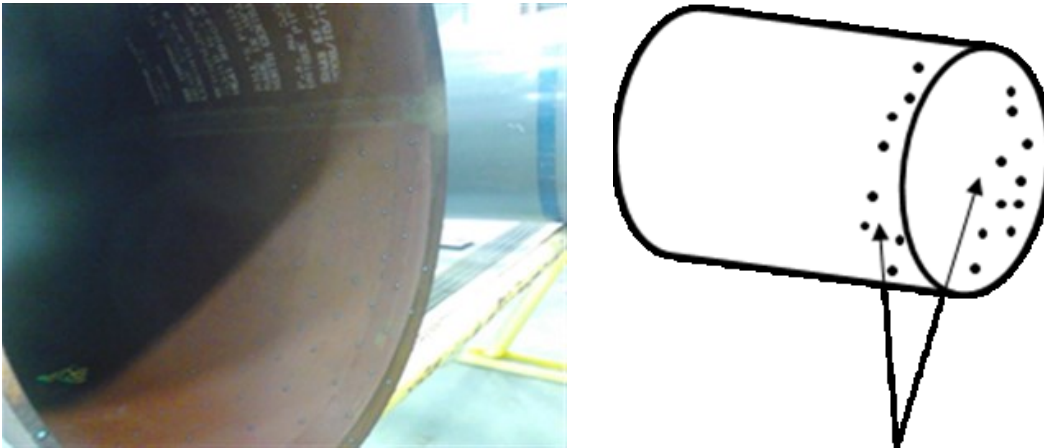


Figure 3.16 Capturing the targets on the inside surface of the pipe

The camera is pointed towards the pipe edge so that the targets on the outside surface of one side and the targets on the inside surface on the other side of the pipe appear in the same picture multiple times. The relative distance between the inside and outside surface targets are thus picked up in the captured pictures and added to the photogrammetry model. After taking pictures from all sides and angles, the preliminary photogrammetry model is created using the data acquisition software. The model is inspected to detect faulty targets and to make sure that each targets appeared a sufficient number of times in the pictures, so that the photogrammetry model is accurate. If required, more photos are taken until the photogrammetry model is deemed acceptable. A photogrammetry model of the targets is shown in Figure 3.17:

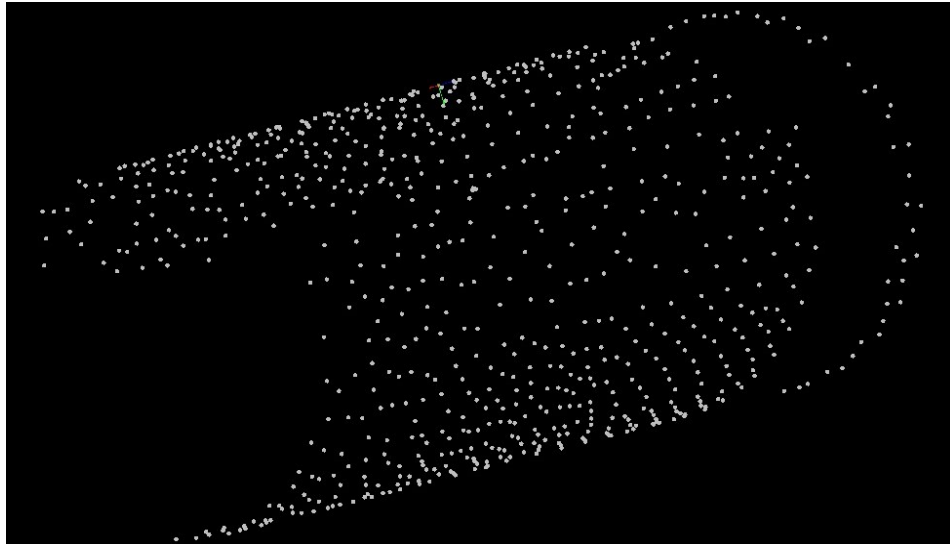


Figure 3.17 Photogrammetry model of the targets on the pipe

After creating the photogrammetry model, the coded targets, reference cross and scale bars are taken off of the pipe and the scanning procedure is started. The laser power and the shutter speed are set to an optimum amount depending on the ambient light so that the cameras perform perfectly (Figure 3.18).

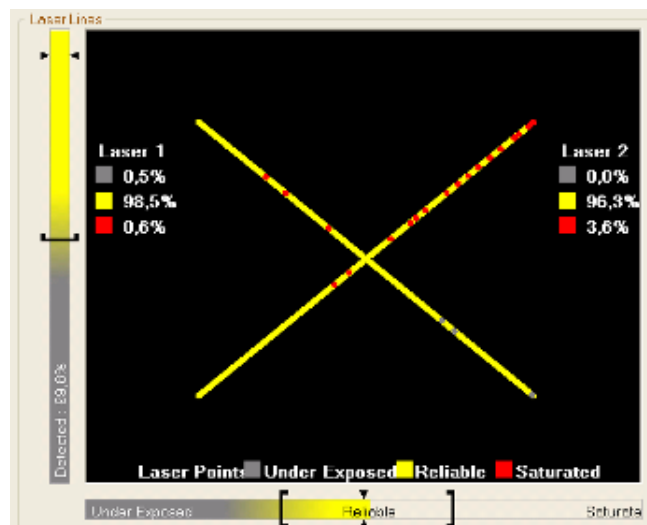


Figure 3.18 Configuration of laser power and shutter speed (Creaform Handyscan Manual)

An appropriate resolution for scanning is selected based on the size of the pipe segment. High resolution produces better surface data, but takes longer time for acquisition. The scanner is pointed towards the pipe surface and held at a distance of approximately 300 mm. The surface acquisition is monitored in real time using the acquisition software. The laser cross is swept over the surface at an optimum speed maintaining the optimum distance, ensuring that the laser path is recorded perfectly by the scanner (Figure 3.19).

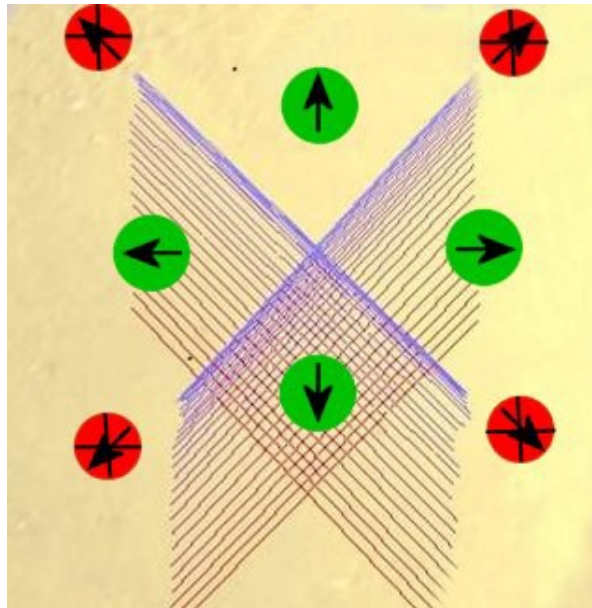


Figure 3.19 Laser paths recorded by the scanner during scanning (Creaform Handyscan Manual)

The outside surface, inside surface, and the seam weld are captured in this manner, while monitoring for missing data or discrepancies in the acquired surface. The scanning is stopped as required to look at the acquired surface and determine the next move. The outside surface, weld surface and inside surface near the edge of a sample pipe segment captured by the scanner is shown in Figure 3.20.

The data acquisition procedure developed for scanning large diameter pipes is very time efficient. A 3 meter segment of an NPS 42 inch pipe was completely scanned within 3 hours. This included all of the above mentioned tasks from preparing the pipe to getting a good quality surface data.

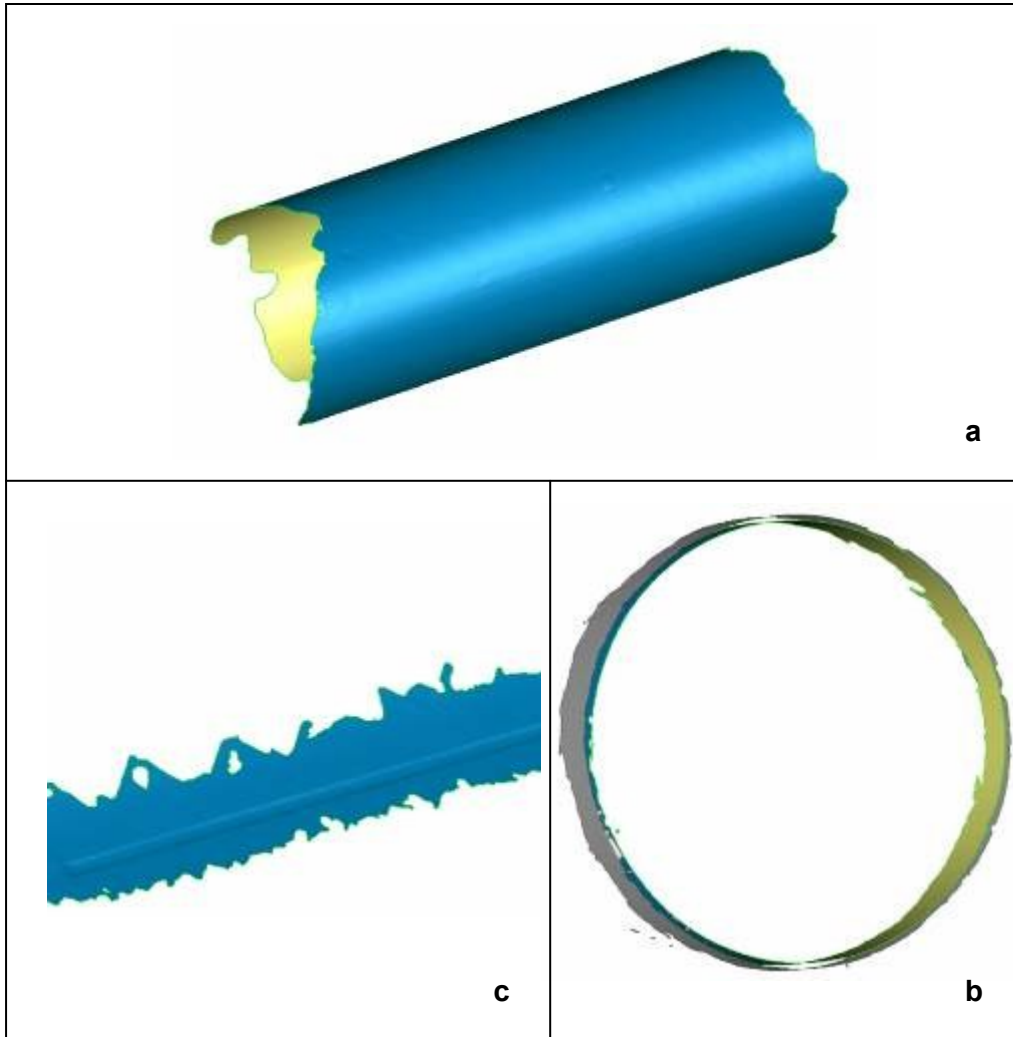


Figure 3.20 a) Outside surface of pipe, b) Outside and inside surface near pipe edge, c) Weld surface

3.4.3 Accuracy Verification of the 3D Scanner

The 3D scanner is being employed as a means of acquiring surface data of large diameter pipes to investigate the out of roundness and pipe wall thickness imperfections. The scanner produces an optimized surface in STL format, which is importable in various 3D reverse engineering software. In this research, the 3D inspection and reverse engineering software Geomagic® is chosen for analysing the surface data on account of its advanced 3D metrological capabilities. In this section, a verification of the scanners measurement accuracy will be discussed without going into the details of the reverse engineering and geometric analysis procedure of pipe segments, which will be discussed in the following sections.

The reduction of accuracy of a captured surface has a direct relationship with its curvature. The positioning targets applied on a curved surface do not appear completely circular on the scanner's field of view (Creaform Handyscan Manual). Therefore, the higher is the curvature, the greater is the measurement uncertainty. Additionally, the method adopted for measuring the wall thickness of a pipe involves acquiring the outside and the inside surfaces separately using the same reference coordinate system and photogrammetry model of the attached targets. As mentioned earlier, during the creation of photogrammetry model, the targets on the inside surface are captured relative to those on the outside surface (Figure 3.16). The ability of the photogrammetry model to measure the coordinates of the targets on the inside surface of a pipe will govern the accuracy of the wall thickness measurement. Failure to capture the relative position of the outside and inside surfaces will result in misleading thickness values. The scope of the accuracy verification is to investigate the effect of the photogrammetry model on the quality of the acquired surface data, and to compare the wall thickness values obtained using the reverse engineering software with physical measurements.

Pipe wall thickness values are generally measured using ultrasonic devices or micrometers. Micrometer measurements are widely accepted and frequently used in the pipe line industry, and is therefore used for taking physical measurements in the verification of the scanner's accuracy.

The verification is performed in two stages. First, the wall thickness values of a specimen were measured through the geometric analysis of the scanned surfaces in Geomagic®. The wall thickness values were then compared with those obtained from micrometer measurements. In the second stage, a straight pipe specimen was scanned twice, one with the use of a photogrammetry model, and another one without the photogrammetry model. The geometric attributes obtained from the analysis of the two scans were then compared. The details of the two stages of accuracy verification are elaborated below.

3.4.3.1 Comparison with Micrometer Measurements

An NPS 30 inch pipe clamp is selected as a specimen for this task. The specimen is uncoated and has a rough surface. The specimen is setup with the reflective targets (Figure 3.21), and scanned including the photogrammetry

model using the procedure previously discussed. The resolution for scanning is set to 4.0 mm. The scanned data is then imported into Geomagic® (Figure 3.22).



Figure 3.21 NPS 30 inch pipe clamp set up with reflective targets

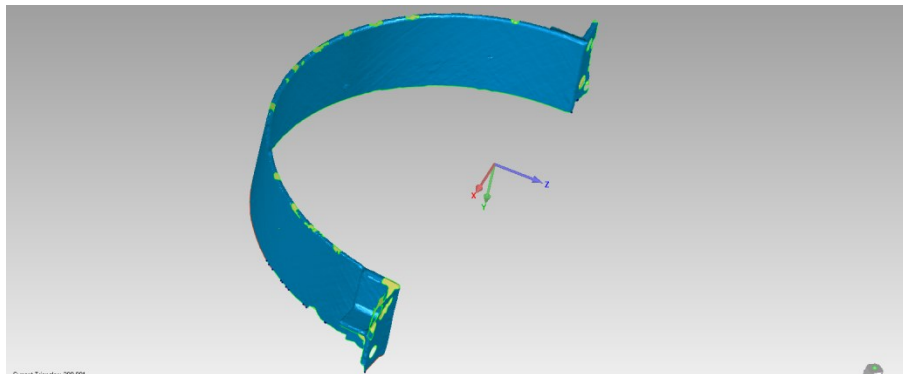


Figure 3.22 STL surface imported in Geomagic®

The axis of the cylindrical surface of the pipe clamp is obtained and the scanned surface is aligned with its axis oriented along one of the coordinate axes, the other two being parallel and perpendicular to the flange of the clamp. A cross section of the scanned surface is taken on a plane normal to the axis of the clamp and 25 mm inside from the edge. The cross section shows two concentric lines corresponding to the outside and inside surfaces. The cross sections are intersected with radial lines emanating from the centre of the clamp at 5 degrees

angular interval. The thickness values are then measured at each intersection of the lines with the clamp cross sections (Figure 3.23).

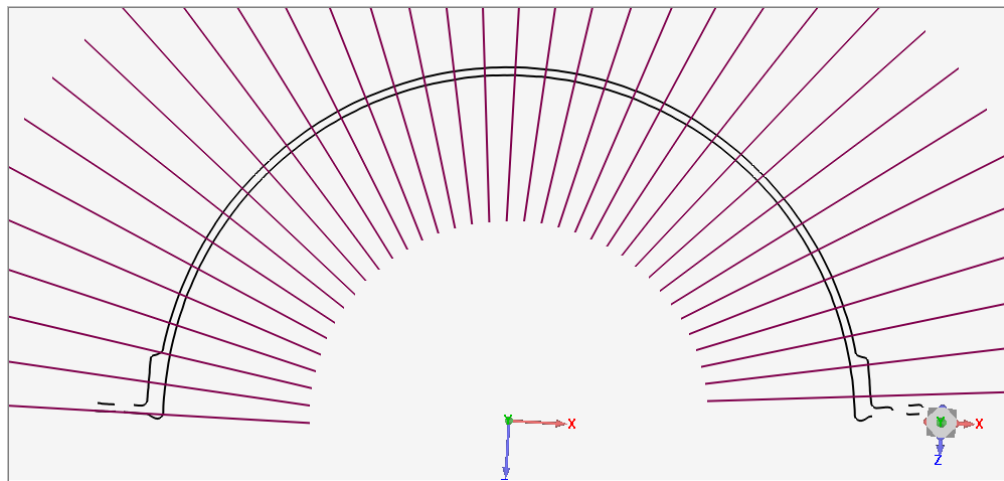
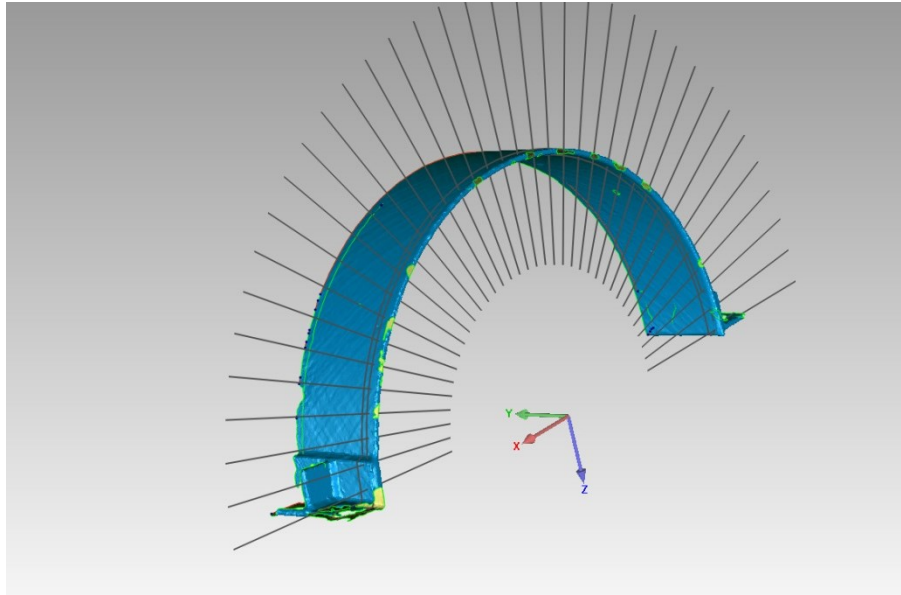


Figure 3.23 Cross section of clamp and reference lines for measuring wall thickness

The radius of a cylinder fitted to the outside surface is obtained, and from the relationship between the arc length and subtending angle ($S = r \theta$), the angles are converted to distances on the outer surface of the pipe. A paper scale is used on the actual clamp to define the exact distances on its outside surface. The distances corresponding to the angular intervals previously calculated are then

marked carefully on the clamp, resulting in a very simple grid for physical measurements.



Figure 3.24 Measuring grid on the pipe clamp

The micrometer used for measurement is manufactured by Mitutoyo, and specifically designed to measure the wall thickness of various tubing. It is a digital micrometer with spherical anvils. It has a measurement range of 0 mm to 25.4 mm. its resolution of graduation is 0.001 mm and accuracy is ± 0.00254 mm as specified in the manual. The micrometer is used to measure the wall thickness values on the grid points 25 mm inside from the clamp edge (Figure 3.25).

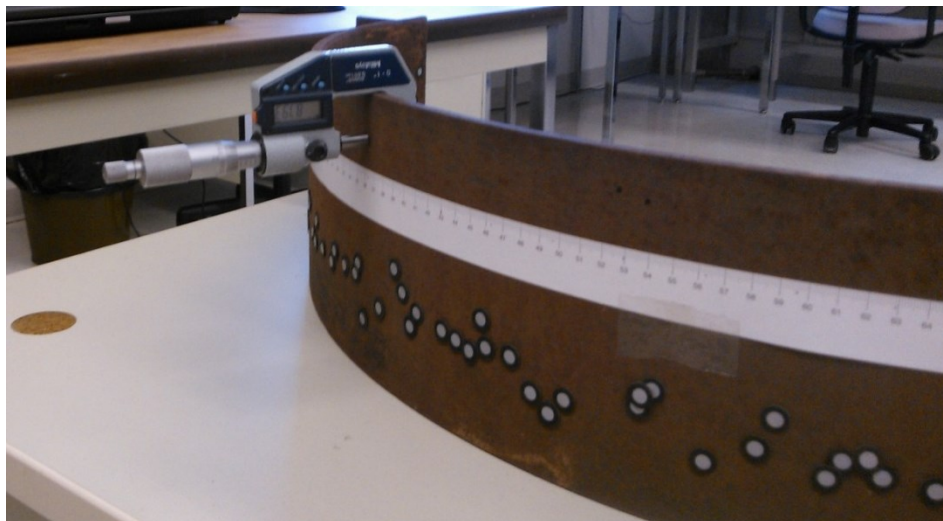


Figure 3.25 Wall thickness measurement using the micrometer

The thickness measurement results and their differences are shown in Table 3.1.

Table 3.1 Comparison between micrometer and Geomagic® measurements

Angle (Degrees)	Thickness (mm)		Absolute Difference (mm)
	Geomagic®	Micrometer	
15	8.663	8.689	0.026
20	8.678	8.72	0.042
25	8.720	8.741	0.021
30	8.808	8.732	0.076
35	8.896	8.741	0.155
40	8.757	8.75	0.007
45	8.553	8.732	0.179
50	8.727	8.721	0.006
55	8.797	8.72	0.077
60	8.577	8.725	0.148
65	8.653	8.734	0.081
70	8.693	8.727	0.034
75	8.972	8.753	0.219
80	8.674	8.79	0.116
85	8.820	8.736	0.084
90	8.779	8.772	0.007
95	8.740	8.747	0.007
100	8.804	8.772	0.032
105	8.559	8.744	0.185
110	8.743	8.745	0.002
115	8.731	8.754	0.023
120	8.862	8.753	0.109
125	8.805	8.736	0.069
130	8.707	8.804	0.097
135	8.692	8.762	0.070
140	8.630	8.771	0.141
145	8.852	8.818	0.034
150	8.707	8.819	0.112
155	8.620	8.809	0.189
160	8.770	8.802	0.032
Average Absolute Difference (mm)			0.079
Maximum Absolute Difference (mm)			0.219
Minimum Absolute Difference (mm)			0.002

From the table it is seen that the micrometer measurements gives a maximum thickness of 8.819 mm and a minimum thickness of 8.689 mm, the difference between the two being 0.13 mm. This indicates that the pipe clamp has very consistent wall thickness around its perimeter.

The analysis using Geomagic® show a wider range of wall thickness values compared to the micrometer measurements. The maximum and minimum wall thicknesses recorded from the geometric analysis are found to be 8.972 mm and 8.553 mm, with a difference of 0.419 mm between them. The absolute difference values of the measured wall thickness corresponding to same locations around perimeter and obtained from the two measurement methods are also listed in the table. It is seen that the average absolute difference between the micrometer measurement and geometric analysis is 0.079 mm. The maximum and minimum absolute difference values are 0.219 mm and 0.002 mm respectively.

In Figure 3.26 the two measurements are plotted against each other:

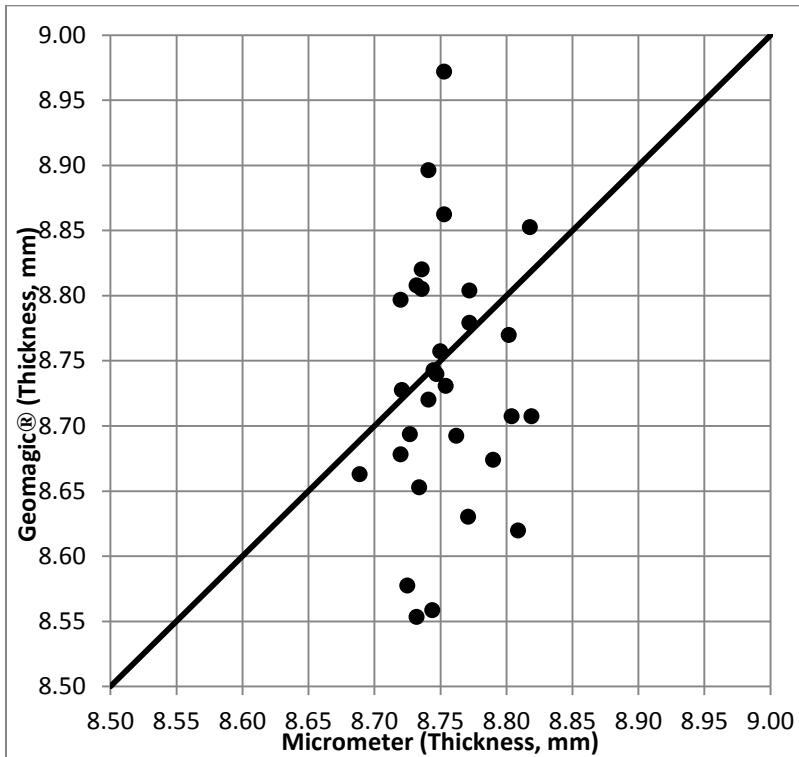


Figure 3.26 Micrometer and Geomagic® measurements plotted against each other

The standard deviation of the thickness values obtained from Geomagic© is 0.098, and the standard deviation of the micrometer measurements is 0.032. This indicates that there is more variability in the data from Geomagic©, which can be visualized from the scattering of the points about the forty five degree line in Figure 3.26. The average thickness values obtained from Geomagic© and the micrometer are 8.733 mm and 8.754 mm respectively, with a difference of 0.021 mm between them. A paired t test performed on the two data sets gives a P-value of 0.26, indicating no significant difference was found between the two means.

3.4.3.2 Influence of the Photogrammetry Model on the Acquired Data

To investigate the influence of the photogrammetry model on the acquired data, a 12 feet segment of an NPS 12 inch pipe with girth weld in the middle is selected as specimen. The pipe surface is scanned twice, with and without the photogrammetry model. All other attributes including the targets on the pipe surface and the scanning resolution were kept the same. The two scans are then imported into Geomagic© for analysis (Figure 3.27).

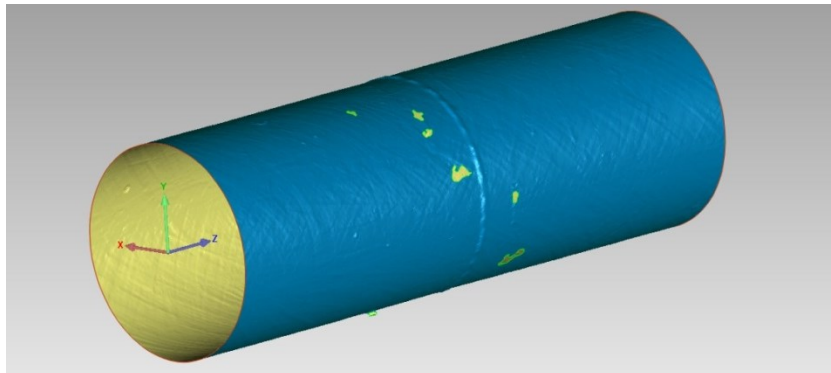


Figure 3.27 Scanned surface of the NPS 12 inch pipe segment

The two scanned surfaces are analysed through the exact same procedure to ensure the validity of the comparison between them. The surfaces are first fitted with a best fit cylinder to determine their axes. Then they are aligned to the coordinate system with the origin set at the centre of one edge, and the pipe axis oriented along one of the coordinate axes (in this case, Z axis, Figure 3.27). A small feature (a #6 nut in this case) was glued on to the pipe surface prior to scanning to assist towards a perfect alignment of the two scans. Using this feature, the scanned surface without photogrammetry is superimposed on to the scanned surface with photogrammetry, and aligned using a best fit alignment.

The scanned surface with photogrammetry is taken as a reference, and the deviation of the other surface from the reference is then analysed. A 2D comparison of a cross section of the two pipes shows that the scan without photogrammetry has issues with capturing the curvature of the pipe accurately. The deviation between the two cross sections is represented as a colour coded spectrum. The coloured whiskers represent the magnitude of deviation. Cold colours (blue) indicate negative deviation, and warm colours (red) indicate positive deviation. It is seen that all the whiskers are blue and are directed towards the centre of the pipe cross section. This indicates that the surface points obtained from scanning without photogrammetry are all located inside the cross section of the surface scanned with photogrammetry. Therefore, the scan without photogrammetry registers lower values of pipe radius, which is identified by the surface data points being inside the reference surface (scanned surface with photogrammetry) in all cross sections along the pipe length. A typical cross section is shown in Figure 3.28:

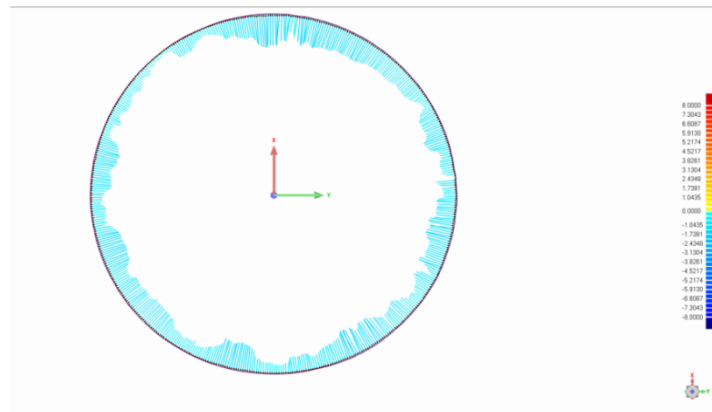


Figure 3.28 Cross sectional deviation of pipe surfaces scanned with and without the photogrammetry model

The issue with the curvature is further confirmed by comparing the girth weld surface cross sections of the two scans (Figure 3.29). It appears that the scan without a photogrammetry model fails to capture the abrupt changes in the curvature of the surface and acquires inaccurate data. In the figure, the solid line corresponds to the cross section of the girth weld obtained from the scan using photogrammetry, while the points correspond to the cross section of the girth weld obtained from the scan without using photogrammetry. A 3D comparison

analysis performed in Geomagic® indicates that the maximum positive deviation of the weld surface without photogrammetry from the weld surface with photogrammetry is 1.76 mm and the maximum negative deviation is 3.4 mm.

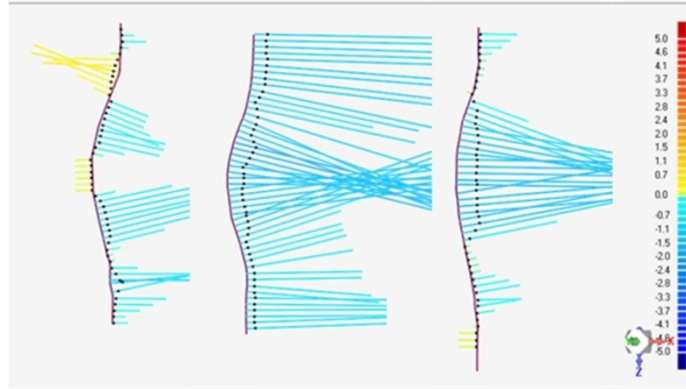


Figure 3.29 Comparison of the cross sections of girth weld surfaces scanned with and without a photogrammetry model

The two scans were next compared to a reference CAD cylinder with a constant OD of 323 mm. The 2D comparisons of the cross sections from the two scanned pipes are shown in Figure 3.30:

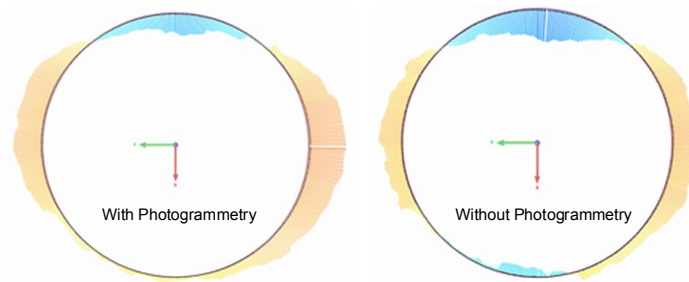


Figure 3.30 Comparison of the two scanned surfaces with a reference cylinder of fixed radius

As stated previously, the scan without photogrammetry shows lower radial values. The scan with photogrammetry has a smaller region of negative deviation (blue whiskers). The scan without photogrammetry has negative deviation on two sides, as well as the positive deviations are smaller in magnitude (shorter red whiskers). A 3D comparison of the two scanned surfaces is performed in Geomagic©. It is seen that the maximum positive deviation of the surface without

photogrammetry from the surface with photogrammetry is 1.65 mm, and the maximum negative deviation is 7.18 mm. This is further confirmed by measuring the minimum and maximum OD of the two scanned surfaces and calculating the ovalization values at consecutive cross sections along the length of the pipe. The results are listed in the following table:

Table 3.2 Maximum OD, Minimum OD, and Ovalization values calculated from the two scans

With Photogrammetry			Without Photogrammetry			
Longitudinal Distance	Max Min OD	Ovalization	Longitudinal Distance	Max Min OD	Ovalization	Difference in Ovalization
100	328.8579	0.022	100	327.7877	0.025	-0.003
	321.6963			319.643		
200	328.4602	0.024	200	328.3527	0.028	-0.004
	320.6767			319.3818		
300	327.2832	0.021	300	327.3074	0.023	-0.002
	320.4584			319.9206		
400	326.9928	0.014	400	326.4269	0.015	-0.001
	322.3257			321.4462		
500	330.1808	0.019	500	329.5359	0.019	0.0
	323.6984			323.351		
600	325.9927	0.005	600	326.3914	0.009	-0.004
	324.2639			323.5088		
700	325.8913	0.006	700	325.7337	0.006	0.0
	323.9528			323.6738		
800	325.9727	0.006	800	326.1521	0.008	-0.002
	324.0329			323.5265		
900	326.3296	0.007	900	326.3156	0.008	-0.001
	324.084			323.7952		

It is seen from the table that the scan without photogrammetry produced lower values of pipe diameter, which results in higher ovalization values compared to the scan with photogrammetry. The maximum difference in ovalization is seen to be 0.004.

3.4.3.3 Discussion on Accuracy

The accuracy verification of the wall thickness measurement is performed by comparing wall thickness values obtained from a micrometer measurement. The micrometer has a minimum division of 0.001 mm, and has a higher accuracy (± 0.00254) compared to the accuracy specified for the scanner. Therefore, the micrometer measurement results are considered as the true thickness values for the purpose of the accuracy verification. From the paired T test, the P-value was found to be 0.26, which is greater than 0.05, which indicates that no significant difference was found between the two paired measurements. The volumetric accuracy of the scanner is specified as 0.02 mm + 0.025 mm/m. The length of the pipe clamp scanned for the accuracy verification is 2.356 m, considering both the outside and the inside surfaces. Therefore, the error expected in the scan is $0.02 \text{ mm} + (0.025 \text{ mm/m} \times 2.356 \text{ m}) = 0.0789 \text{ mm}$.

From the comparison of the wall thickness measurements (Table 3.1), it is seen that the average difference between the micrometer measurement and the geometric analysis of the scanned surface is 0.079 mm, while the minimum difference is 0.002 mm. The maximum difference is, however, 0.219 mm. It should be noted that the specimen was deliberately selected to be an uncoated pipe clamp with a rough surface, in order to involve the possibility of noise in the scanned surface data due to the inferior surface quality. In this regard, the maximum difference of 0.219 mm can be considered as an outlier. The average difference is seen to be exactly equal to the expected error from the scan as specified by the manufacturer. Therefore, it is confirmed that the accuracy of the scanner is exactly as specified by the manufacturer, which is 0.02 mm + 0.025 mm/m.

The influence of using photogrammetry model on the quality of the acquired data is very prominent. The scan without photogrammetry shows lower values of pipe diameter in all cross sections along the pipe (Table 3.2). The 2D comparison spectrums obtained from taking sections at successive distances along the pipe length are very consistent. All of the cross sections show that the scan without photogrammetry produces lower values of OD compared to the scan with photogrammetry. The 3D comparison shows a maximum negative deviation of

7.18 mm. All of the above findings confirm that the absence of a photogrammetry model prior to scanning will lead to inaccurate values of measured pipe diameter.

It is important to ensure that the observed deviation of the cross sections is not a result of misalignment of the two pipe surfaces. If the deviation resulted from a faulty alignment of the scanned surfaces, the 2D comparisons would show both positive and negative deviations, indicating that the axes of the two pipes did not coincide and diverged in direction. This fact was confirmed by monitoring the direction cosines of the vectors corresponding to each axis in Geomagic®. The direction cosines of the axes of the pipes scanned with and without photogrammetry are (0.0, 0.0, 1.0) and (0.0001, 0.0004, 1.0) respectively.

The cross sections of the girth weld obtained from the scanned surface with photogrammetry are very smooth and continuous, whereas the scanned surface without photogrammetry shows fluctuations from the smooth transitioning curve (Figure 3.29). The observed fluctuations are random in nature, indicating that the absence of photogrammetry model results in noise whenever there is an abrupt change of curvature in the scanned surface.

The accuracy of the scanner as specified by the manufacturer is verified to be true. However, it should be investigated if this accuracy is acceptable for the purpose of this research. The scope of this research includes straight pipes ranging from NPS 20 inch to NPS 42 inch. The specified wall thicknesses of these pipes range from 7.925 mm to 14.275 mm. The errors in measuring thicknesses expected from scanning the inside and outside surfaces of these pipes are tabulated below:

Table 3.3 Expected values of error in pipe wall thickness measurement

Nominal OD	Wall Thickness	Expected Error	
		mm	% of Wall Thickness
508	7.925	0.059898227	0.76%
864	9.525	0.087858401	0.92%
1067	10.312	0.103801984	1.01%
1067	14.275	0.103801984	0.73%

As can be seen from the table, the expected error in wall thickness measurement varies from 0.73% to 1.01% of the specified wall thickness. The significance of these errors will depend on the measured thickness deviation values, and will be considered accordingly.

3.5 Geometric Analysis of Pipes, Sleeves, and Elbows

In the previous sections, the general procedure for acquiring pipe surface data using the 3D scanner has been discussed. The accuracy of measurement using the scanned data has also been validated. The aforementioned methods have been applied for the surface data acquisition of UOE manufactured straight pipe segments, pipe sleeves, and ninety degree elbows. In the next sections, the developed methods for the geometric analysis of the straight pipes, sleeve fittings, and pipe elbows through reverse engineering will be discussed.

3.5.1 Geometric Analysis of UOE Manufactured Pipes

Ten straight pipes are analysed for geometric imperfections in this research, eight of them are UOE manufactured. The outside diameters of the scanned pipes are NPS 20 inch, NPS 34 inch, and NPS 42 inch. The specifications of the scanned pipes are shown in Table 3.4:

Table 3.4 Specifications of the scanned pipes

	Nominal Diameter		Nominal Thickness		Grade	D/t Ratio	Manufacturing Process
	Inch	mm	Inch	mm			
NPS 20 A	20	508	0.312	7.925	X70	64.10	Unknown
NPS 20 B	20	508	0.312	7.925	X70	64.10	Unknown
NPS 34 A	34	864	0.375	9.525	X100	90.71	UOE
NPS 34 B	34	864	0.375	9.525	X100	90.71	UOE
NPS 42 A	42	1067	0.406	10.312	X100	103.47	UOE
NPS 42 B	42	1067	0.406	10.312	X100	103.47	UOE
NPS 42 C	42	1067	0.562	14.275	X100	74.75	UOE
NPS 42 D	42	1067	0.562	14.275	X100	74.75	UOE
NPS 42 E	42	1067	0.562	14.275	X100	74.75	UOE
NPS 42 F	42	1067	0.562	14.275	X100	74.75	UOE

The following tasks are performed to analyse and detect geometric imperfections of the pipes:

3.5.1.1 Alignment

The scanned pipe surfaces first need to be aligned with the coordinate system in Geomegic®. In order to do that, the axis of a pipe needs to be determined. This is done by fitting a best fit cylinder to the scanned pipe surface. The best fit cylinder refers to fitting a cylinder to the scanned pipe surface by measuring from point to point and adjusting the location of the cylinder to the stationary reference pipe surface, until the average deviation between the cylinder and the reference surface is as low as possible.

The bulge due to the presence of the seam weld on the outer surface of a pipe is ignored during this process to ensure that the best fit algorithm only considers the pipe surface. The axis of this cylinder is therefore considered as the axis of the pipe (Figure 3.31). This axis will be aligned to one of the coordinate axes at a later stage.

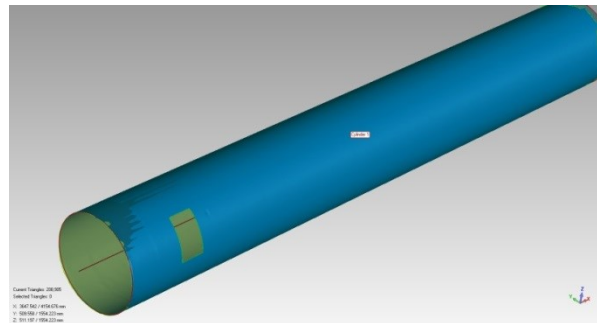


Figure 3.31 Longitudinal axis of a pipe extracted from best fit cylinder

Next, the intersecting point of the pipe axis and a plane fitted to the end of the pipe is obtained. This point will be considered as the coordinate origin at a later stage of alignment (Figure 3.32).

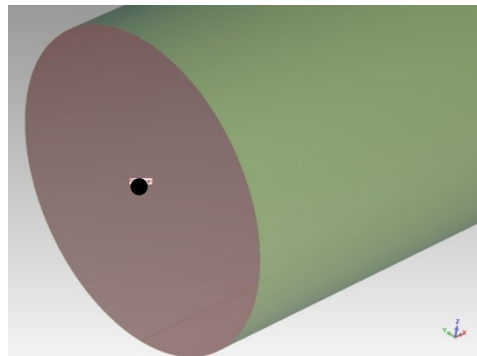


Figure 3.32 Extracted point at pipe end to be used as coordinate origin

With the origin and one axis determined, the alignment only requires one more definition, a plane that coincides with one of the coordinate planes. The seam weld is a very good feature with consistent geometric attributes, and is utilized to define a plane. The objective is to obtain a plane that bisects the seam weld. For this purpose, the seam weld needs to be separated from the pipe surface.

Two planes through the pipe axis are created to trim the weld off of the pipe surface. The planes are rotated about the pipe axis to intersect the weld edges (Figure 3.33). The intersection process is approximate and performed visually.

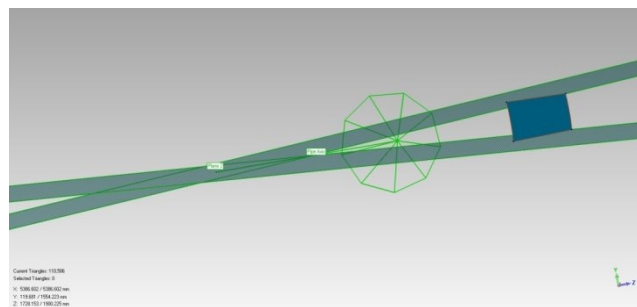


Figure 3.33 Separating the weld surface with trimming planes

Next, the centroid of the weld surface is obtained. Geomagic is able to calculate the centroid of a surface from its point cloud. Therefore, the centroid is in the middle of the selected surface (Figure 3.34)

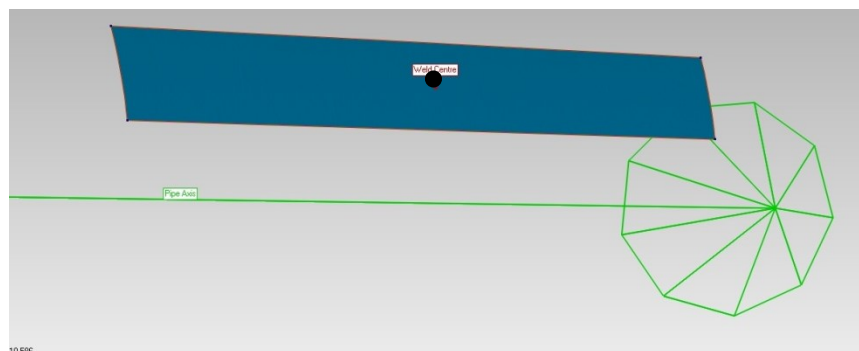


Figure 3.34 Centroid of weld surface

A plane is then created that goes through the pipe axis and the centroid of the weld, thus bisecting the weld surface. This plane is the remaining definition required for the alignment.

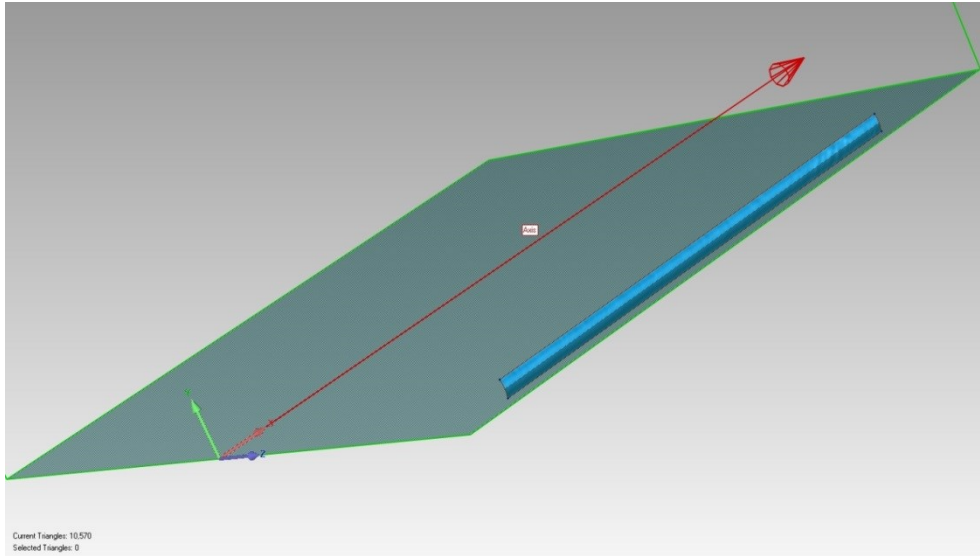


Figure 3.35 Plane bisecting the weld surface

The point (Figure 3.34) is paired with the origin of the coordinate system, the pipe axis (Figure 3.31) is paired with the coordinate X axis, and the plane (Figure 3.35) is paired with the coordinate XZ plane. The pairing and the final alignment are shown in Figure 3.36, and Figure 3.37.

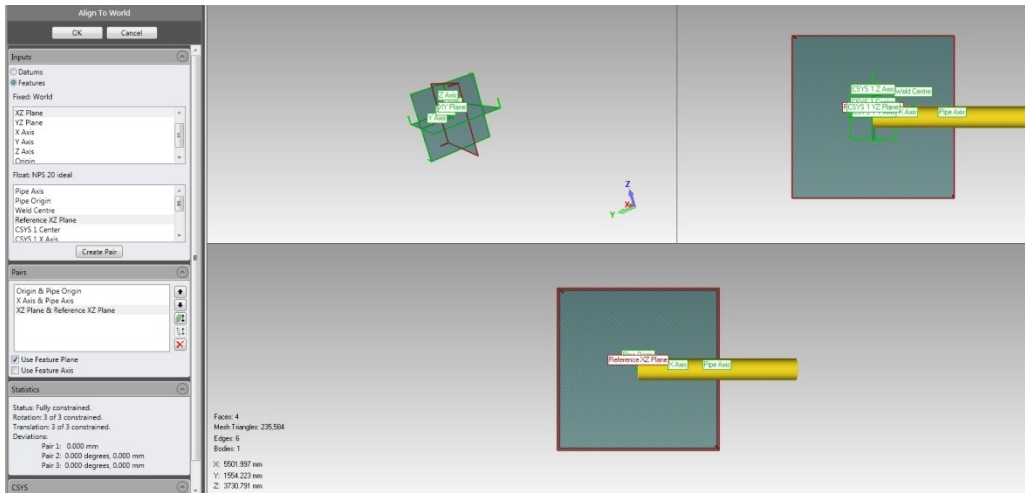


Figure 3.36 Pairing the point, line and plane features with the global coordinate system

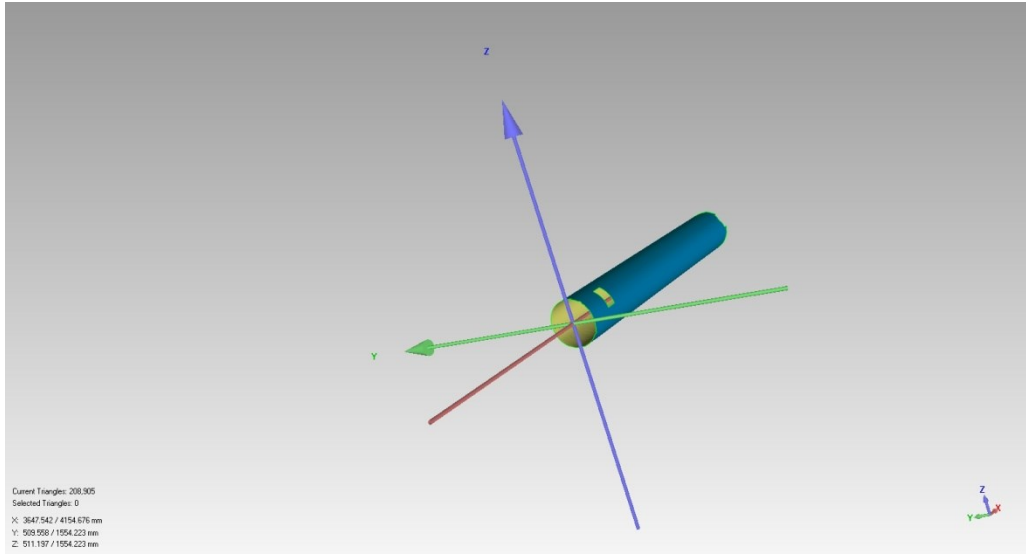


Figure 3.37 Pipe surface after alignment

3.5.1.2 Reference Ideal Pipe

In order to accurately describe the imperfections, it is required to measure the variations of the outside diameter (OD) of pipe, the variations and the extent of ovalization along the pipe length, and the changes in the thickness of the pipe wall. A reference or ideal pipe is required for these measurements. The reference pipe is created by modifying the best fit cylinder. The diameter of the best fit cylinder is set equal to the specified OD of the pipe, and is considered as the ideal pipe during the measurement process (Figure 3.38).

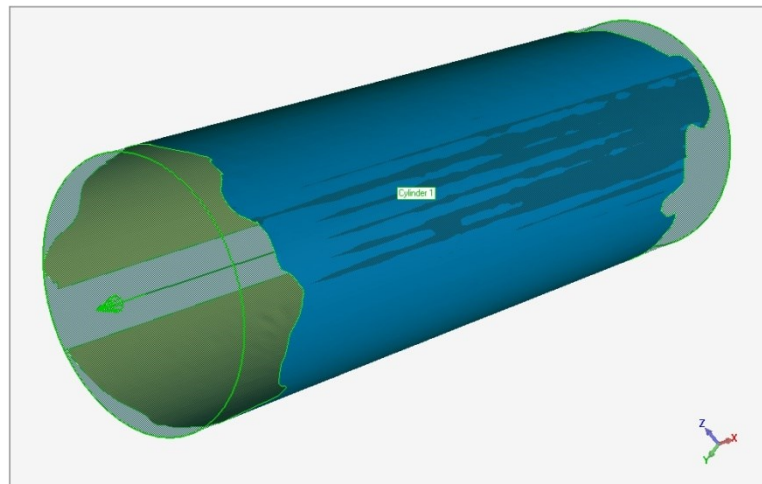


Figure 3.38 Best fit cylinder modified with the specified OD of the scanned pipe

The ideal pipe is then converted to a polygon object with triangulated surface mesh similar to the scanned pipe surface. Segments of the scanned pipe surface are seen to lie outside the perfect cylindrical surface and a few other segments lie inside as can be seen in Figure 3.39:

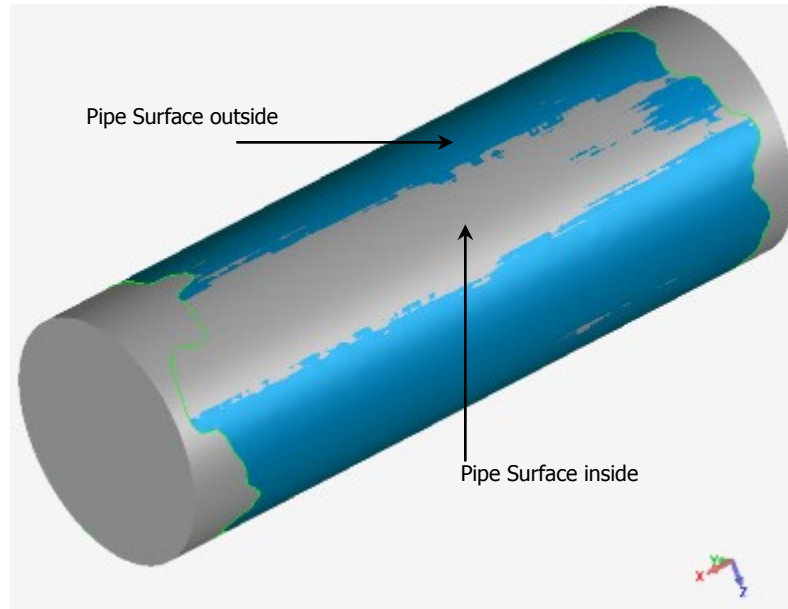


Figure 3.39 Deviation of the scanned pipe surface from the ideal cylinder

3.5.1.3 Comparison between Ideal and Actual Pipe

3D comparison tool is used to compare the scanned pipe surface (test object) and the ideal pipe (reference object). This tool generates a three dimensional color-coded mapping of the differences between the test and the reference objects (Figure 3.40).

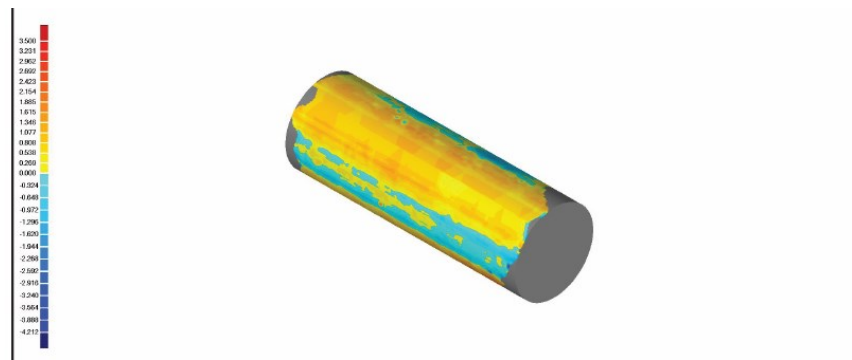


Figure 3.40 3D deviation spectrum

Deviations are reported as the shortest distance from the test object to the closest point on the reference object. The critical angle is set to the lowest value. This angle specifies the divergence of two triangles' normal directions, beyond

which the 3D comparison will not be performed. Thus it is ensured that the measured deviation is in fact the deviation between analogous points on the test and reference objects that lie on a plane perpendicular to the pipe axis.

Corresponding cross sections of the test and reference objects are compared using a 2D compare tool. This tool generates a two dimensional color-coded deviation spectrum which visualizes the deviation of the pipe cross section from the perfect circular cross section of the ideal pipe, and calculates the values of the deviations (Figure 3.41).

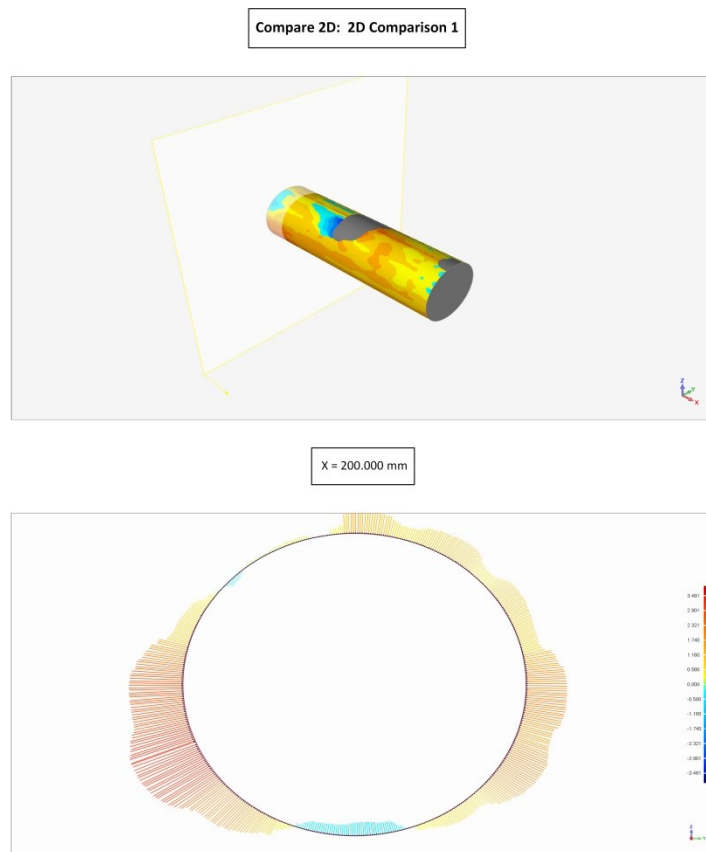


Figure 3.41 2D cross sectional deviation spectrum

Planes perpendicular to the pipe axis are created at 200 mm intervals from one end of the pipe. Sections of the scanned and ideal pipes on these planes are taken to observe the deviations of the pipe OD from the perfect cylinder. Pipe OD being greater and smaller than the nominal OD are designated as positive and negative deviations respectively. In the deviation spectrum, warmer (red) and colder (blue) colours indicate positive and negative deviations respectively.

3.5.1.4 Measuring Ovalization

Ovalization is the measurement of out of roundness of pipe section. As per CSA Z662-11, ovalization deformation should be calculated according to the formula:

$$\text{ovalization deformation} = 2[(D_{\max} - D_{\min}) / (D_{\max} + D_{\min})] = \Delta D / D_{\text{average}}$$

Where,

D_{\max} = maximum pipe outside diameter, mm

D_{\min} = minimum pipe outside diameter, mm

$\Delta D = D_{\max} - D_{\min}$

$D_{\text{average}} = (D_{\max} + D_{\min}) / 2$

To measure the maximum and minimum values of pipe outside diameters, sections through the pipe are taken using consecutive planes perpendicular to the pipe axis and at 200 mm intervals. These are sections with points located both inside and outside of the perfect circle. Therefore they have varying radius when measured around their center.

A hypothetical circle that goes through the points located on the outermost proximity of a section has a diameter equal to the maximum diameter at that section. Similarly, a hypothetical circle that goes through the points located on the innermost proximity of a section has a diameter equal to the minimum diameter at that section. Consequently, the maximum and minimum diameters are measured by grasping the outer and inner points of each section respectively. The process is demonstrated in Figure 3.42. The double line represents a perfect circle that corresponds to the cross section of the ideal pipe. For simplicity, the imperfect cross section of a pipe is assumed to be elliptical and is shown with a single solid line. The hypothetical circles going through the outermost and innermost points of the imperfect cross section are shown with dashed lines. Therefore, the maximum and minimum diameters of the imperfect cross section are equal to the diameters of the large and small hypothetical circles respectively.

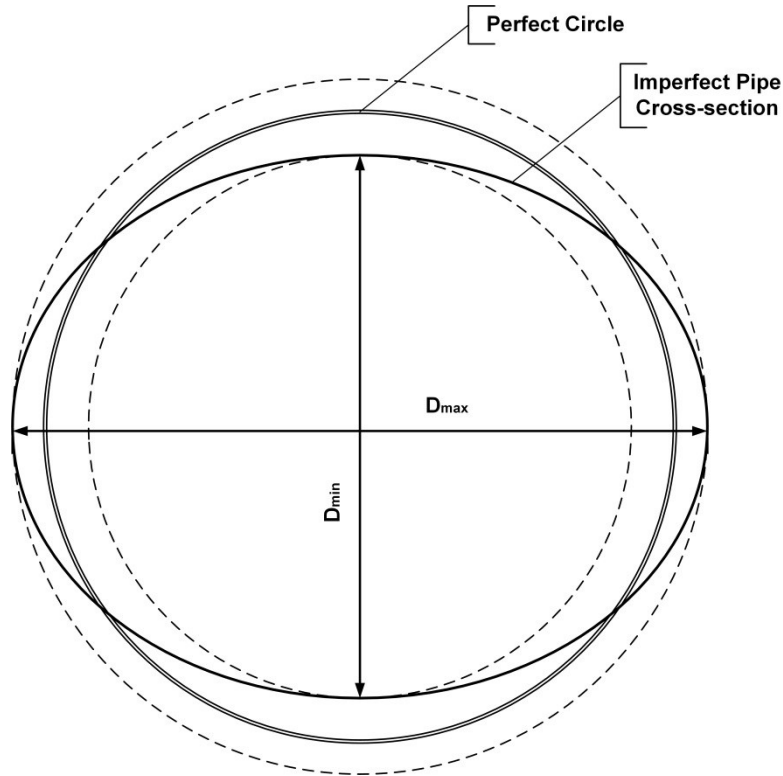


Figure 3.42 Minimum and maximum diameter measuring process at a cross section of a pipe

3.5.1.5 Measuring Pipe Wall Thickness

Variation of the pipe wall thickness is measured around its perimeter using successive planes through the pipe axis at 5 degrees angular interval. Multiple planes perpendicular to the axis are taken to observe thickness variation along the length of the pipe (Figure 3.43).

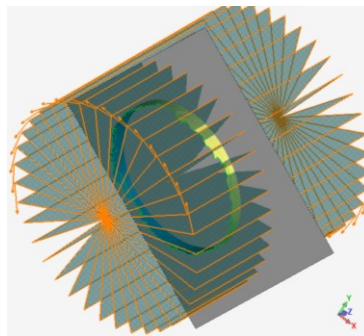


Figure 3.43 Planes through and normal to pipe axis for thickness measurement

A line passing through the centre of the ideal pipe cross section and the centre of the seam weld is used as the reference line, and all angles are measured towards a clockwise direction with respect to this line (Figure 3.44). Therefore, 0

degree and 360 degree angles correspond to the location of the seam weld in any pipe cross section.

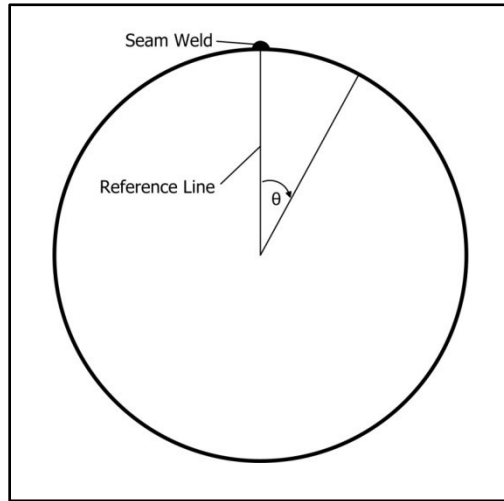


Figure 3.44 Thickness measurement scheme

When a cross section of the pipe on a plane normal to the pipe axis is viewed, the thickness of the pipe wall and several intersecting lines are seen. These lines correspond to the successive planes through to the pipe axis at 5 degrees angular interval. The angle of each line from the reference line is known. Therefore, the values of pipe wall thickness around its perimeter and along the length of the pipe can be measured and recorded. Figure 3.45 illustrates a sample cross section of pipe wall with measured wall thickness dimensions.

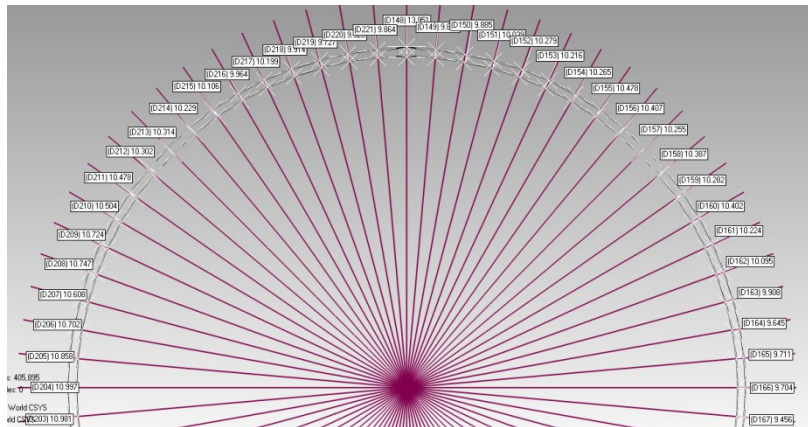


Figure 3.45 Cross section of pipe wall thickness with measured dimensions

3.5.1.6 Measuring Seam Weld Geometry

The remaining geometric feature of the straight pipe to be measured is the longitudinal seam weld. The ideal way to measure the seam weld dimension is to

scan both the outside and the inside surfaces of the seam weld, and measure the weld thickness from the acquired data. However, only a 500 mm length of the inside surface of a pipe is accessible for scanning due to safety concerns. So, it is not possible to measure the actual thickness of the weld for the whole length of the pipe. A method is therefore devised to determine the weld geometry variations using only the outside surface of the seam weld.

When a cross section of the seam weld is viewed on a plane normal to pipe axis, it shows a continuous curve as shown in Figure 3.46

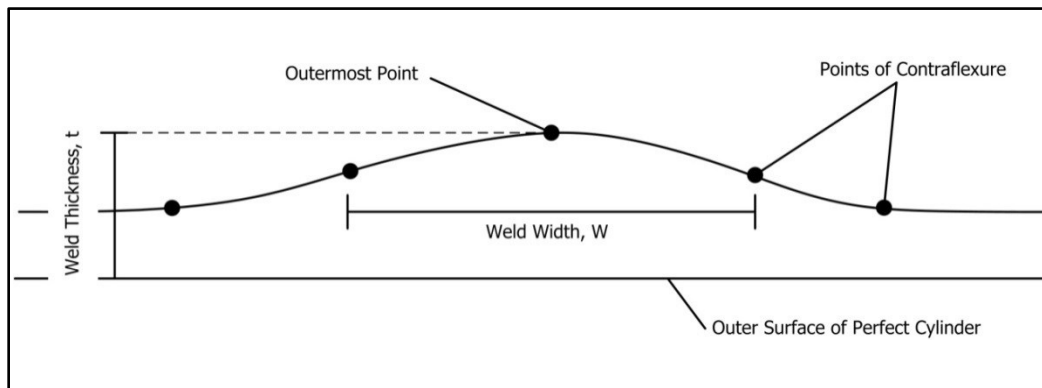


Figure 3.46 Representation of idealized weld dimensions

As the curve transforms from pipe cross section to seam weld cross section, the direction of its curvature changes twice before reaching the point of zero curvature (outermost point). It is evident that there exist two points of contraflexure on either side of the centre of the seam weld. For the purpose of this research, the shortest distance between the points of contraflexure closest to the centre of the seam weld is considered as weld width (W), and the normal distance between the outermost point and the outer surface of the perfect cylinder is designated as the thickness of the weld (t). These simplified assumptions can be considered appropriate as the research focuses on the variation of weld dimensions rather than its actual values. This method is applied to three of the ten specimens in this research. Two of the specimens had their seam weld grinded, and for the other four specimens, both the inside and outside surfaces of the seam weld were scanned up to 500 mm from their end. It was therefore possible to measure the actual thickness of the seam weld for these four specimens. The seam weld thickness measurement is shown schematically in Figure 3.47.

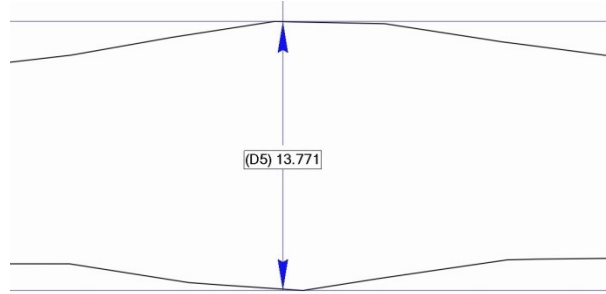


Figure 3.47 Measuring the seam weld thickness in Geomagic©

The results of geometric analysis of the UOE manufactured straight pipe segments will be discussed in Chapter 4.

3.5.2 Geometric Analysis of Fiber Glass Reinforcement Sleeve Fitting

This analysis is intended to investigate the geometry of protective pipe sleeves made of Fiber Glass. Six pipes fitted with Fiber Glass sleeves are studied. The objective is to get detailed information of the sleeve geometry and compare them with conceptual support designs. Ultimately, the geometric compatibility between the sleeves and the supports are captured.

3.5.2.1 Sleeve and Support Details

The sleeves are fitted on the pipe surface using adhesive. The average width of the sleeves is 12 inch. The sleeves are located either at the mid length of the pipe, or near the edge of the pipe. All six pipes are NPS 30 inch. The details are shown in Table 3.5:

Table 3.5 Pipe and Sleeve Description

	OD (inch)	Coated/Uncoated	Weld Type	Location of Sleeve Relative to Pipe
Pipe 1	30	Coated	Seam	Edge
Pipe 2	30	Coated	Seam	Middle
Pipe 3	30	Coated	Helical	Edge
Pipe 4	30	Coated	Helical	Middle
Pipe 5	30	Uncoated	Seam	Middle
Pipe 6	30	Uncoated	Helical	Middle

The pipes have either a longitudinal or a helical seam weld. In the case of the longitudinal weld, the sleeve is discontinued at the location of the weld. In the case of the helical weld, it was observed that the inner surface of the sleeve was

grounded to follow the contour of the weld. Only the portion near the edge of the sleeve was visible, so it is not possible to report the inner surface condition of the sleeve away from its edges.

The conceptual support design consists of shoe, directional anchor, guide, base support, flange support, field support and gusset. Only the shoe is supposed to be in direct contact with the sleeve. The detailed specifications of the support are shown in Figure 3.48. The inner diameter (ID) of the support shoe is specified to be 30.5 inch. The shoes will be welded to 7/8 inch thick plates. These plates will be bolted to each other on either side of the pipe to ensure rigid clamping of the shoe to the sleeve. The gap between the 7/8 inch thick plates is designed to be 1 inch after proper tightening of the hex bolts and nuts.

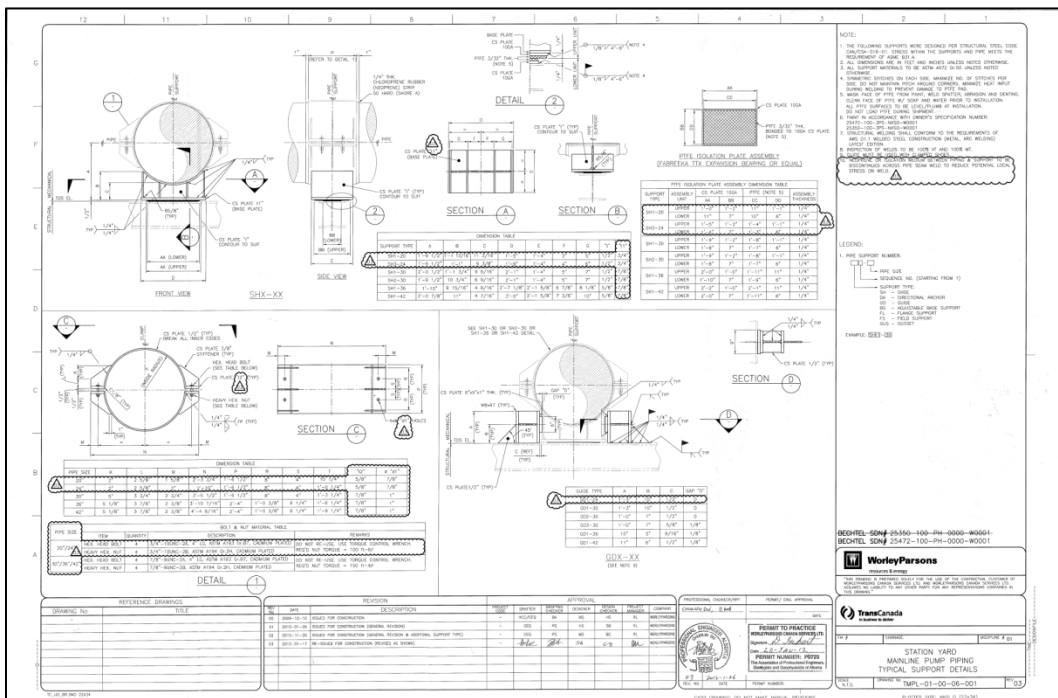


Figure 3.48 Support Specifications

3.5.2.2 *Sleeve Geometry Measurement*

The sleeves and the adjacent portion of the pipes are scanned and the scanned data is exported to Geomagic®. The sleeves were reoriented and aligned with the global coordinate system, so that the X axis denotes the pipe axis, coordinate origin is located at the centre of a pipe, and the Z axis goes through the centre of the longitudinal weld or the centroid of the helical weld underneath the sleeve. The curvature map of the outer surface of the sleeve is plotted to visualize the typical topographic contour of the material.

Two best fit cylinders are created for the outer surface of the sleeve and the outer surface of the pipe. The average distance between the two cylinders is denoted as the average thickness of the sleeve.

A best fit cylinder is created for each sleeve outer surface. The diameters of the best fit cylinders corresponding to each sleeve are recorded and compared with the Inner Diameter (ID) of the shoe.

Diameters of each best fit cylinder are then modified to the value of 774.7 mm (30.5 inch) to represent the support shoe. The cylinders are then converted to CAD objects and compared with the outer surface of the sleeves. Sections are taken at mid length (approximately 6 inches from sleeve edge) of each sleeve to visualize the 2D deviations between the outer surface of the sleeves and the inner surface of the support (shoe). 3D comparison between the sleeves and the supports are performed. Results of the analysis are presented in Chapter 5.

3.5.3 Pipe Elbow Geometry Analysis

Steel elbows are used to change the direction of, otherwise straight, steel pipelines. The most common elbow angles are 45, 90 and 180 degrees. Elbows are subjected to stresses due to the internal pressure that are higher than those in the straight portion of the pipelines. The additional stresses are caused by what is often referred to as “The Bourdon Effect” – which is the tendency of elbows to straighten when subjected to an internal pressure. Currently, there is no clear understanding of the extent of the “Bourdon Effect” on high strength steel large diameter pipeline elbows. The additional stresses caused by the “Bourdon effect” can be exacerbated due to the existence of any manufacturing imperfections.

The details of the studied pipe elbows are shown in Table 3.6:

Table 3.6 Elbow Specifications

Elbow Designation	Outside Diameter [inch (mm)]	Wall Thickness [inch (mm)]	Steel Grade
12inch_GR359_1	12.75 (323.85)	0.375 (9.525)	Grade 359
12inch_GR359_2	12.75 (323.85)	0.375 (9.525)	Grade 359
24inch_GR359_2	24.00 (609.60)	0.375 (9.525)	Grade 359
24inch_Y52_1	24.00 (609.60)	0.375 (9.525)	Y 52
36inch_1	36.00 (914.40)	0.500 (12.700)	Y 70

The ideal representation of a pipe elbow is a torus which can be defined by a circle revolving around an axis coplanar with the circle. In this section, a method is introduced for the geometric analysis of manufactured pipe elbows using geometric idealization. The as-built elbows are scanned and the idealized radius of the circle and the axis of revolution are obtained from the scanned data. The difference between the idealized geometry and the scanned geometry are deemed as imperfections of the pipe elbow.

Before the scanning procedure is started, depending on the elbow size, they are either placed on the ground (small elbows, less than 36 inch Outside Diameter), or lifted above ground using a fork lift (larger elbows, 36 inch Outside Diameter or more). Magnetic reflective targets are installed on the elbow surface. Reference cross and bars are attached to the elbow for creating the photogrammetry model.

In the first step, to create the photogrammetry model, pictures are taken from all sides and angles to capture all the reflective targets, reference cross and bars. Data acquisition software is used to ensure that the number of pictures taken is adequate to generate the photogrammetry model. After taking sufficient pictures, the photogrammetry model is created. The second step involves capturing the surface details of the elbow. The scanner is swept over the elbow surface at a desired speed and from a specific distance. Surface digitization is monitored real-time to detect discrepancies. In addition to the outside surface, the inside surface near the ends are also scanned for wall thickness measurements. Upon

completion of the scanning procedure, the acquired surfaces are inspected in the data acquisition software to identify holes. The missing patches are scanned again until the surfaces are continuous, and the acquired data is deemed satisfactory for geometric analysis.

3.5.3.1 Idealized Geometry

As mentioned previously, the ideal representation of a pipe elbow is a torus, which is defined by revolving a circle about an axis which is coplanar with the circle (Figure 3.49 a). A plane that goes through the axis and bisects the torus is a plane of symmetry of the torus. This plane will be referred to as the vertical plane of symmetry. Again, a plane that is perpendicular to the axis of revolution, and bisects the torus is another plane of symmetry and will be referred to as the horizontal plane of symmetry (Figure 3.49 b). The intersection point of the axis of revolution and the horizontal plane of symmetry is considered to be the centre of the torus.

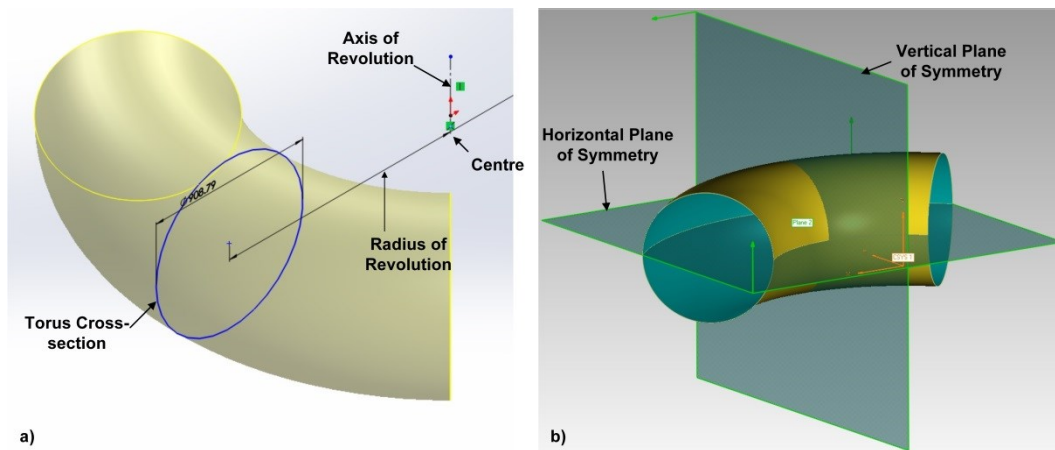


Figure 3.49 a) The centre, axis and radius of revolution, and cross section of an ideal torus, b) Vertical and horizontal planes of symmetry of an ideal torus

If an ideal torus is intersected with the horizontal plane of symmetry, the resulting curves will be two perfect arcs. The average of the two radii of these arcs will be equal to the radius of revolution initially used to define the torus (Figure 3.49a). If cross sections of the torus are taken using planes that go through the axis of revolution of the torus and are rotated about the same axis, the results will be perfect circles having diameters equal to the circle initially used to define the cross section of the torus.

To represent a pipe elbow with an ideal torus, the diameter of the circle that defines the cross section of the torus needs to be acquired in addition to the radius of revolution, i.e., the distance between the centre of the circle to the axis of revolution. It is obvious that for an actual pipe elbow, the diameter of the circle and the distance, due to imperfections, need not be constant. If a cross section of an actual pipe elbow is taken using the horizontal plane of symmetry, the resulting curves will not be perfect arcs with constant radii. Also, if cross sections are taken using planes rotated about the axis of revolution, the resulting circular cross sections will have varying diameters.

To represent an actual pipe elbow with an idealized geometry, the following tasks are performed on the point cloud of the data acquired from scanning the pipe elbows using Geomagic®:

1. The vertical and the horizontal planes of symmetry are obtained. The centre of the ideal torus will be on the intersecting line of these two planes.
2. A cross section of the elbow is taken using the horizontal plane of symmetry, and the average radius of curvature of the exterior curve is measured. This radius will later be utilized to locate the axis of revolution of the torus.
3. A cylinder with a very small height and with a radius equal to the previously measured radius of curvature of the exterior curve is created. This cylinder is fitted to the exterior surface of the elbow. The exterior curve has a lower curvature compared to the interior curve, which ensures a good fit of the cylinder to the elbow outer surface. The axis of this cylinder is deemed the axis of revolution of the torus.
4. The intersecting point of the horizontal plane of symmetry and the axis of revolution is obtained. This point, in our analysis, is defined as the centre of the pipe elbow. The elbow is aligned to the coordinate system so that the planes of symmetry and the centre coincide with two of the coordinate planes and the coordinate origin.
5. Cross sections of the pipe elbow are taken on planes rotated about the axis of revolution of the elbow. The diameters of each circular cross section are measured. The average diameter is taken as the diameter of the circle that defines the cross section of the ideal torus.
6. The centroid of each cross section is obtained, and the distance of each centroid from the centre of the elbow is measured. The average distance is taken as the distance of the centre of the circle from the axis of revolution of the torus. Thus, the two geometric attributes necessary to represent the pipe elbow with an ideal torus are obtained.

The methods for obtaining the idealized geometry and measuring the imperfections are described in detail with figures in the following steps:

Step 1: Planes of Symmetry

A plane of symmetry can be described as an imaginary mirror in which an object can be reflected while appearing unchanged. Based on an initially specified plane where it roughly bisects the objects, Geomagic® fine-tunes the position such that the plane bisects the object more precisely. Using this tool, the two planes of symmetry for each scanned elbow data are obtained as shown in Figure 3.50.

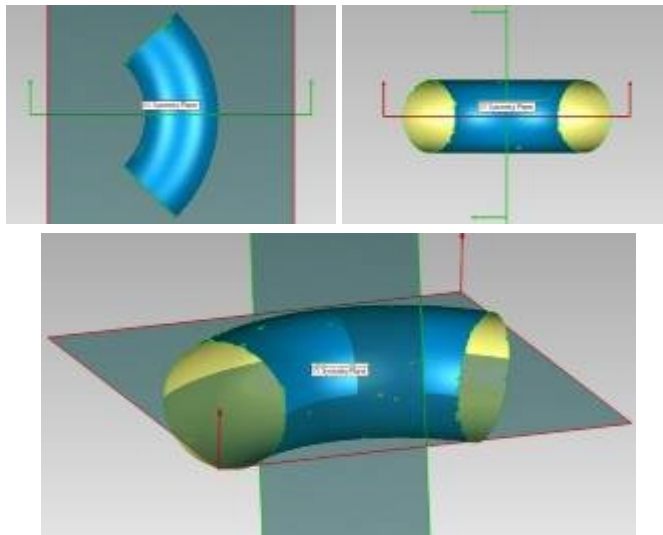


Figure 3.50 Planes of Symmetry

Step 2: Radius of Curvature of the Outer Curve

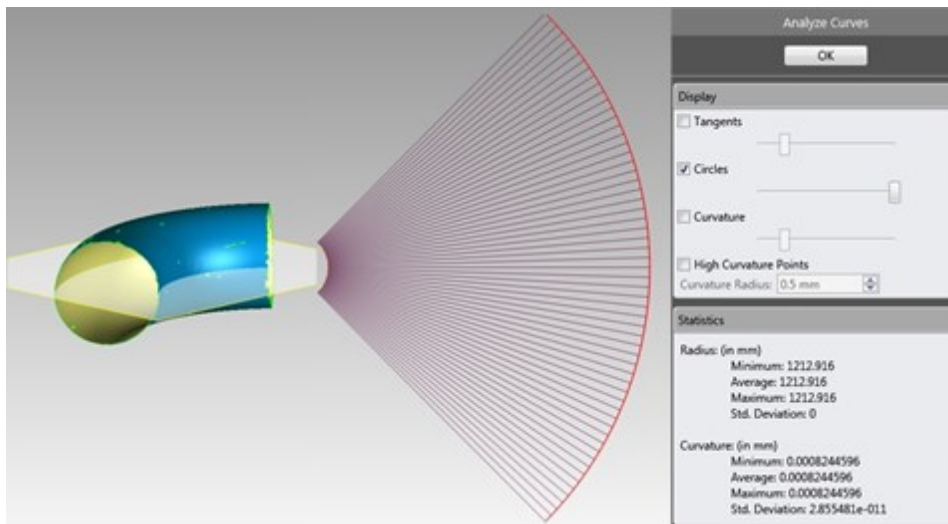


Figure 3.51 Radius of Curvature of the outer curve of the elbow

Using the horizontal plane of symmetry, the outer curve of the elbow is extracted. The type of curve is selected to be 'Arc', and the tolerance is set to 1.0 mm, so that the arc never diverges from the true cross section by more than this value. The radius of curvature of this curve is recorded (Figure 3.51).

Step 3: Axis and Centre of Elbow

A thin slice (5 to 20 mm, depending on the pipe elbow diameter) of the elbow is trimmed using planes offset to the horizontal plane of symmetry. Appropriate thickness value for each elbow is selected so that the surface along the thickness can be assumed planar (Figure 3.52 a). For example, in case of the 12 inch elbow, the trimming planes are taken as 2.5 mm offset on either side of the horizontal plane of symmetry. For the 36 inch elbow, the planes are offset at 10 mm on either side of the horizontal plane of symmetry. As a result, the trimmed surface is almost planar across its thickness and can be approximated as the curved surface of a portion of a target cylinder. A cylinder is created with the radius equal to the measured radius of curvature of the outer curve of the elbow, and the height is set equal to the thickness of the slice (Figure 3.52 b). The two faces of the cylinder are discarded and the rest is trimmed off with two planes through the cylinder axis and at 90 degrees with each other. The resulting CAD object resembles the trimmed slice of the elbow (Figure 3.52 c).

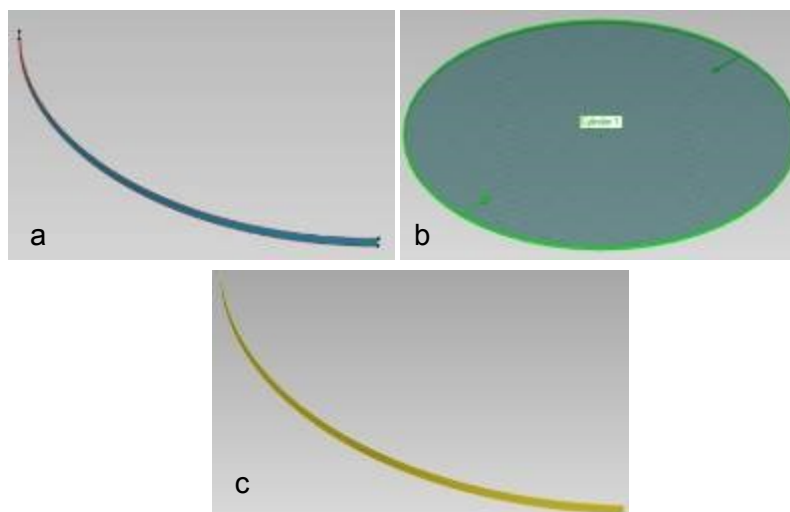


Figure 3.52 a) Trimmed elbow slice, b) Cylinder, and c) Trimmed CAD object

The elbow slice and the CAD object are aligned using the best fit alignment. During this procedure, the elbow slice remains fixed and the CAD object repositions itself with respect to the elbow slice so that the average deviation

between the two surfaces are minimum. After alignment, the axis of rotation of the CAD object is obtained. This axis is deemed the axis of revolution of the torus that represents the elbow, and the intersection point of this axis and the horizontal symmetry plane is the centre of the elbow (Figure 3.53).

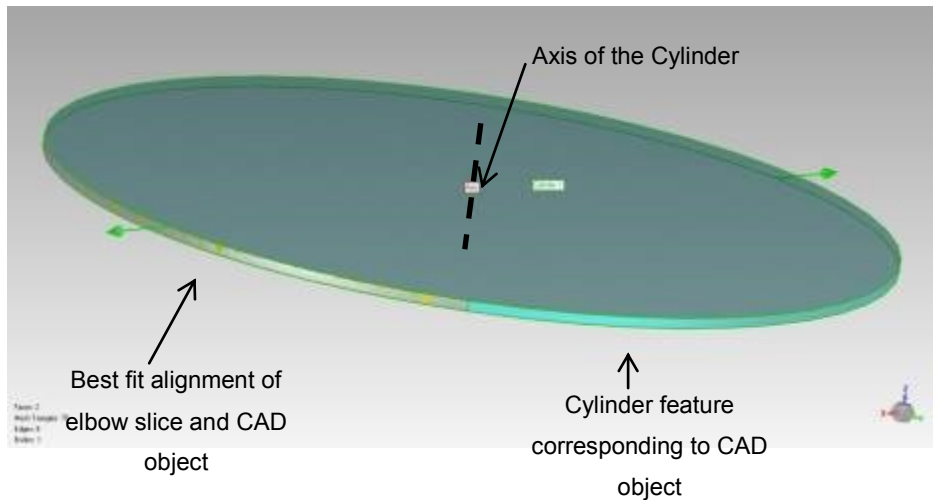


Figure 3.53 Axis of revolution of the pipe elbow

Step 4: Alignment with Coordinate System

The pipe elbow is aligned to the coordinate system using the constraints: a) Coordinate origin coincides with the centre of the elbow (intersection of the axis and the horizontal symmetry plane), and b) The two planes of symmetry coincide with the XZ and XY planes (Figure 3.54)

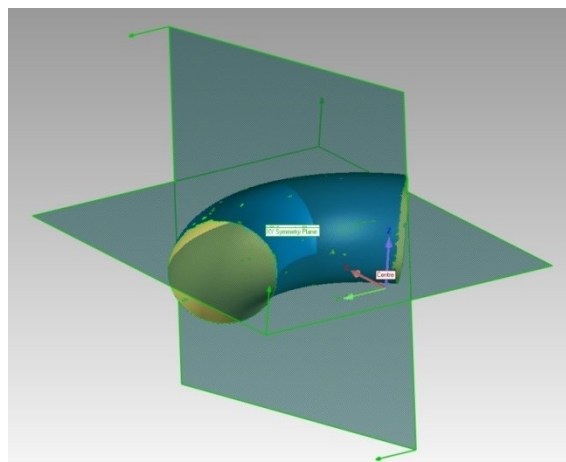


Figure 3.54 Alignment of elbow with the coordinate system

Step 5: Radius of Torus Cross-section

Arc type circular curves are created using planes rotated around the Z axis, which is the axis of revolution of the torus. The average radius of these curves is calculated and is considered to be the radius of the circle that defines the torus cross section (Figure 3.55).

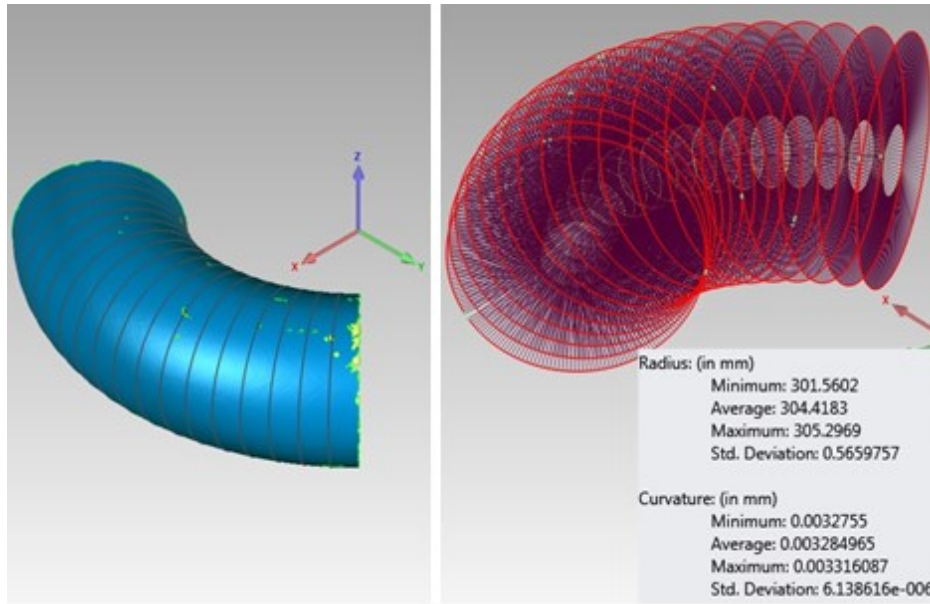


Figure 3.55 Average radius of elbow to be used to define the ideal torus

Step 6: Distance of the Centre of the Circle from the Axis of Revolution

The circular curves are converted to point objects, and the centroid of each cross section is obtained. The average distance of the centroids from the origin is calculated and considered to be the distance of the centre of the circle from the axis of revolution of the ideal torus, i.e., the radius of revolution.

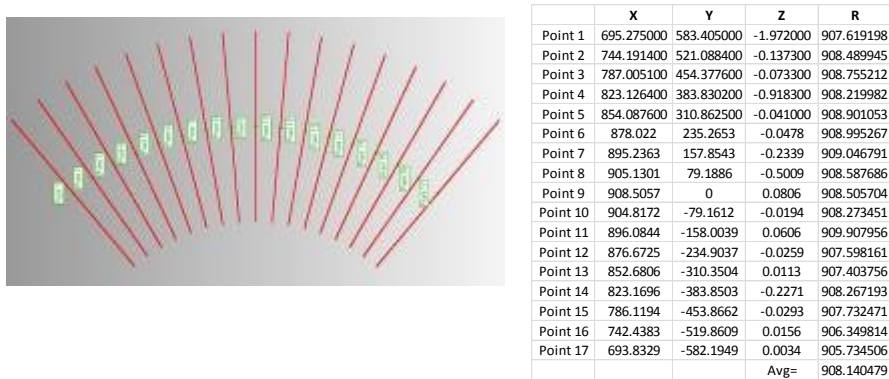


Figure 3.56 Distance of the centre of the circle from the axis of revolution of the ideal torus

Step 7: Comparison with Idealized Geometry

The radius of the circle and the distance of the centre of the circle from the axis of revolution are measured using the above mentioned method. These two geometric attributes define the idealized torus representing each pipe elbow. Using these values, CAD torus objects are created using the software Solid Works. The idealized CAD objects are imported in Geomagic® and compared with the scanned elbow surface. The idealized elbow is repositioned using exact rotations around the coordinate axes, and compared with the scanned elbow (Figure 3.57).

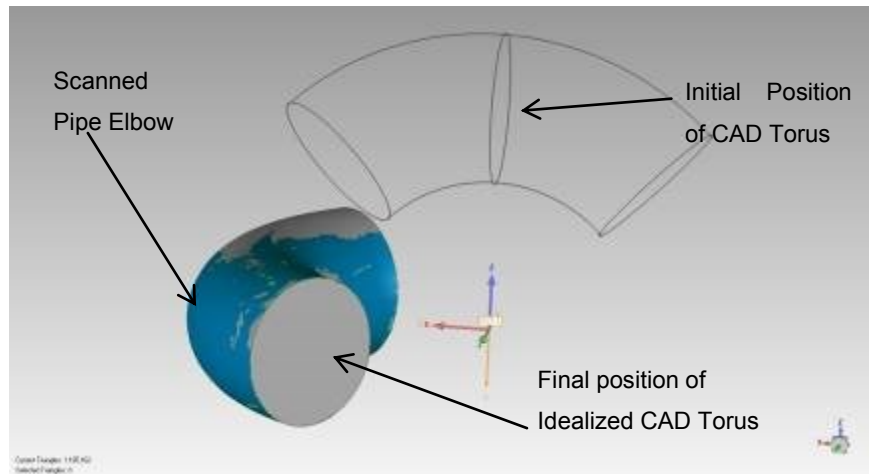


Figure 3.57 Repositioning of the idealized torus with respect to the actual pipe elbow

Step 8: Ovalization Measurement

The maximum and minimum values of the Outside Diameter (OD) are measured at cross sections taken at 5 degrees angular intervals around the Z axis. The ovalization value for each cross section is calculated according to the equation:

$$\text{Ovalization} = [2 \cdot (D_{\max} - D_{\min})] / (D_{\max} + D_{\min})$$

Where D_{\max} = maximum OD, D_{\min} = minimum OD

The average ovalization value is calculated over multiple cross sections for each elbow.

Step 9: Wall Thickness Measurement

Wall thickness values are measured at cross sections taken on planes through the Z axis. The thickness values are presented with respect to angles about a reference line. The reference line is the line connecting the centre of the cross section and the coordinate origin. Angles are measured counter clockwise about the reference line. Therefore, 0 and 360 degree angles correspond to the inside of the elbow cross section. 90 and 270 degrees correspond to the top and bottom of the elbow cross section respectively. 180 degree angle corresponds to the outside of the elbow cross section (Figure 3.58).

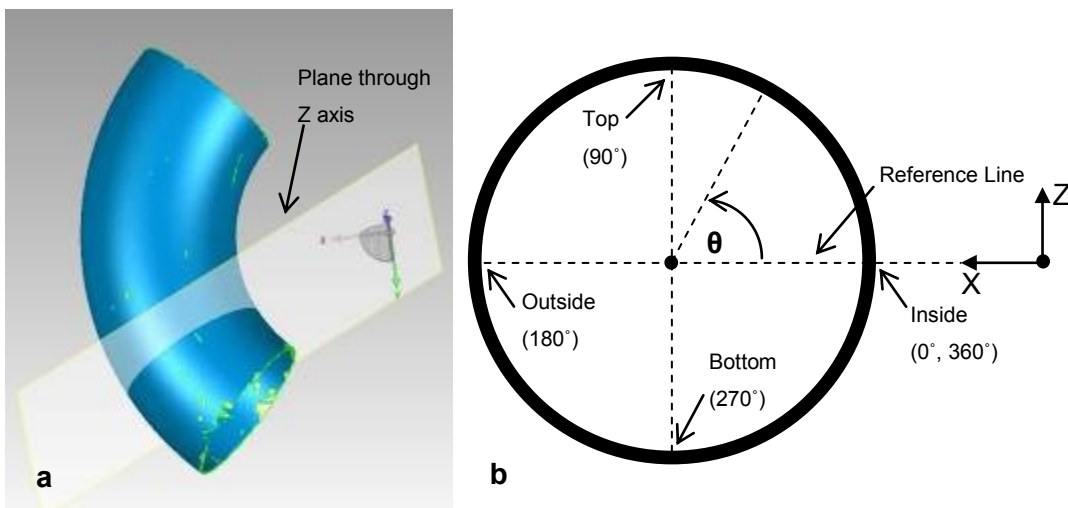


Figure 3.58 a) Plane through Z axis for taking cross section, b) Schematics of wall thickness measurement

The wall thicknesses near the edges of the elbows are measured in two different methods. In the first method (Method 1), a cross section of the outside and the inside surfaces of an elbow is taken using a plane through the Z axis, and the wall thickness values are measured at different angles around the reference line (Figure 3.59 a). In the second method (Method 2), a 3D comparison is performed between the inside and the outside surfaces of an elbow by setting the outside as a reference and the inside as a test object. Then a 2D comparison spectrum is obtained by taking a section on a plane through the Z axis. The deviations between the points on the outside and inside surfaces, which are the wall thickness values, are measured. From the coordinates of the points on the outside surface, the angle around the reference line is calculated for each wall thickness measurement (Figure 3.59 b).

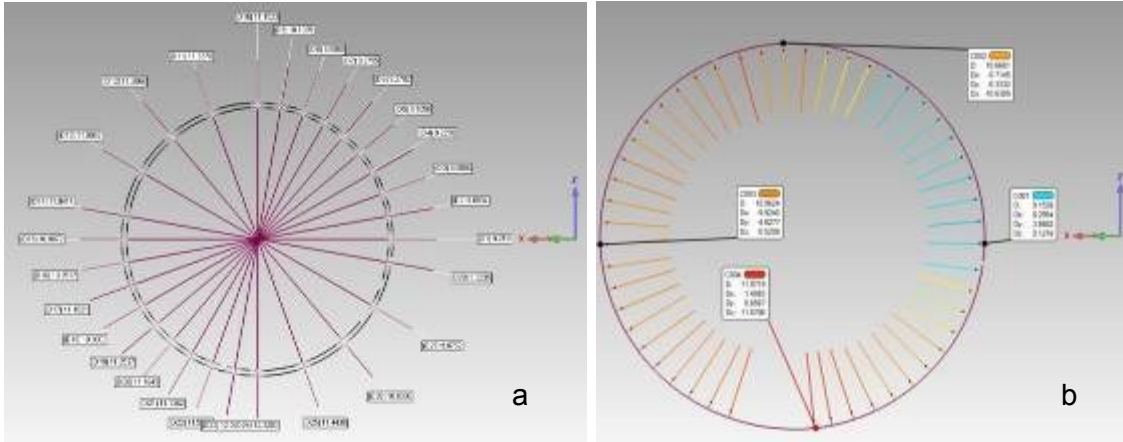


Figure 3.59 a) Method 1, and b) Method 2 for elbow wall thickness measurement

The wall thickness values are presented as the percentage of deviation from the specified value for each elbow. For comparison, the results of thickness measurement at a typical cross section of an elbow using the two methods are shown in Figure 3.60:

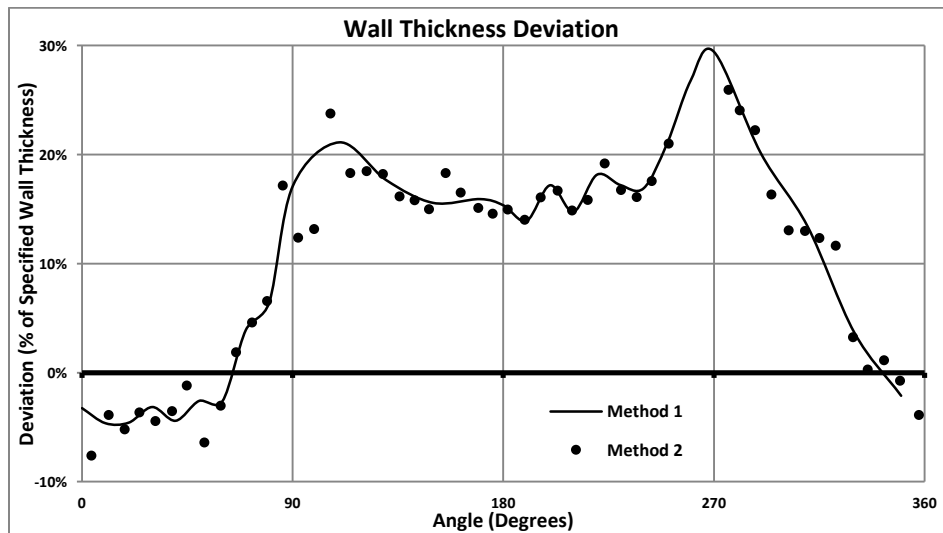


Figure 3.60 Comparison between the two methods of wall thickness measurement

The average difference in thickness value between the two methods of measurement are found to be 0.12 mm, and a paired t test produces a P-value of 0.98, indicating that there is no significant difference between the two paired measurements. Method 2, being faster, is employed in further analysis of the

elbows. The results of the geometric analysis of pipe elbows are presented in Chapter 5.

3.5.4 Summary of the Geometric Analyses

The methods for the geometric analyses of UOE manufactured straight pipe segments, protective pipe sleeves, and ninety degree pipe elbows have been elaborated in this section. The general procedure for the analyses is to import the surface data acquired from 3D scanning to the reverse engineering software Geomagic©, and perform different tasks in order to obtain the required geometric dimensions and measurement results. The tasks are performed through utilizing different general purpose tools available in Geomagic©.

The geometric analysis of straight pipe segments required alignment of scanned surface, locating pipe axis, fitting of best fit cylinder and plane, trimming polygon object, finding the centroid of point clouds, comparing pipe surface points with respect to ideal cylinder in 2D and 3D, measuring pipe diameter, and measuring pipe wall thickness. The fitting analysis of protective sleeves required alignment, locating axis, fitting of best fit cylinder, and comparison in 2D and 3D. The pipe elbow geometry analysis required the extraction of planes of symmetry, measurement of the radius of curvature, fitting of best fit cylinder, trimming polygon object with planes, alignment of scanned surface, measuring radius of curvature, finding the centroid of point clouds, comparison of scanned surface with respect to ideal geometry in 2D and 3D, and measuring wall thickness.

The tools employed to perform these tasks are built into the software. The selection of the required tasks and their sequence is an original work of this research, which was arrived at through experimenting with the available tools and functionalities of the software. Despite employing the built in tools, the geometric analysis methods used for the analyses of straight pipes, sleeves, and pipe elbows are general procedures, and can be adopted into pipeline inspection schemes irrespective of the reverse engineering software being used. It is also possible to develop dedicated software for the geometric analysis of pipes and different pipe fittings based on the general geometric analysis method presented in this section. The development of dedicated software is, however, beyond the scope of this thesis.

3.6 Conclusion

This chapter provides an overview of 3D scanning technology and its application to pipe inspection through reverse engineering. The data acquisition method developed has proved to be very efficient in terms of acquisition time and data size. The merits of this new method over the previous ones are: higher accuracy, larger data size, and faster acquisition of data. In addition, this method is applicable to pipe segments of large diameter and length. The scanner being portable, data acquisition can be performed either in the laboratory or in the field. The only precaution to be taken is to ensure appropriate shades, so that external light sources do not interfere with the scanner. Pipes no longer need to be positioned vertically for taking measurements. A complete scan of a 3 meter segment of an NPS 42 inch line pipe can be performed within 3 hours.

The limitations of the previously developed methods for pipe imperfection measurements have completely been resolved in this new method. This method has overcome the problem of locating pipe axis, and eliminated the necessity of applying corrections to the acquired data. Measurements are taken virtually using reverse engineering software. Therefore, the complications related to maintaining exact position of LVDT and dial gauges no longer exist. The capability of the scanner to scan in high resolution enables obtaining larger number of data points per cross section of a pipe. The enormous amount of data gathered from each pipe enabled a very detailed analysis of geometry, which were not possible using conventional physical measurement techniques. The application of reverse engineering software to analyse straight pipes has been successfully furthered to the analysis of pipe elbows, which are more complicated and computationally demanding.

It should be noted that a number of commercial software for pipe inspection are currently available in the market, such as Creaform Pipecheck. However, these software are specifically designed for inspecting operational damages and corrosion, while the method presented in this chapter using Geomagic© is solely to investigate initial imperfections.

CHAPTER 4: RESULTS OF THE GEOMETRIC ANALYSIS OF UOE MANUFACTURED STRAIGHT PIPES

4.1 Introduction

In the previous chapter, the methods developed for pipe surface data acquisition using the 3D scanner, and their measurement procedure using reverse engineering software has been discussed. In this chapter, the results obtained from the geometric analysis of UOE manufactured pipes will be presented. The typical imperfection patterns observed in these pipes will be discussed.

4.2 Pipe Specifications

Ten UOE manufactured pipes are studied for geometric imperfections. The pipe specifications are as follows:

Table 4.1 Specifications of the scanned pipes

	Nominal Diameter		Nominal Thickness		Grade	D/t Ratio	Manufacturer
	Inch	mm	Inch	mm			
NPS 20 A	20	508	0.312	7.925	X70	64.10	Evrax
NPS 20 B	20	508	0.312	7.925	X70	64.10	Evrax
NPS 34 A	34	864	0.375	9.525	X100	90.71	Sumitomo
NPS 34 B	34	864	0.375	9.525	X100	90.71	Sumitomo
NPS 42 A	42	1067	0.406	10.312	X100	103.47	Sumitomo
NPS 42 B	42	1067	0.406	10.312	X100	103.47	Sumitomo
NPS 42 C	42	1067	0.562	14.275	X100	74.75	Nippon
NPS 42 D	42	1067	0.562	14.275	X100	74.75	Nippon
NPS 42 E	42	1067	0.562	14.275	X100	74.75	Nippon
NPS 42 F	42	1067	0.562	14.275	X100	74.75	Nippon

4.3 Weld Geometry

NPS 20 pipes had their seam weld grinded smooth, so it was not possible to measure weld dimensions for NPS 20 A and B. Weld surfaces on the inside and outside of pipes NPS 34 A, B and NPS 42 A, B were scanned up to 500 mm from the edge. It was therefore possible to measure their actual thickness, and is reported in Table 4.2, along with the average, standard deviation, and coefficient of variation (CV).

Table 4.2 Weld thickness of NPS 34 A, B and NPS 42 A, B

NPS 34 A		NPS 34 B		NPS 42 A		NPS 42 B	
Distance	Thickness	Distance	Thickness	Distance	Thickness	Distance	Thickness
mm	mm	mm	mm	mm	mm	mm	mm
180	13.863	180	12.938	180	13.961	180	15.211
200	13.922	200	13.051	200	13.97	200	14.969
220	13.887	220	13.055	220	14.092	220	14.976
240	13.969	240	13.175	240	13.748	240	14.943
260	13.882	260	13.231	260	13.771	260	14.737
280	13.864	280	13.212	280	13.826	280	14.941
300	13.895	300	13.187	300	13.717	300	14.728
320	13.761	320	13.204	320	13.614	320	14.551
340	13.633	340	13.300	340	13.381	340	15.171
360	13.888	360	13.154	360	13.237		
380	13.918	380	13.183	380	13.807		
400	13.842	400	13.300	400	13.61		
420	13.671	420	13.295	420	13.523		
440	13.851	440	13.269	440	13.239		
460	13.703	460	13.256				
Average	13.837	Average	13.187	Average	13.678	Average	14.914
St. Dev	0.099	St. Dev	0.104	St. Dev	0.263	St. Dev	0.212
CV	0.007	CV	0.008	CV	0.019	CV	0.014

The average values of seam weld thickness for these four pipe specimens are seen to be between 13.187 mm and 14.914 mm. The standard deviations are between 0.099 mm and 0.263 mm. The coefficients of variation are seen to be within 0.007 and 0.019.

NPS 42 C could not be analysed due to loss of data after importing to Geomagic©. Outer surfaces of welds were scanned for pipes NPS 42 D,E, and F, and therefore, the idealized measurement technique mentioned in chapter 3 was utilized to measure weld thickness (t) and weld width (W) for these three pipes. The idealized weld width (W) and thickness (t) values of NPS 42 D, E, and F are shown in Table 4.3. The average, standard deviation, and coefficient of variation are also listed.

Table 4.3 Idealized Weld width and thickness values of NPS 42 D, E, and F

NPS 42 D			NPS 42 E			NPS 42 F		
Distance	Width	Thickness	Distance	Width	Thickness	Distance	Width	Thickness
mm	mm	mm	mm	mm	mm	mm	mm	mm
300	18.105	3.753	400	22.957	4.941	300	16.901	4.725
500	18.129	4.323	600	21.352	3.685	500	17.306	4.318
700	16.089	4.189	800	20.176	4.376	700	17.338	3.896
900	15.17	4.14	1000	18.88	3.807	900	17.685	3.228
1100	17.205	4.138	1200	18.991	3.907	1100	18.722	3.001
1300	16.084	4.236	1400	18.971	3.317	1300	19.01	3.618
1500	18.063	4.241	1600	18.244	3.92	1500	17.028	3.642
1700	18.257	4.233	1800	18.603	3.152	1700	17.158	4.59
1900	17.287	4.407	2000	16.408	4.738	1900	20.386	4.017
2100	18.05	4.195	2200	17.945	4.332	2100	16.868	3.744
2300	19.046	4.362	2400	18.602	4.938	2300	17.031	3.396
2500	18.167	4.265	2600	20.427	4.643	2500	18.937	3.971
Average	17.345	4.162	Average	19.318	4.262	Average	17.819	3.909
St. Dev	1.079	0.166	St. Dev	1.624	0.551	St. Dev	1.394	0.470
CV	0.062	0.039	CV	0.084	0.129	CV	0.078	0.12

The average values of the idealized weld width for these three pipe specimens are seen to be between 17.375 mm and 19.318 mm. Their standard deviations are within 1.079 mm and 1.624 mm, while the coefficients of variation are within 0.062 and 0.084.

The average values of the idealized weld thickness for these three pipe specimens are seen to be between 3.909 mm and 4.262 mm. Their standard deviations are within 0.166 mm and 0.551 mm, while the coefficients of variation are within 0.039 and 0.129. These coefficients of variation from the idealized thickness are seen to be greater than those found from the actual thickness listed in Table 4.2.

4.4 Deviation from Ideal Pipe

The 2D deviation pipes from their ideal geometry were analysed in Geomagic®. The typical deviation patterns of the scanned pipes from their corresponding ideal

geometry at selected cross sections of each pipe group are shown in the following figures:

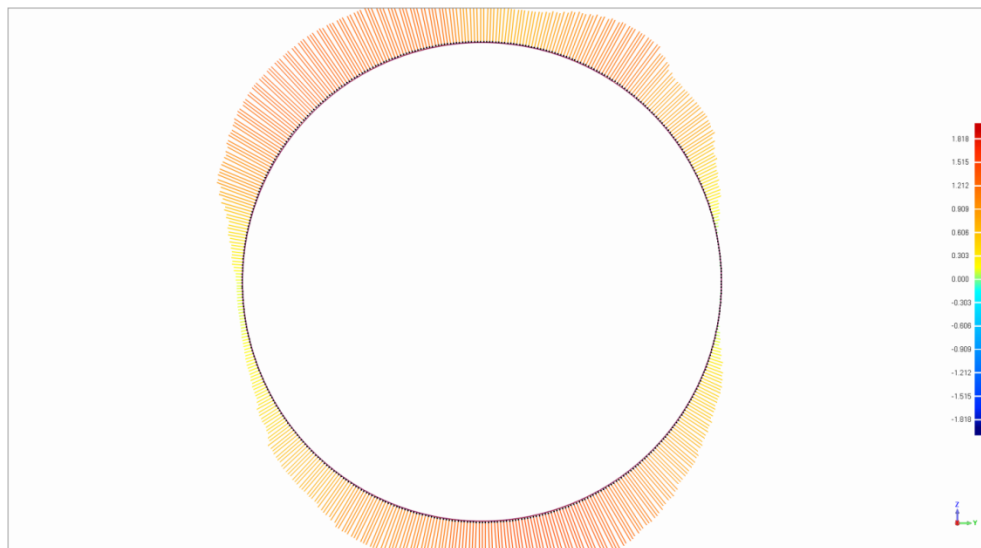


Figure 4.1 2D deviation spectrum, NPS 20 A ($D/t = 64.10$), 2200 mm from edge

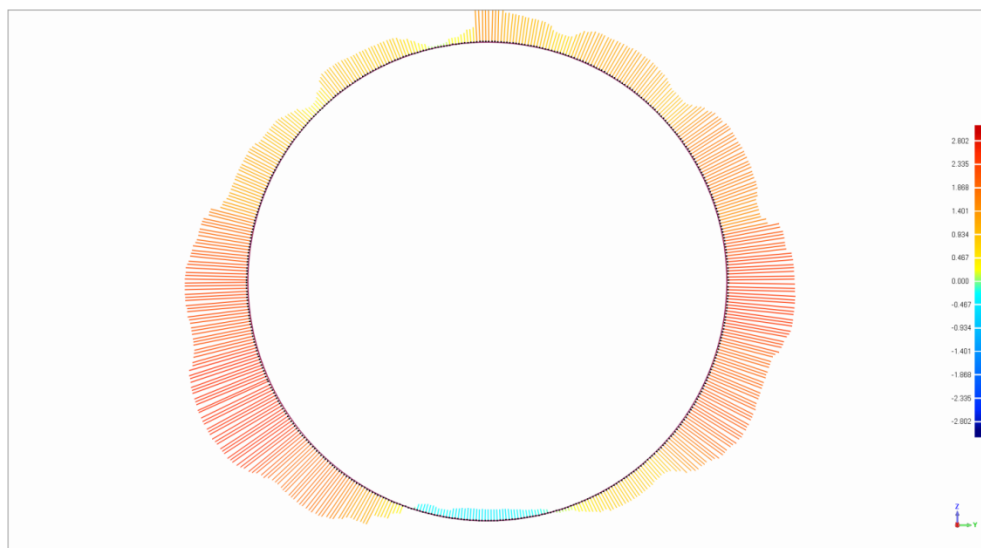


Figure 4.2 2D deviation spectrum, NPS 34 A ($D/t = 90.71$), 400 mm from edge

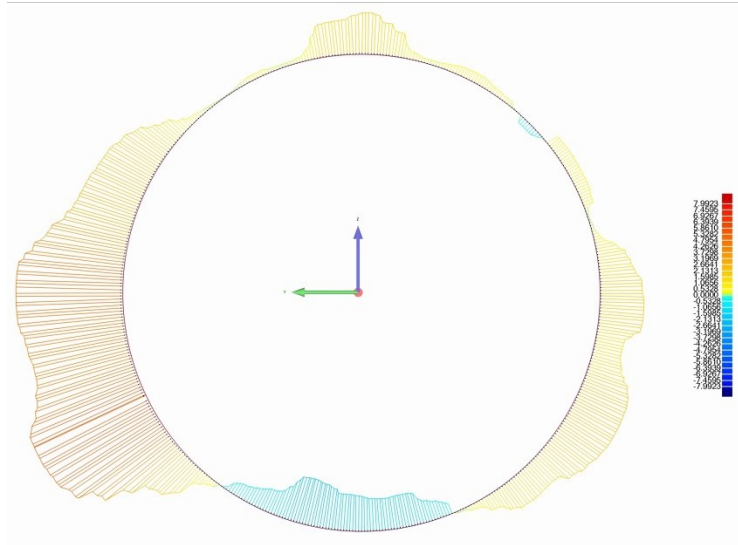


Figure 4.3 2D deviation spectrum, NPS 42 D (D/t = 74.75), 1200 mm from edge

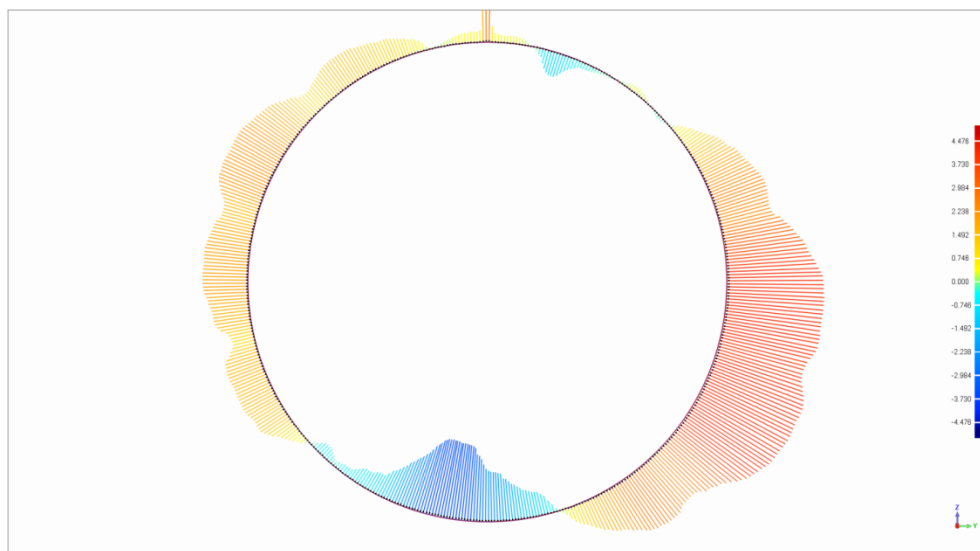


Figure 4.4 2D deviation spectrum, NPS 42 B (D/t = 103.47), 300 mm from edge

The rest of the cross sections Showed similar patterns. As mentioned in Chapter 3, the 2D deviation spectrums are colour coded whiskers, where blue and red colours indicate negative and positive deviations respectively. The deviations are in fact the radial distance of points on the scanned pipes surfaces from corresponding points on the ideal pipe surface. It is seen from the above figures that the NPS 20 inch pipes have positive deviation all around their perimeter. The

NPS 34 inch and NPS 42 inch pipes have wavy patterns of deviations, and the negative deviations are located on the opposite side of the seam weld location.

The maximum and average deviation values of each pipe from their ideal geometry are listed in Table 4.4. The deviation in terms of the percentage of the nominal OD is a better representation for the purpose of comparison between different pipe groups. The NPS 42 D pipe is seen to have the highest maximum positive and negative deviations, 0.791% and 0.495% of nominal OD respectively. The pipe NPS 20 B has the next highest value of maximum positive deviation, 0.613% of nominal OD. The NPS 42 A pipe has the lowest maximum positive and negative deviations, 0.351% and 0.258% of nominal OD respectively. The rest of the specimens have their maximum positive and negative deviation values close to approximately 0.5% of their nominal OD.

Maximum deviations have the possibility of being location specific, and a better representation would be the average deviation. It is seen that the NPS 20 B pipe has the maximum average positive deviation, 0.216% of nominal OD, and the NPS 42 B pipe has the maximum average negative deviation, 0.154% of nominal OD. The maximum average deviation magnitudes in mm are very small. The maximum average positive deviation is seen to be 1.099 mm, and the maximum average negative deviation is 1.643 mm.

Table 4.4 Maximum and Average deviation from nominal OD

Pipe	Maximum Deviation(mm)				Average Deviation(mm)			
	Positive	% OD	Negative	% OD	Positive	% OD	Negative	% OD
NPS 20 A	2.407	0.474	1.757	0.346	0.751	0.148	0.334	0.066
NPS 20 B	3.115	0.613	1.998	0.393	1.099	0.216	0.235	0.046
NPS 34 A	4.231	0.489	4.021	0.465	1.258	0.146	0.74	0.086
NPS 34 B	3.937	0.456	4.103	0.475	1.25	0.145	0.696	0.081
NPS 42 A	3.743	0.351	2.748	0.258	0.839	0.079	0.429	0.040
NPS 42 B	5.452	0.511	5.235	0.491	1.976	0.185	1.643	0.154
NPS 42 C	4.365	0.409	4.312	0.404	1.654	0.155	1.453	0.136
NPS 42 D	8.443	0.791	5.277	0.495	2.052	0.192	0.847	0.079
NPS 42 E	6.035	0.565	4.719	0.442	1.705	0.159	1.632	0.153
NPS 42 F	5.571	0.522	4.822	0.452	1.614	0.151	0.831	0.078

The average deviation values of the pipes' surfaces from their idealized geometry provide an understanding of the imperfection magnitudes. However, the average values of positive and negative deviations are still affected by the location specific maximum values. The distributions of the deviations are therefore investigated for each pipe specimen. The deviation distribution of NPS 34 A is shown in Figure 4.5:

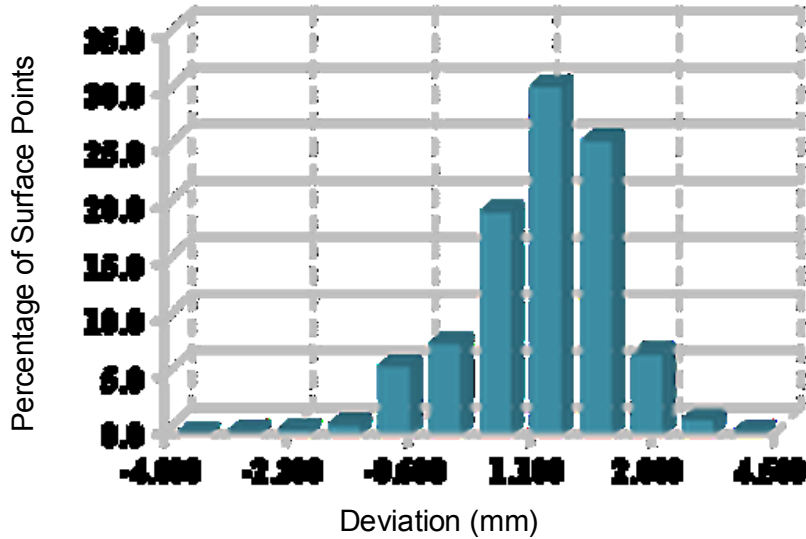


Figure 4.5 Deviation distribution histogram of NPS 34 A

The distribution is generated using the deviation of the surface points of each pipe from their corresponding ideal geometry. The points are presented as the percentage of the total number of points in the point cloud of the scanned surface.

From the histogram, it can be seen that a large percentage of points are within a small deviation range compared to the maximum positive and negative deviation. For example, the distribution in Figure 4.5 shows that almost 90% of surface points are within a deviation range of -0.7 mm to 2.8 mm approximately. From Table 4.4, it can be seen that the maximum deviation values for the NPS 34 A pipe were -4.021 mm and 4.231 mm, while the average values were -0.74 mm and 1.258 mm. Thus, the percentage of surface points within a deviation range provides the best understanding of the deviation of the specimens from their idealized geometry.

The deviation ranges with the maximum percentage of surface points for each pipe are listed in Table 4.5:

Table 4.5 Deviation Range with maximum percentage of surface points

Pipe	Deviation Range (mm)		Deviation Range (% OD)		Percentage of Total Surface Points
	Min	Max	Min	Max	
NPS 20 A	0.000	1.250	0.000	0.246	83.20%
NPS 20 B	0.346	1.730	0.068	0.341	93.46%
NPS 34 A	-0.705	2.821	-0.082	0.327	91.34%
NPS 34 B	-0.456	2.735	-0.053	0.317	87.86%
NPS 42 A	0.000	1.872	0.000	0.175	87.43%
NPS 42 B	-1.817	3.635	-0.17	0.341	85.26%
NPS 42 C	-2.000	2.910	-0.187	0.273	81.07%
NPS 42 D	-2.111	4.222	-0.198	0.396	87.69%
NPS 42 E	-1.632	4.567	-0.153	0.428	86.06%
NPS 42 F	-1.429	4.714	-0.134	0.442	87.71%

The NPS 20 inch pipes have 83% to 93% of surface points in a positive deviation range. NPS 34 A pipe has 91% points in a range of -0.082% OD to 0.327 % OD. NPS 34 B pipe is similar, with the negative deviation being lower (-0.053% OD). NPS 42 A pipe has 87.43% points in a positive deviation range (0.0% to 0.175% OD). NPS 42 B has 85.26% of surface points in a range of -0.17% OD to 0.341% OD. The NPS 42 S, D, E, and F pipes have more than 80% of their surface points in a deviation range that goes from negative to positive, which indicates these four pipes had significant regions around their perimeter with reduced diameter. NPD 42 D has the maximum negative deviation limit of -0.198% OD, and the NPS 42 F has the maximum positive deviation limit of 0.442% OD.

4.5 Ovalization

The different values of ovalization calculated in accordance with the CSA Z662-11 equation at different distances from the pipe ends, their standard deviation, and their Pearson product-moment correlation coefficient (PCC) with the longitudinal distances are listed in Table 4.6. The CSA Z662-11 specified upper limit being 0.03, the numbers are presented up to three decimal places.

Table 4.6 Ovalization Values at different sections

Longitudinal Distance (mm)	Ovalization						
NPS 20 A		NPS 20 B		NPS 34 A		NPS 34 B	
200	0.006	200	0.005	200	0.011	200	0.009
400	0.004	300	0.004	400	0.009	400	0.007
600	0.004	400	0.002	600	0.010	600	0.007
800	0.003	600	0.004	800	0.010	800	0.008
1000	0.005	800	0.004	1000	0.009	1000	0.007
1200	0.003	1000	0.004	1200	0.013	1200	0.011
1400	0.005	1200	0.004	1400	0.005	1400	0.010
1600	0.006	1400	0.006	1600	0.007	1600	0.010
1800	0.006	1600	0.007	1800	0.008	1800	0.010
2000	0.007	1800	0.009	2000	0.008	2000	0.010
2200	0.007	2000	0.005	2200	0.010		
2400	0.006	2200	0.004	2400	0.009		
2600	0.008	2400	0.005	2600	0.010		
2800	0.007	2600	0.004				
3000	0.005						
3200	0.006						
3400	0.005						
St.Dev.	0.001	St.Dev.	0.001	St.Dev.	0.002	St.Dev.	0.001
PCC	0.49	PCC	0.38	PCC	0.22	PCC	0.65
NPS 42 A		NPS 42 B		NPS 42 C		NPS 42 D	
200	0.006	200	0.016	200	0.008	150	0.017
300	0.005	250	0.015	400	0.008	300	0.012
400	0.005	300	0.015	600	0.008	600	0.019
500	0.004	350	0.015	800	0.007	900	0.017
600	0.005	400	0.015	1000	0.007	1200	0.016
700	0.005	450	0.016	1200	0.006	1500	0.015
800	0.004	500	0.016	1400	0.006	1800	0.008
900	0.004	550	0.014	1600	0.008	2100	0.006
1000	0.004	600	0.015	1800	0.007	2400	0.006
				2000	0.005	2700	0.008
				2200	0.005	3000	0.007
						3300	0.010
St.Dev.	0.001	St.Dev.	0.001	St.Dev.	0.001	St.Dev.	0.005
PCC	0.84	PCC	0.33	PCC	0.81	PCC	0.77

Table 4-6 Ovalization Values at different sections (continued)

Longitudinal		Longitudinal	
Distance	Ovalization	Distance	Ovalization
mm		mm	
NPS 42 E		NPS 42 F	
150	0.008	150	0.010
450	0.007	450	0.009
750	0.011	750	0.009
1050	0.010	1050	0.008
1350	0.011	1350	0.006
1650	0.009	1650	0.006
1950	0.011	1950	0.006
2250	0.012	2250	0.006
2550	0.012	2550	0.005
2850	0.009	2850	0.006
3150	0.013	3150	0.007
3450	0.007	3450	0.011
St.Dev.	0.002	St.Dev.	0.002
PCC	0.39	PCC	0.22

From the above tables, it is observed that the ovalization values of cross sections of the scanned pipes are very small. The NPS 20 A and B pipes have ovalization values in the range of 0.002 to 0.009. The NPS 34 A and B pipes have ovalization values in the range of 0.005 to 0.013. The NPS 42 A and B has ovalization values within 0.004 and 0.016. The NPS 42 C, D, E, and F pipes have ovalization values between 0.005 and 0.019.

The standard deviations of the ovalization values are insignificant (0.001 to 0.005), which indicates that the ovalization values are fairly consistent throughout the length of the pipes. From the Pearson product-moment correlation coefficient (PCC) values, it is seen that there is no strong linear correlation between the ovalization values and their distances from the edge of the pipes. NPS 20 A and B, NPS 34 A, NPS 42 B, E, and F have PCC values less than 0.5, and for the rest of the specimens, the PCC values are within 0.65 to 0.84.

The average and maximum values of ovalization of each pipe segment are listed in Table 4.7. The average values of ovalization of all the specimens are within 0.001 and 0.012, the maximum are within 0.006 to 0.019.

Table 4.7 Summary of Ovalization

Ovalization Values				
	Average	Maximum	St. Dev.	PCC
NPS 20 A	0.006	0.008	0.001	0.49
NPS 20 B	0.006	0.009	0.001	0.38
NPS 34 A	0.001	0.013	0.002	0.22
NPS 34 B	0.009	0.011	0.001	0.65
NPS 42 A	0.005	0.006	0.001	0.84
NPS 42 B	0.015	0.016	0.001	0.33
NPS 42 C	0.007	0.008	0.001	0.81
NPS 42 D	0.012	0.019	0.005	0.77
NPS 42 E	0.009	0.013	0.002	0.39
NPS 42 F	0.007	0.011	0.002	0.22

4.6 Pipe Wall Thickness

Wall thickness deviations are presented as the percentage of the specified wall thickness corresponding to each pipe, and plotted against the angular distance from the longitudinal seam weld around their perimeter. The average thickness is also shown in each plot as a solid line. Multiple cross sections of each pipe are considered for wall thickness measurements. The typical thickness deviations observed in each pipe group according to their specified wall thickness are shown in Figure 4.6 to Figure 4.13. NPS 42 C and D specimens had partially missing inside surface data and their wall thickness deviation plots are not shown in the figures.

The NPS 20 pipes have wall thickness close to the specified value near their seam weld location (0% deviation). The thickness increases away from the seam weld and reaches a positive deviation of approximately 15% at the location 60 degrees from the seam weld. The wall thickness then keeps decreasing and reaches a deviation of approximately -7% at 270 degrees from the seam weld in NPS 20 A, and -5% at 240 degrees in NPS 20 B. The wall thickness then increases as we reach the seam weld and attains a value close to the specified wall thickness.

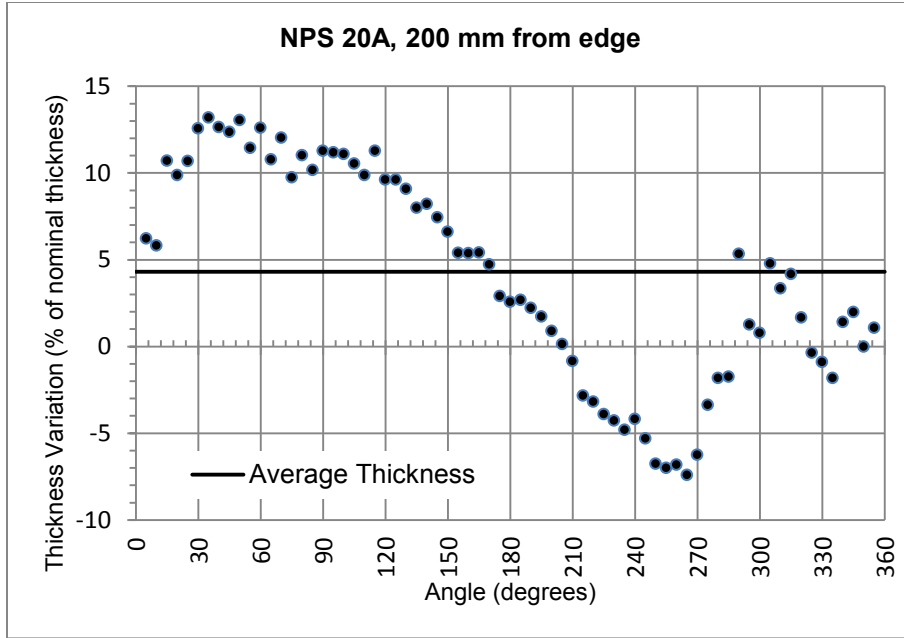


Figure 4.6 Thickness variation (%) of NPS 20 A (wall thickness = 7.925 mm) at a section 200 mm from pipe edge

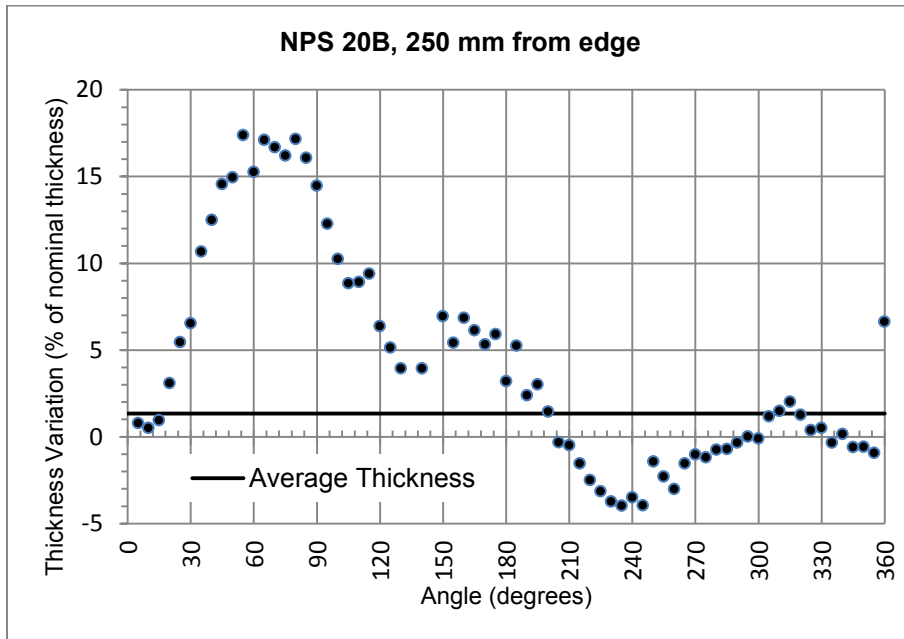


Figure 4.7 Thickness variation (%) of NPS 20 B (wall thickness = 7.925 mm) at a section 250 mm from pipe edge

The NPS 34 A has wall thickness values close to their specified value on either side of the seam weld. The wall thickness increases to 10% up to 60 degrees from the seam weld, then decreases to -5% from 60 degrees to 120 degrees. The thickness deviation then increases and reaches a maximum of 25% at 180 degrees from the seam weld. The thickness is then seen to decrease consistently and reaches the specified thickness at the other side of the seam weld (360 degrees).

NPS 34 B also has wall thickness values close to the specified value near the seam weld. The thickness reaches a maximum deviation of 12% at 160 degrees from the seam weld, and then reduces to 5% at 285 degrees. A sudden reduction to -3% is observed between 285 degrees and 310 degrees. The deviation then reaches to 0% near 360 degrees. It has a similar trend of thickness deviation as NPS 34 A, including the sudden decrease of thickness.

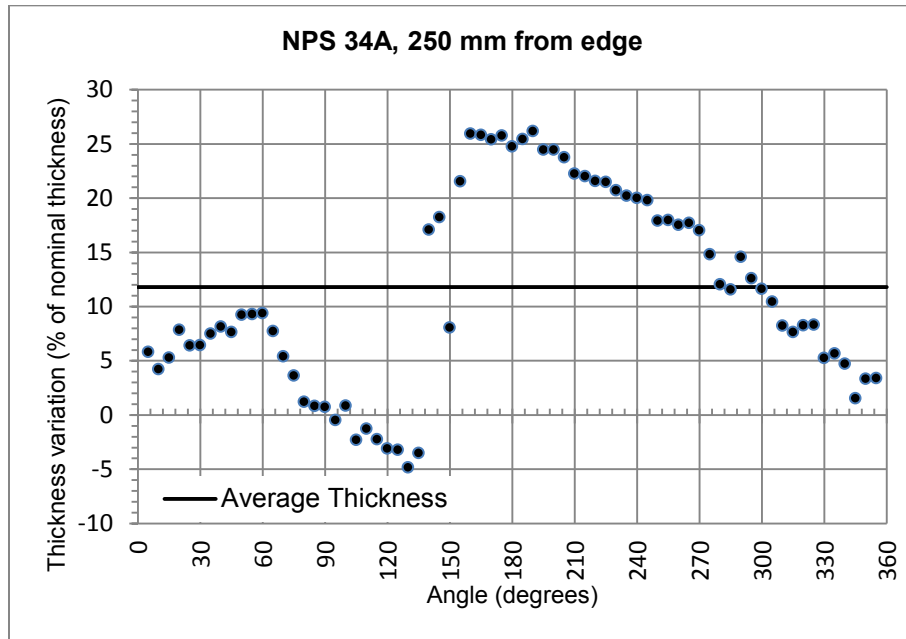


Figure 4.8 Thickness variation (%) of NPS 34 A (wall thickness = 9.525 mm) at a section 250 mm from pipe edge

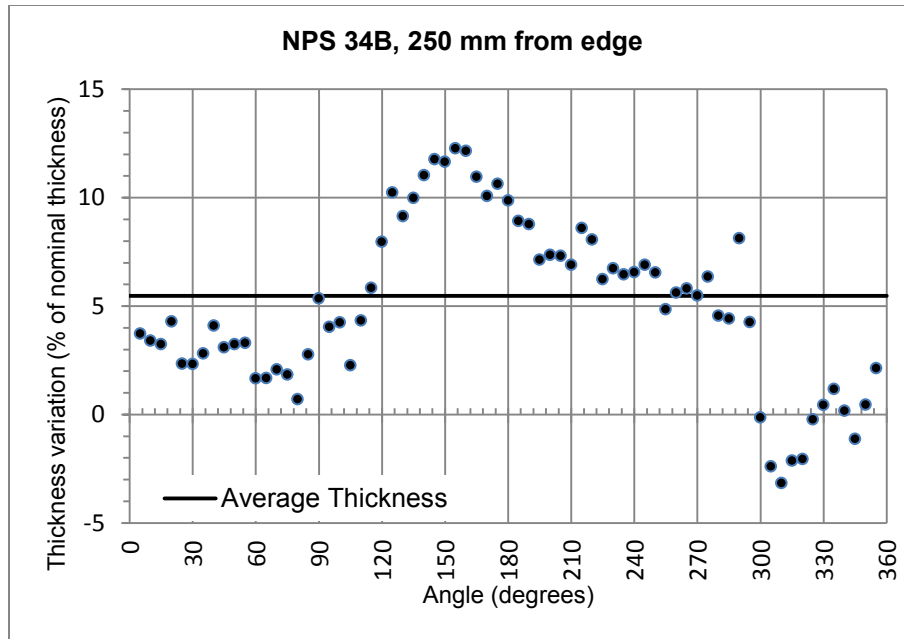


Figure 4.9 Thickness variation (%) of NPS 34 B (wall thickness = 9.525 mm) at a section 250 mm from pipe edge

NPS 42 A had thickness deviations in the range of -4.5% to +7% of specified thickness. The thickness deviations are seen to be clustered near the horizontal axis and no typical trend of increasing or decreasing thickness can be identified from the plot. NPS 42 B also has deviation values close to 0% in majority of the locations around the perimeter. However, a sudden reduction of thickness can be noticed between the locations 150 degrees and 180 degrees. The maximum negative deviation of thickness is seen to be approximately 12% of the specified thickness.

NPS 42 F specimen had partially missing inside surface data. NPS 42 E and F have similar trend of thickness deviation. Their wall thickness is seen to be less than specified near the seam weld. NPS 42 E and F have thickness deviations of -15% and -10% of the specified thickness near the seam weld (0 degrees and 360 degrees). Their thickness is then seen to increase consistently as we move away from the seam weld. NPS 42 E has a maximum deviation of 30% at 150 degrees, and NPS 42 F has a maximum deviation of 23% at 125 degrees from the seam weld. The thickness then keeps reducing as we reach the other side of the seam weld. The region with negative wall thickness deviation subtends an angle of 180 degrees around the perimeter.

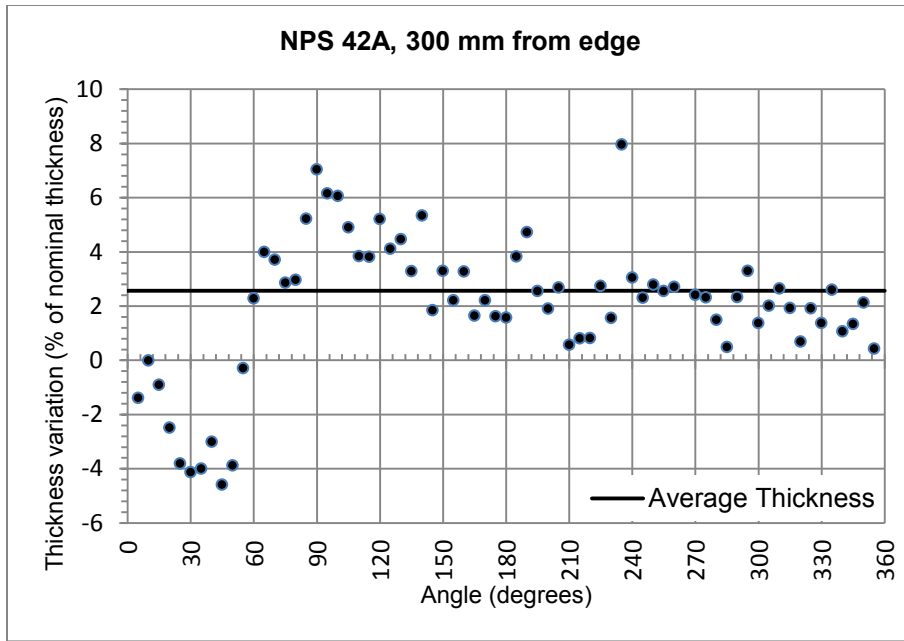


Figure 4.10 Thickness variation (%) of NPS 42 A (wall thickness = 10.312 mm) at a section 300 mm from pipe edge

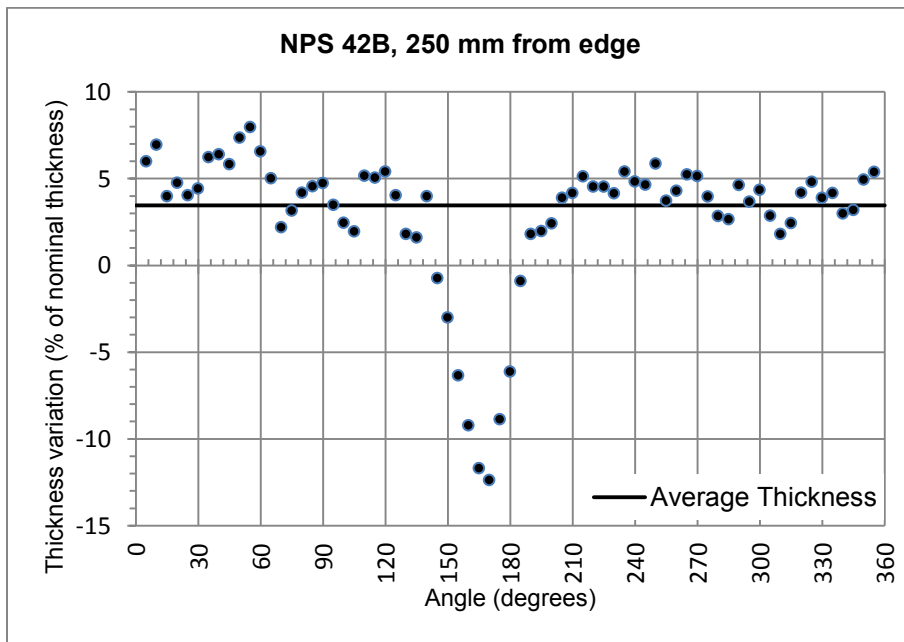


Figure 4.11 Thickness variation (%) of NPS 42 B (wall thickness = 10.312 mm) at a section 250 mm from pipe edge

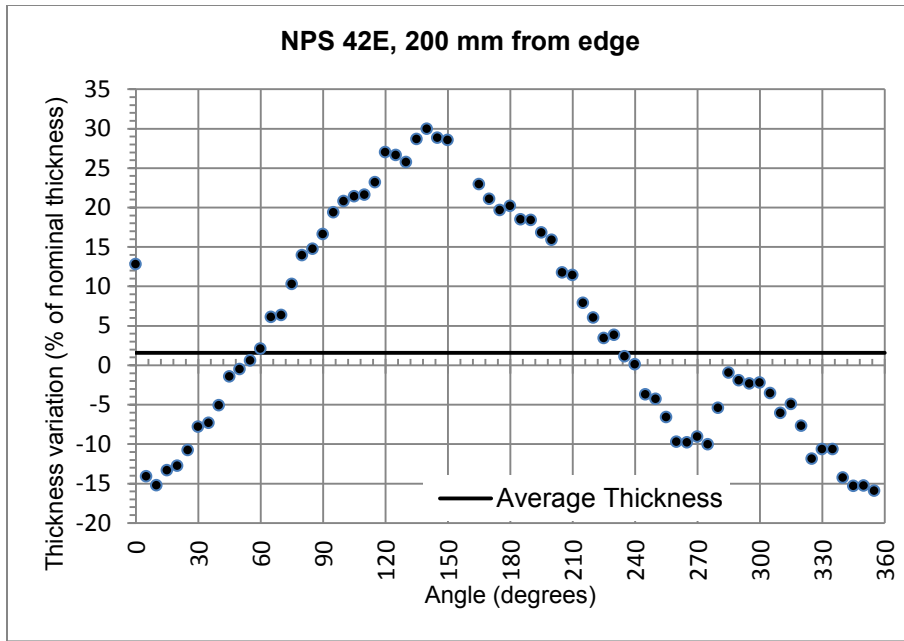


Figure 4.12 Thickness variation (%) of NPS 42 E (wall thickness = 14.275 mm) at a section 200 mm from pipe edge

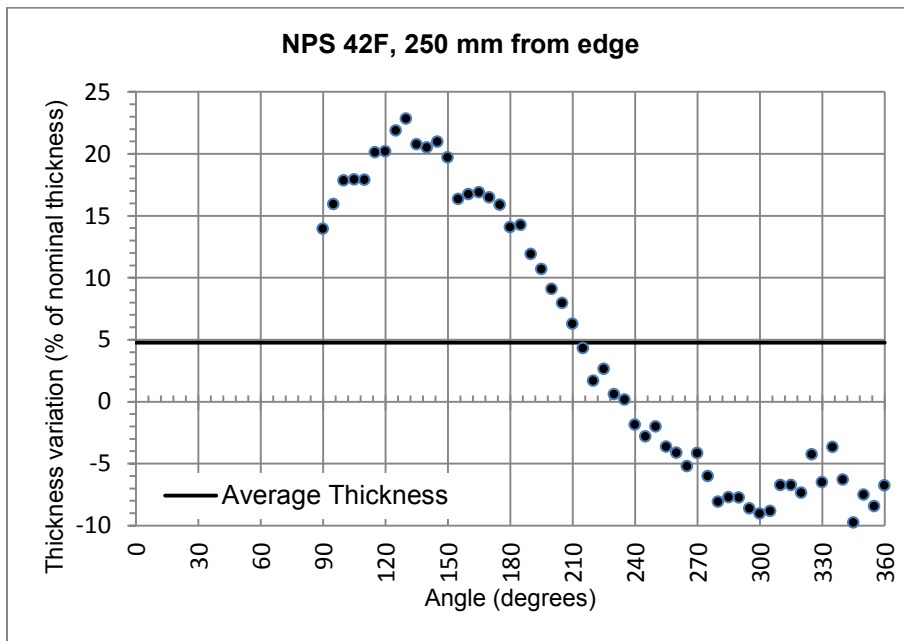


Figure 4.13 Thickness variation (%) of NPS 42 F (wall thickness = 14.275 mm) at a section 250 mm from pipe edge

4.7 Discussion on Results

As mentioned in section 4.3, only the outside surfaces of the seam weld were obtained through scanning the pipes NPS 42 D, E, and F. In the absence of the inside surface data for these welds, an idealised measurement method was developed and employed to measure the weld thickness (t) and width (W) values of these pipes using only the outside surface of the welds. This method enabled the measurements to be performed along the full length of the scanned pipes.

The values of standard deviations of t are within 0.16 mm to 0.47 mm, and the standard deviations of W are within 1.07mm to 1.62 mm. The coefficients of variation of t are within 0.039 and 0.129, and of W are within 0.062 and 0.084. The small values of coefficient of variation indicate that the weld dimensions have very small dispersion about their average values. The idealized weld thickness (t) is seen to have a higher maximum coefficient of variation (0.129) compared to the weld width (W). At this point, it should be recalled that the idealized thickness was chosen to be the distance between the outermost point of the weld cross section and the outer surface of the perfect cylinder (Figure 3.46). Consequently, the variation of diameter of a pipe with respect to its idealized dimension (perfect cylinder) is also captured while measuring the weld thickness. Therefore, the idealized thickness measurement is susceptible to variations, and a higher coefficient of variation in the idealized weld thickness values is expected. Nonetheless, the dispersions are very small and it is concluded that the weld dimension is very consistent along the length of the three pipe specimens (NPS 42 D, E, and F).

The above finding led to the conclusion that the longitudinal seam welding procedure employed during manufacturing these pipes is very efficient in producing consistent weld geometry. Consequently, only a 500 mm length of the inside and outside surfaces of the seam weld from pipe edge was scanned for the rest of the pipe specimens (NPS 34 A, B and NPS 42 A, B). The 500 mm length is the maximum accessible length inside the pipe while acquiring data using the 3D scanner, and can be considered adequate to verify the geometric variation or consistency of the seam welds.

The weld thickness obtained from analysing the outside and inside surfaces of seam welds of the remaining four pipe specimens show even more consistent results. The standard deviation values are in the range of 0.099 to 0.263 mm. The coefficients of variation are seen to be between 0.007 and 0.014. Therefore, it is concluded that the seam weld dimensions in all the pipe specimens are consistent, with insignificant amount of variations from their average values.

From the 2D cross sectional deviation analysis, it is seen that the pipe cross sections show patterns of deviation from a perfect circle when viewed with respect to the location of the longitudinal seam weld. As mentioned earlier in section 4.4, the 2D deviations are the radial distances of the surface points on the scanned pipes from their corresponding ideal geometry. Therefore, the observed deviation patterns are actually the variation of the Outside Radius (OR) of the pipes around their perimeter.

The NPS 20 A and B pipes show that their actual OR is greater than the nominal OR all around the perimeter, as indicated by the red coloured whiskers pointing outwards in Figure 4.1. The NPS 34 and NPS 42 pipes, which were known to be UOE manufactured, have similar patterns of OR deviation. Actual OR is seen to be close to the nominal value near the longitudinal seam weld. The Actual OR of these pipes is seen to increase beyond the nominal OR as we move away from the seam weld on either side. The actual OR values reach a maximum at locations approximately 90 degrees from either side of the seam weld. The OR values then keeps decreasing as we move farther away and reach a location opposite to the seam weld (180 degrees). The actual OR of these pipes is seen to be equal or less than the nominal OR at locations opposite to the seam weld, as indicated by the blue coloured whiskers pointing inwards in Figure 4.3 and Figure 4.4. It should be noted that the specimens were placed randomly on steel beams in a horizontal position. The position of the longitudinal seam weld with respect to the supporting beams of the specimens differed from each other. Despite this randomness, upon geometric analysis, the ovalization and OR deviation patterns of the pipes were observed to be similar when viewed with respect to the location of the seam weld. Therefore, the self-weight of the pipes did not have any evident influence on the observed OR deviation patterns.

The 3D deviation analysis of the pipes from their ideal geometry showed that their points on the surfaces of the scanned pipes are very close to their corresponding ideal geometry. From Table 4.4, it can be seen that the maximum average positive deviation is 2.052 mm (NPS 42 D), and the maximum average negative deviation is 1.643 mm (NPS 42 B). From the deviation distributions of the scanned pipes, it is further noticed that majority of the points on the scanned pipe surfaces are within a smaller deviation range (Table 4.5) compared to the maximum positive and negative deviation values (Table 4.4). From the 2D and 3D deviation analyses, it can be concluded that the UOE manufactured pipes have a similar pattern of OR variation around their perimeter. The average and maximum magnitudes of variations are different in different pipe specimens. Therefore the similarity in these pipes is in their imperfect shape, rather than their imperfection magnitude. However, the average deviations are very small compared to their nominal OD (0.192% to 0.154%).

ASTM A530/A530M-12 (Standard Specification for General Requirements for Specialized Carbon and Alloy Steel Pipe) specifies that for thin walled pipes (D/t ratio greater than 33) the difference in maximum and minimum OD should be less than 1.5% of the specified OD. CSA Z662-11 specifies that the ovalization value should be less than 0.03. The ovalization values at different cross sections of the ten pipes are well below the above specifications. This finding agrees with the previously stated fact that the deviation magnitudes are very small. The ovalization values are fairly consistent throughout the length of the specimens as can be seen from their standard deviation values listed in Table 4.6. No strong correlation between the values of ovalization and the distance from pipe edge could be determined, as can be seen from the PCC values listed in Table 4.6. Therefore, it is concluded that the ovalization magnitude does not vary significantly along pipe length. However, if the average ovalization values for each pipe group with the same D/t ratio are plotted, it can be seen that the values increase with increasing D/t ratio, as shown in Table 4.8 and Figure 4.14. Accordingly, higher values of ovalization can be expected in UOE manufactured pipes with higher D/t ratios.

Table 4.8 Average ovalization of each pipe group

Pipe	D/t Ratio	Average Ovalization
NPS 20 A,B	64.10	0.0059
NPS 42 C,D,E,F	74.75	0.0089
NPS 34 A,B	90.71	0.0090
NPS 42 A,B	103.47	0.0099

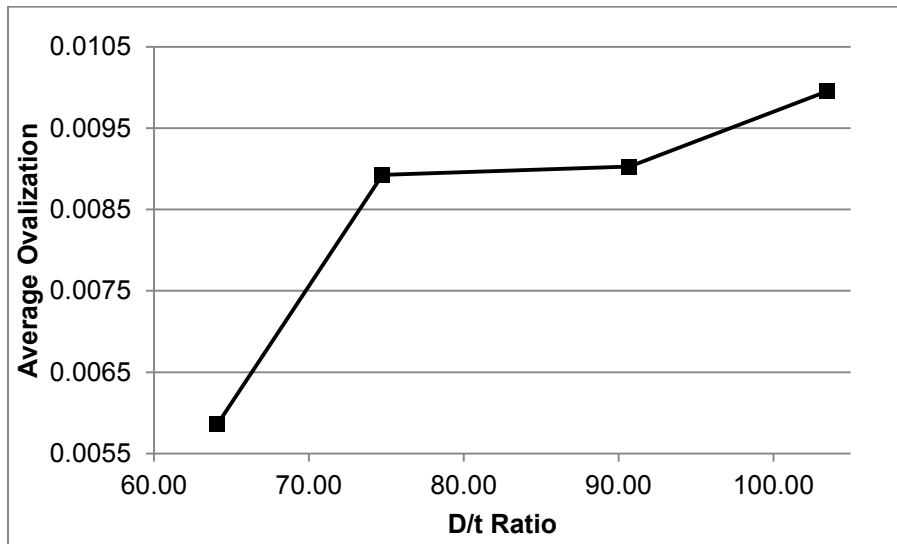


Figure 4.14 Average ovalization values of each pipe group with increasing D/t Ratio

Thickness variations are viewed with respect to the location of the longitudinal seam weld. All pipes in each pipe group exhibit almost similar patterns of thickness variation around their perimeter and along the length scanned.

Wall thickness for NPS 20 A and B pipes ($D/t = 64.10$) are seen to be close to their specified value near the location of the longitudinal seam weld. The deviation from the specified thickness varies within -7.43% to 13.57% in the NPS 20 A pipe, and within -4.57% to 17.9% in the NPS 20 B pipe. The increase and decrease in the wall thickness deviation around the perimeter of these two pipes are seen to be almost identical. Thickness reduction (negative deviation) is seen to be in the region of 240 degrees to 270 degrees from the seam weld.

Wall thickness for NPS 34 A and B pipes ($D/t = 90.71$) are also seen to be close to the specified thickness near the longitudinal seam weld locations. The

deviation from the specified thickness varies within -4.9% to 26.97% in the NPS 34 A pipe, and within -3.3% to 12.36% in the NPS 34 B pipe. A sudden reduction in thickness is seen in both pipes.

Wall thickness for NPS 42 ($D/t = 103.47$) pipes are seen to vary within -5.63% to 8.1% (NPS 42 A), and within -11.73% to 7.9% (NPS 42 B) of the specified thickness. NPS 42 A has thickness values very close to the specified thickness all around the perimeter with no apparent pattern of deviation with change in location (angle). NPS 42 B also shows thickness values close to the specified thickness around its perimeter. However there is a sudden drop in the wall thickness value on the opposite side of the location of seam weld. The maximum negative deviation is seen to be -12.38%, which subtends approximately 30 degree angles to the centre of the pipe cross section. It is very likely that this sudden decrease in thickness pertains to a local defect rather than general initial imperfection. Wall thickness for NPS 42 ($D/t = 74.75$) pipes are seen to vary between -15.6% to +27.9% (NPS 42 E), and between -9.5% to +22.33% (NPS 42 F) of the specified thickness. Pipe walls are seen to have less than nominal thickness near the seam weld and increases to the maximum value halfway around the perimeter. The wall thickness deviation ranges for each pipe is listed in Table 4.9.

Table 4.9 Wall Thickness deviation ranges

	Deviation (% of Nominal Thickness)	
	Maximum Positive	Maximum Negative
	Deviation	Deviation
NPS 20 A	13.57	7.43
NPS 20 B	17.90	4.57
NPS 34 A	26.97	4.90
NPS 34 B	12.63	3.30
NPS 42 A	8.10	5.63
NPS 42 B	7.90	12.38
NPS 42 E	27.90	15.60
NPS 42 F	22.33	9.50

The wall thickness deviation values previously shown in Figure 4.6 through Figure 4.13 are plotted in a single graph and shown in Figure 4.15:

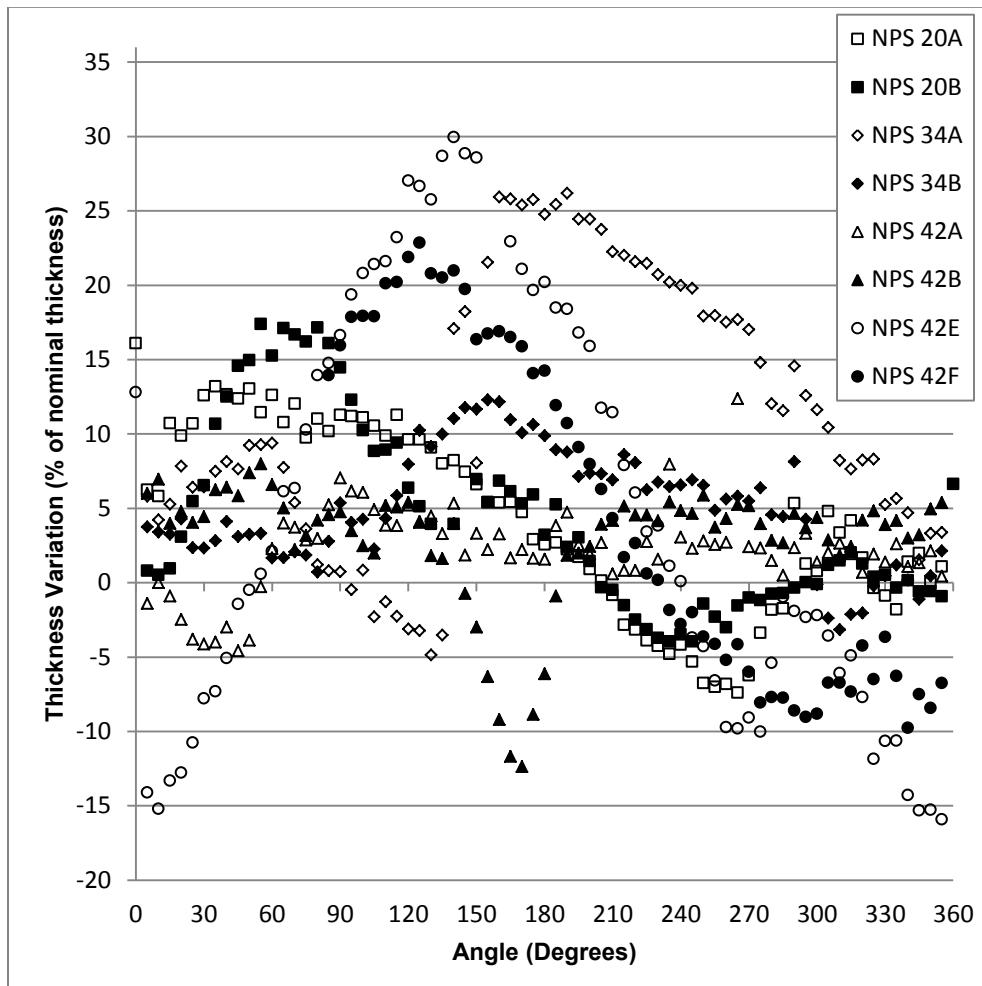


Figure 4.15 Measured wall thickness variations of all eight specimens in a single plot

It was reported previously in Chapter 3 that the thickness measurement has some error associated with it. The expected maximum errors for the pipes were listed in Table 3.3. From the maximum positive and negative thickness deviation values in Table 4.9, it can be concluded that the error is insignificant and can be ignored.

ASTM A530/A530M-12 (Standard Specification for General Requirements for Specialized Carbon and Alloy Steel Pipe) specifies that NPS 20 inch and larger welded pipes with any D/t ratio should have a tolerance of -12.5% to 17.5% of nominal wall thickness (Clause 10.1). It is seen that NPS 42 E specimen exceeds

the tolerance of -12.5%, while NPS 20 B and NPS 42 E and F exceed the tolerance of +17.5%.

ASTM A381-12 (Standard Specification for Metal-Arc-Welded Steel Pipe for Use with High-Pressure Transmission Systems) further specifies that the minimum thickness shall not be more than 0.25 mm under the specified thickness. All specimens analysed have thickness reduction greater than this specified value of 0.25 mm.

4.8 Conclusion

The geometric imperfections in line pipes are believed to be random and the quality control schemes typically involve random measurements to ensure product quality. The findings of the geometric analysis presented in this chapter indicate that the randomness of the imperfections is intrinsic to the magnitude rather than their patterns. The analysis successfully identified distinct patterns of OR and wall thickness deviation, which will be characterized in Chapter 6. Additionally, the possible sources of these imperfections can potentially be traced back to the manufacturing process. The consequences of these imperfections in a structural context are to be investigated.

CHAPTER 5: RESULTS OF THE GEOMETRIC ANALYSIS OF FRP SLEEVES AND ELBOWS

5.1 Introduction

In Chapter 3, the application of the data acquisition and measurement method on 90 degree pipe elbows and protective sleeves have been discussed. In this chapter, the results of the measurements are presented.

5.2 FRP Sleeve Fitting

The specifications of the pipes and sleeves are as follows:

Table 5.1 Pipe and Sleeve Description:

	OD (inch)	Coated/Uncoated	Weld Type	Location of Sleeve Relative to Pipe
Pipe 1	30	Coated	Seam	Edge
Pipe 2	30	Coated	Seam	Middle
Pipe 3	30	Coated	Helical	Edge
Pipe 4	30	Coated	Helical	Middle
Pipe 5	30	Uncoated	Seam	Middle
Pipe 6	30	Uncoated	Helical	Middle

The diameters of the best fit cylinders for each sleeve and their comparison with the ID of the shoe are listed in Table 5.2. In all cases, the ID of shoe is seen to be less than the OD of the sleeves.

Table 5.2 Best Fit Geometry of Sleeves

	Diameter of Best Fit Cylinder		Inner Diameter of Shoe		Difference	
	(mm)	(inch)	(mm)	(inch)	(mm)	(inch)
Pipe 1	777.50	30.61	774.7	30.5	2.80	0.11
Pipe 2	777.00	30.59	774.7	30.5	2.30	0.09
Pipe 3	778.00	30.63	774.7	30.5	3.30	0.13
Pipe 4	776.70	30.58	774.7	30.5	2.00	0.08
Pipe 5	777.70	30.62	774.7	30.5	3.00	0.12
Pipe 6	776.60	30.57	774.7	30.5	1.90	0.07

The average thickness of a typical sleeve is shown in Figure 5.1 . The histogram in the deviation spectrum indicates the trend of the thickness variation. The average thickness of the sleeve is found to be 7.63 mm (0.3004 inch).

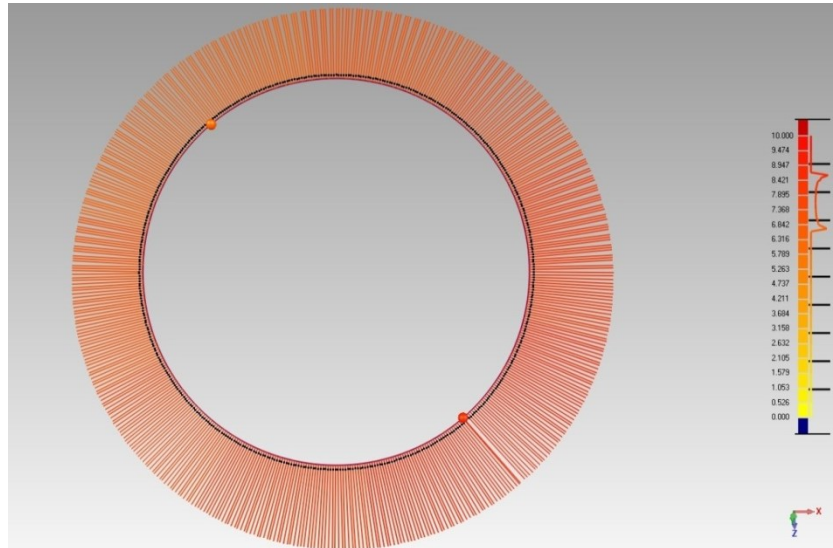


Figure 5.1 Thickness of Sleeve

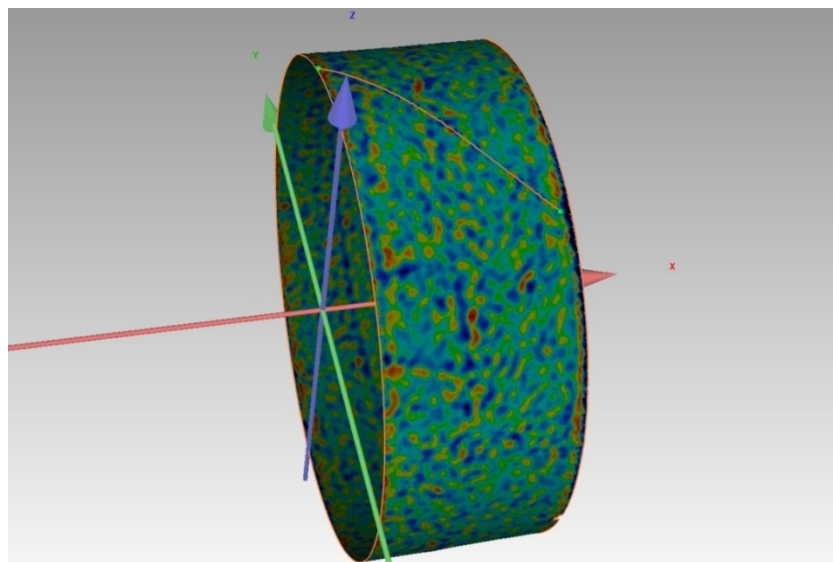


Figure 5.2 Topography of Sleeve Outer Surface

The curvature contour of the sleeve outer surface is shown in Figure 5.2. Cold (blue) colours in the curvature map indicates positive curvature, warm (red) colours indicate negative curvature. Therefore, the cold coloured patches are regions of protuberance, and the warm patches are depressions.

The comparisons between the outer surface of the sleeves and the inner surface of the shoe (pipe support) are shown as 2D colour coded spectrums in Figure 5.3 to Figure 5.8. These figures illustrate the distance of the points on the sleeve outer surface from the shoe inner surface (the solid circle) at a cross section taken half way through the sleeve width (approximately 6 inches from the sleeve edge). Assuming proper installation, with the shoe (support) perfectly centred to the pipe axis, the warm colours indicate that, the inner surface of the shoe will theoretically be inside the sleeve outer surface (i.e. after installation, it will compress the sleeve). Cold colours indicate otherwise (no compression).

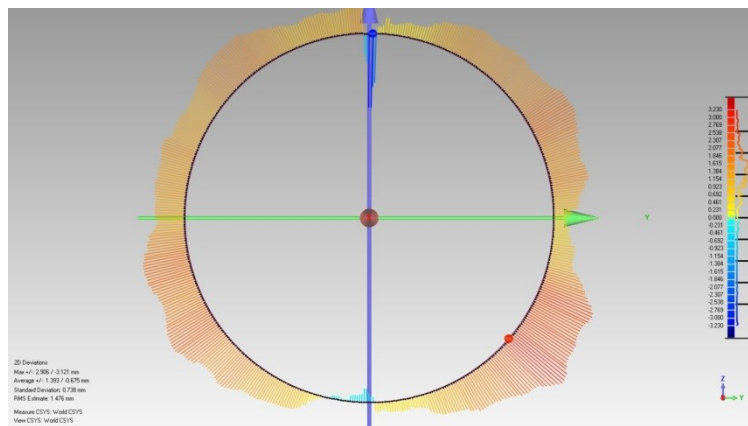


Figure 5.3 Deviation Spectrum for Pipe 1

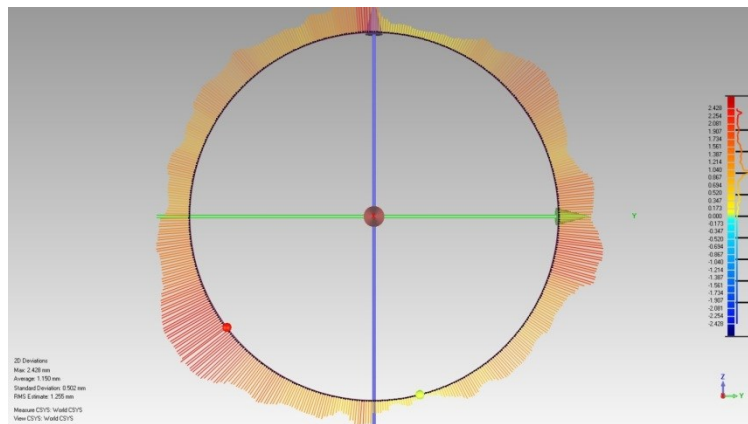


Figure 5.4 Deviation Spectrum for Pipe 2

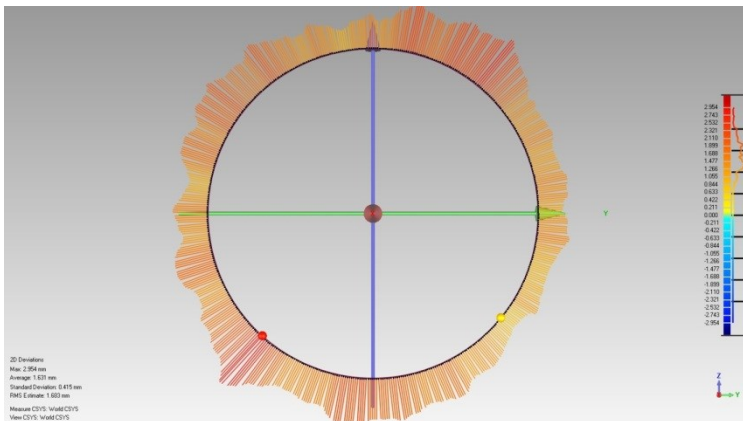


Figure 5.5 Deviation Spectrum for Pipe 3

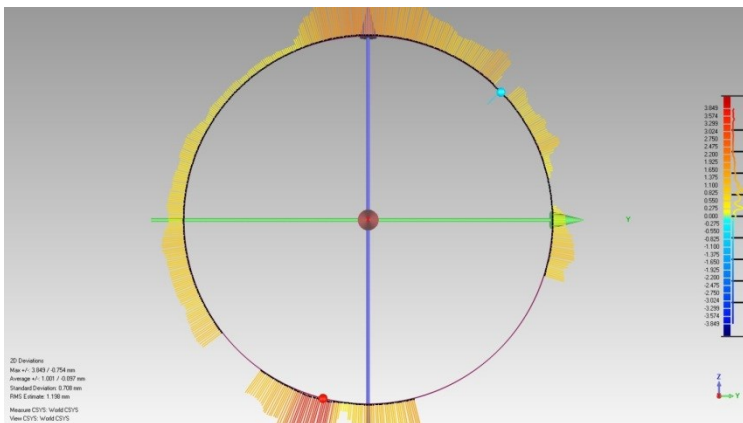


Figure 5.6 Deviation Spectrum for Pipe 4

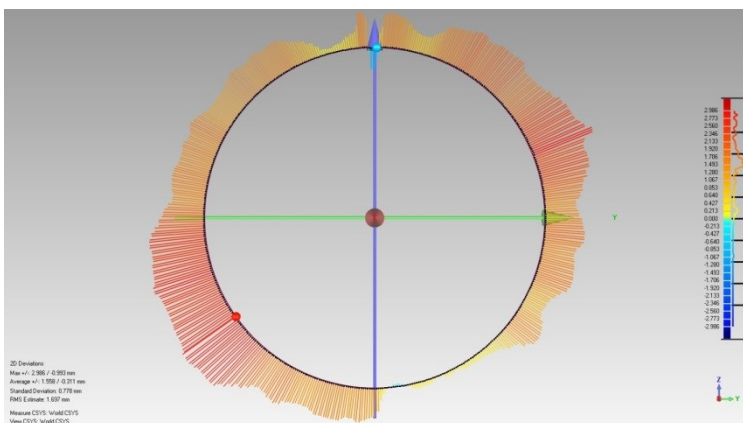


Figure 5.7 Deviation Spectrum for Pipe 5

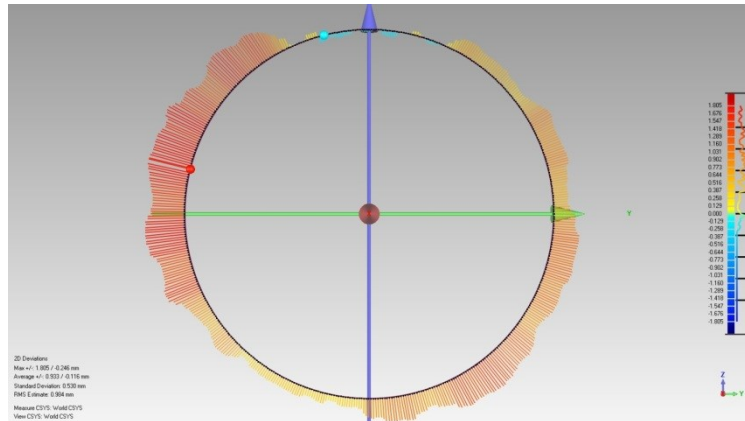


Figure 5.8 Deviation Spectrum for Pipe 6

The results of the 3D comparisons are elaborated in the following sections. The inner surface of the shoe (support) is the reference surface. Data points are the points on the scanned sleeve surface. Number of data points refers to the total number of points on each sleeve surface.

The comparison is performed between the reference surface and the data points. The results are reported in mm. Maximum upper deviation is the distance of the point that is furthest from the reference surface. Average deviation is the average distance of all the data points from the reference surface. Standard deviation indicates how much variation or dispersion exists from the average value.

The deviation distribution tables (Table 5.3 to Table 5.8) show an elaborated breakdown of the deviations. The columns titled “>=Min” and “<Max” indicate the ranges of deviation. “#Points” column shows the number of data points that exist within this deviation range, and the “%” column lists the percentage of the total number of data points that exists within this range. For example, in Pipe 1, 10.473% of the data points exist within the deviation range of 0.714 mm to 1.071 mm.

The deviation ranges, that have a higher percentage of data points than the others, are more significant, and are highlighted in the deviation distribution tables.

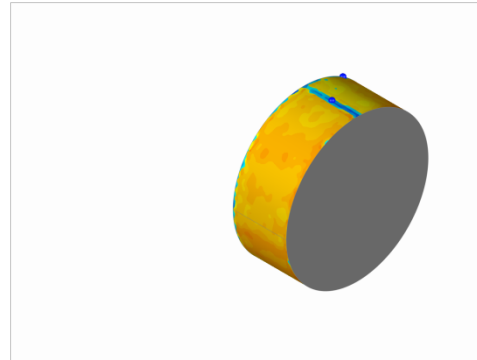
The overall distributions of the deviations are presented as histograms, where the horizontal axis is the deviation range in mm, and the vertical axis is the percentage of data points in each deviation range.

Table 5.3 Pipe 1: 3D Comparison Results

Reference Model	Clamp
Test Model	Pipe 1
No. of Data Points	7161

Tolerance Type	3D Deviation
Units	mm
Max. Critical	5.000
Max. Nominal	0.000
Min. Nominal	0.000
Min. Critical	-5.000

Deviation	
Max. Upper Dev.	3.646
Max. Lower Dev.	N/A
Average Deviation	1.438
Standard Deviation	1.202



Deviation Distribution

>=Min	<Max	# Points	%
-4.643	-4.286	4	0.056
-4.286	-3.929	13	0.182
-3.929	-3.571	23	0.321
-3.571	-3.214	51	0.712
-3.214	-2.857	39	0.545
-2.857	-2.500	77	1.075
-2.500	-2.143	103	1.438
-2.143	-1.786	63	0.880
-1.786	-1.429	62	0.866
-1.429	-1.071	62	0.866
-1.071	-0.714	59	0.824
-0.714	-0.357	84	1.173
-0.357	0.000	212	2.960
0.000	0.357	320	4.469
0.357	0.714	449	6.270
0.714	1.071	750	10.473
1.071	1.429	1666	23.265
1.429	1.786	1503	20.989
1.786	2.143	857	11.968

Deviation Distribution

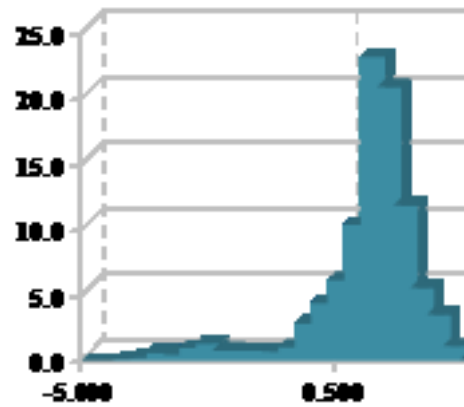
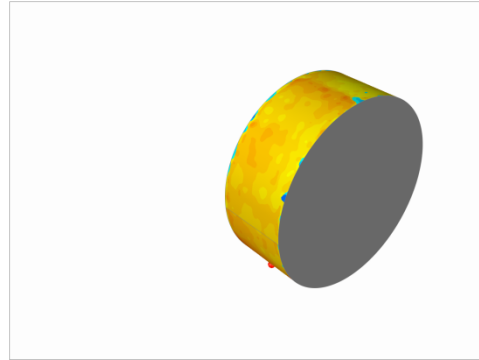


Table 5.4 Pipe 2: 3D Comparison Results

Reference Model	Clamp
Test Model	Pipe 2
No. of Data Points	7058

Tolerance Type	3D Deviation
Units	mm
Max. Critical	5.000
Max. Nominal	0.000
Min. Nominal	0.000
Min. Critical	-5.000

Deviation	
Max. Upper Dev.	4.547
Max. Lower Dev.	N/A
Average Deviation	1.199
Standard Deviation	0.931



Deviation Distribution

>=Min	<Max	# Points	%
-5.000	-4.643	1	0.014
-4.643	-4.286	6	0.085
-4.286	-3.929	1	0.014
-3.929	-3.571	10	0.142
-3.571	-3.214	12	0.170
-3.214	-2.857	19	0.269
-2.857	-2.500	16	0.227
-2.500	-2.143	45	0.638
-2.143	-1.786	44	0.623
-1.786	-1.429	48	0.680
-1.429	-1.071	62	0.878
-1.071	-0.714	82	1.162
-0.714	-0.357	100	1.417
-0.357	0.000	169	2.394
0.000	0.357	541	7.665
0.357	0.714	812	11.505
0.714	1.071	1496	21.196
1.071	1.429	1487	21.068
1.429	1.786	1088	15.415

Deviation Distribution

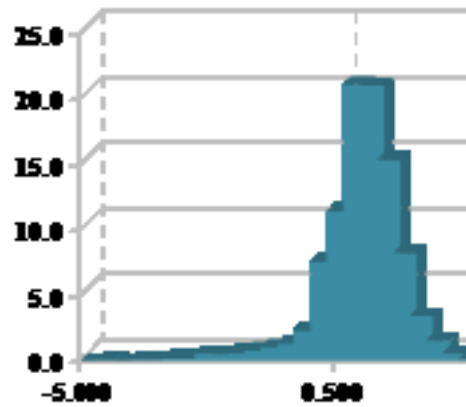
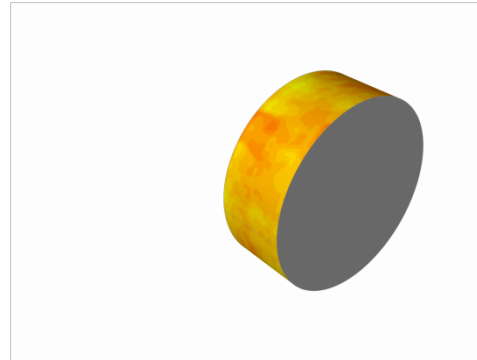


Table 5.5 Pipe 3: 3D Comparison Results

Reference Model	Clamp
Test Model	Pipe 3
No. of Data Points	25432

Tolerance Type	3D Deviation
Units	mm
Max. Critical	5.000
Max. Nominal	0.000
Min. Nominal	0.000
Min. Critical	-5.000

Deviation	
Max. Upper Dev.	4.753
Max. Lower Dev.	N/A
Average Deviation	1.665
Standard Deviation	0.513



Deviation Distribution

>=Min	<Max	# Points	%
-1.786	-1.429	0	0.000
-1.429	-1.071	0	0.000
-1.071	-0.714	3	0.012
-0.714	-0.357	5	0.020
-0.357	0.000	4	0.016
0.000	0.357	61	0.240
0.357	0.714	354	1.392
0.714	1.071	1920	7.550
1.071	1.429	5946	23.380
1.429	1.786	8211	32.286
1.786	2.143	5185	20.388
2.143	2.500	2221	8.733
2.500	2.857	861	3.385
2.857	3.214	361	1.419
3.214	3.571	180	0.708
3.571	3.929	85	0.334
3.929	4.286	28	0.110
4.286	4.643	5	0.020
4.643	5.000	2	0.008

Deviation Distribution

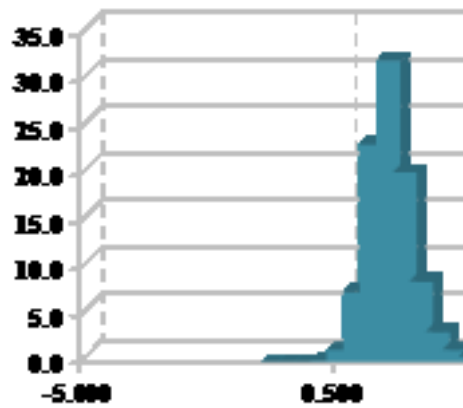
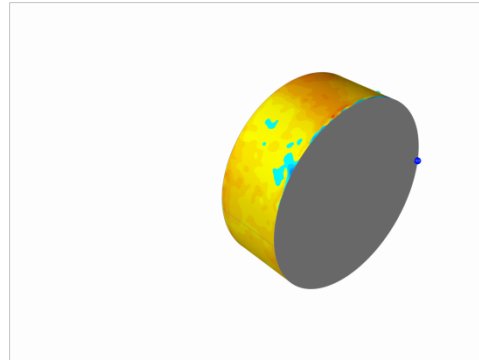


Table 5.6 Pipe 4: 3D Comparison Results

Reference Model	Clamp
Test Model	Pipe 4
No. of Data Points	5683

Tolerance Type	3D Deviation
Units	mm
Max. Critical	5.000
Max. Nominal	0.000
Min. Nominal	0.000
Min. Critical	-5.000

Deviation	
Max. Upper Dev.	4.937
Max. Lower Dev.	N/A
Average Deviation	1.094
Standard Deviation	1.164



Deviation Distribution

>=Min	<Max	# Points	%
-5.000	-4.643	15	0.264
-4.643	-4.286	36	0.633
-4.286	-3.929	24	0.422
-3.929	-3.571	13	0.229
-3.571	-3.214	15	0.264
-3.214	-2.857	31	0.545
-2.857	-2.500	20	0.352
-2.500	-2.143	32	0.563
-2.143	-1.786	34	0.598
-1.786	-1.429	32	0.563
-1.429	-1.071	44	0.774
-1.071	-0.714	61	1.073
-0.714	-0.357	56	0.985
-0.357	0.000	164	2.886
0.000	0.357	607	10.681
0.357	0.714	929	16.347
0.714	1.071	1449	25.497
1.071	1.429	945	16.629
1.429	1.786	466	8.200

Deviation Distribution

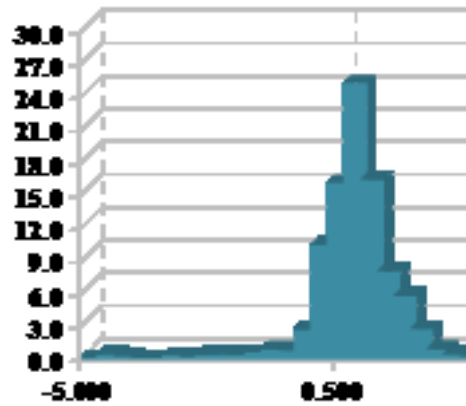
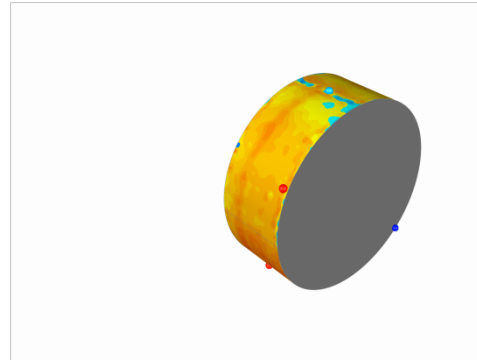


Table 5.7 Pipe 5: 3D Comparison Results

Reference Model	Clamp
Test Model	Pipe 5
No. of Data Points	7136

Tolerance Type	3D Deviation
Units	mm
Max. Critical	5.000
Max. Nominal	0.000
Min. Nominal	0.000
Min. Critical	-5.000

Deviation	
Max. Upper Dev.	4.796
Max. Lower Dev.	N/A
Average Deviation	1.542
Standard Deviation	1.065



Deviation Distribution

>=Min	<Max	# Points	%
-4.286	-3.929	2	0.028
-3.929	-3.571	2	0.028
-3.571	-3.214	18	0.252
-3.214	-2.857	18	0.252
-2.857	-2.500	21	0.294
-2.500	-2.143	28	0.392
-2.143	-1.786	42	0.589
-1.786	-1.429	63	0.883
-1.429	-1.071	58	0.813
-1.071	-0.714	70	0.981
-0.714	-0.357	115	1.612
-0.357	0.000	240	3.363
0.000	0.357	412	5.774
0.357	0.714	468	6.558
0.714	1.071	678	9.501
1.071	1.429	1106	15.499
1.429	1.786	1575	22.071
1.786	2.143	1011	14.168
2.143	2.500	569	7.974

Deviation Distribution

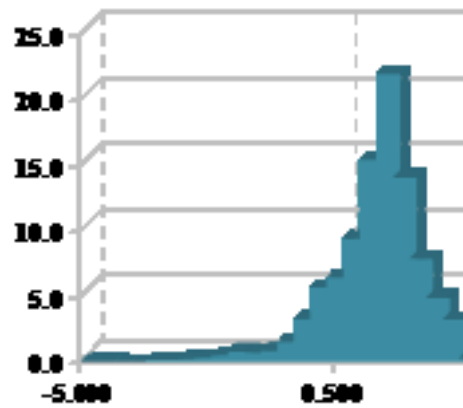
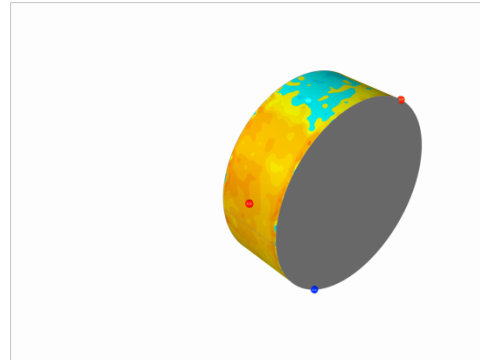


Table 5.8 Pipe 6: 3D Comparison Results

Reference Model	Clamp
Test Model	Pipe 6
No. of Data Points	6967

Tolerance Type	3D Deviation
Units	mm
Max. Critical	5.000
Max. Nominal	0.000
Min. Nominal	0.000
Min. Critical	-5.000

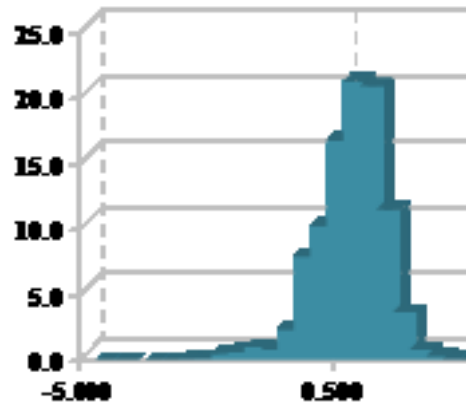
Deviation	
Max. Upper Dev.	4.484
Max. Lower Dev.	N/A
Average Deviation	0.990
Standard Deviation	0.757



Deviation Distribution

>=Min	<Max	# Points	%
-3.929	-3.571	0	0.000
-3.571	-3.214	1	0.014
-3.214	-2.857	2	0.029
-2.857	-2.500	8	0.115
-2.500	-2.143	12	0.172
-2.143	-1.786	39	0.560
-1.786	-1.429	47	0.675
-1.429	-1.071	74	1.062
-1.071	-0.714	61	0.876
-0.714	-0.357	168	2.411
-0.357	0.000	555	7.966
0.000	0.357	718	10.306
0.357	0.714	1172	16.822
0.714	1.071	1486	21.329
1.071	1.429	1463	20.999
1.429	1.786	804	11.540
1.786	2.143	259	3.718
2.143	2.500	59	0.847
2.500	2.857	23	0.330

Deviation Distribution



The summary of the 3D comparison results are listed in Table 5.9:

Table 5.9 Maximum, Average, and Standard Deviations of Data Points

	Maximum Deviation		Average Deviation		Standard Deviation	
	(mm)	(inch)	(mm)	(inch)	(mm)	(inch)
Pipe 1	3.6460	0.1435	1.4380	0.0566	1.2020	0.0473
Pipe 2	4.5470	0.1790	1.1990	0.0472	0.9310	0.0367
Pipe 3	4.7530	0.1871	1.6650	0.0656	0.5130	0.0202
Pipe 4	4.9370	0.1944	1.0940	0.0431	1.1640	0.0458
Pipe 5	4.7960	0.1888	1.5420	0.0607	1.0650	0.0419
Pipe 6	4.4840	0.1765	0.9900	0.0390	0.7570	0.0298

For each sleeve, the significant ranges of deviation, as previously highlighted in the deviation distribution tables, are summarized in Table 5.10:

Table 5.10 Summary of Deviation Distribution

	Total Number of Data Points	Deviation Distribution			
		Deviation Range		Data Points Within Deviation Range	Percentage (%)
		Minimum	Maximum		
		(mm)	(mm)		
Pipe 1	7161	0.714	2.143	4776	66.69
Pipe 2	7058	0.357	1.786	4883	69.18
Pipe 3	25432	1.071	2.500	21563	84.79
Pipe 4	5683	0.000	1.786	4396	77.35
Pipe 5	7136	0.714	2.500	4939	69.21
Pipe 6	6967	0.000	1.786	5643	81.00

It is observed that, the maximum and average deviations are positive, indicating compression in the sleeve after installation. Majority of the points (65% to 80%) exist in the deviation range of 0.0 mm to 2.5 mm (0.0 inch to 0.0984 inch).

5.2.1 Discussion

The curvature map of the sleeve surface shows very irregular topography of the Fiber Glass sleeve. The presence of protuberance and depression may result in non-uniform contact between the sleeve and the shoe (support). The 2D deviation spectrums also indicate the presence of the uneven features on the sleeve surface.

If the hex bolts and nuts are forced to meet the gap specification, this will result in compression on the sleeves. As the thickness of the sleeve and its outer surface is non-uniform, the stresses induced on the sleeve by the shoe will also be of non-uniform nature.

The sleeve outer diameters are found to be greater than the shoe inner diameter in all six specimens. The difference between the diameter ranges from 2 mm to 3.3 mm (0.0787 inch to 0.1299 inch). Once the shoe (support) is installed as per specifications, the sleeve thickness will be compressed. Knowing that the average thickness of the sleeve is 7.63 mm (0.3004 inch); there will be compressive strain on the sleeve and the pipe.

The average thickness of the sleeve is found to be 7.63 mm (0.3004 inch). The support specifications state that the sleeve thickness should be 6.35 mm (0.2500 inch) after installment of the shoe. In that case, the sleeve will be compressed by the shoe in order to reduce its thickness by an average of 1.28 mm (0.0504 inch).

The 3D comparison results further confirm that majority of the points (65% to 80%) on the shoe inner surface are located inside the sleeve outer surface for each pipe sleeve, as highlighted in Table 5.10. The value of deviation is seen to vary between 0.0 mm and 2.5 mm (0.0000 inch to 0.0984 inch).

The pipes measured and analysed were not pressurized. Once the pipes are in service, and are subjected to internal pressure, the outer diameters of the pipes will to increase. This will induce compression on the inner surface of the sleeves as well. Consequently, the overall compression on the sleeves will be higher.

From initial inspection, it was observed that the sleeves were discontinued near the longitudinal seam welds, but the clearance between the discontinued sleeve edge and the weld protrusion was small. In case of helical seam welds, it was not

possible to detect whether the sleeve inner surface was shaped to match the contour of the helical weld. In either case, the longitudinal/helical welds are likely to experience stresses due to clamping, depending on the material.

The surface profiles of the sleeves are very uneven. The average thickness of the sleeves is 7.63 mm, which is greater than the required value of 6.35 mm by 1.28 mm. This difference is expected to induce a compressive strain of 16.8% in the sleeve. The comparison between the outer diameter of the sleeves and the inner diameters of the shoe indicate that there is going to be an interference issue between the shoe (support) and the sleeve. The huge percentage of sleeve surface points with positive deviation confirms the aforementioned interference issue. After installment of shoe, and being subjected to internal pressure in service, the sleeve will experience compression from both pipe and shoe surface. Therefore the compressive strains developed in the sleeves are expected to be more than 16.8% while in service.

5.3 Pipe Elbow Geometry

The pipe elbows measured in this study are manufactured by Tectubi Raccordi. The elbow designations and the specifications are listed in Table 5.11:

Table 5.11 Elbow Specifications

Elbow Designation	Outside Diameter [inch (mm)]	Wall Thickness [inch (mm)]	Steel Grade
12inch_GR359_1	12.75 (323.85)	0.375 (9.525)	Grade 359
12inch_GR359_2	12.75 (323.85)	0.375 (9.525)	Grade 359
24inch_GR359_2	24.00 (609.60)	0.375 (9.525)	Grade 359
24inch_Y52_1	24.00 (609.60)	0.375 (9.525)	Y 52
36inch_1	36.00 (914.40)	0.500 (12.700)	Y 70

5.3.1 Idealized Dimensions:

The idealized dimensions (diameter of the circle and the distance of its centre from the axis of revolution) of the scanned elbows, along with the standard deviation between the ideal tori and the scanned elbows are listed in Table 5.12:

Table 5.12 Idealized geometry of the elbows

Elbow Designation	Diameter of Circle	Distance from the Axis of Revolution	Standard Deviation between Ideal Torus and Actual Elbow
	mm	mm	mm
12inch_GR359_1	322.63	457.37	0.4309
12inch_GR359_2	323.34	456.78	0.3627
24inch_GR359_2	608.84	908.14	0.6794
24inch_Y52_1	609.67	909.18	1.1053
36inch_1	908.79	1370.00	1.1535

From the deviation analysis of each elbow surface and corresponding idealized torus surface, it is seen that 90% of the torus surface are within ± 2 Standard Deviation. 2 Standard Deviation is 0.3% of OD for each elbow. Therefore, 90% of the idealized tori are within 0.3% OD of each scanned elbow.

5.3.2 Ovalization Values:

The XZ plane, which is the vertical plane of symmetry, makes a 0 degree angle about the Z axis. Therefore, the two ends of the elbow make an angle of 45 degree and -45 degree with the Z axis respectively. Planes are taken at 5 degrees angular interval between -40 degrees and 40 degrees to take the cross section of the elbows. At each cross section, the maximum and minimum values of the diameter of the elbow are measured to calculate the ovalization. The calculated ovalization values at different cross sections of each elbow, along with the average and maximum values are listed in Table 5.13. It is seen that the maximum ovalization values of the five elbow specimens range from 0.0101 to 0.0168, and the average values range from 0.0076 to 0.0109.

Table 5.13 Ovalization values of the scanned elbows

Angle	Ovalization Values				
	12inch_GR359_1	12inch_GR359_2	24inch_GR359_2	24inch_Y52_1	36inch_1
-40	-	0.0101	0.0056	0.0051	-
-35	0.0072	0.0075	0.0053	0.0049	0.0107
-30	0.0098	0.0069	0.0061	0.0066	0.0108
-25	0.0105	0.0078	0.0079	0.0072	0.0090
-20	0.0099	0.0074	0.0081	0.0074	0.0067
-15	0.0095	0.0081	0.0086	0.0084	0.0070
-10	0.0108	0.0082	0.0092	0.0080	0.0097
-5	0.0101	0.0079	0.0087	0.0093	0.0083
0	0.0093	0.0077	0.0084	0.0111	0.0094
5	0.0097	0.0082	0.0081	0.0115	0.0109
10	0.0092	0.0087	0.0067	0.0131	0.0116
15	0.0091	0.0075	0.0075	0.0140	0.0112
20	0.0084	0.0074	0.0084	0.0162	0.0075
25	0.0088	0.0077	0.0082	0.0165	0.0100
30	0.0081	0.0078	0.0093	0.0168	0.0146
35	0.0073	0.0056	0.0116	0.0156	-
40	-	0.0048	0.0134	0.0132	-
Average	0.0092	0.0076	0.0083	0.0109	0.0098
Maximum	0.0108	0.0101	0.0134	0.0168	0.0146

5.3.3 Wall Thickness Deviation:

The measured wall thickness deviations are shown in Figure 5.9 to Figure 5.11. The cross sections were taken about a plane through the Z axis, similar to what was done for the ovalization calculation. The full inside surface of the elbows were not accessible for scanning. The wall thickness values were measured near the ends of the elbows.

The wall thickness deviation of the specimen 12inch_GR359_1 at cross sections 25 degrees and 30 degrees about the Z axis are shown in Figure 5.9:

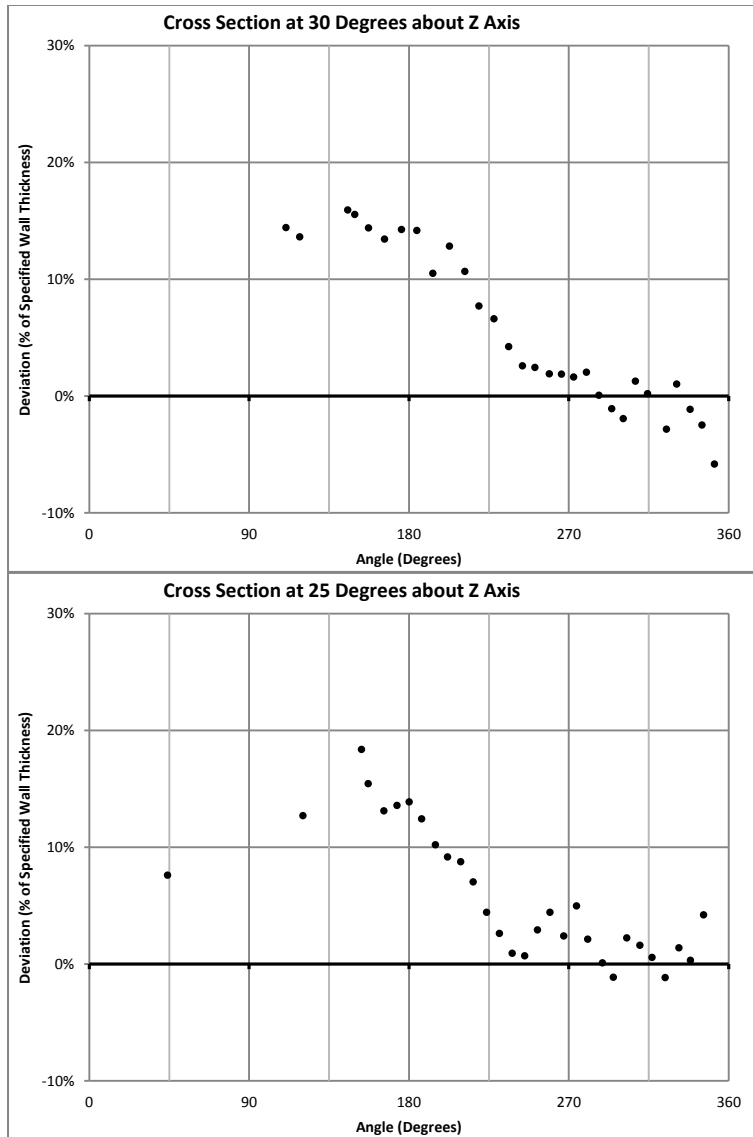


Figure 5.9 Wall thickness deviation of elbow 12inch_GR359_1

It is seen that the wall thickness deviation is close to zero at the intrados (0 and 360 degrees). The thickness gradually increases and becomes maximum at the extrados (180 degrees). -6% deviation is observed at the cross section taken at 30 degrees from the Z axis. Maximum positive deviation is seen to be approximately 20% of the specified thickness. The deviation pattern is symmetric about the horizontal plane of symmetry (180 degree line).

The wall thickness deviation of the specimen 12inch_GR359_2 at cross sections -35 degrees and 35 degrees about the Z axis are shown in Figure 5.10:

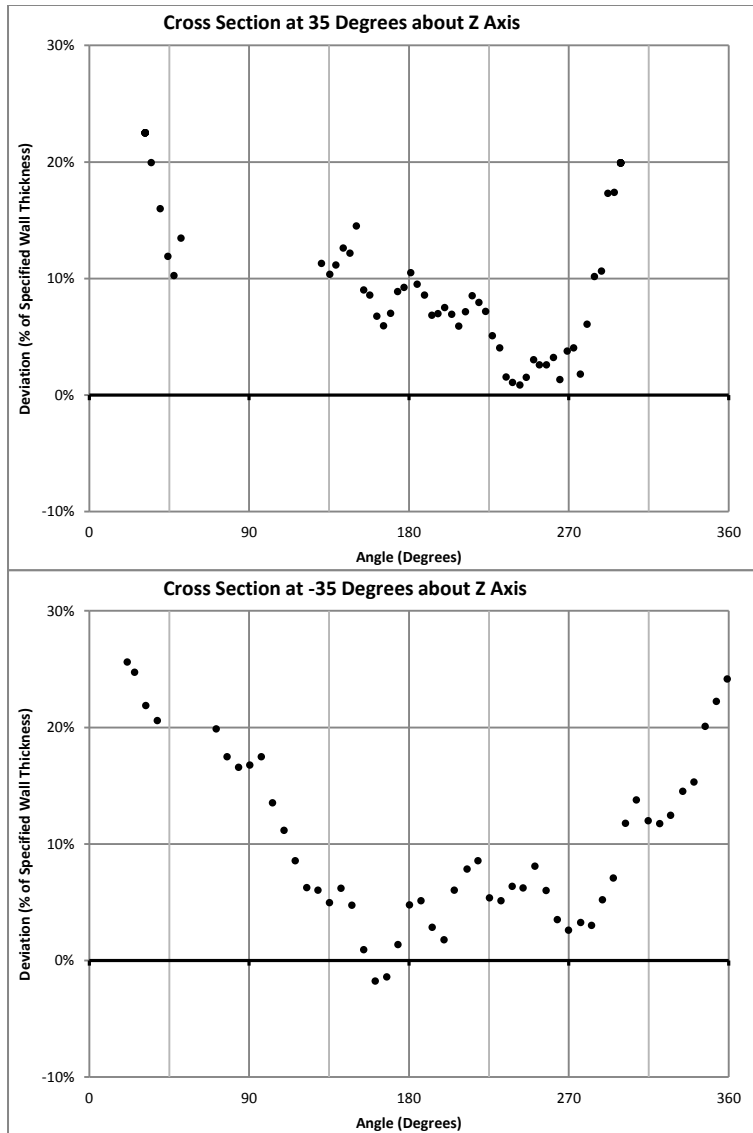


Figure 5.10 Wall thickness deviation of elbow 12inch_GR359_2

This specimen shows a thickness deviation pattern that is opposite to what was observed in the previous specimen. Wall thickness is seen to be greater than the specified thickness at the intrados (0 and 360 degrees), which gradually decreases and reaches a minimum at the extrados (180 Degrees). The positive deviation at the intrados is seen to be greater than 20% in both cross sections. The minimum value of thickness deviation is seen to be close to 0%. The deviation pattern is symmetric about the horizontal plane of symmetry (180 degree line).

The wall thickness deviation of the specimen 24inch_GR359_2 at cross sections -30 degrees and -25 degrees about the Z axis are shown in Figure 5.11:

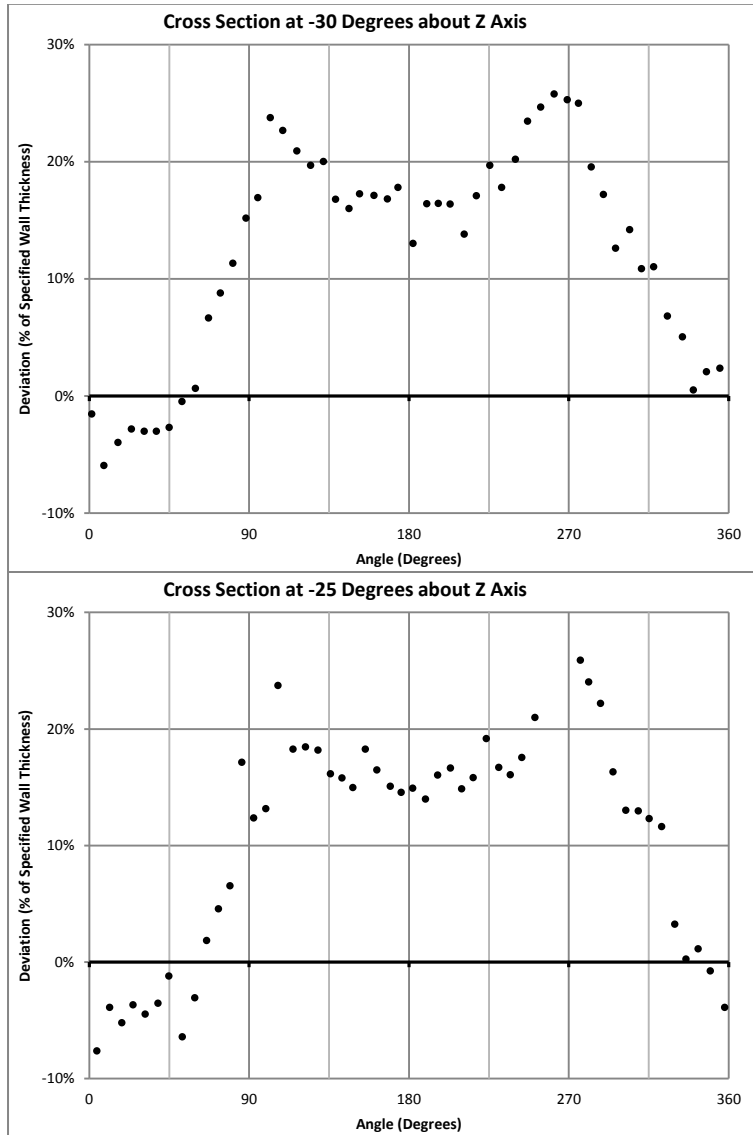


Figure 5.11 Wall thickness deviation of elbow 24inch_GR359_2

Similar to the specimen 12inch_GR359_1, this specimen also shows reduced thickness at the intrados compared to the extrados, although the deviation pattern is slightly different. Negative deviation is seen at the intrados (0 and 360 degrees). The deviation then increases and reaches a maximum value of approximately 20% at 90 degrees and 270 degrees from the intrados. The deviation then slightly decreases to 15% at 180 degrees (extrados). The

deviation pattern is symmetric about the horizontal plane of symmetry (180 degree line).

5.3.4 Discussion

From the comparison between the actual elbows and the idealized tori, it is seen that the idealized geometry is very close to the scanned elbow surfaces. 90% of the points on the idealized tori are within a deviation of $\pm 0.3\%$ OD of each elbow. Therefore, the idealization method developed in this study can be considered accurate.

The average ovalization values of the elbows are in the range of 0.0076 to 0.0109, which are well below the CSA Z662 specified value of 0.03. The maximum ovalization values range from 0.0101 to 0.0168, which are also below the CSA Z662 specification.

To investigate the ovalization patterns, the 3D deviations of the actual and idealized geometry were examined. The deviation patterns were different for each elbow (Figure 5.12). In Figure 5.12 a, the blue colour at the top of the elbow indicate that the 24inch_GR359_2 specimen has its maximum OD oriented along the horizontal plane of symmetry. In Figure 5.12 b, the blue colour at the extrados indicate that the 12inch_GR359_2 specimen has its minimum OD oriented along the horizontal plane of symmetry.

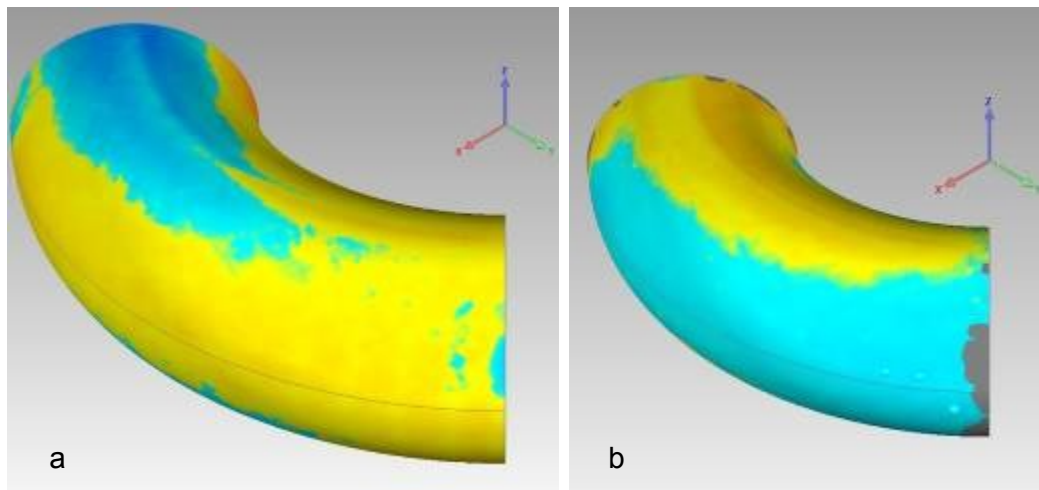


Figure 5.12 Two different patterns of deviation from perfect torus observed through 3D comparison of two elbows a) 24inch_GR359_2, and b) 12inch_GR359_2

An elbow is generally manufactured by bending a straight pipe segment. The initially straight axis of the pipe is thus transformed to a curved axis during manufacturing the elbow. Theoretically, this curved axis should be a perfect arc. In reality, the curved axis of an elbow deviates from a perfect arc. Therefore, the deviation patterns observed from the 3D comparisons are in fact combinations of the ovalization of elbow cross sections, and the deviation of the curved axis of the elbow from a perfect arc. As a result, a typical ovalization pattern could not be identified.

Intuitively, during manufacturing, an elbow should be ovalized in such a way that the minimum OD is oriented along the horizontal plane of symmetry. This pattern, however, was observed in the two 12 inch elbows.

Patterns of wall thickness deviation were observed for the three elbows. 12inch_GR359_1 had wall thickness deviation values close to 0% on the inside (0° , 360°), which increased uniformly to about 20% of the specified thickness on the outside (180°). 12inch_GR359_2 had increased wall thickness (25% of specified thickness) on the inside and close to 0% deviation on the outside. 24inch_GR359_2 had decreased wall thickness (7.5% of specified thickness) on the inside and increased thickness (25% of specified thickness) near the top (90°) and bottom (270°) of the elbow.

Thickness reduction is seen to be within 10% of the specified thickness of all three elbows. Increased thickness is seen to be more prominent in all elbows (15% to 25% of specified thickness). The thickness deviation is seen to be symmetric about the horizontal plane of symmetry of the three elbows.

5.4 Conclusion

The results of measurements of the pipe sleeves and the elbows are presented in this chapter. The geometric analysis of the sleeves concluded that the dimensions of the sleeves do not comply with the specified dimensions of the shoe. In all six specimens, the sleeve outer surface is seen to be inside the shoe surface after installation. The average thickness of the sleeves is seen to be 7.63 mm, while according to the specifications, it should be 6.35 mm. This is likely to induce a compressive strain of 16.8% on the sleeves. While in service, the pipes will be subjected to internal pressure and their diameter will increase, which will

increase the compressive strain on the sleeves even further. It was concluded that the sleeves did not comply with the specifications and are not suitable for service.

This study successfully devised a method for the geometric analysis of pipe elbows. The idealized geometry obtained from the developed method is very close to the actual geometry of the scanned elbows. The ovalization imperfections present in the elbows are below the limit specified by CSA Z662-11. The patterns of ovalization are different for different elbows. Finite Element Analysis of elbows with ovalization imperfections is required to investigate their influence on bourdon effect. Patterns of wall thickness deviation were identified in this study. Increased thickness in the range of 15% to 25% of the specified thickness was observed. The patterns were seen to be symmetric about the horizontal plane of symmetry. The influences of different patterns of wall thickness deviations on bourdon effect should also be investigated through Finite Element Analysis.

CHAPTER 6: INITIAL GEOMETRIC IMPERFECTION MODELS FOR UOE MANUFACTURED PIPES

6.1 Introduction

The geometric analysis provided insight into the types of imperfections typically present in the UOE manufactured straight pipes. Recurring patterns of deviation from the specified OR and wall thickness have been identified and reported. To investigate the significance of these geometric imperfections on the structural behaviour of line pipes through finite element analysis, it is required that the imperfections are first characterized, and then expressed as imperfection models. Models are commonly based on assumptions and simplifications. The assumption behind the models developed in this chapter is that both the OR and wall thickness deviation imperfections are symmetric about the line connecting the centre and seam weld of a pipe cross section. The models are simplified by ignoring the geometry of the seam weld. The details of these assumptions are discussed and justified in the following section.

6.2 Qualitative Characterization of Initial Geometric Imperfection Patterns

The 10 pipe specimens analysed in the research provided sufficient results for further investigations of the geometric imperfection patterns. The results show that the seam weld geometry is very consistent and no imperfection patterns were identified. However, the OR and wall thickness show certain amounts of deviations. The patterns of OR and wall thickness deviations observed are discussed in this section.

6.2.1 Outside Radius Deviation Patterns

The NPS 20 inch pipes are made from grade X70 steel and manufactured by Evraz. The owners of these pipes in the storage facility were unable to provide definite information about whether they were UOE manufactured or not. It is seen from the results that these two pipes clearly show a different pattern from the rest of the specimens. The actual OR deviation pattern is shown in Figure 6.1. An ideal ellipse (solid line) is able to envelop major parts of the deviation spectrum whiskers, which indicates that the imperfect shape of these pipes resembles that

of an ellipse. It is seen that the major axis is very closely aligned with the line that goes through the centre and the seam weld (11.0 degrees).

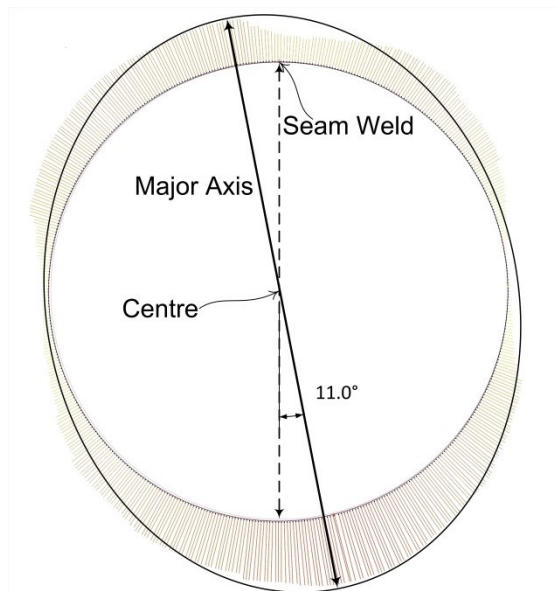


Figure 6.1 OR deviation pattern in NPS 20 pipe

Both NPS 20 pipes showed this typical type of deviation which is consistent along their length, with minor changes in magnitude.

The NPS 34 inch and NPS 42 inch pipes are made from grade X100 steel and UOE manufactured by Sumitomo and Nippon, both Japanese manufacturers. The OR deviation pattern of these pipes are shown in Figure 6.2 to Figure 6.9.

The deviation magnitudes are the radial difference between points on the scanned pipe surface from their idealized geometry. The deviation spectrums show whiskers that are proportional to the magnitude of deviation. It is observed in the following figures that the whiskers increase and decrease in length in a regular manner. The shape of the deviation spectrum whiskers can be considered as an exaggerated representation of the shape of the scanned pipe cross section. It is, therefore, seen that the UOE manufactures pipes show a very typical and recurring pattern of OR deviation from nominal. The pattern resembles that of a wave with a fairly constant period. The waves are more prominent in the pipes that have a higher average ovalization and consequently higher deviations from their specified OR.

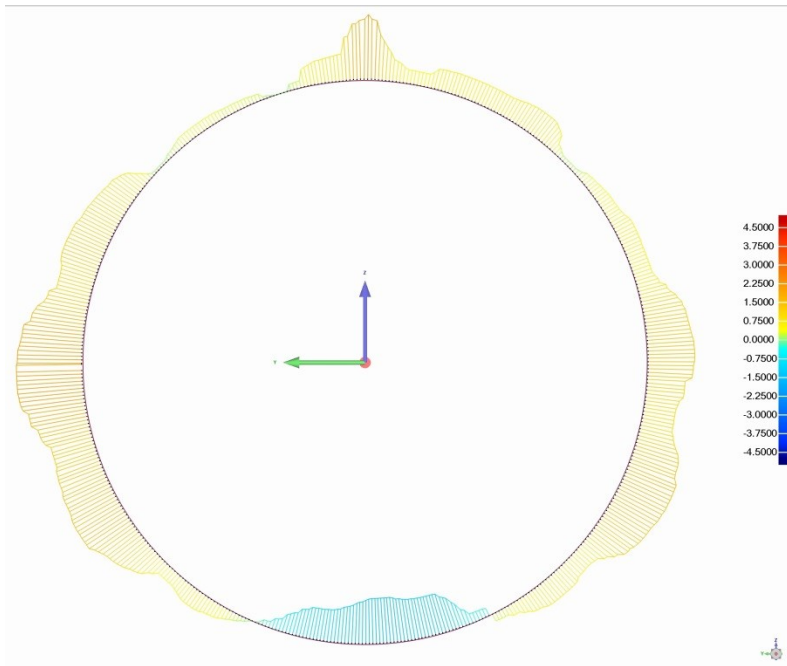


Figure 6.2 OR deviation pattern of NPS 34 A, D/t = 90.71, average ovalization 0.0092, manufactured by Sumitomo

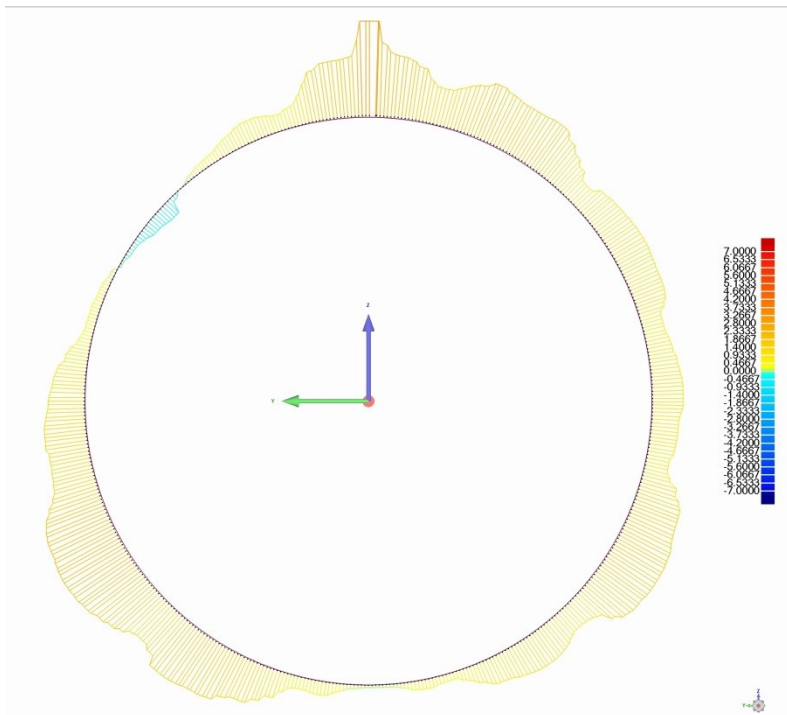


Figure 6.3 OR deviation pattern of NPS 34 B, D/t = 90.71, average ovalization 0.0089, manufactured by Sumitomo

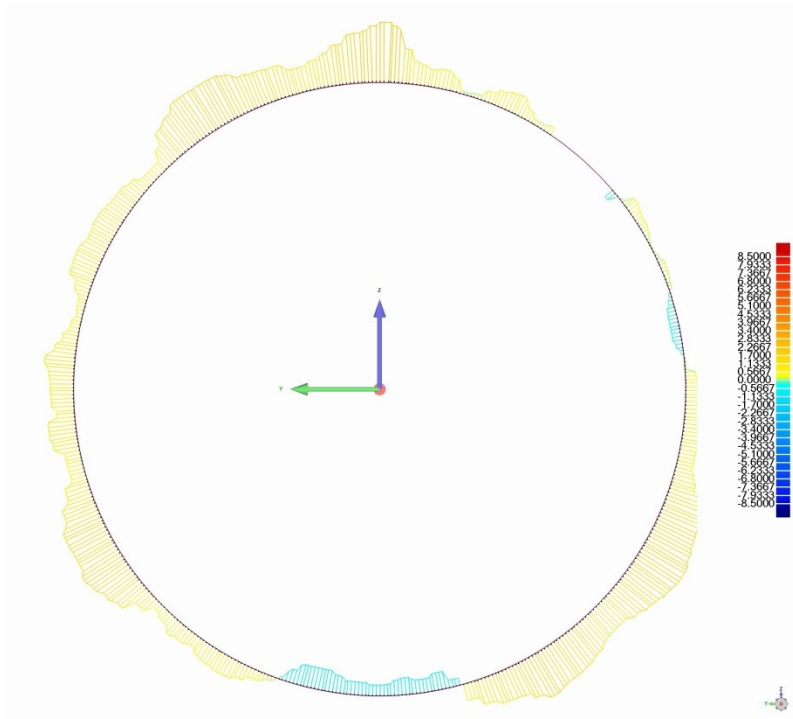


Figure 6.4 OR deviation pattern of NPS 42 A, $D/t = 103.47$, average ovalization 0.0049, manufactured by Sumitomo

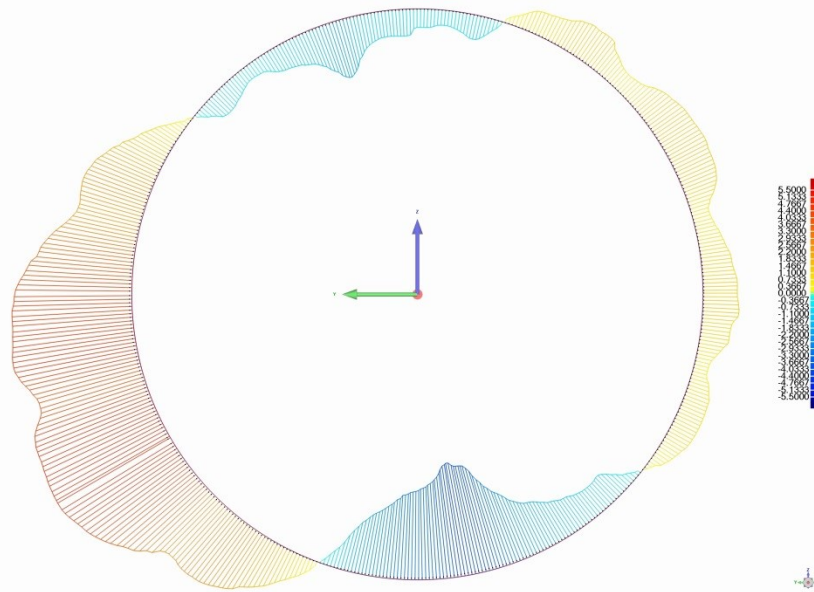


Figure 6.5 OR deviation pattern of NPS 42 B, $D/t = 103.47$, average ovalization 0.0150, manufactured by Sumitomo

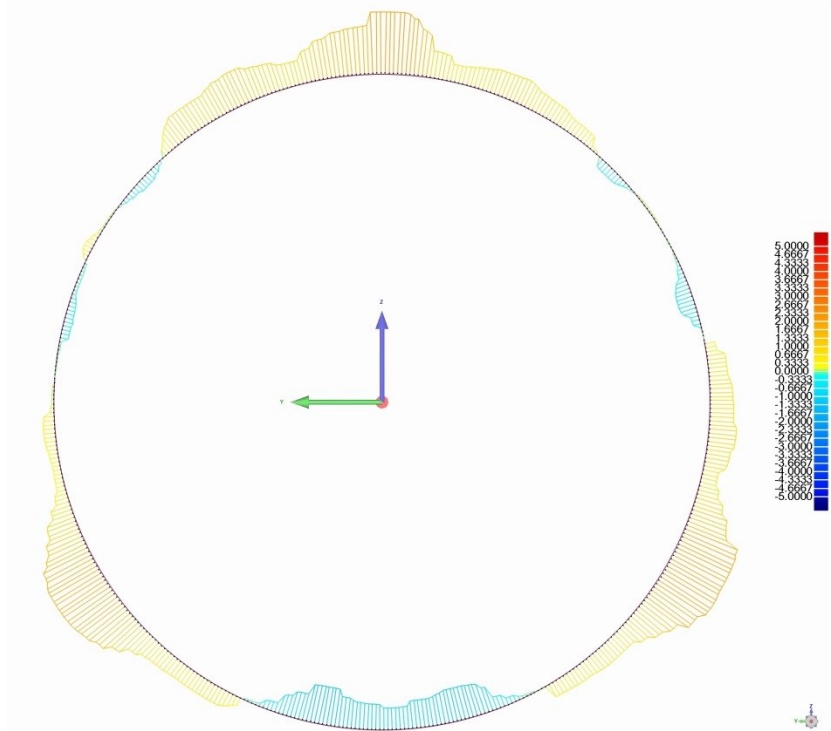


Figure 6.6 OR deviation pattern of NPS 42 C, D/t = 74.75, average ovalization 0.0067, manufactured by Nippon

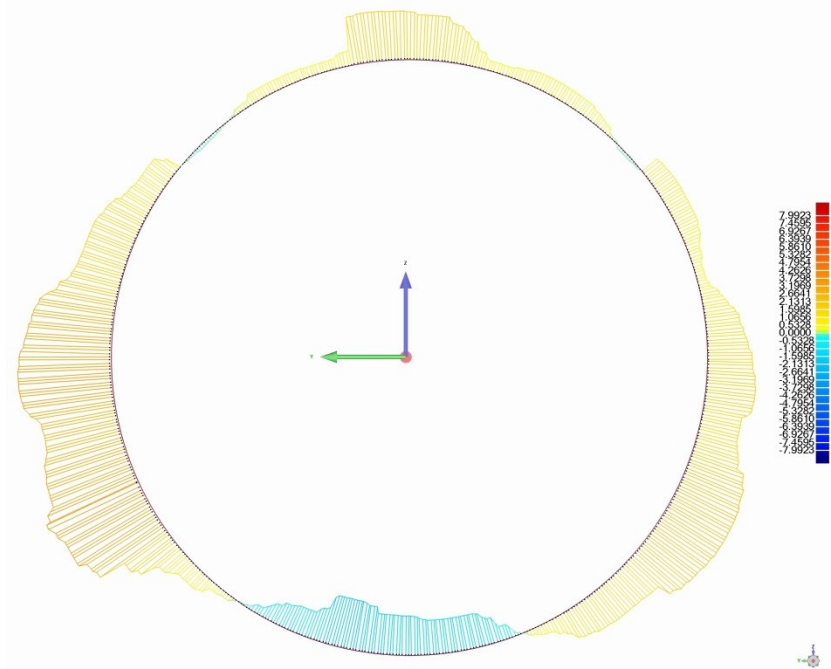


Figure 6.7 OR deviation pattern of NPS 42 D, D/t = 74.75, average ovalization 0.0117, manufactured by Nippon

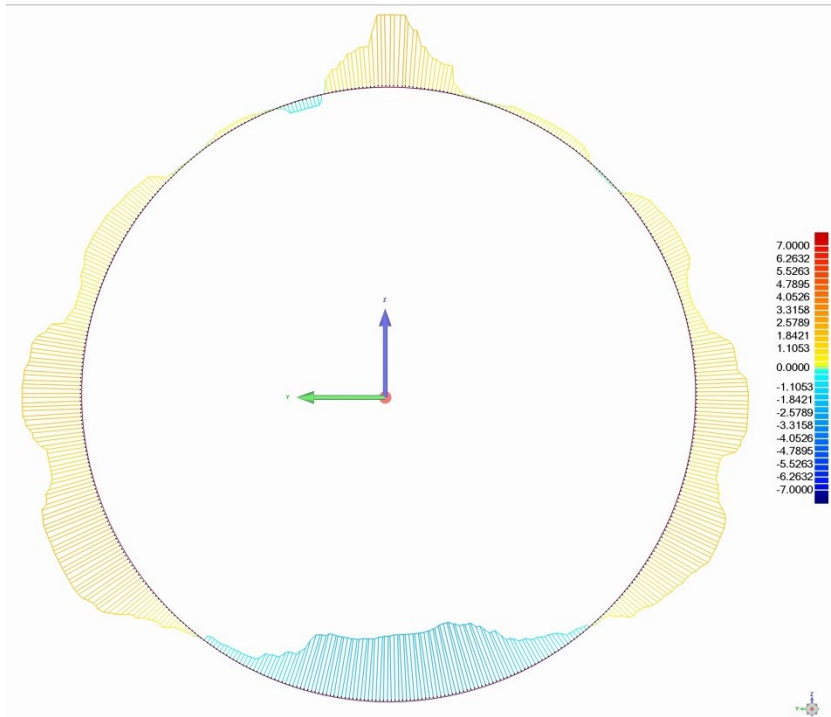


Figure 6.8 OR deviation pattern of NPS 42 E, D/t = 74.75, average ovalization 0.0099, manufactured by Nippon

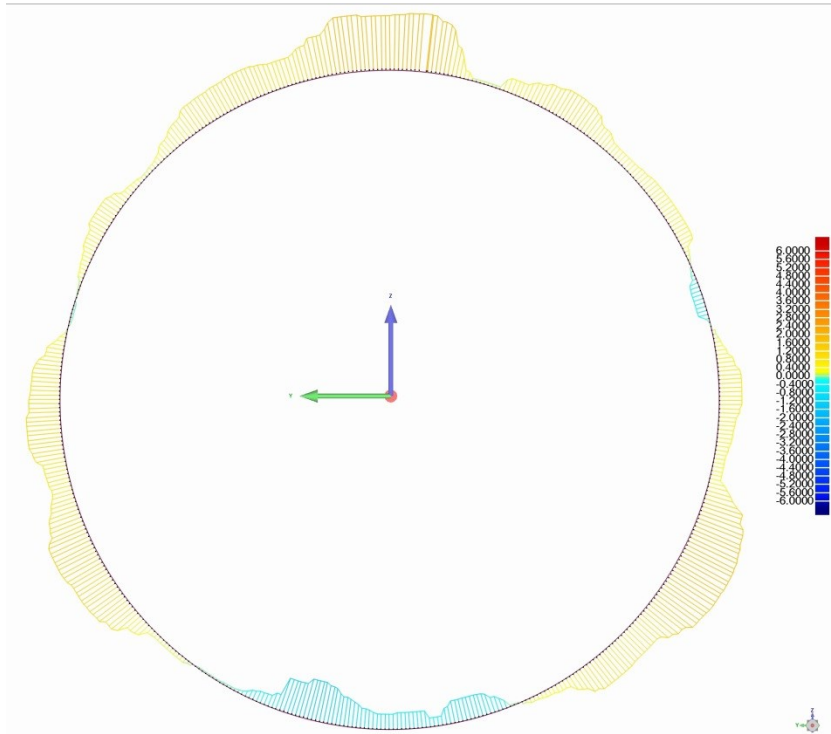


Figure 6.9 OR deviation pattern of NPS 42 F, D/t = 74.75, average ovalization 0.0073, manufactured by Nippon

In order to characterize the OR deviation pattern, the period of the wavy shape in terms of angle around the perimeter of a pipe cross section needs to be measured. The results of the measurements are shown in the following figures:

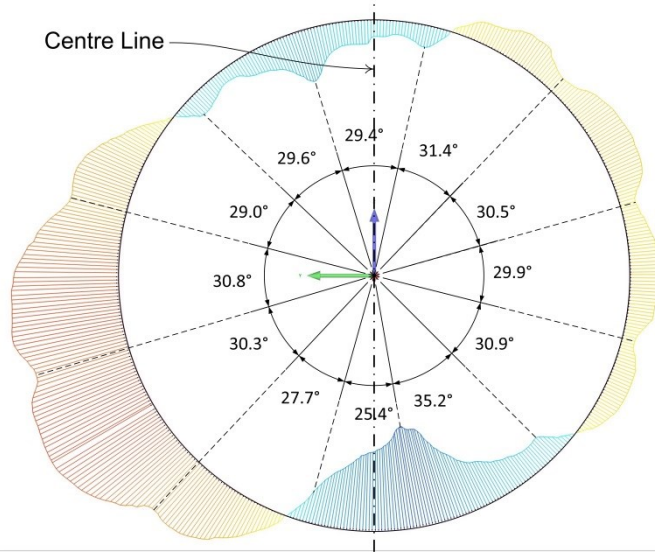


Figure 6.10 Angle subtended by the OR deviation waves of NPS 42 B to its centre

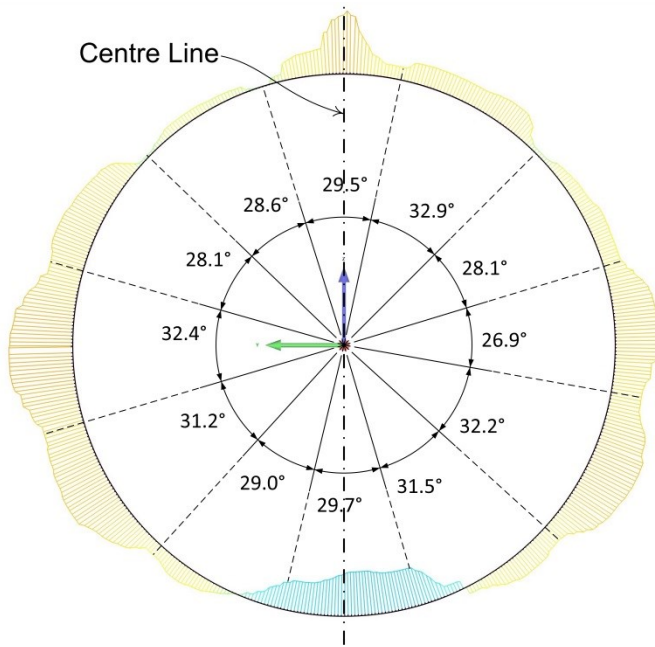


Figure 6.11 Angle subtended by the OR deviation waves of NPS 34 A to its centre

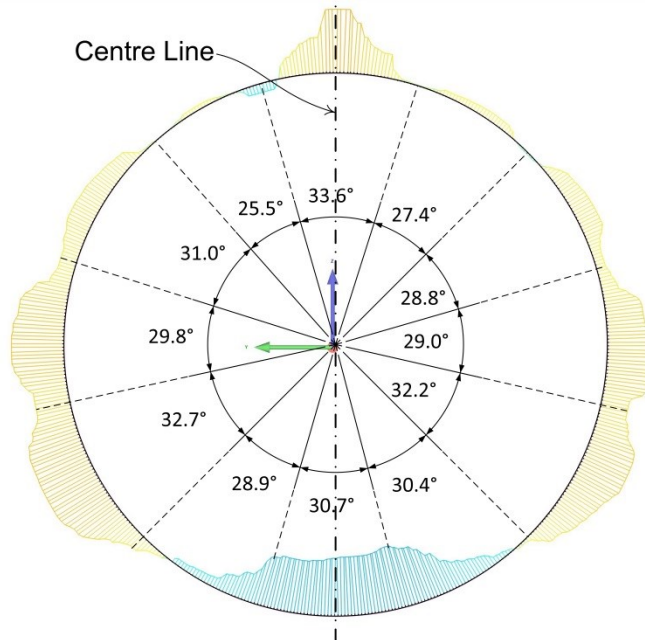


Figure 6.12 Angle subtended by the OR deviation waves of NPS 42 E to its centre

It is observed that the undulating deviations in the UOE manufactured pipes can be divided into 12 segments. Their subtended angles to the centre vary between 25.4 degrees to 35.2 degrees, and the average is close to 30 degrees. It is also observed that the patterns are fairly symmetric about the centre line connecting the centre of the pipe cross section and the location of the longitudinal seam weld.

The positive deviation waves in these pipes are prominent on both sides of the centre line. The negative deviation waves are seen on the opposite side of the seam weld. The NPS 42 B pipe, which has the highest D/t ratio, shows negative deviations near the seam weld locations as well (Figure 6.10), which is not a common character of the other specimens with lower D/t ratios. The symmetry in NPS 42 B pipe is also seen to be slightly skewed from the centre line. It is possible to express the OR deviation pattern in terms of the symmetric deviation segments subtending 30 degree angles to develop an OR deviation model.

A closer look into the OR deviation patterns reveals the possibility that the overall deviation may be approximated by an ellipse with its minor axis aligned with the centre line. An ellipse is a rather coarse approximation of the deviation pattern which only captures the maximum positive and negative deviations and ignores

the undulating patterns. However, the deviation magnitudes are negligible, and pipeline codes and standards tend to address this imperfection in terms of ovalization. Therefore the ellipse approximation of the deviation pattern is another logical and straight forward approach towards an imperfection model. The approximate ellipse or “ovalized” shapes are shown in Figure 6.13.

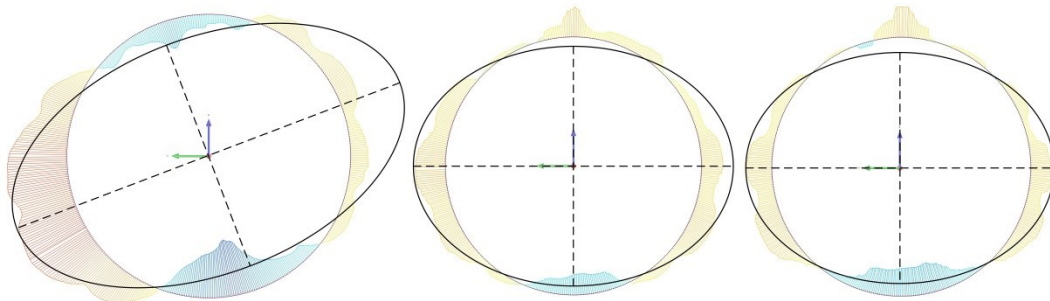


Figure 6.13 Ellipse or ovalization approximation of the OD deviations

It is to be noted that the NPS 34 and 42 inch pipes not only have different D/t ratios, but are also produced by different manufacturers. The only common aspect of these pipes is that they have been manufactured by the UOE process.

6.2.2 Pipe Wall Thickness Deviation Patterns

It was observed from the results of the wall thickness measurements that the UOE manufactured NPS 34, and 42 inch pipes clearly show different patterns than the NPS 20 inch pipes. Moreover, the magnitudes of deviations are seen to be more extreme in the pipes with lower D/t ratios. The NPS 42 A, and B pipes had the lowest specified wall thickness (10.312 mm) and the highest D/t ratio (103.47), and it is seen that their thickness deviation magnitudes are within $\pm 10\%$ of the specified thickness. The thicker pipes, NPS 34 (D/t = 90.71) and NPS 42 C to F (D/t = 74.75) not only have severe magnitudes of deviation, but also exhibit similar deviation pattern as shown in the following figure qualitatively:

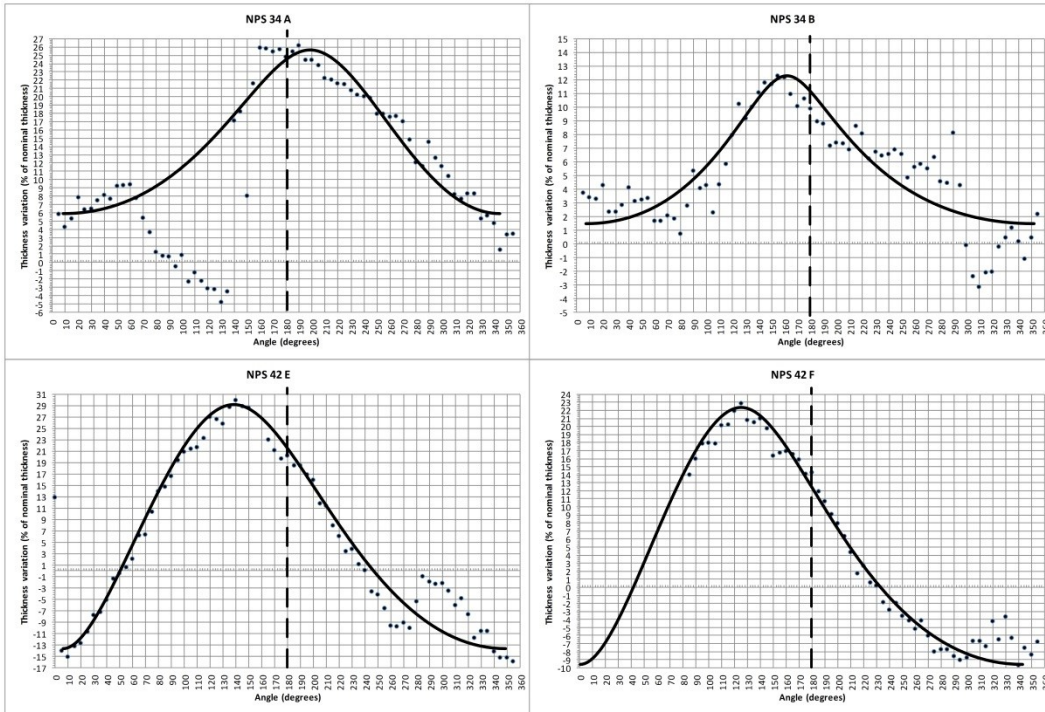


Figure 6.14 Typical wall thickness deviation pattern in the UOE manufactured pipes

It was observed that The NPS 20 inch X70 pipes have a different thickness deviation pattern compared to the UOE manufactured X100 pipes. The wall thickness deviation of the UOE manufactured pipes, when plotted against their location in terms of angles around their perimeter, resembles a bell shaped curve (Figure 6.14). All X100 UOE manufactured pipes exhibit decreased pipe wall thickness at locations near both sides of the seam weld. The negative deviation is seen to be as much as 15% of specified thickness. Increased pipe wall thickness is seen at locations opposite to the seam weld. The location of maximum positive deviation is within 20 degrees to 60 degrees from the 180 degree line showed in Figure 6.14 (dashed line). The transition of the thickness deviation of these pipes from negative to positive is smooth. From these observations, it can be concluded that the thickness deviation pattern can also be considered to be symmetric about the centre line of the pipe cross section and a thickness deviation model can be arrived at by fitting an appropriate curve to the observed deviation pattern. The typical thickness variation is shown in Figure 6.15:

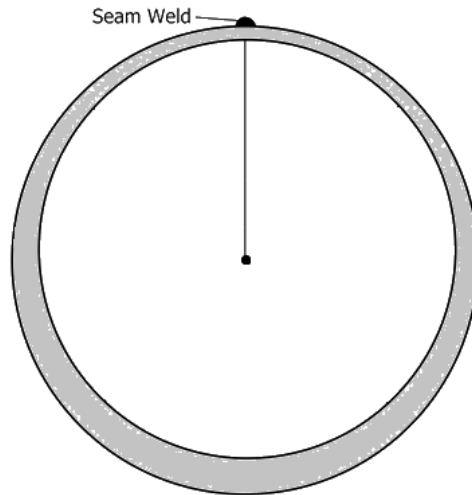


Figure 6.15 Schematic representation of the typical thickness deviation pattern of UOE manufactured pipes

6.3 Possible Sources of Initial Geometric Imperfection

From the OR and wall thickness deviations identified in the previous section, it is seen that the pipes are indeed very similar in terms of their imperfection patterns. The imperfection magnitudes however are different and vary with their D/t ratios and manufacturers. Therefore, it is possible that these imperfection patterns are the aftereffects of the UOE manufacturing process itself. Without any knowledge of the manufacturing details, it is not possible to quantitatively trace these sources of imperfections back to the manufacturing process. Nonetheless, a qualitative reasoning behind the possible sources of the identified imperfections is put forward.

The UOE manufacturing process involves the cold forming of 40 to 60 feet (12.2 to 18.3 meter) long steel plates. These plates are cold formed into a circular cylindrical shape through different mechanical punch, press and expansion. The two long edges of the plate are first crimped into circular arcs of specific radius to ensure that they would align perfectly when brought together to make the pipe (Figure 6.16 a). The plate is then deformed into a U-shape using a U-punch with dimensions specific to the OD of the pipe being manufactured (Figure 6.16 b).

In the next stage, the U-shaped plate is deformed into a circular shape using an O-press, also specific to the dimension of the pipe being manufactured (Figure 6.16 c). The end product of this stage is a nearly cylindrical pipe with the crimped edges aligned with each other, forming a seam.

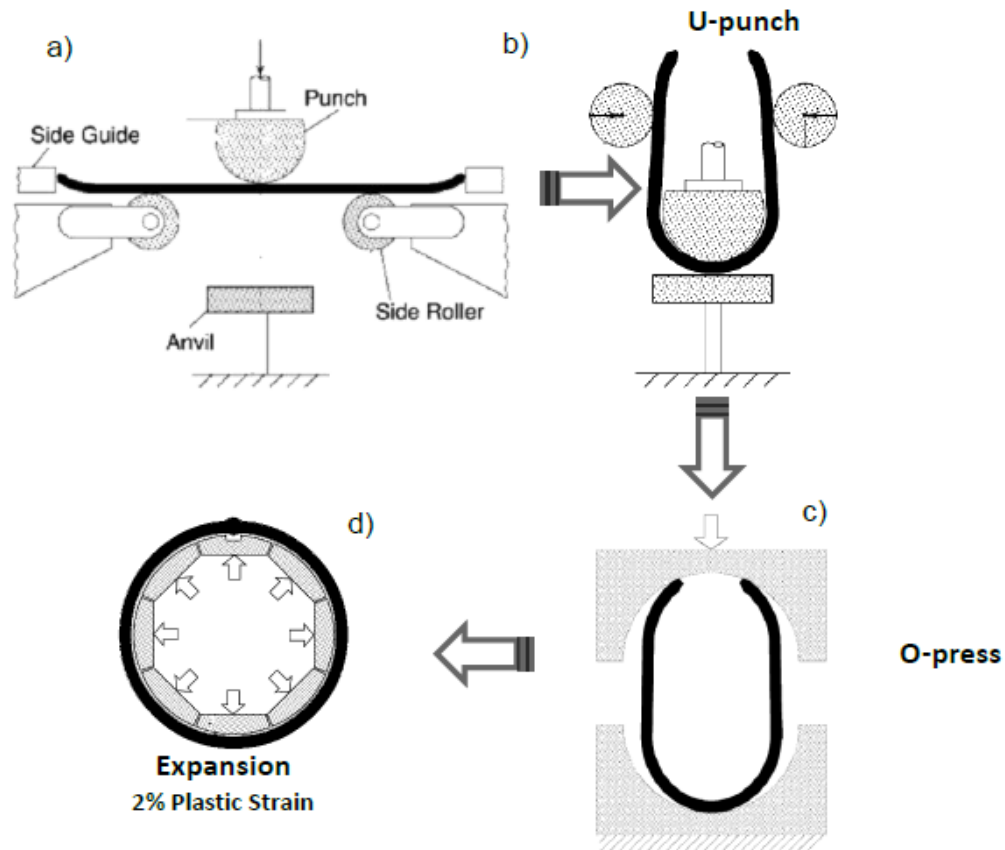


Figure 6.16 The four stages of the UOE manufacturing process: a) Crimping, b) U-punch, c) O-press, and d) Expansion (Herynk et al., 2007)

At this stage of manufacturing, the seam is welded from the inside and outside using submerged arc welding. In the final stage the pipe is mechanically expanded from the inside using hydraulically actuated mandrels in order to achieve the specified OD of the pipe and to improve its circularity (Figure 6.16 d). The mandrel typically consists of 8, 10, or 12 segments with specific dimensions corresponding to the inside diameter of the pipe being manufactured. An expansion is applied at this stage depending on the specified wall thickness of

the pipe. This typically results in a 2% plastic strain in the hoop direction of the pipe (Herynk et al., 2007).

From the review of the UOE manufacturing process, and from the identified patterns of OR deviation, it is seen that the OR deviation waves are very consistent with the arrangement of the mandrels used in the expansion process. It can be deduced that the outwards pressure exerted by the mandrel segments resulted in the observed wavy or undulating pattern of OR deviation. In the previous section, the number of undulations of deviations were found to be twelve, subtending approximately 30 degree angles to the centre, indicating that the expansion mandrel used in manufacturing these pipes had twelve segments.

The identified oval shapes of the pipes demonstrate that the minor axis of the fitted ellipse goes through the centre and the seam weld of a pipe cross section. The arc welded seam of the manufactured pipe is generally stronger than the pipe material and is the stiffest part of the pipe cross section. During the expansion process, the plate metal goes through plastic deformation, while the weld metal expands to a much lesser extent due to its higher stiffness. It is reasonable to assert that during this stage, the seam weld tends to move inside towards the centre of the pipe along the aforementioned minor axis, reducing its OR along that direction. For the same reason, the pipe OR is increased along the major axis. This scenario explains the observed ovalization pattern in the UOE pipes.

The thickness deviation patterns identified can either be an intrinsic property of the steel plate initially used to manufacture the pipes, or may have resulted during one of the stages of manufacturing. The plates are typically manufactured by hot rolling and this process may be responsible for the ends being thinner than the specified thickness. Crimping and expansion are the two stages that involve plastic deformation of the plate edges. However, the expansion process is a more likely source of the thickness imperfection since it exerts severe stress concentration near the proximity of the seam weld. This is the most probable reason behind the pipe walls being thinner near the seam weld compared to the locations away from the weld.

6.4 OR Deviation Model

From the discussions in Chapter 4, and from the characterizations in 6.2.1, the following can be summarized:

1. The OR deviation pattern is not random, the randomness is in the deviation magnitude
2. The OR deviation magnitudes are very small, can be considered insignificant
3. The OR deviation patterns can be considered symmetric, and expressed in terms of angles around the perimeter of the pipe
4. The OR deviations are in the form of waves subtending an average angle of 30 degrees to the centre
5. The OR deviation can also be coarsely approximated by an ellipse

It has been reported previously that the OR deviations are very insignificant compared to the specifications. These small magnitudes of deviations are not expected to have any significant effect on the buckling behaviour of the pipes. Pipes in service are generally under the application of internal pressure, which will tend to reduce the effect of the OR deviation imperfection even further. Therefore, the worst observed case, i.e. the specimen with the maximum observed deviations will be considered while developing the OR deviation models. Two OR deviation models, one fine and one coarse, will be developed, with the fine being able to capture the wavy shape and the coarse being simply an ellipse. These two models with the maximum observed magnitude of deviation will enable us to decide whether this imperfection is influential on the buckling behaviour through Finite Element Analysis.

The maximum and average OR deviations and ovalization values corresponding to each pipe have been reported previously in Chapter 4. It was observed that the pipe NPS 42 B exhibited higher magnitudes of imperfection compared to the rest. It had an average positive and negative deviation of 1.98 mm and 1.64 mm respectively. The maximum and average values of ovalization were found to be 0.016 and 0.015 respectively. Therefore, the OR deviations of NPS 42 B is chosen as the basis for developing the OR deviation models.

The ovalization value of NPS 42 B between 200 mm to 400 mm from its edge is seen to be 0.015, which is equal to its average ovalization value. Therefore, a cross section of the pipe at 300 mm from edge is deemed an appropriate reference for the OR deviation model. Details of the model development procedure are presented in the following sub sections.

6.4.1 Reference Deviation Data

For the OD deviation models, it is necessary to acquire the deviation profile of the selected cross section exhaustively. This is accomplished through the following steps. First the cross section is converted to a high resolution point cloud in Geomagic®. The resolution is set to be a point for each 1.0 degree of angular interval around the centre of the cross section. This results in a total of 360 points as shown in Figure 6.17:

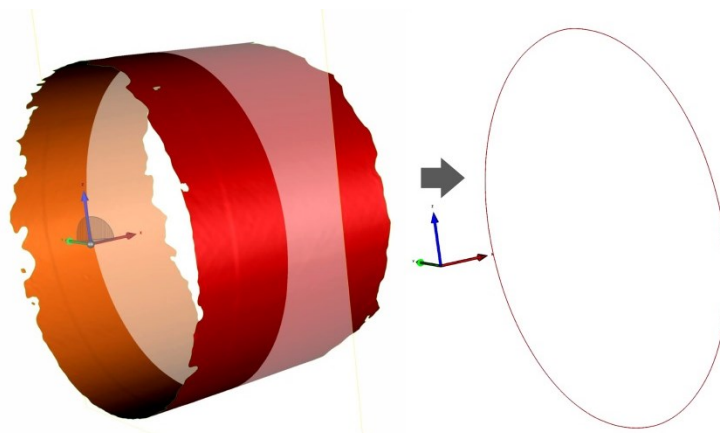


Figure 6.17 Extraction of points from the reference cross section

Next, the Cartesian coordinate values of these points are extracted. The pipe was previously aligned with the global coordinate system in a specific way as was discussed in Chapter 3. Therefore, the exact orientations of these points are already known. The Cartesian coordinates are further converted into polar coordinates, producing the (r, θ) value for each point. These are the required raw data for the development of the OR deviation models.

The (r, θ) values in the range 0 degree to 270 degrees along with the specified outside radius (OR) of the pipe are plotted in Figure 6.18. The higher radii values near 0 degrees correspond to the outer surface of the seam weld captured during scanning, and are not to be considered as imperfection. From the trend, it is seen

that the radii values decrease towards the specified radius at the seam weld location (0 degree). It was mentioned previously that this specific pipe specimen had its OR deviation pattern slightly skewed about the centre or reference line. Accordingly, the minimum radius is seen at 190 degrees from the seam weld.

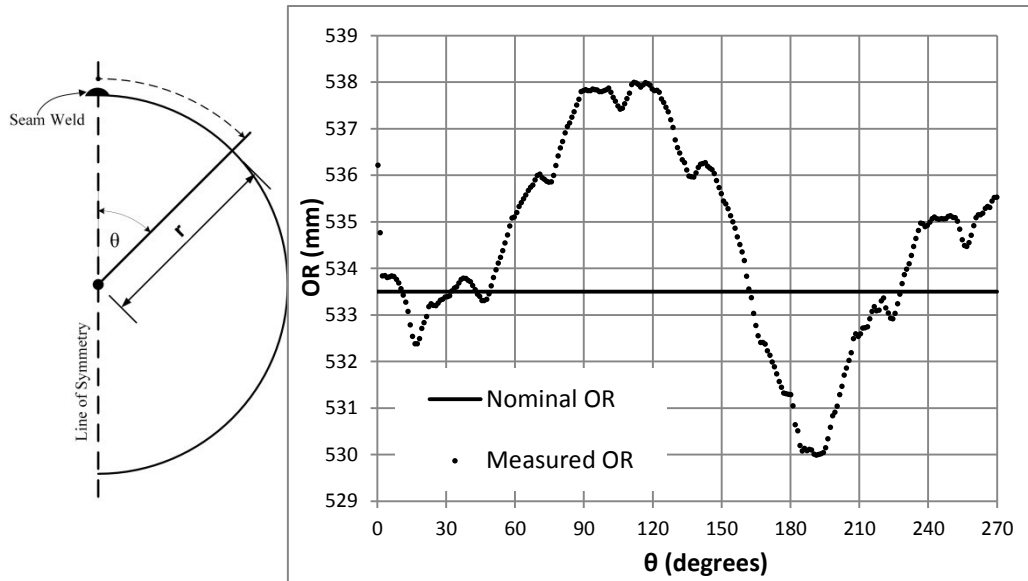


Figure 6.18 Measured OR values at the reference cross section

As mentioned earlier, the OR deviation are assumed to be symmetric and only half of the pipe cross section (0 degree to 180 degree) needs to be considered. In order to comply with the assumptions, the raw data are slightly modified as follows:

1. The OR value at 0 degree is taken to be equal to the specified OR
2. The radii values are shifted towards the seam weld by 10 degrees so that the maximum negative deviation is at 180 degrees
3. Points are assumed between 0 degree and 12 degrees to ensure a smooth transition of the radii values

The radii values are then expressed as the percentage deviation from the nominal radii to facilitate the development of a generalized model applicable to pipes with different nominal OD. The modified values are plotted in Figure 6.19. This is the initial data to be used as reference for the development of the OR deviation models.

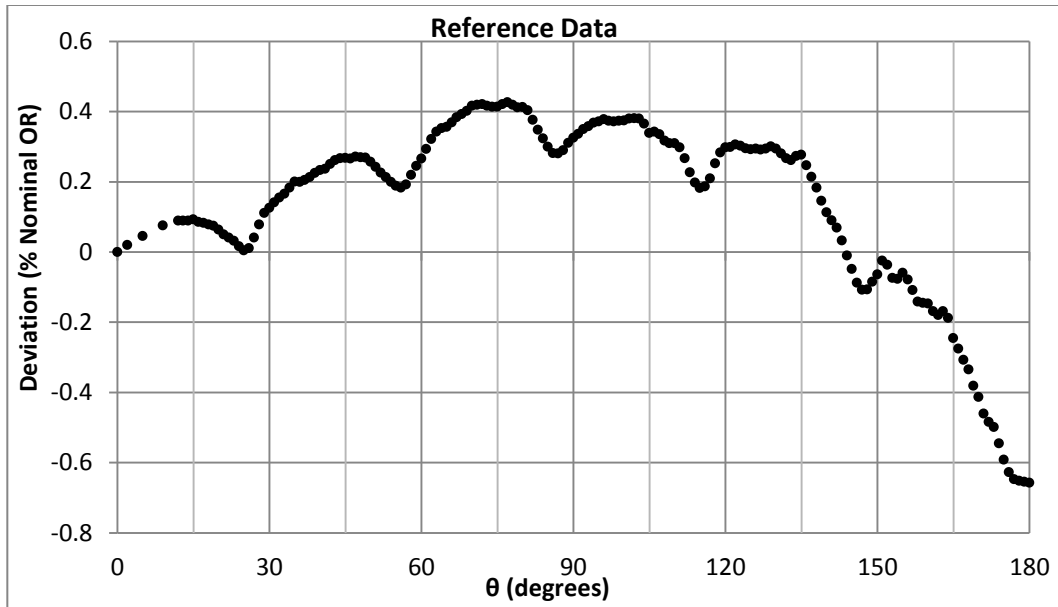


Figure 6.19 Modified radii values expressed as percentage deviation from nominal OR

Based on this reference data, the following OR deviation models are developed.

OR Deviation Model 1

The first OR deviation model developed is the most rigorous model capable of capturing the deviation profile very precisely. A cubic spline interpolation is performed using the reference data to develop this model. Cubic spline interpolation is a widely used interpolation method in numerical analysis, where the spline is piecewise cubic between the data. The control points required for the cubic spline interpolation are set at the highest and lowest amplitudes of each of the waves of the reference deviation. The control points and the interpolated cubic spline are shown in Figure 6.20 along with the reference data.

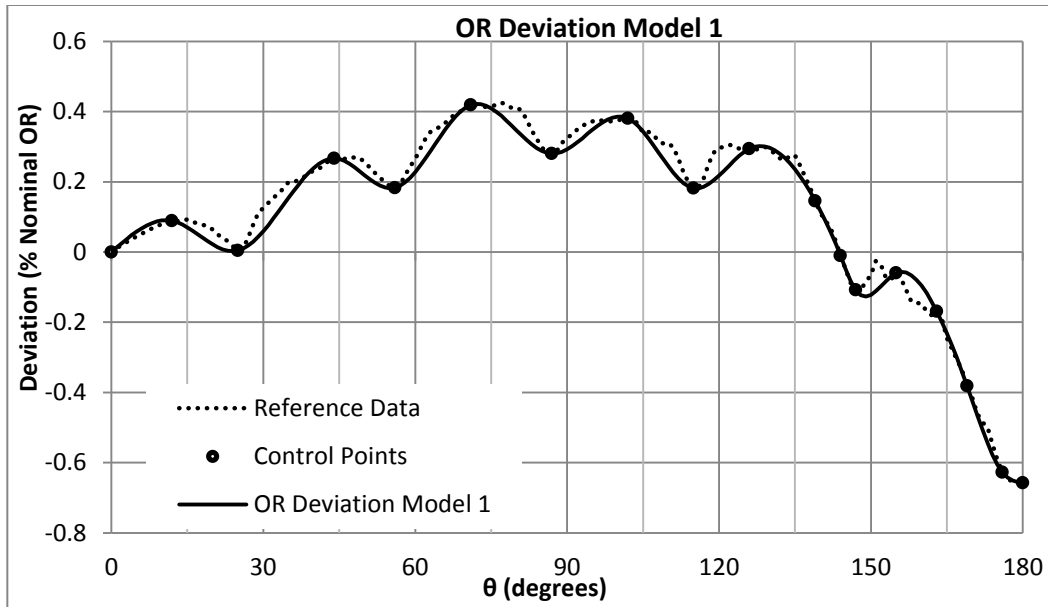


Figure 6.20 OR Deviation Model 1

The average difference between the reference data and the model is found to be 0.023% of the Nominal OR (0.13 mm), and the R^2 value is found to be 0.98. This model captures the actual shape of the imperfect cross section very accurately.

It is required to verify if this method for developing the OR deviation model is applicable to the other pipe cross sections. The reference data was slightly modified to reduce the noise and to make it symmetric before developing the model. In the verification, the noise reduction is not performed, only the surface points corresponding to the longitudinal seam weld are discarded.

The verification is performed on three selected cross sections of the specimens NPS 34 A, NPS 34 B, and NPS 42 C. The control points for the cubic spline interpolation are selected at the highest and lowest amplitudes of the OR deviation waves. The deviation models fitted to the measured OR deviations are shown in Figure 6.21 to Figure 6.23. The R^2 values and the differences in the measured deviation value and the fitted model are calculated for each cross section. It is seen that the OR deviation model 1 fits to the NPS 34 A with an average difference of 0.0213% of nominal OR (0.092 mm) and an R^2 value of 0.97. For NPS 34 B, the average difference is 0.0293% of nominal OR (0.127 mm) and the R^2 value is 0.88. For NPS 42 C, the difference is 0.02% of nominal OR (0.108 mm) and the R^2 value is 0.95.

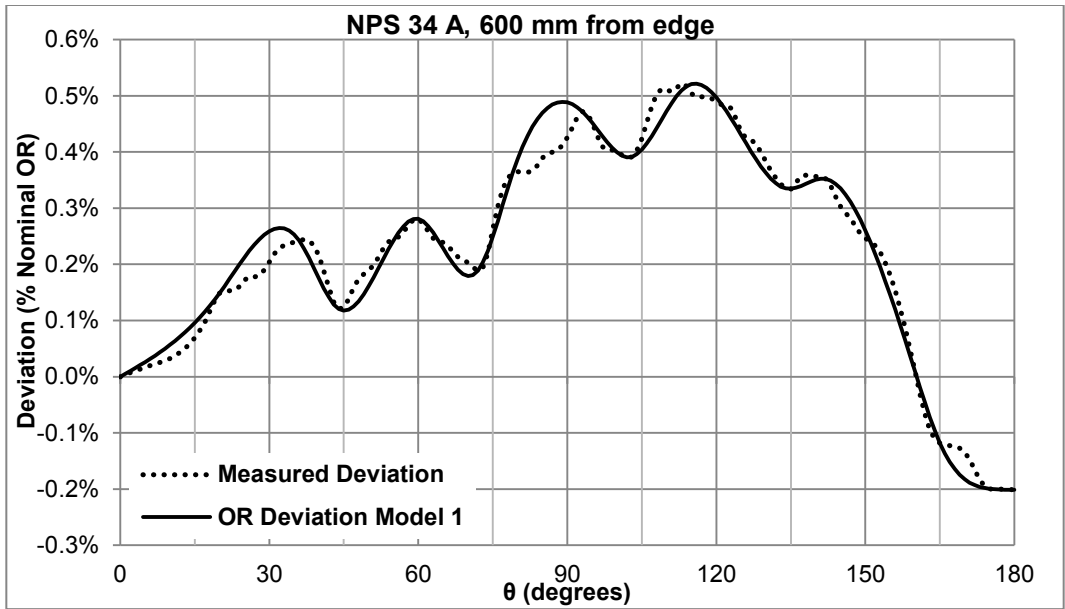


Figure 6.21 OR Deviation Model 1 fitted to the measured OR deviation of NPS 34 A at a cross section 600 mm from edge

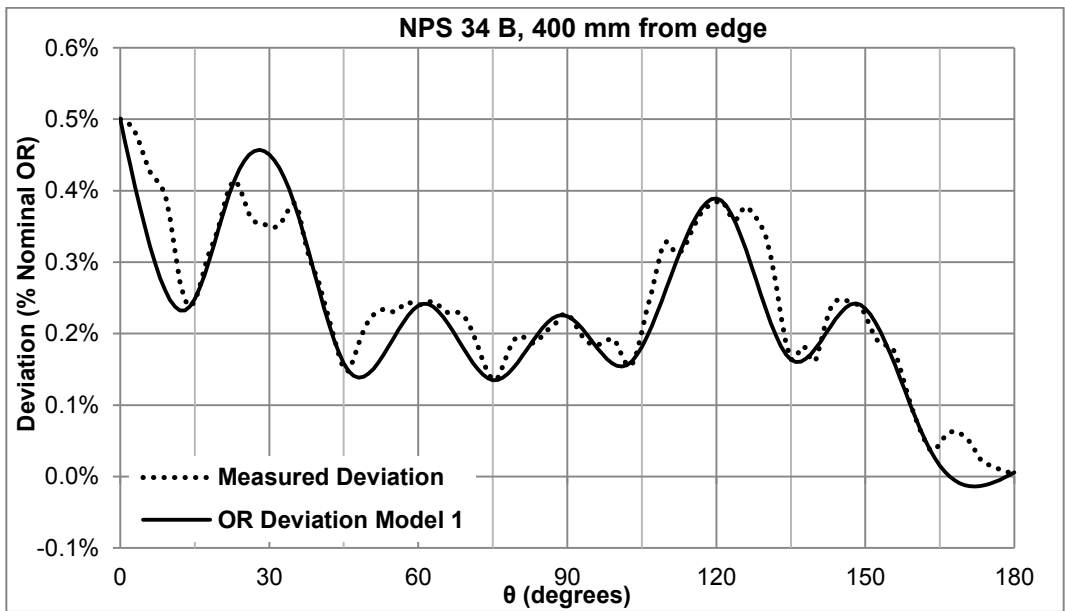


Figure 6.22 OR Deviation Model 1 fitted to the measured OR deviation of NPS 34 B at a cross section 400 mm from edge

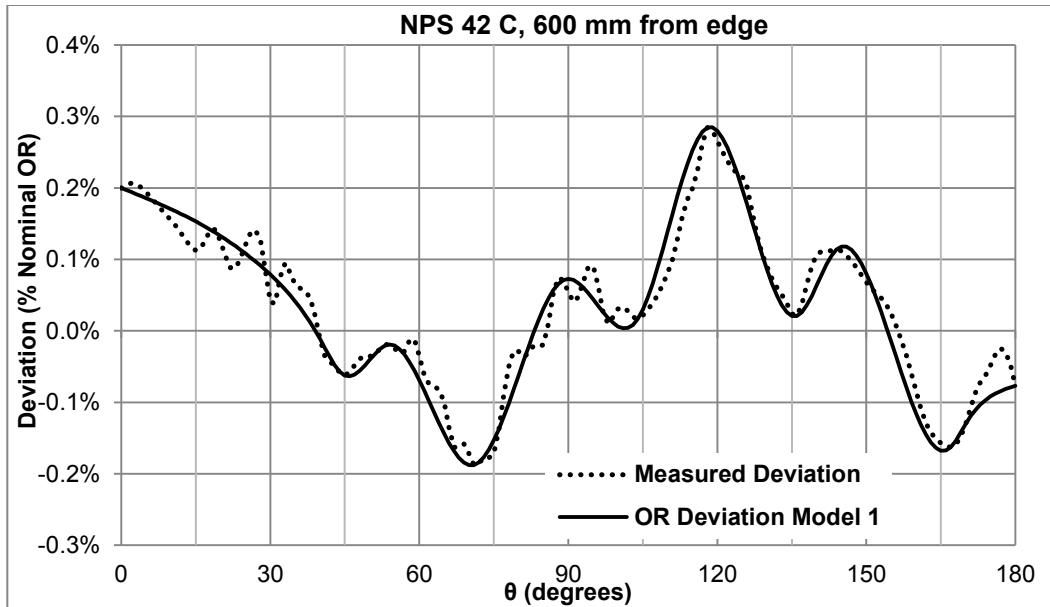


Figure 6.23 OR Deviation Model 1 fitted to the measured OR deviation of NPS 42 C at a cross section 600 mm from edge

OR Deviation Model 2

The second model is a crude approximation of the reference data. As discussed previously, the OR deviation patterns can be coarsely approximated with an ellipse with its minor axis aligned with the symmetry line, and which only considers the maximum positive and negative deviations. The equation of an ellipse, whose major and minor axes are aligned with the two Cartesian axes, is as follows:

$$\frac{x^2}{a^2} + \frac{y^2}{b^2} = 1 \quad 6-1$$

The constants a, and b correspond to the two vertices of the ellipse. Therefore the values of a, and b will be equal to the maximum and minimum measured OR values respectively. The maximum and minimum OR values are calculated from the maximum positive and negative deviation values in the reference data. The parametric form of the ellipse equation is as follows:

$$x(\theta) = a \cos \theta , \quad y(\theta) = b \sin \theta \quad 6-2$$

The radii values of the ellipse are calculated from the above equation and plotted alongside the reference data in Figure 6.24

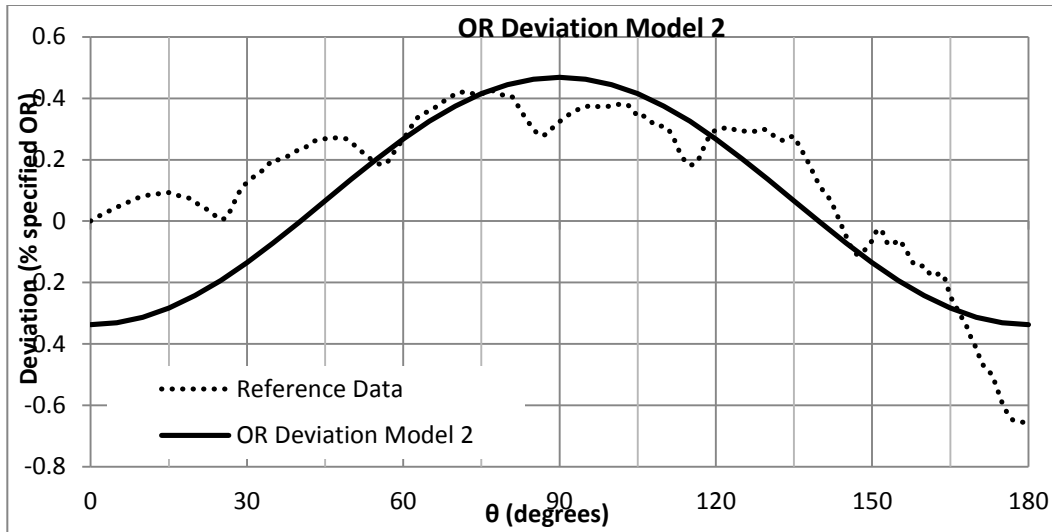


Figure 6.24 OR Deviation Model 2

The average difference between the reference data and the model is found to be 0.145% of the nominal OR (0.77 mm). However, the ovalization value is calculated to be 0.015, which is equal to the ovalization value of the selected cross section of NPS 42 B.

A verification of the model is performed on the previous three cross sections of NPS 34 A, NPS 34 B, and NPS 42 C. The maximum and minimum values of OR are calculated from their measured deviation values. OR deviation model 2 fitted to the measured OR deviations are plotted in Figure 6.25 to Figure 6.27. It is observed that the OR deviation model 2 is not capable of capturing the shape of the deviation accurately. The average difference between the measured deviation and the model for the NPS 34A, NPS 34 B, and NPS 42 C specimens are seen to be 0.24% of nominal OR (1.04 mm), 0.23% of nominal OR (1.0 mm), and 0.28% of nominal OR (1.51 mm) respectively. The ovalization values calculated from the maximum and minimum radii in the model fitted to these three sections are 0.01 (NPS 34 A), 0.007 (NPS 34 B), and 0.008 (NPS 42 C), which is equal to the measured ovalization at these cross section previously reported in Table 4.6. Therefore the OR deviation model 2 is capable of capturing the overall ovalization of the pipe cross section.

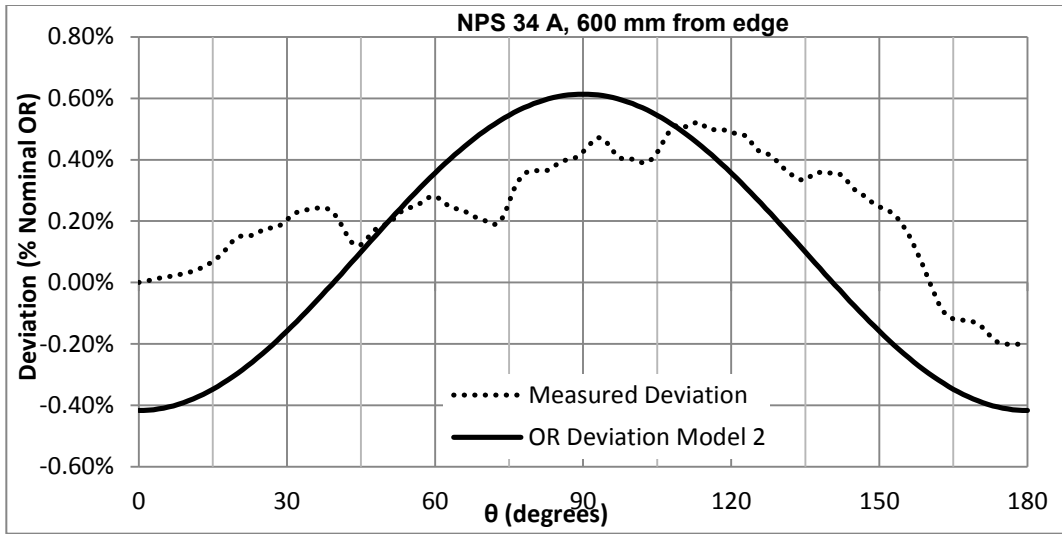


Figure 6.25 OR Deviation Model 2 fitted to the measured OR deviation of NPS 34 A at a cross section 600 mm from edge

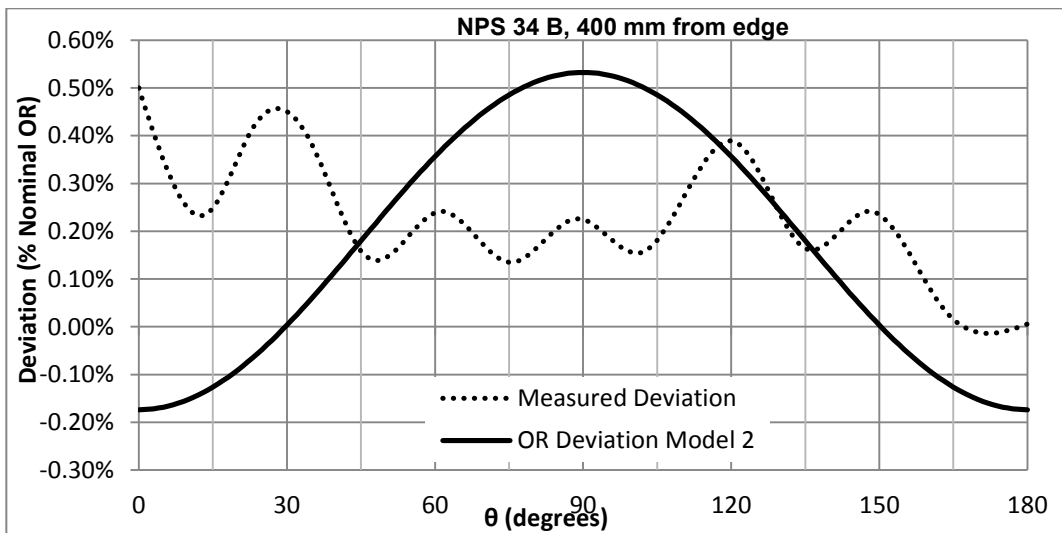


Figure 6.26 OR Deviation Model 2 fitted to the measured OR deviation of NPS 34 B at a cross section 400 mm from edge

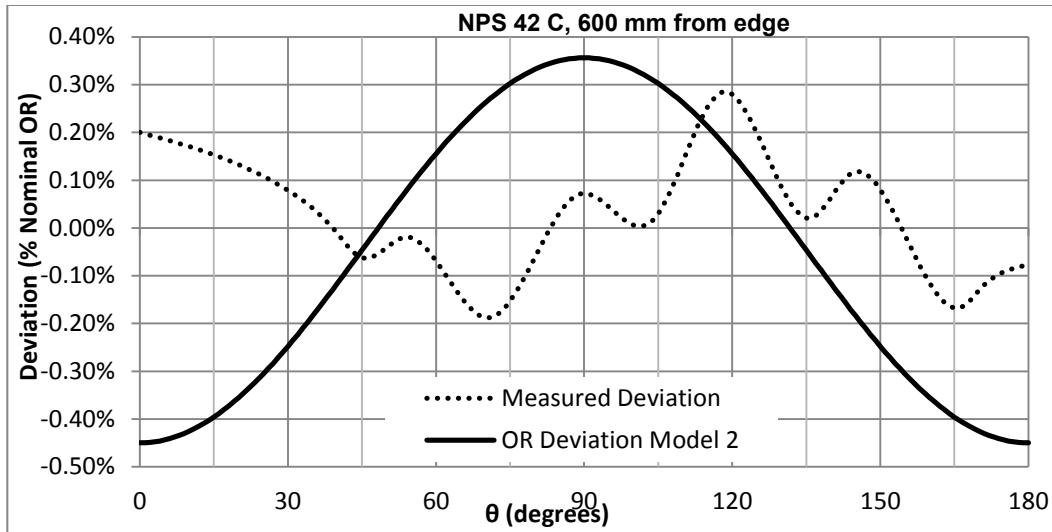


Figure 6.27 OR Deviation Model 2 fitted to the measured OR deviation of NPS 42 C at a cross section 600 mm from edge

Figure 6.28 illustrates the difference in shape between the two OR deviation models qualitatively. It is seen that the OR Deviation Model 1 is able to capture the wavy shape of the imperfect cross section, while the OR Deviation Model 2 is in the shape of an ellipse, which does not capture the actual shape but only has the maximum and minimum radii values associated with the imperfect cross section.

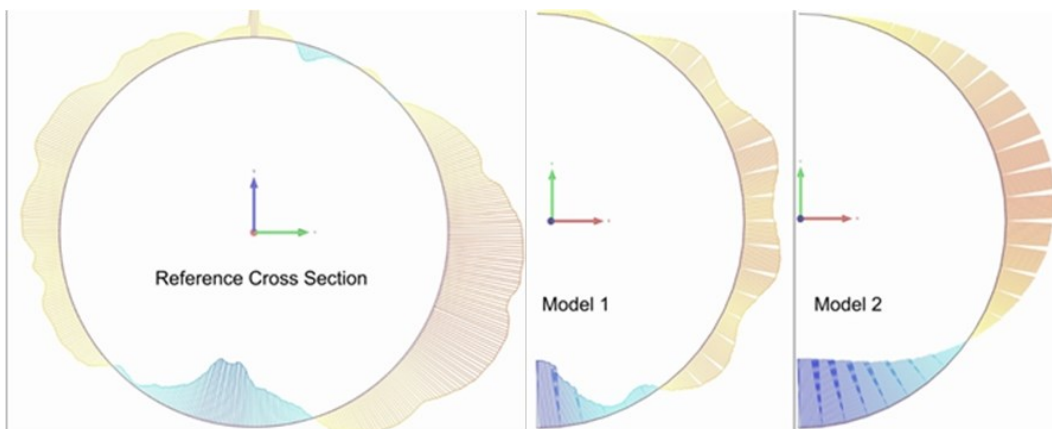


Figure 6.28 Qualitative comparison between the reference cross section and the two OR deviation models

6.5 Wall Thickness Deviation Model

From the characterization in section 6.2.2, it can be summarized that the wall thickness deviation of the pipes resembles a bell shaped curve, which is fairly symmetric about the reference line (the line connecting the centre and the point on the pipe cross section corresponding to the location of the longitudinal seam weld). Once again, the worst observed case, i.e. the specimen with the maximum deviation magnitudes will be considered to develop the thickness deviation model.

It was previously reported that the specimen NPS 42 E had the maximum magnitudes of positive and negative thickness deviations (Table 4.9). Accordingly, the measured thickness deviation of this pipe is chosen as the basis for developing a thickness deviation model.

In Figure 6.29, a plot of the pipe wall thickness deviations of the specimen NPS 42 E (14.275 mm specified wall thickness) is shown. It is observed that the thickness deviation pattern assumes a bell shaped curve. A Gaussian function in the domain of $-\pi$ to $+\pi$ is deemed best suited to express the deviation pattern mathematically.

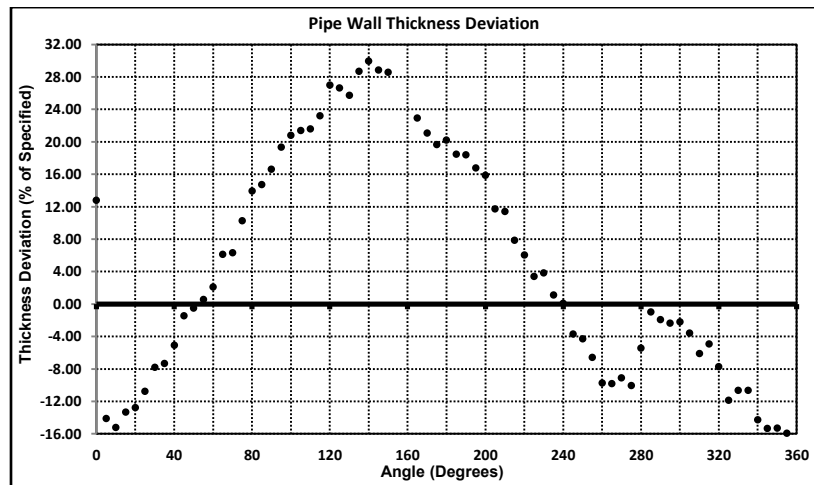


Figure 6.29 Measured deviation of wall thickness of NPS 42 E, 1067 mm nominal OD and 14.275 mm specified wall thickness

The thickness deviation is expressed in a cylindrical coordinate system through the following equation:

$$\% \text{ Thickness Deviation} = a e^{\left(\frac{-(\theta-b)^2}{c}\right)} - d \quad 6-3$$

In Equation 6-3, θ is the angle around the center of the pipe cross section with respect to the reference line ranging from $-\pi$ to $+\pi$, where both $-\pi$ and $+\pi$ correspond to the location of the longitudinal seam weld. The letters a, b, c, and d, are equation constants that can be manipulated to produce bell shaped curves of desired amplitudes of deviation. A regression analysis is performed to fit this model to the deviation data. The thickness deviation model fitted to the measured thickness deviation is shown in Figure 6.30:

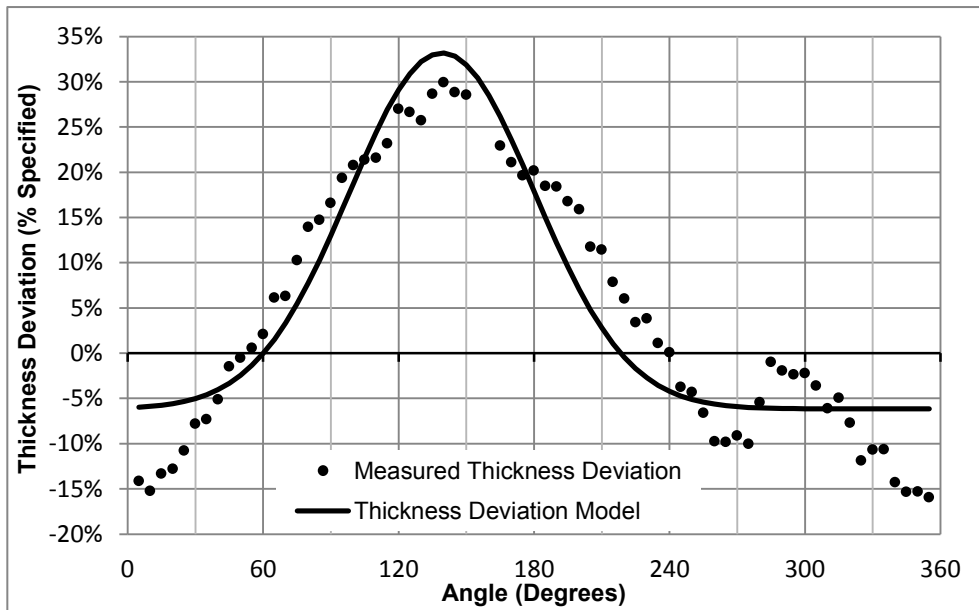


Figure 6.30 Thickness Deviation Model fitted to the measured deviation through regression analysis

The model fits to the measured deviation with an average difference of 0.05% of the specified thickness (0.71 mm) and an R^2 value of 0.87. However, the regression analysis overestimates the negative thickness deviation values. It is observed that the maximum measured negative deviation is close to -15.0%, while the regression produces a value of -6.0%. The maximum measured positive deviation is close to 30.0%, and the regression produces a value of 33%. A regression analysis will always overestimate the maximum positive and negative values of deviation, while trying to fit the model to the data by reducing the error. A 15.0% reduction of the wall thickness is very likely to have huge effects on the buckling behaviour of pipes. It is important that the thickness

deviation model captures the maximum positive and negative deviations accurately, in addition to capturing the shape of the deviation profile. Therefore, it is concluded that fitting the thickness deviation model to the measured deviation data through regression is not an appropriate approach.

In order to capture the maximum positive and negative deviation values and the deviation shape, the thickness deviation model should ideally be fitted through a weighted regression, where the maximum positive and negative deviation points and the points with 0.0% deviation have higher weightage. The benefit of a Gaussian Function is that its amplitude and shape can be manipulated by tweaking the equation constants. Instead of performing a weighted regression, the equation constants are slightly modified to ensure that the thickness deviation model produces the maximum positive and negative deviation values equal to the measured maximum values, while preserving its shape. A plot of the thickness deviation model manually fitted to the measured deviations is shown in Figure 6.31:

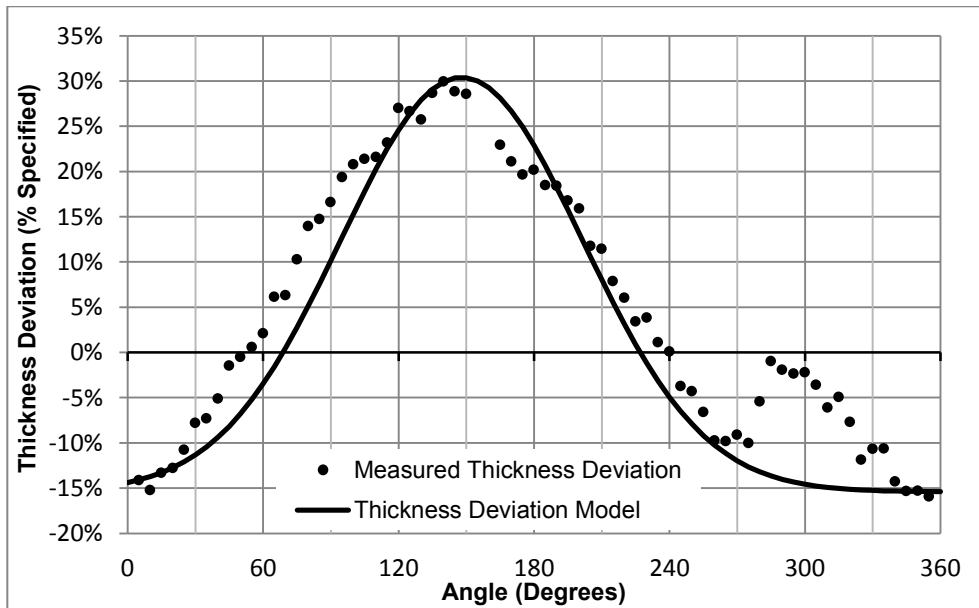


Figure 6.31 Thickness Deviation Model manually fitted to the measured deviation

An average difference of 4.13% of the specified thickness (0.59 mm) and an R^2 value of 0.85 are calculated between the measured deviation and the fitted

model. The model is able to produce the maximum positive and negative deviations equal to the measured deviations accurately.

Similarly, the thickness deviation model is fitted to the measured thickness deviation of the specimens NPS 34 A, NPS 34 B, and NPS 42 F at selected cross sections. The fitted models are shown in Figure 6.32 to Figure 6.34. The average differences between the model and the measured deviation for the specimens NPS 34 A, NPS 34 B, and NPS 42 F is found to be 5.58% of the specified thickness (0.53 mm), 2.44% of the specified thickness (0.23 mm), and 1.53% of the specified thickness (0.15 mm) respectively. In all cases, it is ensured that the maximum positive and negative deviation values are captured accurately by the thickness deviation model.

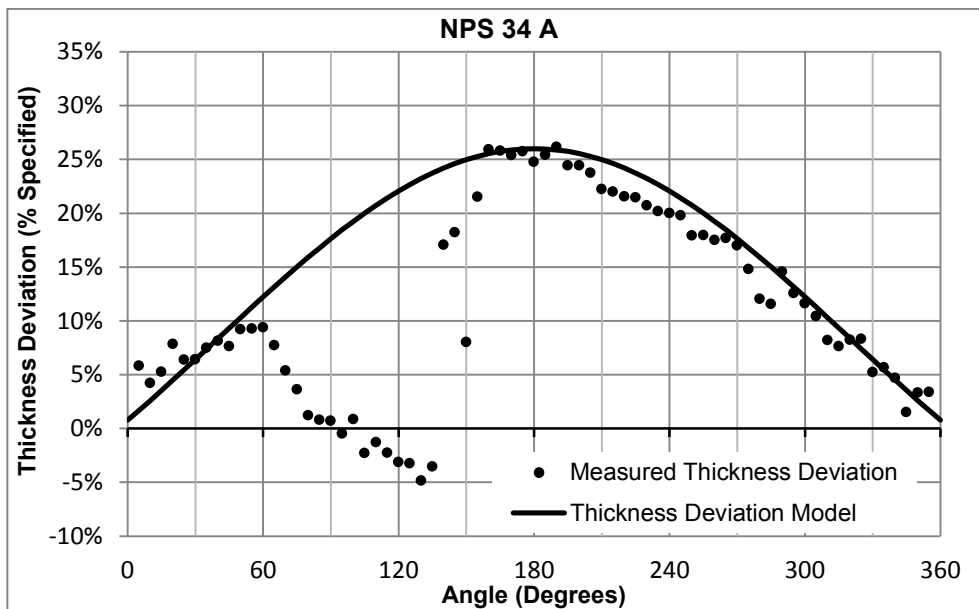


Figure 6.32 Thickness Deviation Model fitted to the measured deviation of NPS 34 A at a section 250 mm from edge

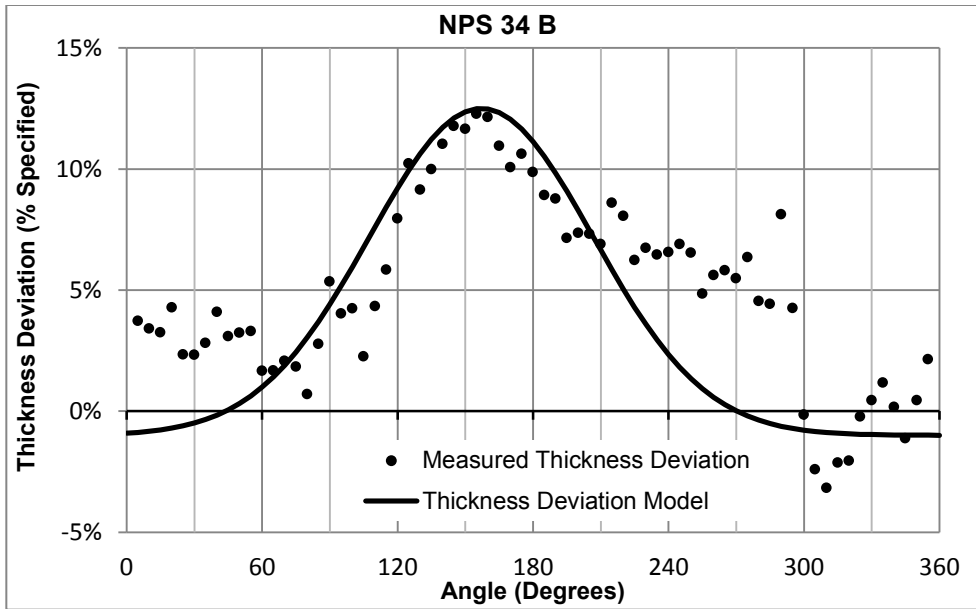


Figure 6.33 Thickness Deviation Model fitted to the measured deviation of NPS 34 B at a section 250 mm from edge

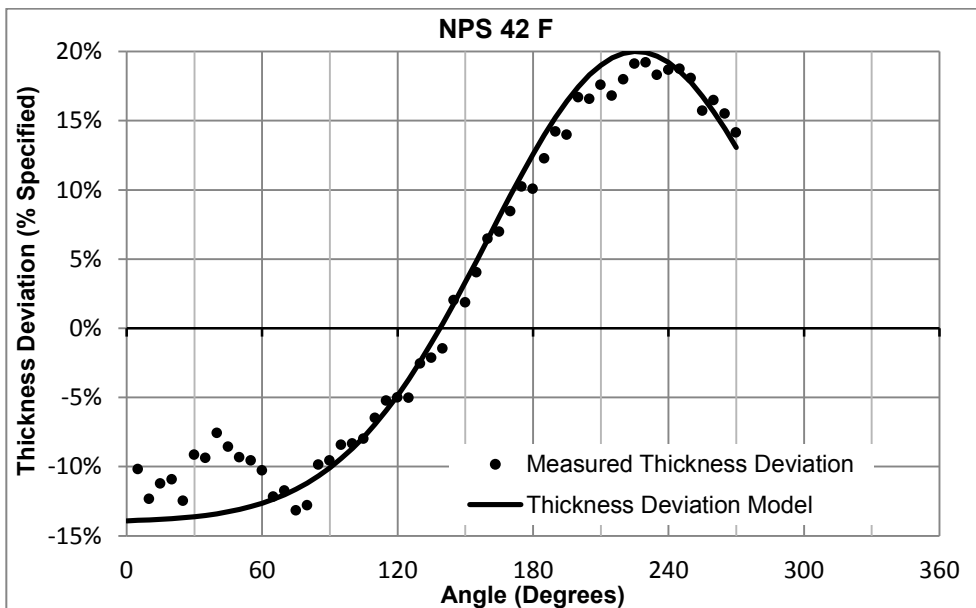


Figure 6.34 Thickness Deviation Model fitted to the measured deviation of NPS 42 F at a section 300 mm from edge

It is noted that the exponential function used to describe the thickness deviation imperfection is a non-harmonic function. In case of the thickness deviations that are asymmetric about the location of the longitudinal seam weld, the use of this function results in a discontinuity at 0 degrees and 360 degrees. However, the maximum magnitude of such discontinuity is observed to be 0.009 mm (NPS 42

E, Figure 6.31), which is significantly small and is deemed acceptable. The discontinuity vanishes in case of symmetric deviation models.

From the thickness deviation patterns observed in the UOE manufactured pipes, it was seen that the magnitude of the maximum positive and negative deviations are different in different specimens. The angle subtended to the centre of the cross section by the region with negative deviation is also a variable. In order to perform a parametric study of the effects of thickness deviation on the buckling behaviour of pipes, the above mentioned attributes have to be considered. The Gaussian function, as mentioned previously, can be changed in shape and magnitude by changing the equation constants. The thickness deviation for the parametric study is assumed to be symmetric about the centre line of the pipe cross section (180 degree line in the plots). The angle subtended by the region with negative deviation is labeled as the extent of negative deviation, and is termed $\theta_{\text{neg dev}}$. By changing the equation constants, different curves with different magnitudes and varying extents of negative deviations can be produced. Figure 6.35 shows the sample plot of three thickness deviation models with different maximum magnitudes and extents of negative deviations. The solid line shows a thickness deviation curve with maximum magnitudes of -5.0% and +10.0%, with the extent of negative deviation being 120 degrees, i.e., the region with negative deviation subtends 120 degree angles to the centre of the cross section.

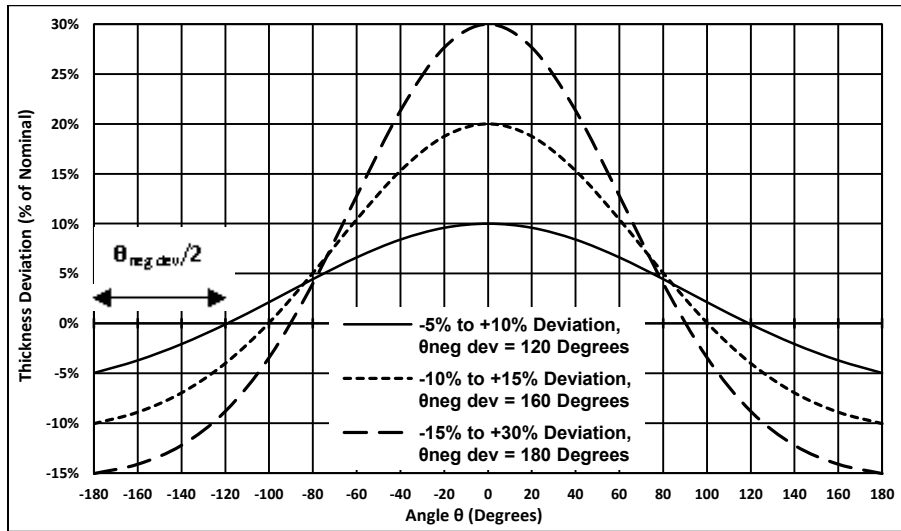


Figure 6.35 Sample plots of deviation from Equation 6-3 with different magnitudes and extents of deviation

6.6 Imperfections in the Longitudinal Direction

The OR and thickness deviation models developed and discussed so far are limited to the pipe cross section, with no variations in the longitudinal direction. It was previously reported in Chapter 4 that the OR deviation is consistent along the length of the pipes in all the studied specimens. Therefore, the variation of the OR deviation in the longitudinal direction will not be considered. The thickness deviations were also seen to be consistent within the measured length in all the specimens. The thickness deviations, however, were only measured from the end of the pipes up to 500 mm length inside, and it cannot be concluded if the deviations remain consistent throughout the full length of the specimens or if there is indeed some variations longitudinally. Therefore, the possibility of thickness variation in the longitudinal direction should be considered.

It is assumed that the shape of the cross sectional thickness deviation remains unchanged, while the magnitudes of the deviation vary longitudinally. With the thickness deviation model already developed, it is rather straight forward to impose the longitudinal variation over them. The longitudinal variation is assumed to be in the shape of a Cosine wave. The thickness is assumed to vary within 80% to 100% of the cross sectional thickness deviation in the longitudinal direction. Three types of hypothesised longitudinal variations are considered (Figure 6.36). Type 1 variation has 80% of the cross sectional deviation at the end of the pipe, reaches 100% at half length, then reduces to 80% at the other end of the pipe. Type 2 is an inversion of Type 1, with 100% at the two ends, and 80% at half length. Type 3 assumes two full waves with the cross sectional thickness deviation varying within 100% and 80% in every quarter length of the specimen. The longitudinal variation can be produced by simply multiplying Equation 6-3 with the following Cosine function:

$$\text{Longitudinal Variation} = 0.8 + 0.1 \left(1 + \cos \left(m\pi + \frac{n\pi\theta}{L} \right) \right) \quad 6-4$$

For Type 1, $m=1$, $n=2$; for Type 2, $m=2$, $n=1$; and for Type 3, $m=4$, $n=1$. L is the length of the pipe.

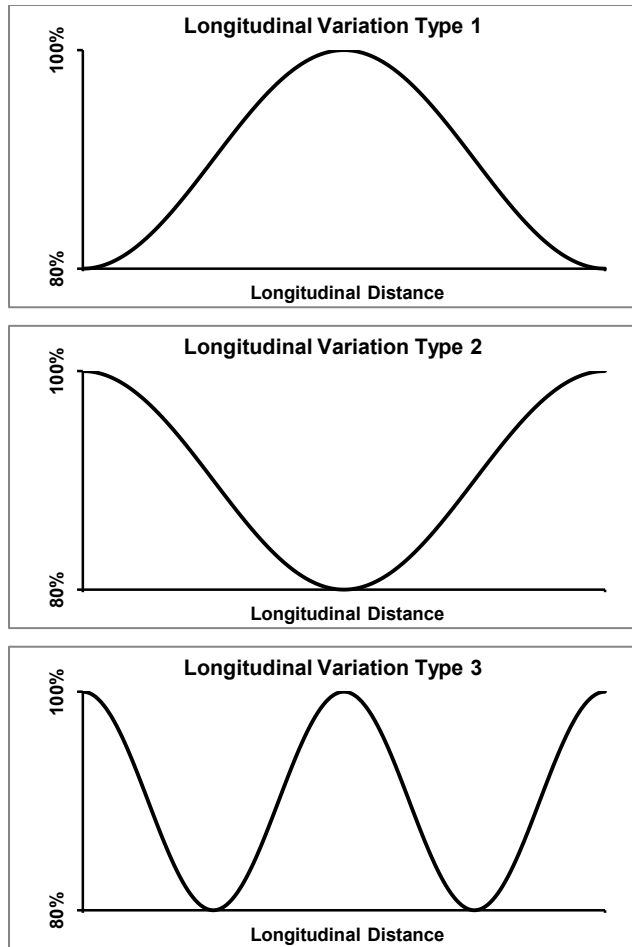


Figure 6.36 Assumed types of longitudinal variation of pipe wall thickness deviation

6.7 Conclusion

The UOE manufactured pipes show distinct patterns of OR and wall thickness deviation, which is different from pipes manufactured in a different process. The patterns of OR and wall thickness deviations have been characterized in this chapter. The possible sources of these geometric imperfections have also been traced back to the UOE manufacturing process. Through reverse engineering, it is concluded that the studied UOE manufactured pipe specimens were expanded using expansion mandrels with twelve segments, which resulted in the wavy shape of the pipe cross sections. The expansion process is also the most likely source of the reduction of pipe wall thickness near the longitudinal seam weld.

Based on the characterization of the OR deviations, two OR deviation models for UOE manufactured pipes have been developed. The OR deviation models include one fine model capable of capturing the actual imperfect shape of the pipe cross sections, and one coarse model which only considers the maximum and minimum measure OD and assumes that the imperfect shape of the pipe cross section is elliptical.

A thickness deviation model for the UOE manufactured pipe has been developed. This model is a Gaussian Function capable of capturing the measured maximum positive and negative deviations, as well as the extent of negative deviation, i.e., the angle subtended by the region with negative deviation to the centre of the cross section. The model can be used to perform a parametric study on the buckling response of pipes. Three types of assumed longitudinal variation of thickness have also been proposed, which will be imposed on the cross sectional thickness deviations.

The OR and thickness deviation model will be incorporated into a Finite Element Analysis model to study the effects of these geometric imperfections on the buckling response of the pipes in the following chapter.

CHAPTER 7: EFFECTS OF INITIAL GEOMETRIC IMPERFECTIONS ON PIPE BUCKLING

7.1 Introduction

In the previous chapter, the geometric imperfection models corresponding to OR deviation and pipe wall thickness deviation have been developed. These models have been developed based on the measurement of the imperfections previously presented in Chapter 4. The models are based on the worst observed cases in the measurement results. The severity of the influence of these imperfections on pipes' buckling behaviour cannot be anticipated based on their magnitudes alone. The individual effects of these imperfections need to be studied to identify which imperfections are more important to be considered in the design of pipes against buckling. The combined effect of these imperfections should also be investigated in order to understand the interaction between them.

Finite Element Analysis (FEA) is a powerful tool for investigating structural behaviour in the absence of full scale tests. Several FEA software packages are available commercially. In this chapter, the effects of the geometric imperfections on the buckling behaviour of pipes will be investigated using the Finite Element Analysis software ABAQUS.

In the first part of this chapter, a general description of the FEA model will be presented. The FEA model of an ideal NPS 42 inch pipe with constant OD and 14.275 mm wall thickness will then be analyzed with three different material properties. The material properties are obtained from coupon test results reported by Neupane et al. (2012). The findings of Neupane et al. (2012) will be verified, and the buckling capacity corresponding to an anisotropic material model developed by Neupane et al. (2012) will be considered as a reference. All FEA models hereafter will be analyzed with the anisotropic material model.

The geometric imperfection models will be imposed on the ideal NPS 42 inch pipe model individually and in combinations to study their effects. The sensitivity of these imperfection models will also be studied by imposing them on the NPS 42 inch ideal pipe model, looking at both ovalization and thickness deviation. Finally, the applicability of these imperfection models will be investigated through

a parametric study on pipes with three different D/t ratios. The organization of the FEA models throughout this chapter is summarized in Figure 7.1:

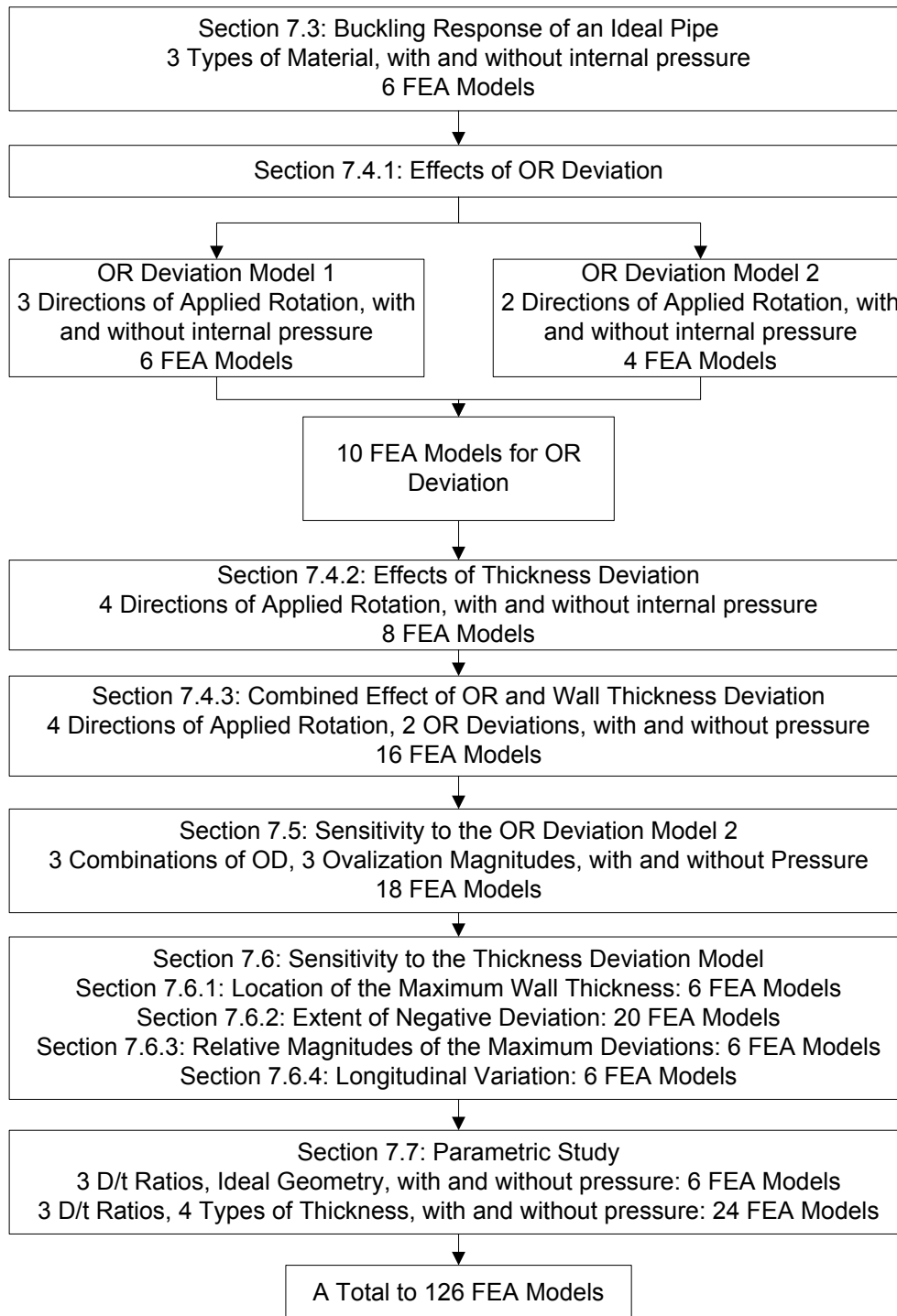


Figure 7.1 Organization of FEA models

7.2 FEA Model

7.2.1 Geometry, Mesh, and Element

A cylindrical shell is considered to be “Thin Walled” if its radius is at least 20 times its wall thickness (Novozhilov, 1964). In terms of D/t ratio, a pipe with a D/t ratio of 40 and higher can be considered as a thin walled cylindrical shell. The UOE manufactured pipes measured in this study had D/t ratios ranging from 74.75 to 103.47, and therefore can be considered as thin walled cylindrical shells. Consequently, in the FEA, the pipe geometry is modeled as a 3D deformable shell.

The cross section of the pipe is first sketched in ABAQUS. For an ideal pipe, the cross section is simply a circle with a radius equal to the nominal OR of the pipe. In case of the pipes with variable radii, two radii deviation models developed in Chapter 6 are used. The OR Deviation Model 1 was developed by fitting an interpolating cubic spline to the highest and lowest amplitude points of the OR deviation data. The coordinates of these control points are first calculated, and then input into the sketch. A cubic spline is then fitted to these control points, which results in a pipe cross section with varying radii corresponding to the OR Deviation Model 1.

The OR Deviation Model 2 was in the form of an ellipse, and its corresponding pipe cross section was sketched by specifying an ellipse with the measured maximum and minimum diameter values. The OR and thickness deviation were defined in terms of the location of the longitudinal seam weld. To ensure conformity of the two models, a fixed convention for the orientation of the cross section with respect to the Cartesian coordinate system has to be maintained.

The centre of the cross section is defined to be at the origin of the Cartesian coordinate system. The positive Y axis points towards the location of the longitudinal seam weld, and the Z axis is considered to be the longitudinal axis of the pipe. The cross sections of the pipes with and without radii variation are then extruded along Z to a length of 2.5 OD. The orientation of the pipe cross section is shown in Figure 7.2:

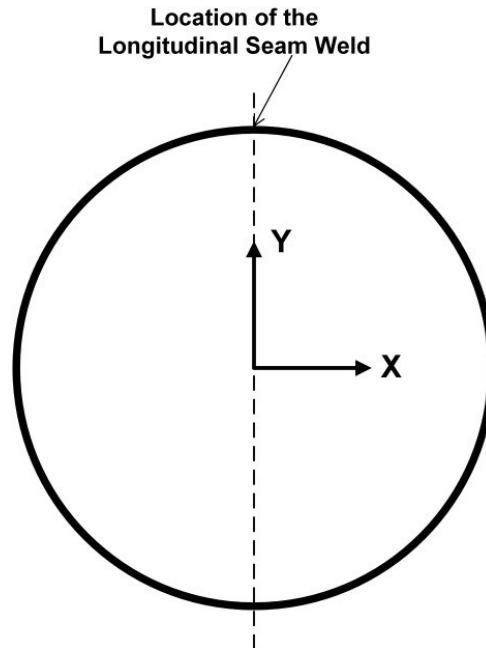


Figure 7.2 Orientation of pipe cross section with respect to the Cartesian Coordinate system

In finite element analysis, the size of mesh is an influential aspect regarding the accuracy of results and computation time. A fine mesh is always computationally demanding while superior in accuracy. On the other hand, a coarse mesh will reduce the computation time at the cost of reduced accuracy. For the optimum performance of an FEA model, a mesh size needs to be selected that reduces the computation time while preserving sufficient accuracy of the results. It has been reported previously that 40 quadrilateral elements around half of a pipe's circumference with an aspect ratio smaller than 2.0 results in an optimum performance (DelCol et al., 1998; Dorey et al., 2001). The mesh size for this study is selected to be finer than this recommendation to be on the conservative side. For the NPS 42 inch pipes, the mesh size is chosen to be 30 mm with an aspect ratio of less than 1.0, which results in 112 elements around the pipe's circumference (56 elements around half of the circumference). For the NPS 34 inch pipes, the mesh size is chosen to be 25 mm with an aspect ratio of less than 1.0, resulting in 109 elements around the circumference. The generated mesh for the model of an NPS 42 inch pipe is shown in Figure 7.3:

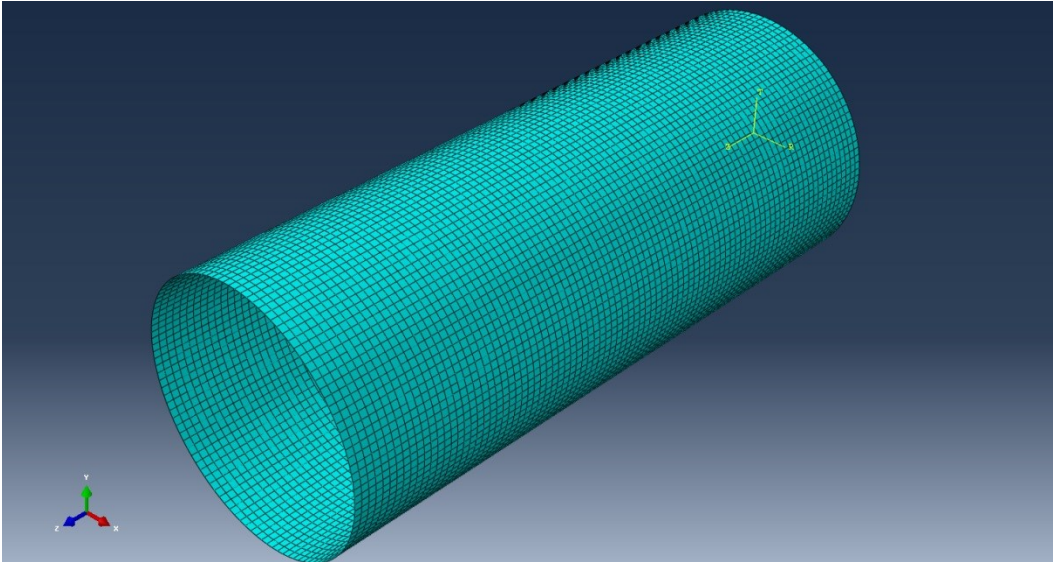


Figure 7.3 Mesh generated in ABAQUS corresponding to an NPS 42 inch pipe model

The selection of an appropriate type of element is another important aspect in finite element analysis. There are several types of elements available in the element library in ABAQUS. The element “S4R” is a 4-node doubly curved quadrilateral reduced integration element with hourglass control, which is applicable to both thin and thick shell structures (Hibbit, Karlsson, & Sorenson, Inc., 2003). The element nodes have three translational and three rotational degrees of freedom. They adopt finite-membrane-strain-formulation, which can account for shell thickness reduction. This particular type of element is capable of modeling large deformations typically observed in the buckling behaviour of pipes, while being computationally less demanding due to its reduced integration scheme. S4R elements are therefore deemed appropriate and selected for this finite element study.

The OR deviation models were developed considering the measured outside radii of the pipes. The thickness deviation model was developed based on the measured distance between the outside and inside surfaces of the pipes. The shell thickness in the FEA model is therefore defined from the top surface. This results in a pipe geometry that is representative of the measured OR and thickness deviations. For an ideal pipe, a shell thickness equal to the pipe’s specified wall thickness is assigned. For pipes with thickness deviation, the shell thickness needs to be assigned according to the equation corresponding to the

thickness deviation model. ABAQUS has the capability of defining shell thicknesses as a variable through analytical expressions. In order to ensure the compatibility of the thickness deviation model with the orientation of the OR deviation, an appropriate coordinate system has to be employed. The thickness deviation model was developed based on a cylindrical coordinate system, where 0 and 360 degree angles corresponded to the location of the longitudinal seam weld. The input parameter of the equation was the angle of any point on the pipe's circumference. A cylindrical coordinate system with appropriate orientation is therefore used to assign the thickness deviation model to the pipe. ABAQUS uses a cylindrical coordinate system in terms of the parameters: R , θ , Z , where R is the radial distance, and θ is the angle evaluated in radians from $-\pi$ to π . The cylindrical coordinate system is oriented with the coordinate origin at the centre of the pipe, the R axis pointing towards the location opposite to the seam weld (along negative Y axis), the θ axis along negative X axis, and the Z axis aligned with the longitudinal axis of the pipe.

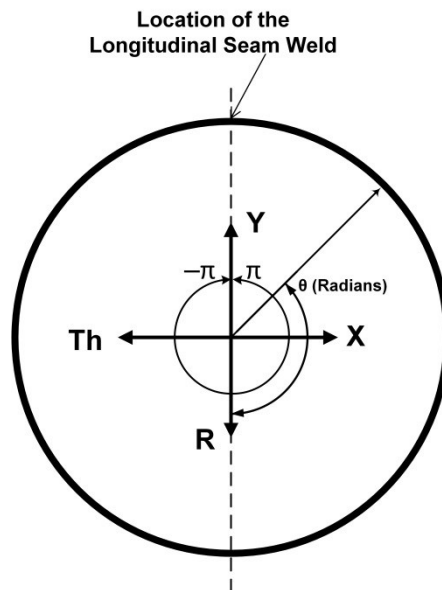


Figure 7.4 Cylindrical Coordinate system adopted for assigning the thickness deviation model

The thickness deviation model is then assigned in the form of an analytical expression in terms of this cylindrical coordinate system. This particular orientation of the cylindrical coordinate system establishes the conformity of the wall thickness deviation model with the OR deviation model (Figure 7.5).

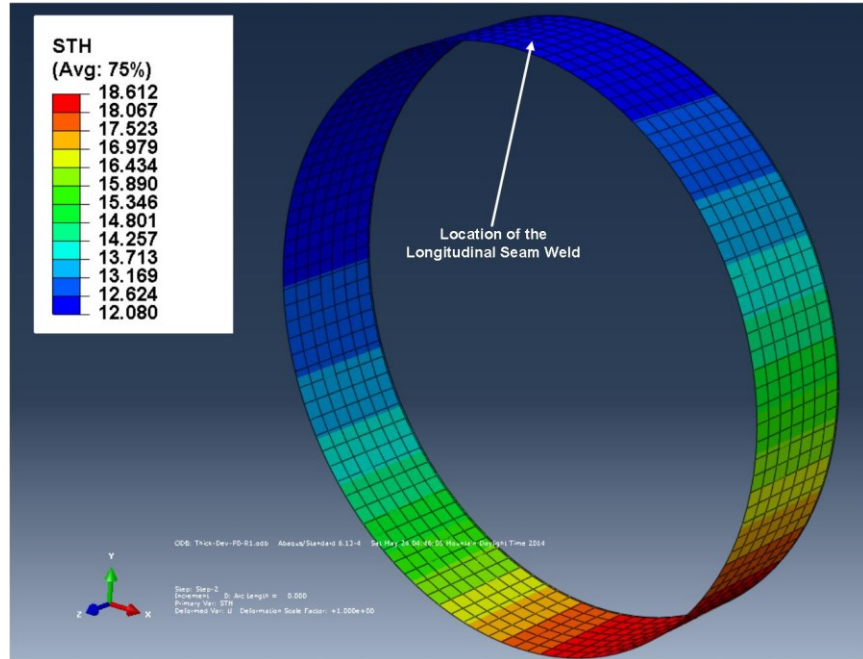


Figure 7.5 Shell thickness deviation spectrum and its orientation

7.2.2 Anisotropic Material Model

UOE manufactured high strength steel pipes show plastic anisotropy, where the stress strain response of the pipe material is different along the longitudinal and circumferential directions. A coupon obtained from the circumferential direction and tested in tension shows a higher yield point than a coupon obtained from the longitudinal direction and tested in tension. The stress strain curves obtained from tension coupon tests of an HSS UOE pipe are shown in Figure 7.6. Neupane et al. (2012) showed that for an accurate prediction of the buckling response of high strength steel pipes under the combined effects of internal pressure and bending moment, a material model capable of imitating this anisotropic behavior is required for the Finite Element Analysis.

The material model developed for X100 pipes by Neupane et al. (2012) is used in this study. The model was based on tension coupon test data. The tension coupons were obtained from an X100 pipe of 762 mm OD and 12.7 mm wall thickness. An analytical virgin material curve was first developed from the circumferential stress strain data obtained from the tension test. Armstrong-Frederick law was chosen for backstress evolution. The material parameters corresponding to the specific pipe, as optimized and presented by Neupane et al. (2012) are used to calculate the values of backstress at different plastic strain

values. The assumed virgin material curve, the parameters, and the backstress values along with the Elastic Modulus and Poisson's ratio altogether define the anisotropic material model.

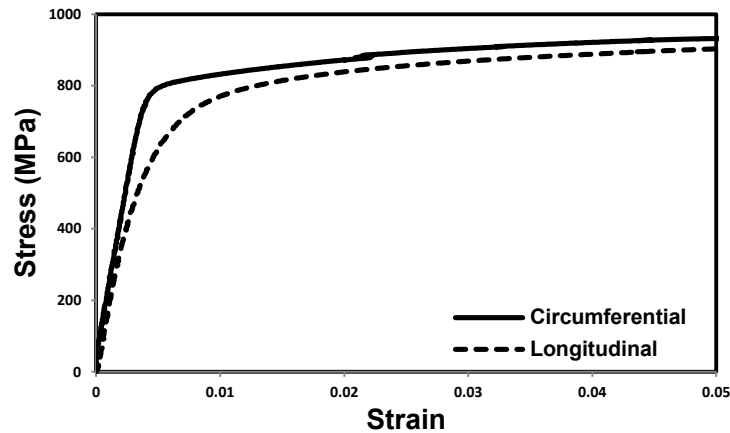


Figure 7.6 Plastic Anisotropy in HSS UOE pipe material (Neupane et al., 2012)

The material model is input into ABAQUS to verify the expected anisotropic behavior. Two methods are applied for this purpose. First, the material model is assigned to a single four node, rectangular, plane stress shell element. To simulate the expansion process during manufacturing, an initial condition is introduced to the model. 2% plastic strain and the corresponding backstress value from Armstrong-Frederick law are assigned as initial conditions in the circumferential direction. The element is then loaded in the longitudinal and circumferential directions separately to observe its stress strain response in each direction.

Next, the material model is assigned to a 3D cylindrical shell of S4R elements representing a pipe of 1067 mm OD, along with the initial conditions simulating the expansion process. The cylindrical coordinate system previously employed for the thickness deviation model is used to define a specific material orientation of the shell elements. Axis 1 is oriented along the circumferential direction, Axis 2 along the longitudinal direction, and the third axis along the radial direction. 2.0% plastic strain and the corresponding backstress value from Armstrong-Frederick law are then assigned as initial conditions in the circumferential direction (Axis 1). The cylinder is then loaded in the longitudinal and circumferential directions

separately by applying axial tension and internal pressure respectively. The stress strain responses of an element on the pipe in each direction are then observed. The stress strain curves from tensile tests (Neupane et al., 2012) and FEA results are shown in Figure 7.7. The stress strain response obtained from the FEA is seen to be very accurate. It is capable of producing the different behaviours in the two directions of loading. The responses from FEA closely resemble the responses obtained from the tension coupon tests. This material model is deemed appropriate for the buckling analysis.

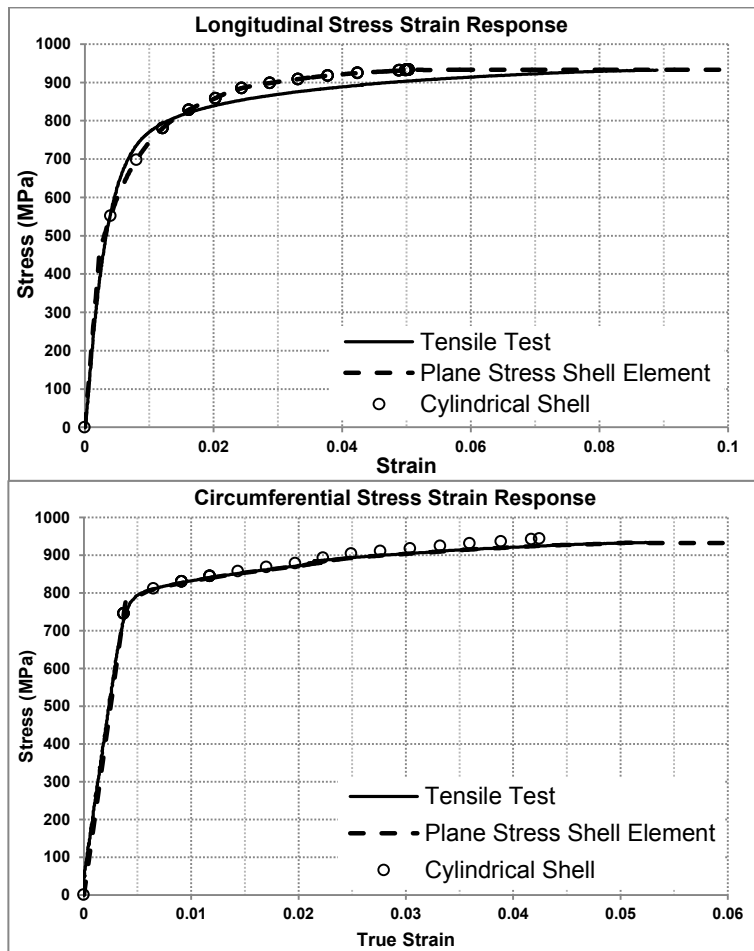


Figure 7.7 Stress Strain responses along the longitudinal and circumferential directions obtained from tension coupon test and FEA

7.2.3 Applied Boundary Conditions, Load and Rotation

Symmetry boundary condition is assigned to one end of the pipe in order to reduce computation time. The pipe was previously extruded to a length of 2.5

OD, and the application of the Z-Symmetry boundary condition (symmetry across the X-Y plane) results in a model that will simulate the buckling behaviour of a pipe with a length of 5 OD. At the other end of the pipe a reference point is created at the centre of the pipe cross section. The element nodes at this pipe end are constrained to the reference point. The reference point is then restrained from all translations and rotations except for translation along the Z-axis (pipe axis), and rotation about either X-axis or Y-axis depending on the direction of the applied end rotation. These applied boundary conditions enable the end of the pipe to rotate about X or Y axis and translate along Z axis.

It should be noted that the Z-Symmetry boundary condition applied to the pipe end element nodes restricts their rotational degrees of freedom in all directions, and can only capture the symmetric buckling mode. The phenomenon is shown through an idealized representation in Figure 7.8:

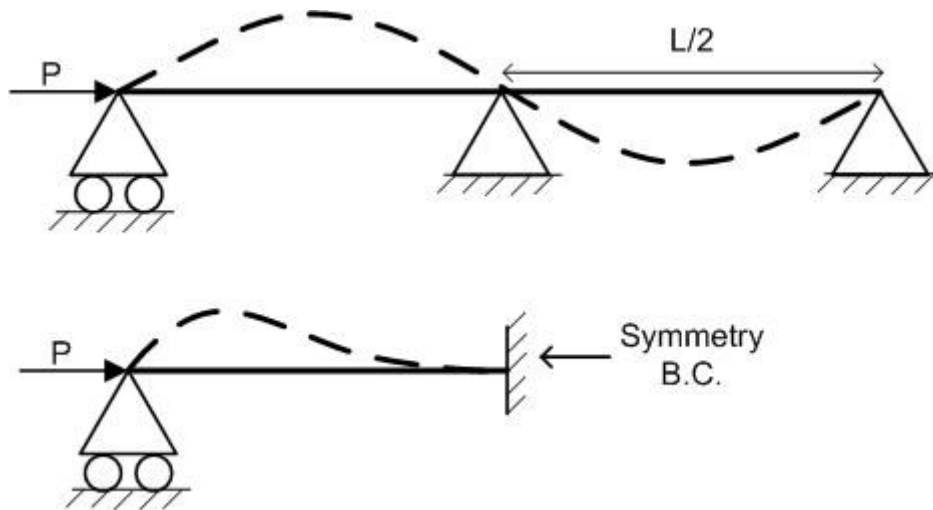


Figure 7.8 Idealized representation of symmetry boundary condition

The beam shown in Figure 7.8 is under axial compression with a pin support at mid span. When an axial compressive load is applied, the buckling mode of the beam will not be symmetric for these particular boundary conditions. The application of symmetry implicates considering only half of its length, and restraining the rotation at mid span. As a result, the buckling mode of the beam with the symmetry boundary condition is symmetric, and is different from the original beam. Based on this analogy, it is evident that applying the Z-Symmetry

boundary condition to the FEA models of the pipes will restrict their buckling to the symmetric buckling mode.

Different types of constraints are available in ABAQUS. A rigid body constraint, which constrains the motion of the nodes at the pipe end to the motion of the reference point, is generally deemed appropriate for buckling analysis. However, this type of constraint also restricts the nodes from translating along the radial direction of the pipe. As a result, upon the application of internal pressure, the stress field at the pipe end gets distorted from a uniform stress distribution. This also results in a bulge shape at the pipe end, and a pressurized pipe, instead of buckling at mid length, buckles at the end.

A kinematic coupling constraint is seen to be able to overcome this complication. This specific type of constraint allows for the direction of constraints along the coordinate axes to be specified. The cylindrical coordinate system previously assigned to the model is again used for the constraint definition. The nodes are allowed to translate along the radial direction (R-axis) with respect to the reference point, and all other translational and rotational degrees of freedom are restricted. The kinematic coupling constraint assigned in this method permits the end of a pressurized pipe to expand in the radial direction throughout the arbitrary rotation applied to the reference point, which results in a uniform stress field and the pipe buckles at mid length. This phenomenon will be shown at a later part of this chapter.

Internal pressure corresponding to a hoop stress of 80% of the SMYS is applied to the inside surface of the pipe in order to study the buckling behaviour of pressurized pipes. The internal pressure value is calculated according to the equation:

$$0.8 \text{ SMYS} = P \cdot D / 2t_{\text{specified}} \quad 7-1$$

Here, D is the pipe diameter, and $t_{\text{specified}}$ the specified wall thickness. CSA Z662-11 specifies that D should be taken as the outside diameter according to Barlow formula, which produces slightly conservative values of internal pressure. Using the inside diameter will result in higher internal pressure. This study involves pipes with high D/t ratios, and the differences in the internal pressure value from

using either diameter will be small. Consequently, the average diameter is used for the internal pressure calculations through this chapter.

The buckling analysis is performed using Riks method, where a finite rotational displacement is applied to the reference point. Due to the applied symmetry boundary condition, the relative rotation between the two ends of the full length of the pipe (5 OD) is twice as much as the applied rotation. The directions of the applied rotations are denoted R_x , R_{-x} , R_y , and R_{-y} , where the subscript indicates the axis around which a positive rotation is applied. Therefore, an applied rotation of R_{-x} indicates compression at the location of the seam weld in the pipe cross section (Figure 7.2). The results of the buckling analysis are reported in terms of Moment Vs Rotation (M-R) curves corresponding to different directions of applied rotation.

The buckling capacity of a pipe is generally expressed in terms of its critical buckling strain. The critical buckling strain corresponds to the longitudinal compressive strain developed in a pipe at the onset of buckling. Dorey et al. (2001) undertook an extensive experimental program on the critical buckling capacity of line pipes at the University of Alberta. Their experimental results confirmed that the local moment curvature response of a pipe is identical to the global moment curvature response prior to buckling. They concluded that there are two linear relationships between the local and global strains corresponding to the pre-buckling and post-buckling regions, and the local strain at the intersecting point indicates the critical buckling strain.

The objective of the buckling analysis through FEA is to quantify the relative changes in a pipe's behaviour corresponding to the introduction of geometric imperfections. Based on the above discussion, it is decided that the peak end moment and its corresponding critical end rotation (CER) from the global Moment-Rotation (M-R) response of the pipe is an acceptable output parameter for the purpose of this study. Changes in peak moment and CER in excess of 2% of an ideal pipe's response will be considered as significant in this study.

7.3 Buckling Response of an Ideal Pipe

The dimensions of an NPS 42 inch pipe with a specified wall thickness of 14.275 mm are selected for the buckling analysis of an ideal pipe. The pipe is analysed

with and without the application of internal pressure. The internal pressure corresponding to 80% of SMYS is calculated to be 15 MPa according to Equation 7-1.

In the numerical analysis of pipe buckling, a small geometric imperfection is usually introduced in order to trigger buckling at the middle of the pipe. In this study, no such imperfection was introduced to initiate buckling. A rigid body constraint applied to the end of the pipe results in the development of a bulge near the pipe end upon the application of internal pressure. The application of end rotation to the pressurized pipe leads to a buckling failure at the end of the pipe model (Figure 7.9 a). This issue is resolved by applying a kinematic coupling constraint to the pipe end, and allowing the pipe to expand in the radial direction. As a result, the bulge no longer appears after applying internal pressure, and the pipe buckles in the middle when end rotation is applied, despite the absence of any imperfection to initiate buckling (Figure 7.9 b).

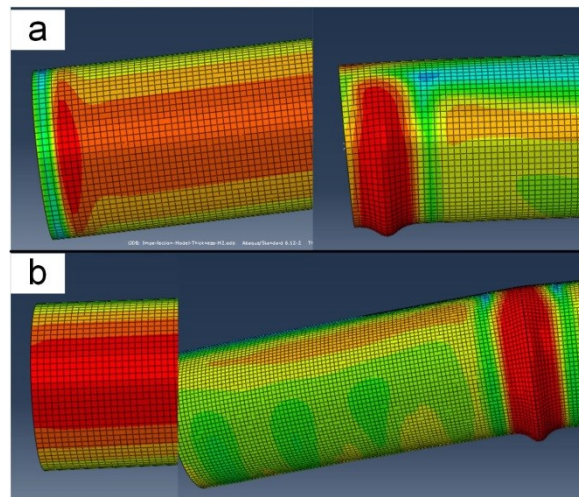


Figure 7.9 Von Mises stress distribution after applying internal pressure and the location of buckle after applying rotation using a) Rigid Body Constraint, and b) Kinematic Coupling Constraint

From the FEA results, it is observed that the pipe without internal pressure buckles in diamond shape, where the pipe wall buckles inwards at mid length. The pressurized pipe on the other hand buckles in bulge shape, with the pipe wall protruding outwards at mid length. The buckled shapes of unpressurized and pressurized ideal pipe are shown in Figure 7.10:

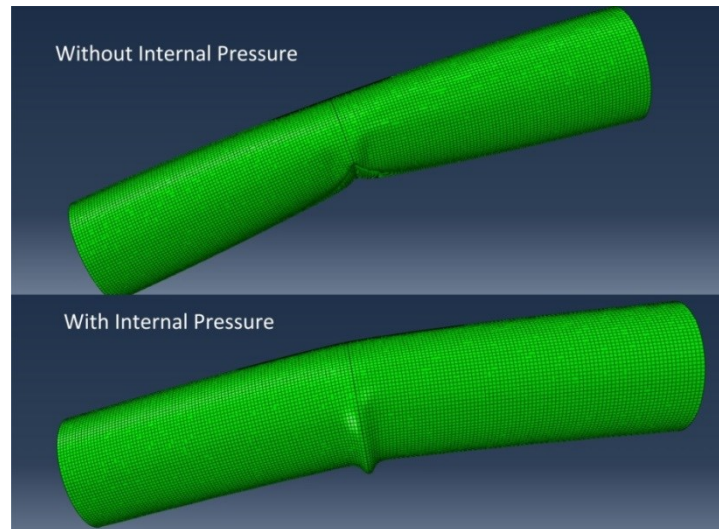


Figure 7.10 Buckled shape of an ideal pipe with and without internal pressure

The pipes are analyzed using three material models: anisotropic according to Neupane et al., (2012), isotropic corresponding to longitudinal stress strain, and isotropic corresponding to circumferential stress strain, to verify their effects. The anisotropic material is the combined isotropic-nonlinear kinematic hardening model previously developed by Neupane et al., (2012). The isotropic with longitudinal stress strain is an isotropic hardening model generated from the stress strain data obtained from the tensile test of a coupon from the longitudinal direction of a UOE pipe reported by Neupane et al., (2012). The isotropic with circumferential stress strain is another isotropic hardening model, that is generated from the stress strain data obtained from the tensile test of a coupon from the circumferential direction of a UOE pipe reported by Neupane et al., (2012). The moment rotation responses of unpressurized and pressurized pipes corresponding to these three material models are shown in Figure 7.11. It is observed that for both unpressurized and pressurized conditions, the response corresponding to the anisotropic material is between the two responses corresponding to the two isotropic material models. For unpressurized condition, the longitudinal isotropic material model's response is comparatively closer to the

anisotropic material model's response, where the peak moment is reduced by 1.1% and the CER is increased by 20.83% of the anisotropic material model's response. The isotropic circumferential material model results in a higher range of linear elastic behaviour, increased peak moment (6.75% of the anisotropic model's response) and reduced CER (32.32% of the anisotropic model's response). Both isotropic models' responses start to diverge from the anisotropic model's response at an end moment of approximately 6000 kN-m.

For the pressurized pipes, it is observed that the circumferential isotropic model's response is closer to the anisotropic material model's response. where the peak moment is increased by 3.04% and the CER is reduced by 12.09% of the anisotropic material model's response. The isotropic longitudinal material model's response is seen to have diverged from the anisotropic response in the entire range of loading, with a 9.88% increase in the CER.

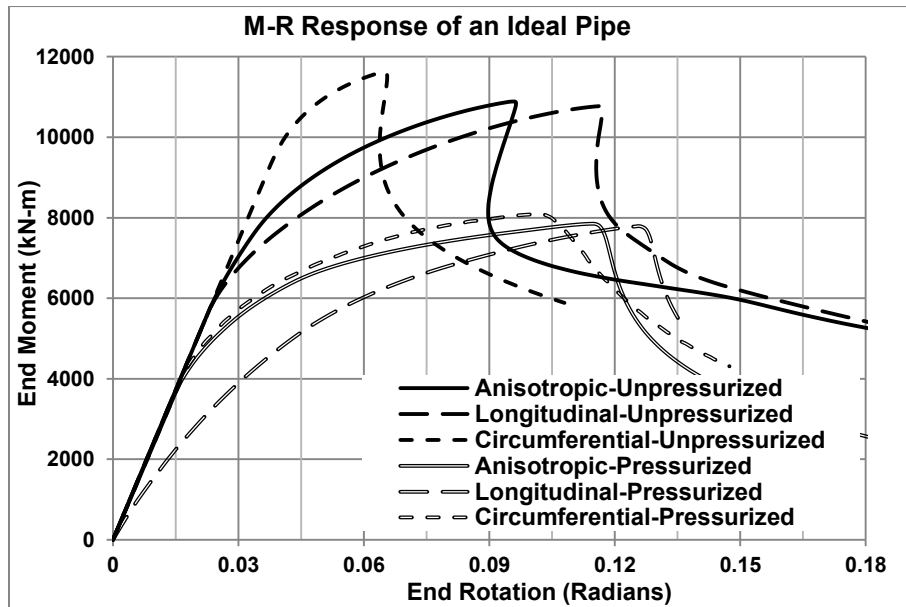


Figure 7.11 Moment-Rotation response of an NPS 42 inch ideal pipe with 14.275 mm specified wall thickness

From the responses corresponding to the anisotropic material model, it is observed that the pipe without internal pressure attains a peak end moment of 10887 kN-m and a corresponding CER of 0.0959 radians (5.5 degrees). The pipe with 15 MPa internal pressure (corresponding to a hoop stress of 80% of the SMYS) attains a peak end moment of 7851 kN-m and a corresponding CER of

0.1146 radians (6.57 degrees). The qualitative changes in behaviour corresponding to the three different material models agree with the findings of reported by Neupane et al., (2012). The peak end moment and its corresponding CER value corresponding to the anisotropic material model is considered as a reference for the purpose of comparing changes in the buckling capacity upon the introduction of the geometric imperfection models in the following sections.

7.4 Effects of the Geometric Imperfections on Buckling Response

7.4.1 Effects of OR Deviation

The two OR Deviation Models (OR Deviation Model 1 and 2) are incorporated into the FEA model of the ideal pipe. The wall thickness is kept to a constant value of 14.275 mm to observe the effect of the measured OR deviations alone. OR Deviation Model 1 produces a cross section that is symmetric about the Y-axis, but asymmetric about the X-axis. To investigate the behaviour of a pipe with OR Deviation Model 1, end rotation is applied in three directions, R_x , R_{-x} , and R_y . The M-R responses are shown in Figure 7.12 and Figure 7.13. In both unpressurized and pressurized conditions, the responses corresponding to the three directions of rotation are seen to be identical up to the onset of buckling, and diverge slightly in the post buckle stage.

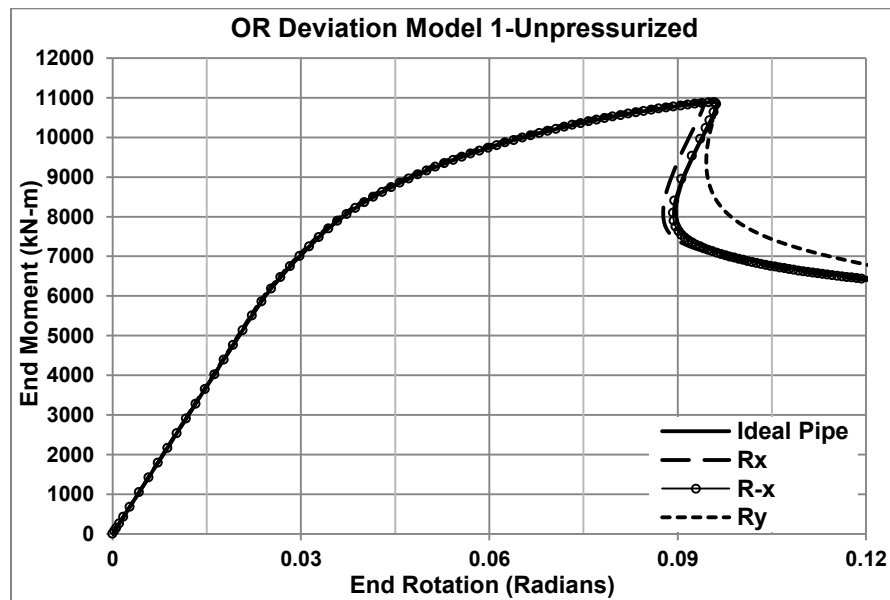


Figure 7.12 M-R responses of unpressurized pipe with OR Deviation Model 1

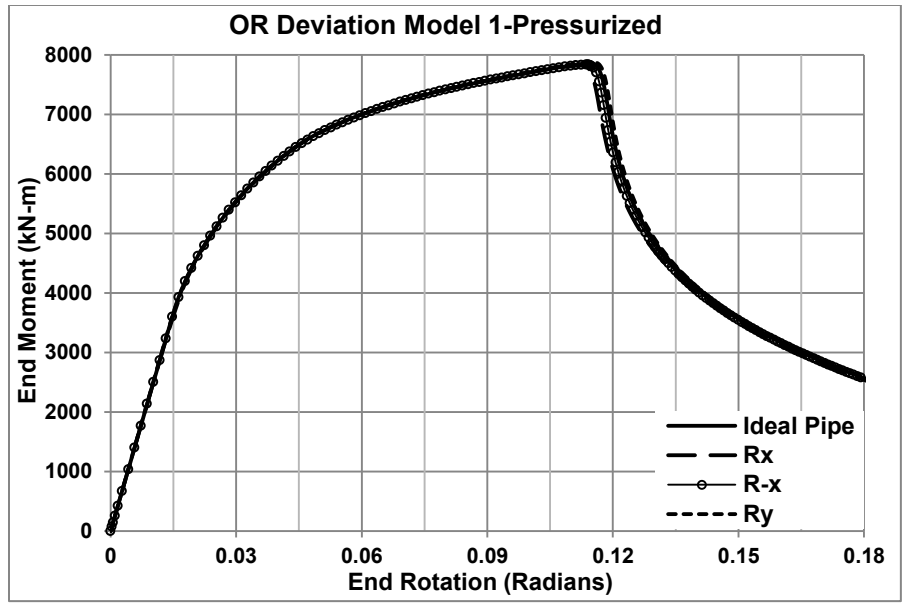


Figure 7.13 M-R responses of pressurized pipe with OR Deviation Model 1
 The OR Deviation Model 2 produces an ellipse, and is symmetric about both the X and Y axes. Therefore only R_x and R_y are applied for the buckling analysis of a pipe with OR Deviation Model 2. The M-R responses are as follows:

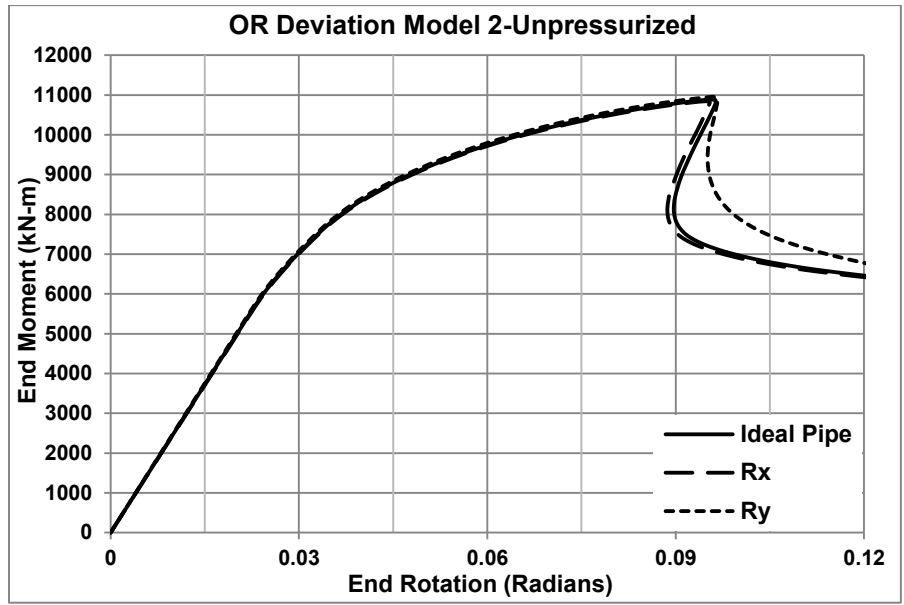


Figure 7.14 M-R responses of unpressurized pipe with OR Deviation Model 2

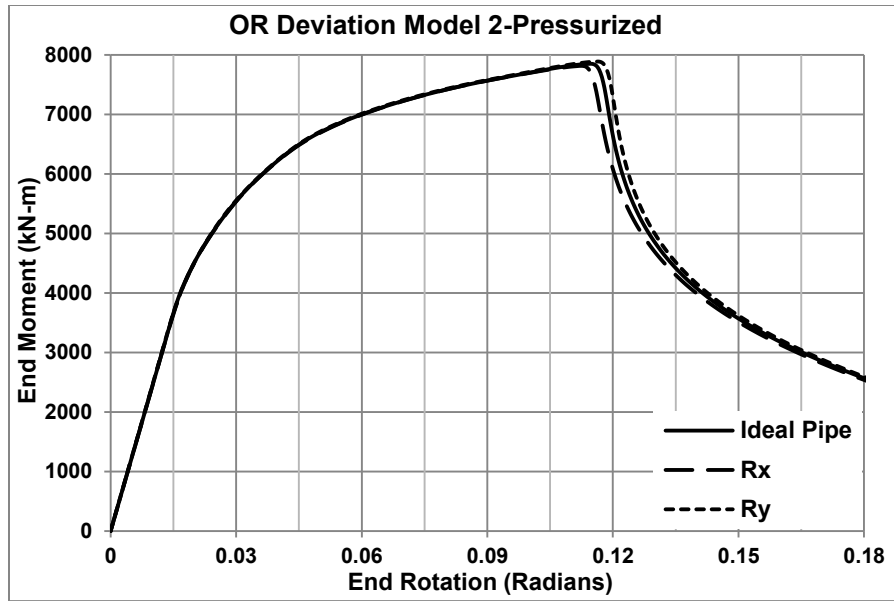


Figure 7.15 M-R responses of pressurized pipe with OR Deviation Model 2

Table 7.1 Peak Moment and CER values corresponding to the OR deviation models

OR Deviation Model 1					
	Direction Of Rotation	Peak Moment (kN-m)	Difference (% Ideal)	CER (Radians)	Difference (% Ideal)
Without Pressure	R _x	10847	-0.36%	0.0936	-2.51%
	R _{-x}	10882	-0.05%	0.0949	-1.09%
	R _y	10939	0.48%	0.0958	-0.11%
With Pressure	R _x	7824	-0.35%	0.1126	-1.83%
	R _{-x}	7835	-0.20%	0.1139	-0.70%
	R _y	7877	0.33%	0.1153	0.51%
OR Deviation Model 2					
	Direction Of Rotation	Peak Moment (kN-m)	Difference (% Ideal)	CER (Radians)	Difference (% Ideal)
Without Pressure	R _x	10845	-0.39%	0.0948	-1.18%
	R _{-x}	-	-	-	-
	R _y	10954	0.62%	0.0961	0.10%
With Pressure	R _x	7816	-0.44%	0.1125	-1.85%
	R _{-x}	-	-	-	-
	R _y	7889	0.48%	0.1163	1.44%

The peak end moment and corresponding CER values obtained from analysing the two OR deviation models are listed in Table 7.1. The differences with respect to the peak moment and CER of the ideal pipe are also listed. It is observed that the introduction of OR deviation has insignificant effects on the pipe's behaviour.

7.4.2 Effects of Wall Thickness Deviation

The wall thickness deviation model produces a thickness deviation that is asymmetric about both the X and Y axes. Therefore, end rotations were applied in all four directions. The M-R responses are shown in Figure 7.16 and Figure 7.17:

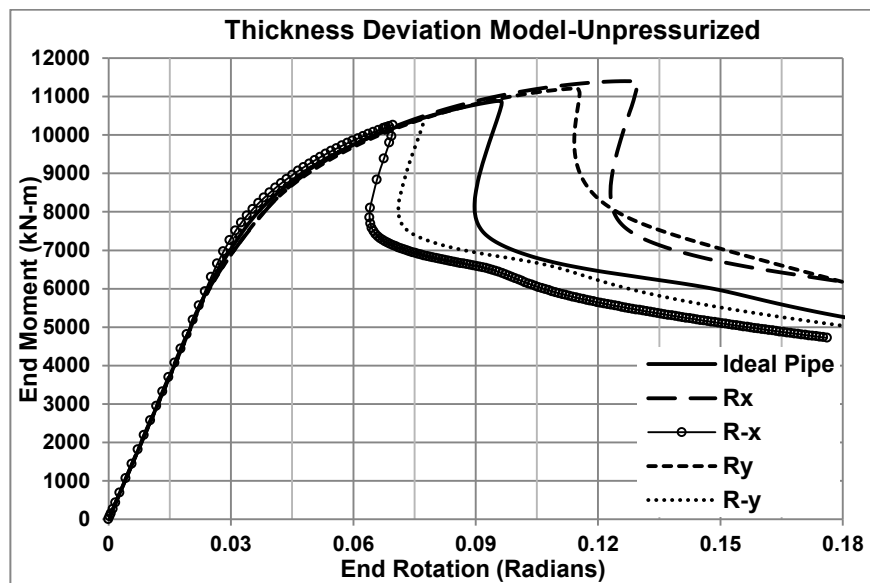


Figure 7.16 M-R responses of unpressurized pipe with Thickness Deviation

From the responses of the unpressurized pipe, it is observed that the applied compression in the region of the pipe cross section with reduced wall thickness reduces the peak moment and the CER and the applied compression in the increased wall thickness region increases the peak moment and the CER. The responses corresponding to R_x and R_y are higher than the ideal while those corresponding to R_x and R_y are lower. The responses in the pre and post buckling stages assume similar shapes in all cases with the initial part of the curves overlapping with each other. For the pressurized pipes, it is observed that the changes in wall thickness not only affect the peak moments and CER, but also changes the range of the linear portion of the responses. The response

corresponding to compression at reduced thickness (R_x) ceases to be linear around an end moment of approximately 2500 kN-m and an end rotation of 0.01 radians, whereas the ideal response remains linear up to approximately 4000 kN-m of end moment and 0.02 radians of end rotation. For an applied rotation of R_x , the response is linear up to approximately 6000 kN-m of end moment and 0.026 radians of end rotation.

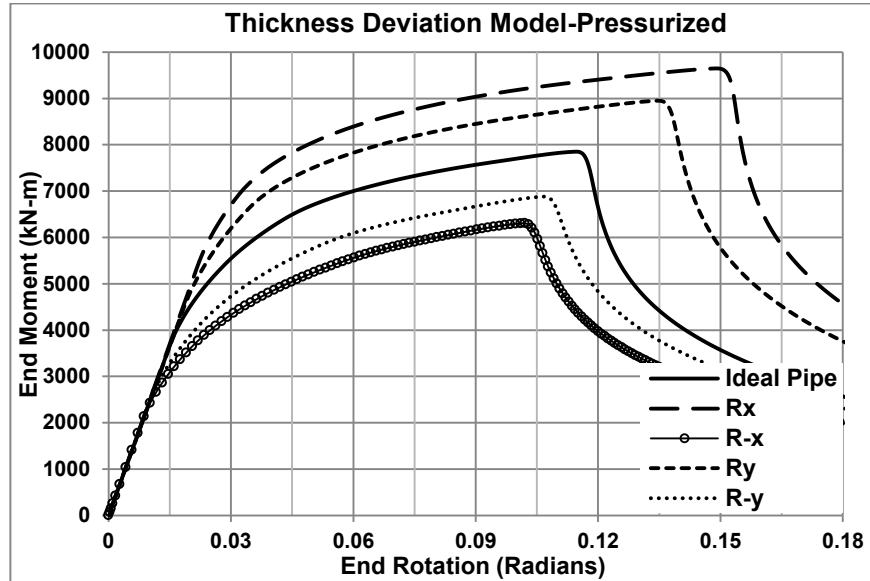


Figure 7.17 M-R responses of pressurized pipe with Thickness Deviation

Table 7.2 Peak Moment and CER values corresponding to the thickness deviation model

Wall Thickness Deviation Model					
	Direction Of Rotation	Peak Moment (kN-m)	Difference (% Ideal)	CER (Radians)	Difference (% Ideal)
Without Pressure	R_x	11401	4.72%	0.1271	32.41%
	R_x	10254	-5.81%	0.0697	-27.32%
	R_y	11211	2.97%	0.1141	18.89%
	R_y	10411	-4.37%	0.0768	-20.01%
With Pressure	R_x	9647	22.88%	0.1488	29.76%
	R_x	6305	-19.69%	0.1021	-11.00%
	R_y	8950	14.00%	0.1345	17.30%
	R_y	6880	-12.37%	0.1064	-7.24%

From Table 7.2 it is observed that the CER decreases by 27.32% in the unpressurized condition, and the peak moment decreases by 19.69% in the pressurized condition corresponding to an applied rotation of R_x . The effect of introducing wall thickness deviation is therefore considered significant.

7.4.3 Combined Effect of OR and Wall Thickness Deviation

The wall thickness deviation model is combined with the two OR deviation models separately. The M-R responses are shown in the following figures:

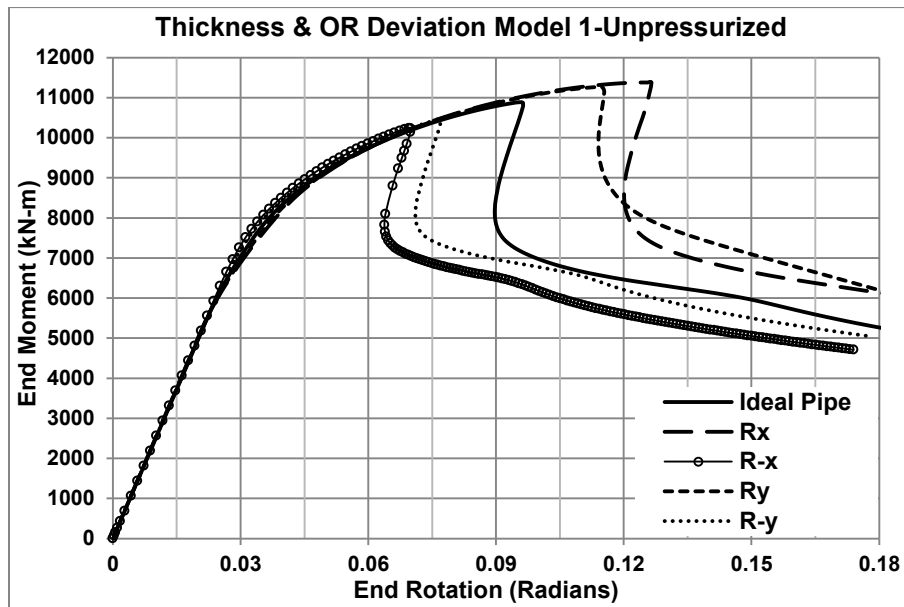


Figure 7.18 M-R responses of unpressurized pipe with Thickness Deviation and OR Deviation Model 1

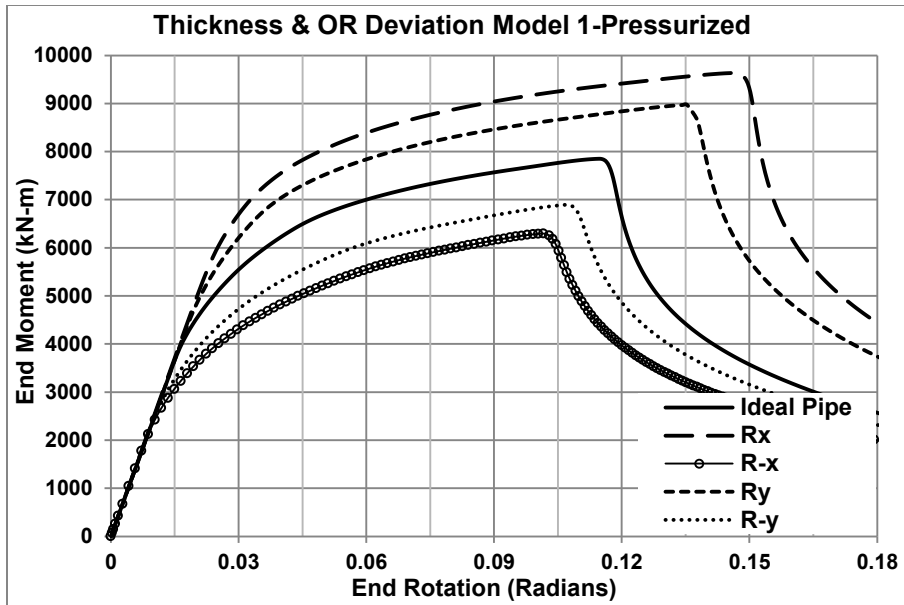


Figure 7.19 M-R responses of pressurized pipe with Thickness Deviation and OR Deviation Model 1

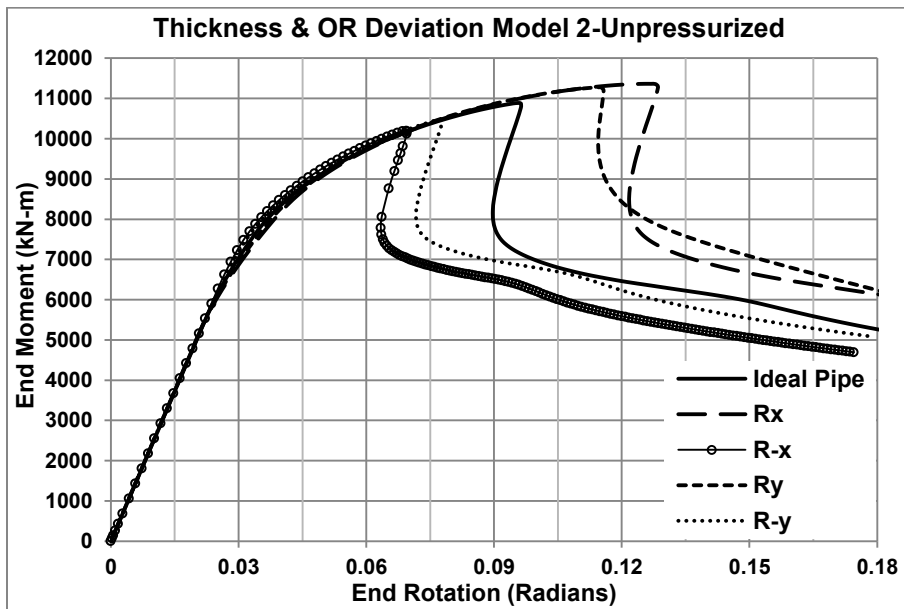


Figure 7.20 M-R responses of unpressurized pipe with Thickness Deviation and OR Deviation Model 2

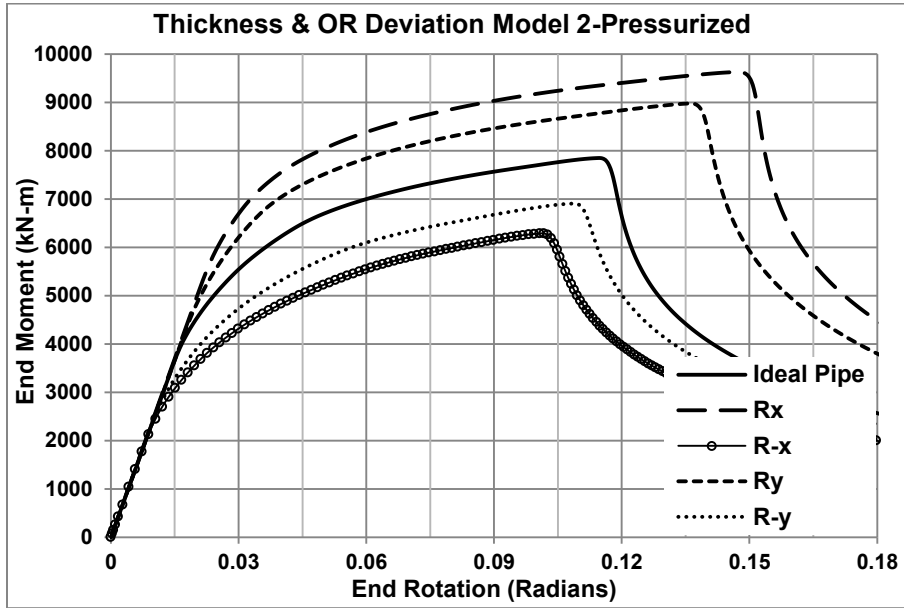


Figure 7.21 M-R responses of pressurized pipe with Thickness Deviation and OR Deviation Model 2

The peak end moment and corresponding CER values obtained from analysing the thickness deviation models are listed in Table 7.3. It is observed that the addition of either of the OR deviation models to the thickness deviation model produces similar changes in magnitudes of the peak moment and the CER for both unpressurized and pressurized pipes. These magnitudes are very close to the magnitudes produced by the thickness deviation model alone (Table 7.2). Therefore, the addition of the OR deviation to the thickness deviation does not have any significant effect.

Table 7.3 Peak Moment and CER values corresponding to the combination of the thickness and OR deviation models

Wall Thickness Deviation and OR Deviation Model 1					
	Direction Of Rotation	Peak Moment (kN-m)	Difference (% Ideal)	CER (Radians)	Difference (% Ideal)
Without Pressure	R _x	11379	4.52%	0.1245	29.74%
	R _{-x}	10239	-5.95%	0.0695	-27.54%
	R _y	11267	3.49%	0.1134	18.80%
	R _{-y}	10463	-3.89%	0.0767	-20.09%
With Pressure	R _x	9635	22.72%	0.1465	27.79%
	R _{-x}	6296	-19.80%	0.1016	-11.39%
	R _y	8971	14.26%	0.1354	18.06%
	R _{-y}	6893	-12.20%	0.1071	-6.63%
Wall Thickness Deviation and OR Deviation Model 2					
	Direction Of Rotation	Peak Moment (kN-m)	Difference (% Ideal)	CER (Radians)	Difference (% Ideal)
Without Pressure	R _x	11363	4.38%	0.1258	31.15%
	R _{-x}	10197	-6.33%	0.0694	-27.65%
	R _y	11274	3.55%	0.1142	18.97%
	R _{-y}	10471	-3.82%	0.0777	-19.02%
With Pressure	R _x	9631	22.67%	0.1468	27.99%
	R _{-x}	6290	-19.89%	0.1017	-11.30%
	R _y	8980	14.38%	0.1365	19.02%
	R _{-y}	6908	-12.01%	0.1086	-5.25%

It is observed that the addition of either of the OR deviation models to the thickness deviation model produces similar changes in magnitudes of the peak moment and the CER for both unpressurized and pressurized pipes. These magnitudes are very close to the magnitudes produced by the thickness deviation model alone (Table 7.2). Therefore, the addition of the OR deviation to the thickness deviation does not have any significant effect.

7.4.4 Discussion on the Effects of the Geometric Imperfection Models

From the moment rotation response corresponding to different material models it is observed that the effects of the material anisotropy observed in this study agree with the findings of Neupane et al., (2012). They reported that the isotropic longitudinal material's response in unpressurized pipe and the isotropic circumferential material's response in pressurized pipe are closer to the response of unpressurized and pressurized pipes with the anisotropic material, as was observed from this finite element study.

The mode of buckling is found to be different for pressurized and unpressurized pipes. Unpressurized pipes have higher peak moment and CER values for all cases compared to pressurized pipes. Unpressurized pipes buckle inward at mid length, while pressurized pipes buckle with outward protuberance at mid length. These modes are termed as diamond mode and bulge mode respectively. The buckling modes corresponding to pressurized and unpressurized pipes observed in this study are similar to previous full scale experiments and FEA studies carried out by Dorey et al., (2001). They conducted a series of full scale buckling tests and observed that the development of the two buckling modes is highly influenced by the magnitude of the internal pressure. They reported that the diamond shape buckle appeared in the unpressurized specimens, and all the pressurized specimens failed in a bulge shaped buckle.

The two OR deviation models showed no significant changes in response compared to that of the ideal pipe. However, the peak moment and CER values corresponding to applied rotations of R_x and R_x are seen to slightly decrease from the ideal response in both pressurized and unpressurized cases for the two OR deviation models. The responses are seen to be slightly higher than the ideal response for an applied rotation of R_y . This is due to the fact that, the imperfect OR is less than the nominal OR along the X-axis, and greater than the nominal OR along the Y-axis.

The OR Deviation Model 1 was an accurate model capturing the wavy shape of the imperfect pipe cross sections, while the OR Deviation Model 2 was an idealized model that only considers the ovalization of a pipe cross section in the shape of an ellipse. The two models produce similar changes in response in

terms of peak end moment and CER values. Their effects on buckling response are not influenced by the application of internal pressure. The OR Deviation Model 2 is simpler and faster to generate compared to the OR Deviation Model 1. Therefore, the OR Deviation Model 2 is deemed an appropriate model to be included in the buckling analysis. The sensitivity of OR deviation, and the parametric study at a later part of this chapter will be performed using OR Deviation Model 2.

The pipe wall thickness deviation model suggests that the behaviour of the pipe is sensitive to the direction of the applied rotation. For both pressurized and unpressurized conditions, the CER values are significantly different corresponding to different directions of applied rotation. It is observed that for an applied rotation of R_x the peak moment and CER values reduce significantly. The reduction in peak moment is seen to be 5.81% and 19.69% for unpressurized and pressurized pipes respectively. The reduction in CER is seen to be 27.32% and 11.0% for unpressurized and pressurized pipes respectively. For pressurized condition, the differences in peak moments are more significant compared to the differences in CER. An applied rotation of R_x results in reduced buckling capacity in both pressurized and unpressurized conditions due to the fact that this direction of applied rotation induces compressive strains in the region of the pipe cross section with wall thickness values less than the specified thickness. Applied rotation of R_x results in very high CER and peak moments compared to the ideal pipe. The increase in peak moment is seen to be 4.72% and 22.88% for unpressurized and pressurized pipes respectively. The increase in CER is seen to be 32.41% and 29.76% for unpressurized and pressurized pipes respectively. This improvement in buckling capacity can be attributed to the development of compressive strains in the region of the pipe cross section with higher than the specified wall thickness value. The applied rotation of R_x induces tensile strains at the pipe cross section where the wall thickness is less than the specified value, and the possibility of pipe rupture before buckling needs to be investigated. The equivalent plastic strain at the extreme tension side of the pipe at the onset of buckling is seen to be 2.76% and 3.33% for the unpressurized and pressurized conditions respectively. Therefore it is concluded that the

improvement in buckling capacity for the applied rotation of R_x does not lead to a failure due to rupture before the onset of buckling.

From the individual effects of OR deviation and wall thickness deviation, it can be concluded that both types of geometric imperfections render the pipe to be weak corresponding the same direction of applied rotation. This direction of rotation is R_x , which induces compressive strains in the region of the pipe cross section where both the OR and wall thickness are less than the ideal dimensions. However, the individual effect of the wall thickness deviation is much more significant than the individual effect of the OR deviation.

From the results of the combined effects of the OR and wall thickness deviation, it is evident that the wall thickness deviation is more influential than the OR deviation. The reductions in the peak moments corresponding to R_x are seen to be 6.33% (unpressurized) and 19.89% (pressurized) for the combination of OR Deviation Model 2 and the wall thickness deviation model, while the thickness deviation alone reduced the peak moments by 5.81% (unpressurized) and 19.69% (pressurized). Similarly, the reductions in the CER corresponding to the combination of the deviation models are seen to be 27.65% (unpressurized) and 11.30% (pressurized), whereas the thickness deviation model alone reduced the CER by 27.32% (unpressurized) and 11.0% (pressurized). This again justifies using the OR deviation Model 2 for the buckling analysis instead of the more complicated OR Deviation Model 1.

In the following sections of this chapter, the sensitivity of the OR Deviation Model 2 and the wall thickness deviation model will be investigated individually. The reduction in buckling capacity due to an applied rotation of R_x is of utmost importance, since both types of imperfections (OR and thickness deviation) tend to reduce the buckling capacity of a pipe in this particular direction of applied rotation. Therefore, the sensitivity will be studied corresponding to an applied rotation of R_x .

7.5 Sensitivity of the OR Deviation Model 2

It has been established from the previous buckling analyses that the reduction of OR results in minor reductions in the peak moment and CER values. The OR Deviation Model 2 employed in the previous buckling analyses produces an

ovalization value of 0.015, which is equal to the measured ovalization value of the pipe cross section used as a basis for developing this model. CSA Z662-11 allows for a maximum ovalization value of 0.03 in the absence of detailed information. This specified value will be considered as an upper limit in the sensitivity investigation. Three ovalization values of 0.01, 0.02, and 0.03 will be considered.

According to CSA Z662-11, the ovalization value of a pipe's cross section is calculated using its maximum and minimum measured OD (D_{max} and D_{min}). Equal value of ovalization can result from different combinations of D_{max} and D_{min} values. Therefore, three types of combinations are considered in this sensitivity study as follows:

Combination 1: D_{min} is kept to a constant value equal to the nominal OD, while D_{max} is increased, resulting in an increasing average OD

Combination 2: D_{max} is kept to a constant value equal to the nominal OD, while D_{min} is decreased, resulting in a decreasing average OD

Combination 3: D_{max} is increased and D_{min} is decreased by an equal amount, resulting in a constant average OD

For each combination of D_{max} and D_{min} , three OR Deviation Model 2 with ovalization values of 0.01, 0.02, and 0.03 are generated, resulting in a total of nine FEA models. The combinations are shown in Table 7.4:

Table 7.4 Combinations of D_{max} and D_{min} for the sensitivity investigation

	D_{max} (mm)	D_{min} (mm)	$D_{average}$ (mm)	Ovalization	ΔD (% Nominal OD)
Combination 1	1077.67	1067.00	1072.34	0.01	1.00%
	1088.60	1067.00	1077.80	0.02	2.02%
	1099.50	1067.00	1083.25	0.03	3.05%
Combination 2	1067.00	1056.35	1061.68	0.01	1.00%
	1067.00	1045.90	1056.45	0.02	1.98%
	1067.00	1035.50	1051.25	0.03	2.95%
Combination 3	1072.34	1061.67	1067.00	0.01	1.00%
	1077.67	1056.33	1067.00	0.02	2.00%
	1083.01	1051.00	1067.00	0.03	3.00%

Each model is analysed with an applied rotation of R_x (for OR Deviation Model 2, R_{-x} and R_x are essentially the same due to symmetry), with and without internal pressure, resulting in a total of eighteen M-R responses. The peak moment and corresponding CER for these eighteen FEA models are recorded. The peak moment and CER values are expressed as the percentage of the peak moment and CER of the ideal NPS 42 inch pipe with a constant OD of 1067 mm and a wall thickness of 14.275 mm. The variations of the peak moments with increasing ovalization for the three combinations are shown in Figure 7.22:

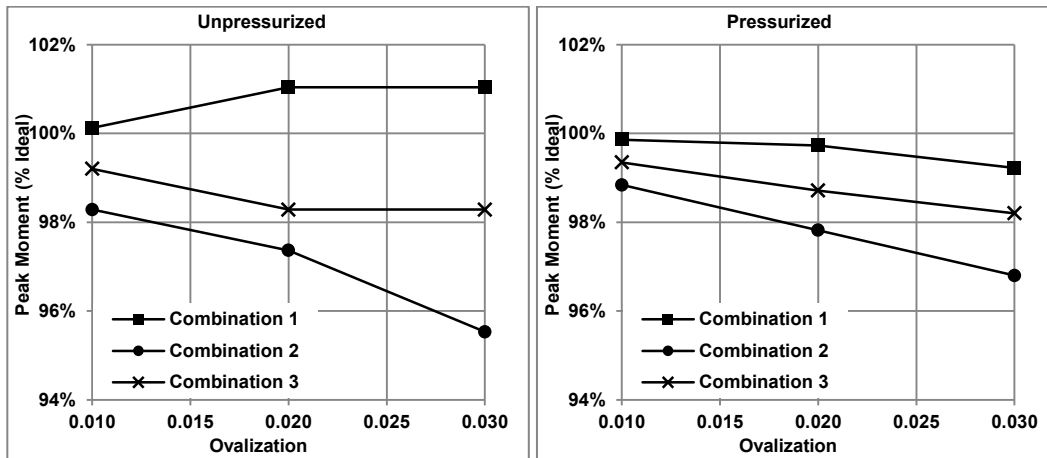


Figure 7.22 Variations of peak moments with increasing ovalization for the three combinations of D_{max} and D_{min}

It is observed that, for unpressurized pipes, Combination 1 increases the peak moment capacity with increasing ovalization. Combinations 2 and 3 on the other hand, reduce the peak moment capacity with increasing ovalization. In Combination 1, D_{min} is kept constant while D_{max} is increased. As a result, the average OD of the pipe increases with increasing ovalization. In an unpressurized pipe during the application of rotation, D_{max} is oriented along the neutral axis of the pipe cross section. An increase in D_{max} results in a bigger pipe perimeter with more cross sectional area in both the tension and the compression sides to withstand bending, resulting in an improvement in the peak moment capacity. In Combinations 2, the average OD decreases with increasing ovalization, resulting in a reduction of the peak moment capacity. In Combination 3, the average OD remains constant with increasing ovalization. Accordingly, the line corresponding to Combination 3 is seen to be between the other two combinations.

For the pressurized pipes, all three combinations tend to reduce the peak moment capacity with increasing ovalization. When an internal pressure is applied to a thin walled pipe, it behaves like a membrane where the circumferential stress distribution is uniform across its thickness. An ideal pipe with an initially circular cross section expands uniformly after applying internal pressure and retains its circular form. On the other hand, an imperfect pipe with an initially ovalized cross section tends to acquire a circular shape by respectively reducing and increasing its D_{\max} and D_{\min} during pressurization (Figure 7.23)

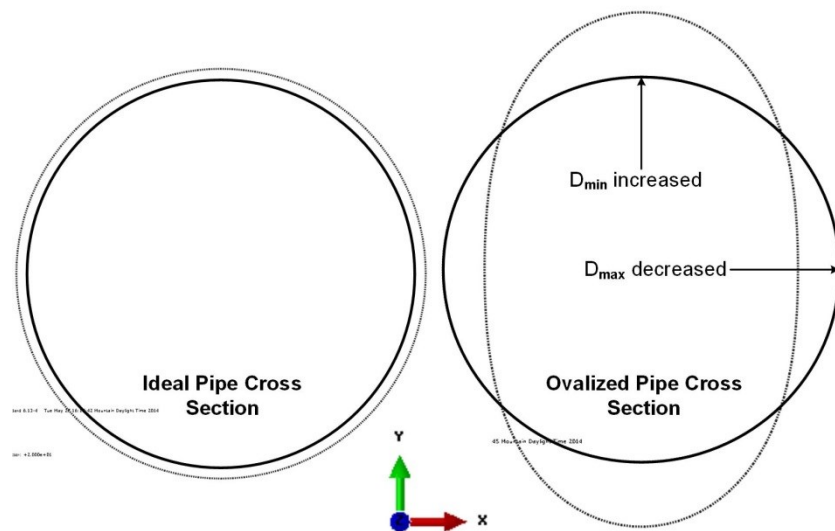


Figure 7.23 Deformation (scaled by a factor of 20) due to pressurization of an ideal and an ovalized pipe cross section at mid length

As a result, the final shape of the cross section becomes more circular and less oval after pressurization. The level of the acquired circularity depends on the extent of the initial ovalization and D/t ratio. Consequently, all three combinations demonstrate consistently decreasing peak moment with increasing ovalization.

The variations of the CER with increasing ovalization for the three combinations are shown in Figure 7.24. For the unpressurized pipes, Combinations 1 and 2 demonstrate an increase in CER and Combination 3 reduces the CER with increasing ovalization up to 0.02. Further increase in ovalization reduces the CER for Combinations 1 and 2, and increases it for Combination 3. For

pressurized pipes, Combinations 1 and 2 reduce the CER with increasing ovalization. Combination 3 reduces the CER up to an ovalization value of 0.02, and then increases it for an ovalization value of 0.03.

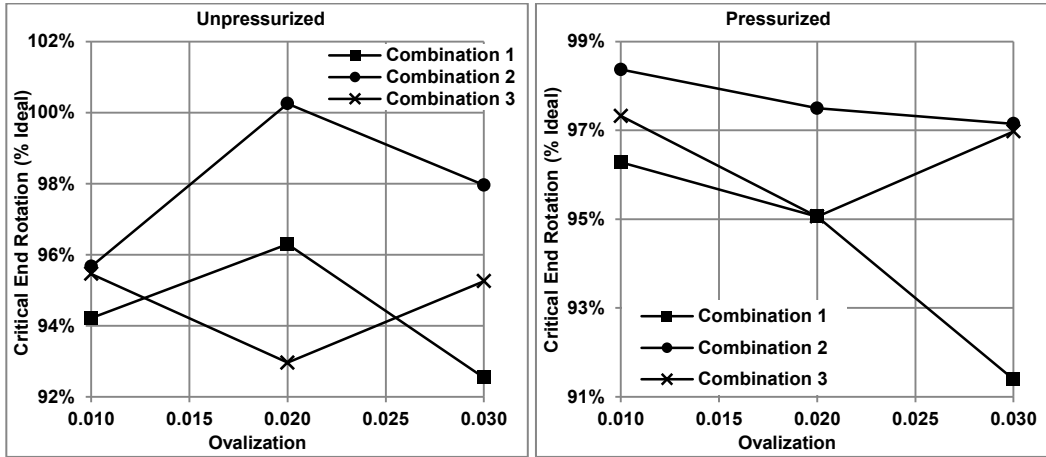


Figure 7.24 Variations of critical end rotations with increasing ovalization for the three combinations of D_{max} and D_{min}

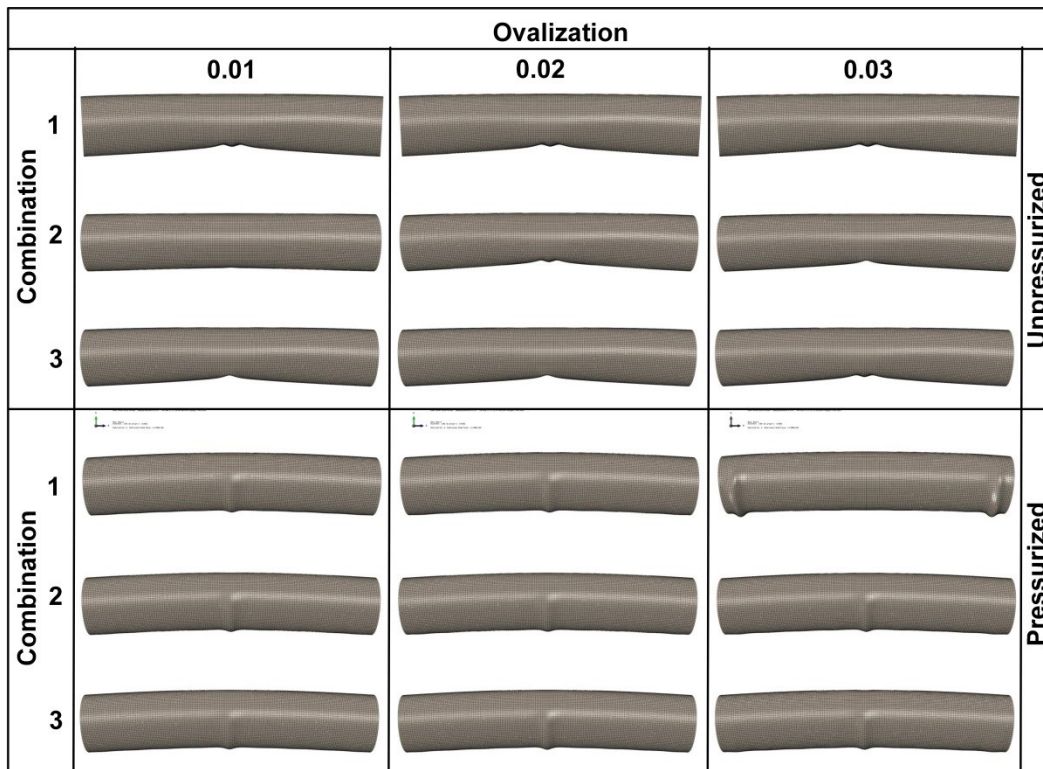


Figure 7.25 Deformed shapes of pipes corresponding to the three combinations of ovalization (full lengths of pipes are shown for visual clarity)

This unusual behaviour can be depicted from the deformed shapes of the pipes shown in Figure 7.25. For the unpressurized condition, pipes with Combination 1 are seen to buckle in diamond shape. The location of the buckle is slightly away from the mid length of the pipe. The applied symmetry boundary condition in this case signifies the appearance of another buckle on the other side, as can be seen from the figure. In an actual situation, an unpressurized pipe will usually buckle in the weakest location. The excessive deformation in that location will prevent the initiation of another local buckle in any other location. Therefore the CER values obtained from analysing these three models are not indicative of the true response.

The location of the buckle for Combination 2 is seen to be at the middle corresponding to 0.01 and 0.03 ovalization. For an ovalization of 0.02, the buckle again appears away from mid length. The CER values from these models are also not indicative of the true response.

For Combination 3, the buckle locations are in the middle up to an ovalization of 0.02, and the CER decreases. For a 0.03 ovalization, the buckle again forms away from the middle and the CER value cannot be considered indicative of the true buckling response.

For pressurized condition, Combination 2 demonstrates consistently decreasing CER with increasing ovalization. The deformed shapes show that the bulge appears in the middle for all three ovalization values. Combination 1 shows a sudden reduction in CER corresponding to an ovalization of 0.03. From the deformed shape, it is observed that for this case the bulge forms at the end of the pipe instead of at the middle. The pipe remains almost straight while the end rotates and fails in buckling. As a result, the CER is reduced drastically for a 0.03 ovalization, and is not indicative of the true buckling response.

Combination 3 produces bulge shape for all three ovalization values, but the CER corresponding to a 0.03 ovalization is higher than that corresponding to a 0.02 ovalization. This is due to the fact that, for an ovalization of 0.03, a bulge appears at the end of the pipe at a very early stage of applied rotation (37% of CER). Although the pipe buckles in the middle, the bulge at the end adds up to the total

end rotation and results in an increased CER. The longitudinal cross section of the pipe at 37% of the CER is shown in Figure 7.26:

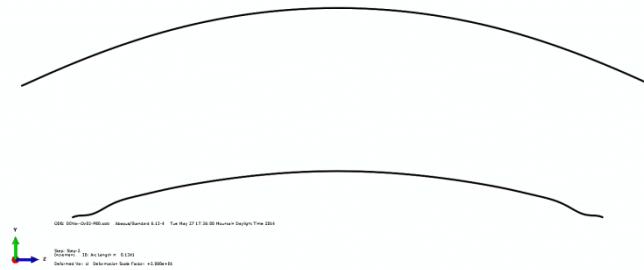


Figure 7.26 longitudinal cross section of the pipe with Combination 3, ovalization of 0.03, and at 37% of CER

The behaviour of the models in terms of CER with increasing ovalization can be attributed to the application of the symmetry boundary condition. To investigate the influence of symmetry, a pipe was modeled with full length without internal pressure, and the OR Deviation model with Combination 2 and a 0.02 ovalization was imposed on it. Rotation was applied on the two ends of the pipe, and it was observed that this model failed in buckling in the middle. The peak moment is found to be 97% of the ideal response, similar to the symmetric model. The CER was found to be 99% of the ideal CER, where the symmetric model predicted 100.2%. It is concluded that despite slightly over estimating the CER, the symmetric pipe models are capable of predicting the peak moments accurately. The differences in end rotation will be more in the post buckle stage (Figure 7.27)

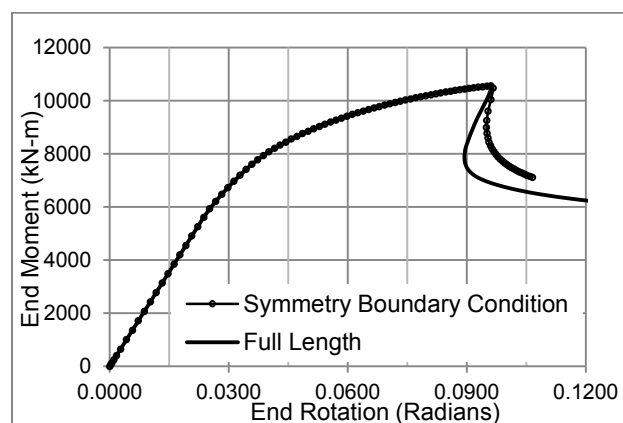


Figure 7.27 Moment Rotation responses of the half pipe model with symmetry boundary condition and the full pipe model

From the OR deviation measurement results previously reported in Chapter 4, it was observed that both D_{\max} and D_{\min} respectively increase and decrease from the nominal OD in the UOE manufactured pipes. Furthermore, the measured average ovalization values of the UOE pipes were seen to be less than 0.01. The OR deviation Model 2 with Combination 3, which accounts for changes in both D_{\max} and D_{\min} , and which is capable of producing consistent analysis results up to an ovalization of 0.02, is therefore the best choice for an ovalization imperfection model. This model will be employed in the parametric study later in this chapter.

7.6 Sensitivity of the Thickness Deviation Model

The wall thickness deviation model employed in the buckling analyses so far had a maximum positive deviation of 30% and a maximum negative deviation of 15%. The location of the maximum positive deviation was at 145 degrees from the seam weld location (Figure 7.28). The extent of the negative deviation ($\theta_{\text{neg dev}}$) was 200 degrees. In the sensitivity study, the effects of: a) the location of the maximum thickness, b) the extent of the negative deviation, c) the relative magnitudes of the maximum positive and negative deviations, and d) longitudinal variation of the cross sectional thickness deviation are investigated.

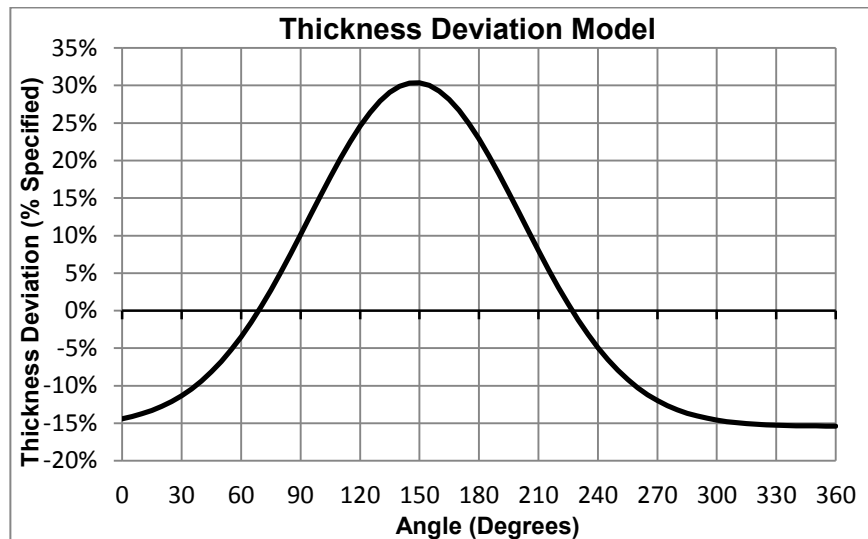


Figure 7.28 The thickness deviation model used in the buckling analysis

7.6.1 Effects of the Location of the Maximum Wall Thickness

To investigate the effects of the location of the maximum wall thickness, three thickness deviation models are generated using the thickness deviation model

equation (Equation 6-3). The maximum positive and negative deviations are kept to a constant value of 30% and 15% respectively, while the position of the maximum positive deviation is shifted by 40 degrees, 20 degrees, and 0 degrees from the location of the longitudinal seam weld. The resulting curves of the three thickness deviations are shown in Figure 7.29:

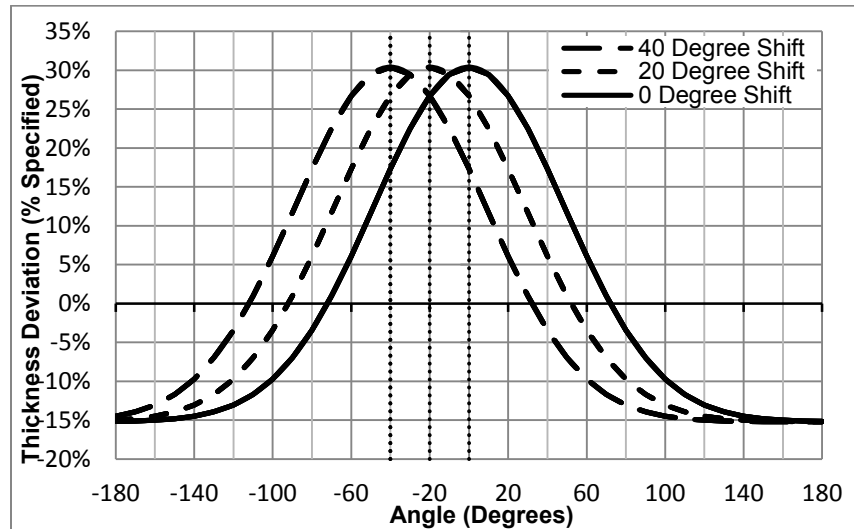


Figure 7.29 Thickness deviation models for investigating the sensitivity of the location of maximum thickness

These three thickness deviations are imposed on the FEA model of a 1067 mm OD pipe, and an end rotation is applied in the R_x direction. The resulting buckling responses for unpressurized and pressurized pipes are shown in Figure 7.30 and Figure 7.31:

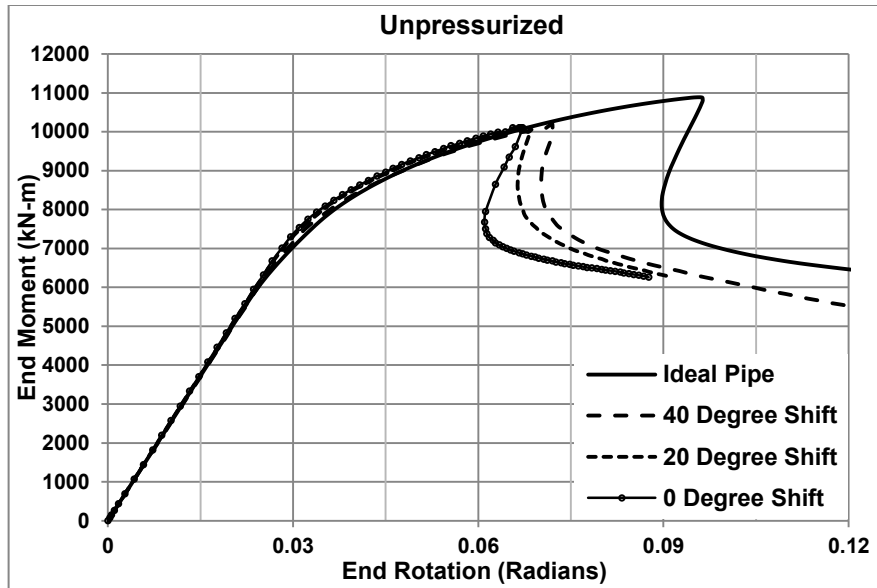


Figure 7.30 Buckling responses of unpressurized pipe with varying locations of maximum wall thickness

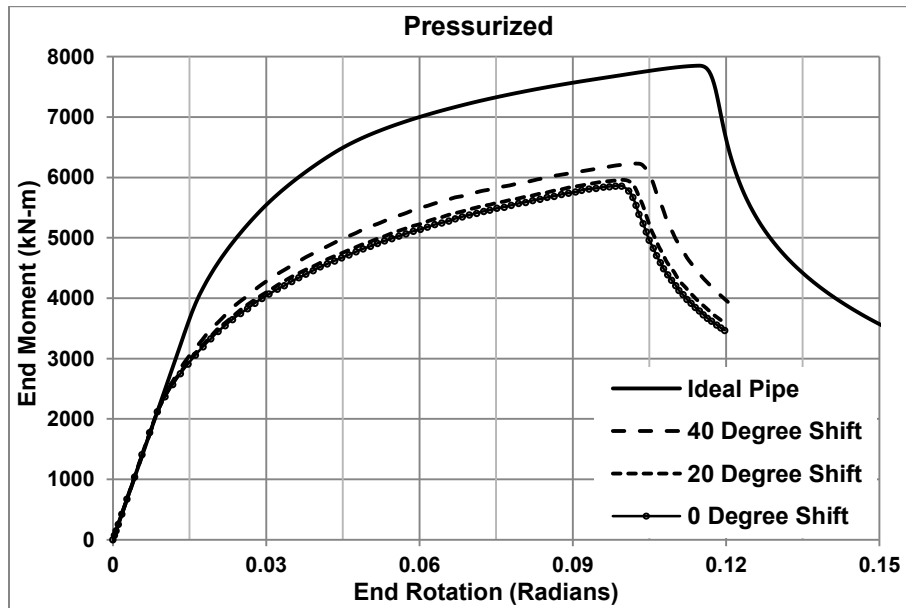


Figure 7.31 Buckling responses of pressurized and pressurized pipes with varying locations of maximum wall thickness

The peak end moment and corresponding CER values are expressed as percentages of the peak moment and CER of the ideal pipe. The variations of the

peak moment and CER with changes in the maximum wall thickness location are shown in Figure 7.32:

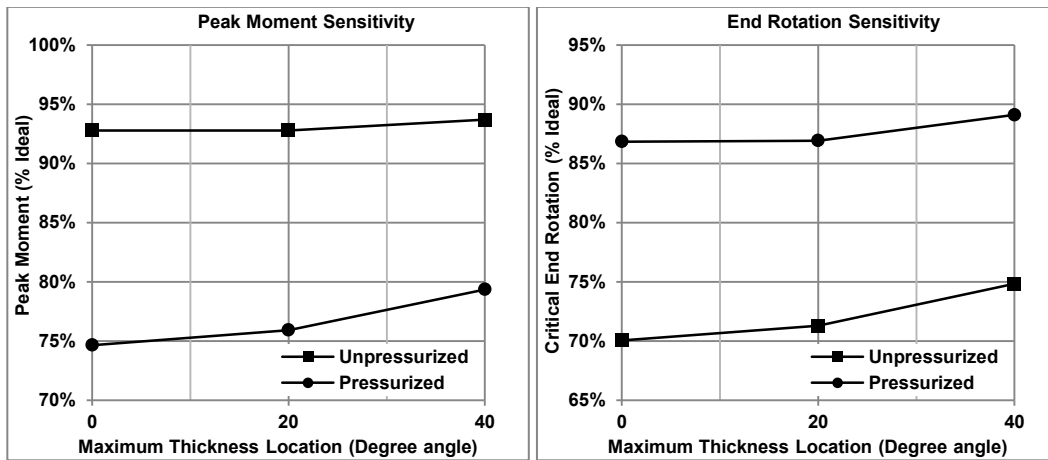


Figure 7.32 Variations in peak moment and CER with changes in the location of maximum thickness

It is observed that shifting the location of the maximum deviation from 0 degree to 20 degrees has insignificant effects on the peak moment and CER in both the unpressurized and the pressurized pipes. Shifting the location from 0 degree to 40 degrees also has minor effects on the peak moment of the unpressurized pipe (0.92% increase) and the CER of the pressurized pipe (2.26% increase). However, for the 40 degree shift, the CER of the unpressurized pipe is increased by 4.79% and the peak moment of the pressurized pipe is increased by 4.71%. In all cases, the symmetric thickness deviation model (0 degree shift) produces the lowest peak moment and CER values. Based on these results, it is concluded that the buckling analysis using a symmetric thickness deviation model will produce slightly conservative results in terms of peak moment and CER.

From the thickness deviation measurement results in Chapter 4, it was observed that the thickness deviations are not exactly symmetric with respect to the location of the longitudinal seam weld. The shift in the location of the maximum thickness from the line of symmetry was seen to be as high as 35 degrees. The sensitivity study shows that a shift of 40 degrees of the maximum thickness location from 0 degree slightly improves the buckling capacity for the applied rotation of R_x . Therefore, the slightly conservative symmetric thickness deviation model is considered to be an acceptable model for pipe buckling analysis.

7.6.2 Effects of the Extent of Negative Deviation

To investigate the effects of the extent of negative deviation, five symmetric thickness deviation models are generated using the thickness deviation model equation (Equation 6-3). The maximum positive and negative deviations are kept to a constant value of 30% and 15% respectively, and the position of the maximum positive deviation is kept fixed at the location opposite to the longitudinal seam weld. The extent of negative deviation ($\theta_{\text{neg dev}}$) is increased from 120 degrees to 200 degrees at 20 degrees intervals (Figure 7.33). These five thickness deviations are imposed on the FEA model of the 1067 mm OD pipe. The models are then analyzed with an applied rotation of R_x with and without internal pressure, resulting in a total of ten M-R responses. From the buckling responses, the peak moment and corresponding CER are recorded and expressed as the percentages of the peak moment and CER of the ideal pipe. The variations of the peak moment and CER with increasing $\theta_{\text{neg dev}}$ values are shown in Figure 7.34.

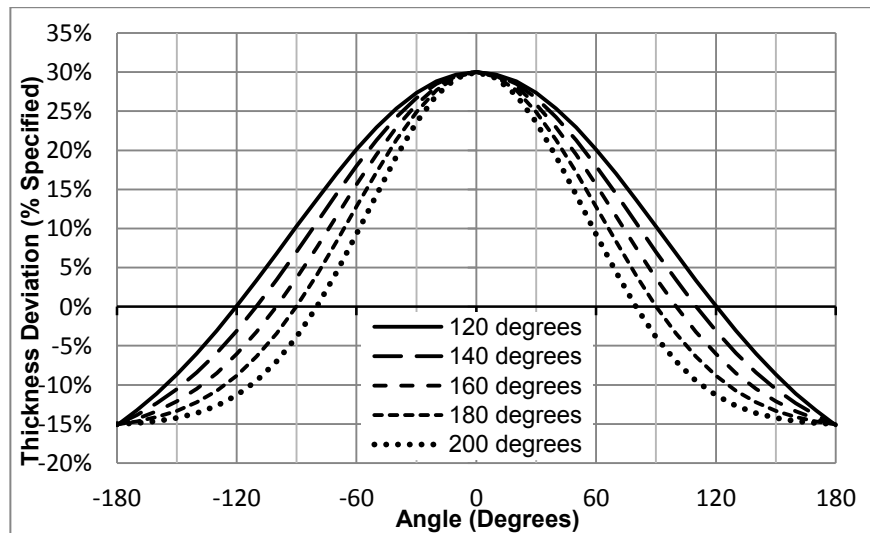


Figure 7.33 Thickness deviation models with $\theta_{\text{neg dev}}$ increasing from 120 degrees to 200 degrees

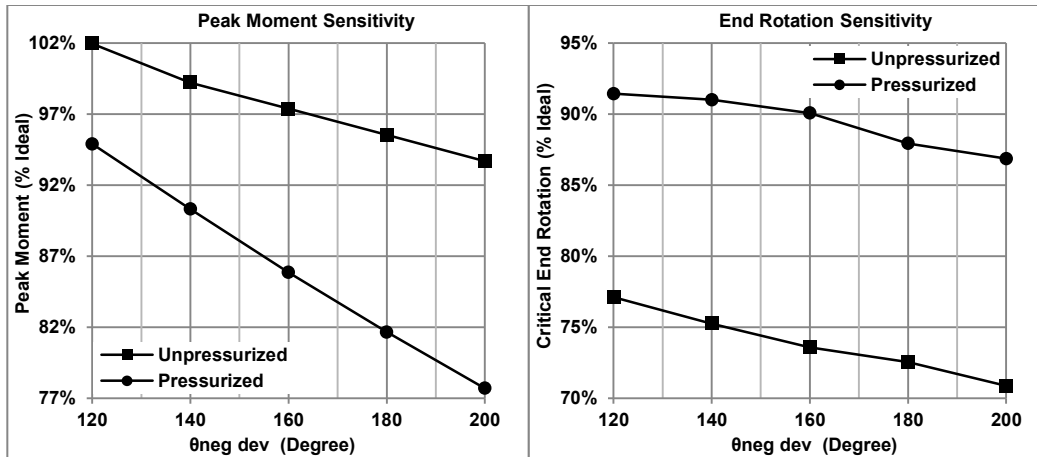


Figure 7.34 Variations in peak moment and CER with $\theta_{neg\ dev}$ increasing from 120 degrees to 200 degrees

From Figure 7.34, it is evident that the effect of the extent of deviation is more prominent in the peak moment than the CER in both pressurized and unpressurized pipes. Increasing the value of $\theta_{neg\ dev}$ from 120 degrees to 200 degrees reduces the peak moment by 8.27% and 17.19% of the ideal peak moment in the unpressurized and pressurized pipes respectively. The reductions in CER for the unpressurized and pressurized pipes are seen to be 6.25% and 4.58% of the ideal pipe respectively. It is also observed that for $\theta_{neg\ dev} = 120$ degrees, the peak moment of the unpressurized pipe is higher than the ideal response (101.96%).

From the five deviation models presented in Figure 7.33 it can be seen that increasing the $\theta_{neg\ dev}$ parameter not only reduces the positive deviation extent of the curves, but also changes their shape, rendering the exponentially decreasing part more dominant. In Figure 7.35, the two curves corresponding to $\theta_{neg\ dev}$ value of 120 degrees and 200 degrees are shown. The decreasing part of the 120 degree $\theta_{neg\ dev}$ curve is almost linear, while in the 200 degree $\theta_{neg\ dev}$ curve, the exponential behaviour in the decreasing part is very prominent. This change of shape results in the high sensitivity of the buckling response to the extent of negative deviation.

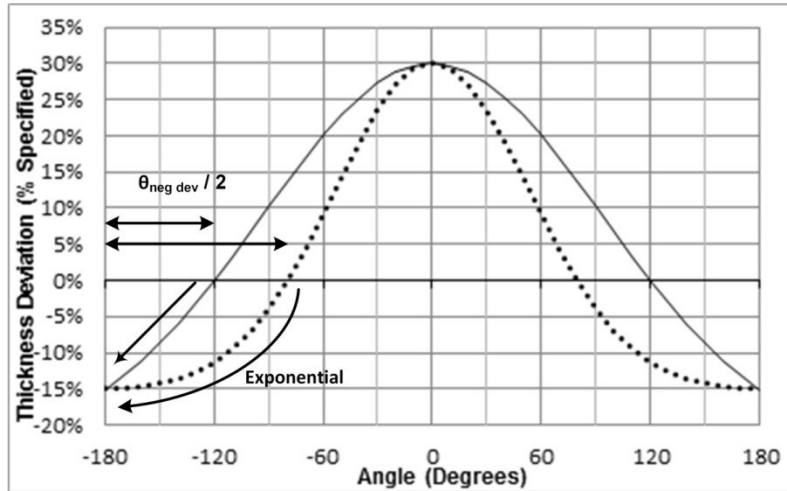


Figure 7.35 Change in shape of the thickness deviation models with $\theta_{\text{neg dev}}$ increasing from 120 degrees to 200 degrees

The peak end moment and corresponding CER values obtained from analyzing the ten FEA models are listed in Table 7.5:

Table 7.5 Peak Moment and CER values corresponding to increasing values of $\theta_{\text{neg dev}}$

Unpressurized				
$\theta_{\text{neg dev}}$ (Degrees)	Peak Moment (kN-m)	Difference (% Ideal)	CER (Radians)	Difference (% Ideal)
120	11100	1.96%	0.0740	-22.88%
140	10800	-0.80%	0.0722	-24.76%
160	10600	-2.63%	0.0706	-26.43%
180	10400	-4.47%	0.0696	-27.47%
200	10200	-6.31%	0.0680	-29.14%
Pressurized				
$\theta_{\text{neg dev}}$ (Degrees)	Peak Moment kN-m	Difference % Ideal	CER Radians	Difference % Ideal
120	7450	-5.11%	0.1048	-8.57%
140	7090	-9.70%	0.1044	-8.99%
160	6740	-14.15%	0.1033	-9.93%
180	6410	-18.36%	0.1008	-12.07%
200	6100	-22.30%	0.0996	-13.15%

It is observed that the buckling capacities corresponding to $\theta_{\text{neg dev}} = 180$ degrees are close to the capacities previously reported in Table 7.2 (peak moment and CER corresponding to R_x) for both unpressurized and pressurized pipes. This is due to the fact that, imposing symmetry to the thickness deviation model reduces the buckling capacities, at the same time decreasing $\theta_{\text{neg dev}}$ from 200 degrees to 180 degrees improves the capacities to such extent that the effects of the two balance each other out.

The buckling responses of the original thickness deviation model and the symmetric model with $\theta_{\text{neg dev}} = 180$ degrees are shown in Figure 7.36. It is seen that for pressurized pipe, both models produce identical responses. For the unpressurized pipe, the model responses are identical up to the buckling point and diverge in the post-buckle stage.

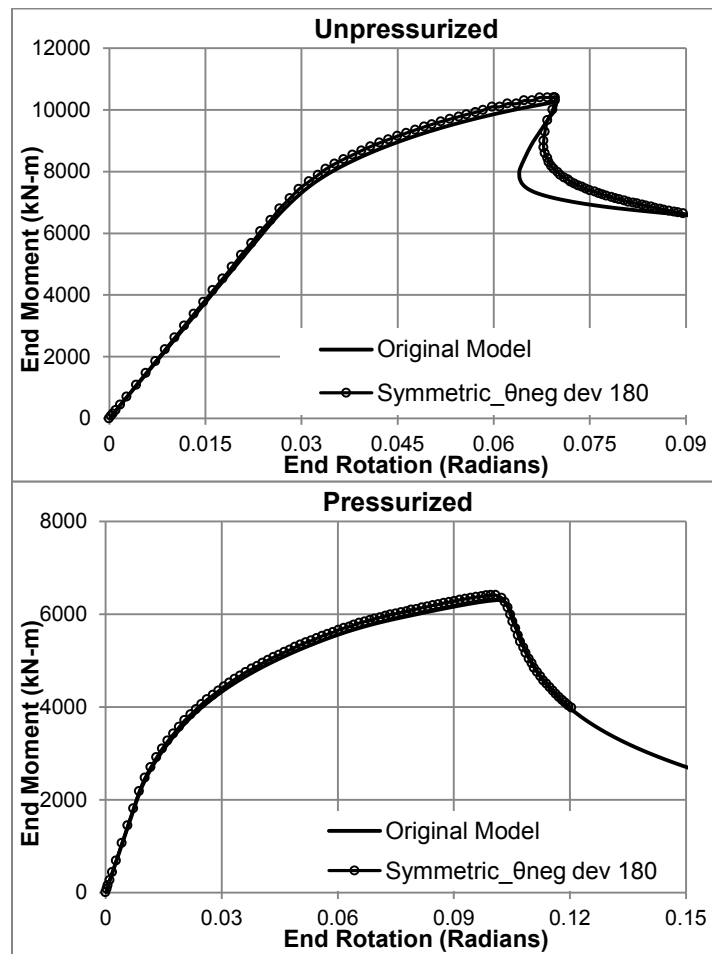


Figure 7.36 Buckling responses of unpressurized and pressurized pipes with the original and the symmetric ($\theta_{\text{neg dev}} = 180$ degrees) thickness deviation models

Therefore, using a symmetric thickness deviation model with $\theta_{\text{neg dev}} = 180$ degrees is justified against the previous model with $\theta_{\text{neg dev}} = 200$ degrees and maximum thickness's location shifted by 35 degrees.

7.6.3 Effects of the Relative Magnitudes of the Maximum Deviations

To investigate the effects of the relative magnitudes of the maximum positive and negative deviations, three symmetric thickness deviation models with $\theta_{\text{neg dev}} = 180$ degrees are generated. The maximum negative deviation is kept at a constant value of -15%, while the maximum positive deviation is decreased from 30% to 20% and 15%. The three thickness deviation models are shown in Figure 7.37:

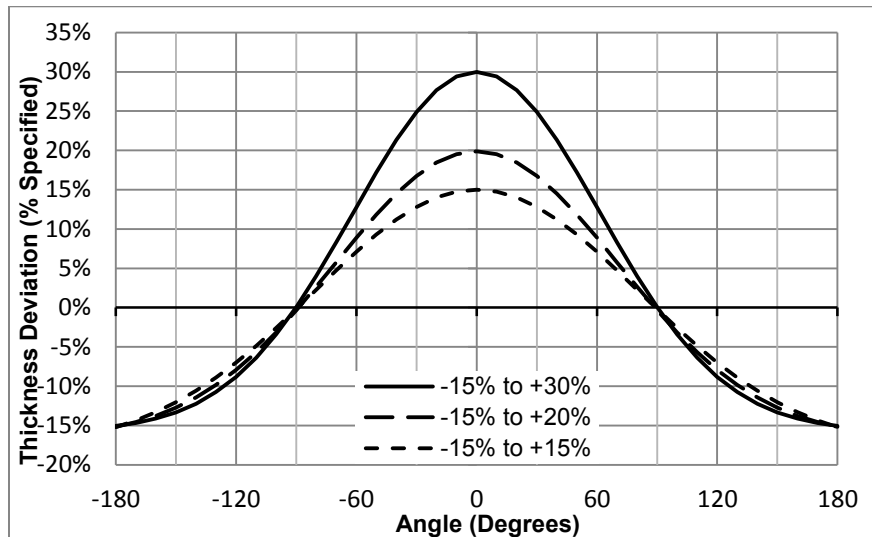


Figure 7.37 Thickness deviation models with maximum positive deviation decreasing from 30% to 15%

These three thickness deviations are imposed on the FEA model of the 1067 mm OD pipe. The models are then analyzed with an applied rotation of R_x with and without internal pressure, resulting in a total of six buckling responses as shown in Figure 7.38. It is seen that the buckling responses corresponding to decreasing the maximum positive thickness deviations are almost identical for both unpressurized and pressurized pipes. For the pressurized pipes, the maximum differences in peak moment and CERs are found to be respectively 0.38% and 2.89% of the ideal response. For the unpressurized pipes, these differences are 1.84% and 3.33% respectively.

A 3.33% reduction in end moment corresponding to a reduction of the maximum positive deviation from 30% to 15% of the specified thickness indicates minor sensitivity of the buckling response to this particular parameter. It is therefore concluded that the relative magnitudes of the maximum thickness deviations do not have any significant effects on the buckling capacity. The responses are primarily dictated by the magnitude of the maximum negative deviation. However, the post buckling behaviours of the unpressurized pipes are seen to be slightly different for the three thickness deviation models.

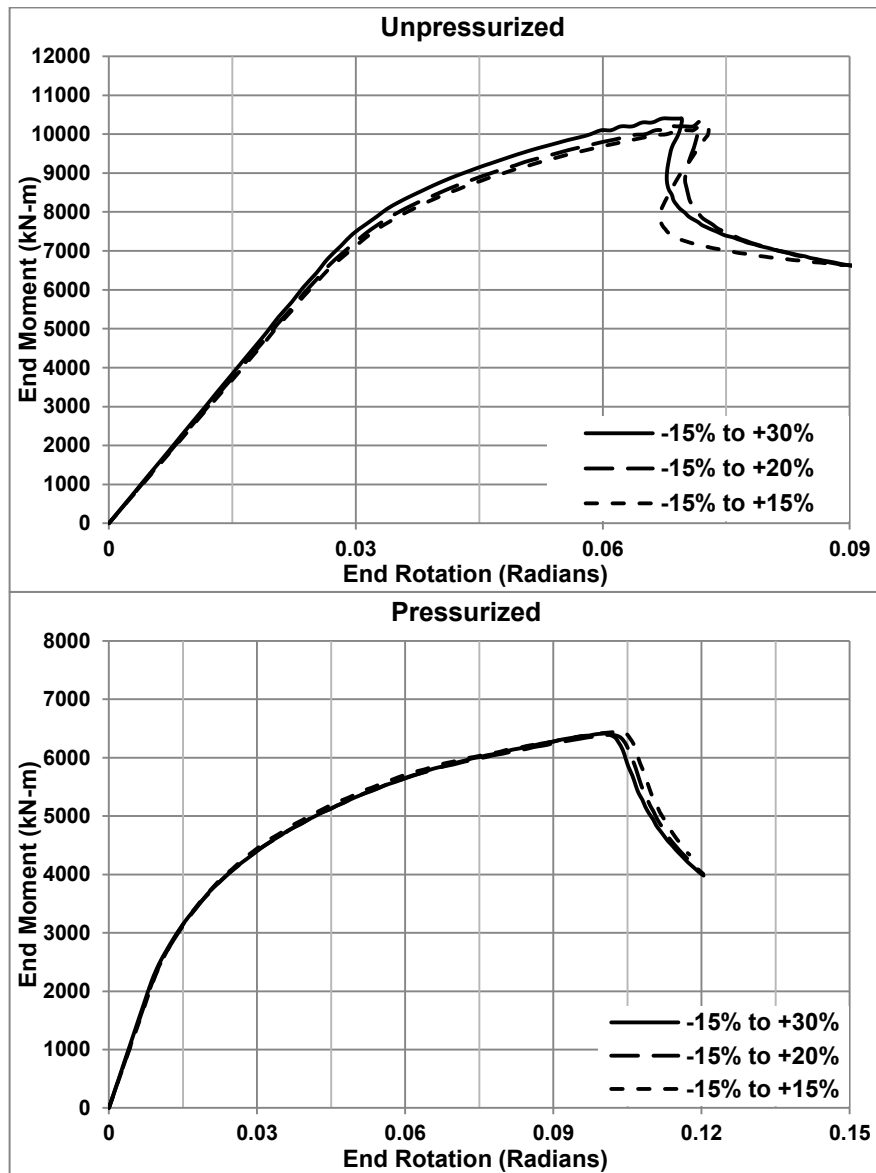


Figure 7.38 Buckling responses of unpressurized and pressurized pipes with the maximum thickness deviation decreasing from 30% to 15%

7.6.4 Effects of Longitudinal Variation of the Thickness Deviations

The three types of longitudinal variations previously presented in Chapter 6 are employed to investigate their effects on buckling. The cross sectional thickness deviation model is chosen to be -15% to +30% with $\theta_{\text{neg dev}} = 180$ degrees.

The longitudinal variation is imposed on the cross sectional thickness deviation according to the equation:

$$t = t_{\text{specified}} \pm \text{Cross-Sectional Deviation} \times \text{Longitudinal Variation} \quad 7-2$$

Where, $t_{\text{specified}}$ is the specified wall thickness. The resulting wall thickness contours are shown in Figure 7.39:

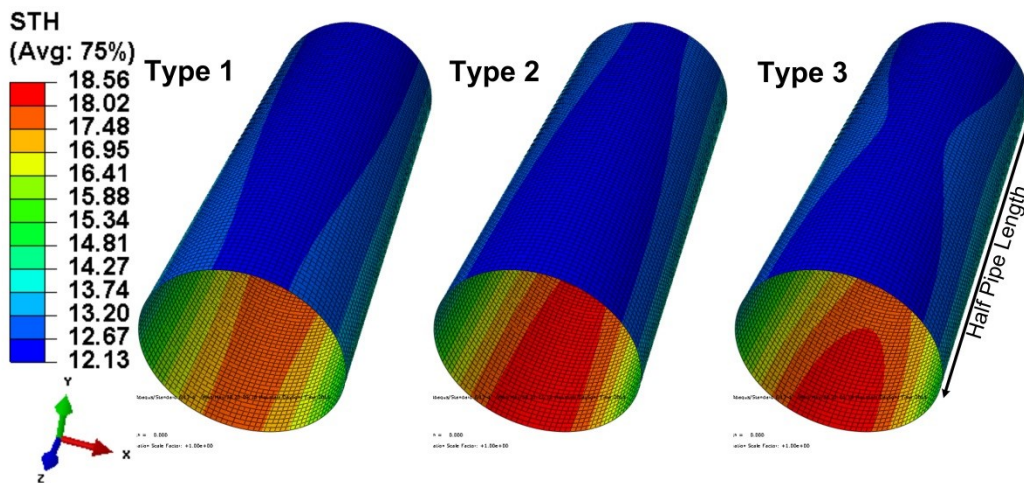


Figure 7.39 Three types of longitudinal variations of the cross sectional thickness deviations

Longitudinal variation of Type 1 results in a lowest cross sectional thickness deviation of -12% to +24% at the two ends of the pipe, and increases to a highest deviation of -15% to +30% at mid length. Longitudinal variation of Type 2 is the exact opposite of Type 1, where the highest cross sectional thickness deviation is at the two ends of the pipe, and the lowest deviation is at mid length. Type 3 imposes the lowest deviations at 1/3 and 2/3 lengths of the pipe. The highest deviations appear three times, at the two ends and in the middle. In the three types of longitudinal variations, a smooth transition of the cross sectional deviation along the length of the pipe is defined by the Cosine function.

These three types of longitudinal variation of cross sectional thickness deviations are imposed on the FEA model of the 1067 mm OD pipe. The models are then

analyzed with an applied rotation of R_x with and without internal pressure, resulting in a total of six buckling responses as shown in Figure 7.40 and Figure 7.41 along with the response with no longitudinal variation.

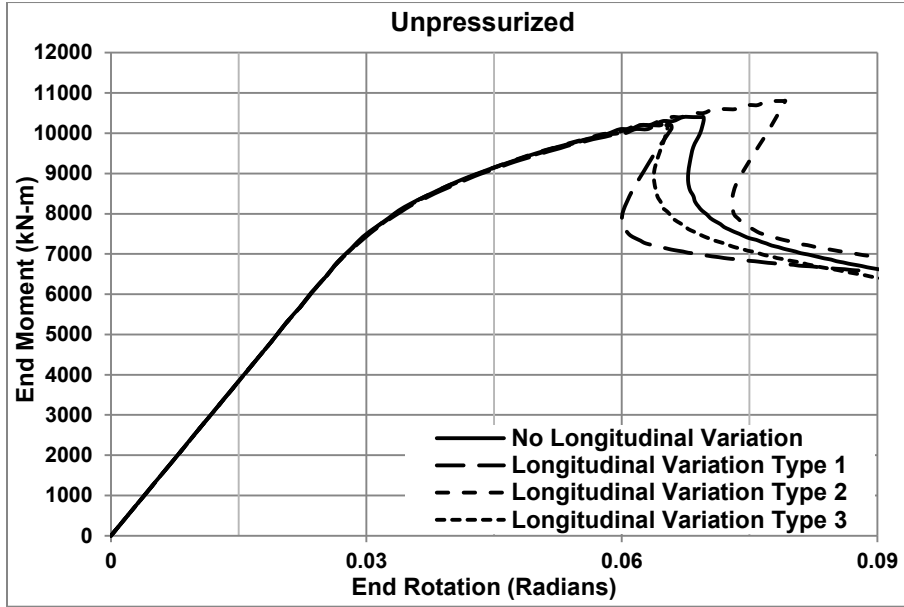


Figure 7.40 Buckling responses of unpressurized pipes with longitudinal variations

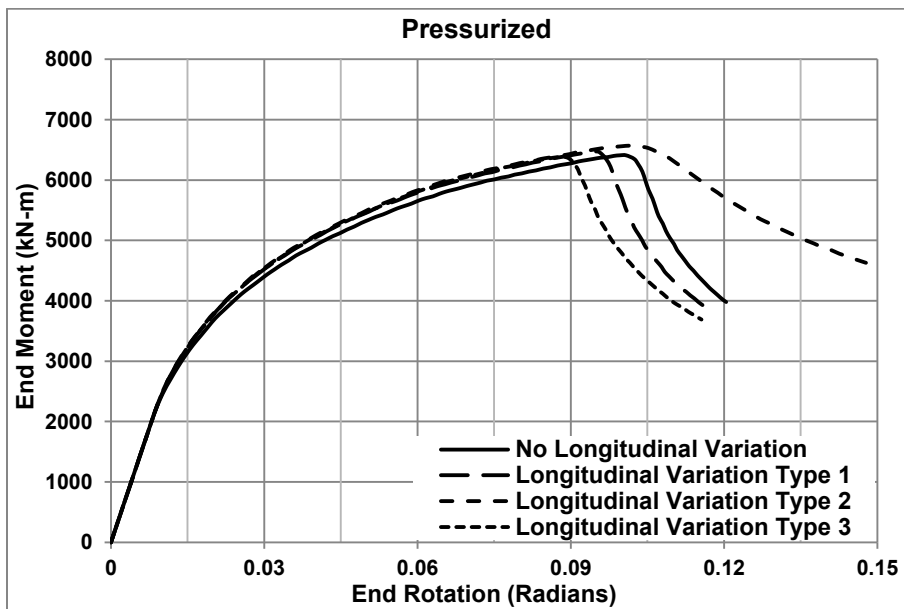


Figure 7.41 Buckling responses of pressurized pipes with longitudinal variations

It is observed that for the unpressurized condition, the variation Type 1 results in a 1.92% decrease of peak moment and a 4.76% decrease of CER compared to the response of the pipe with no longitudinal variation. The decrease in the cross sectional thickness at mid length relative to the thickness at the end contributes to this reduction of buckling capacity. The increased cross sectional thickness at mid length corresponding to variation Type 2 produces a 3.85% increase of peak moment and a 14.58% increase of CER. Type 3 reduces the peak moment and the CER by 0.96% and 3.57% respectively. Therefore, for unpressurized condition, the imposed longitudinal variations have minor effects on the peak moment capacity.

For the pressurized pipes, longitudinal variation Type 1 has no effects on the peak moment, but reduces the CER by 5.25%, the pipe buckles in the middle in bulge shape. Type 2 has no effects on the peak moment and CER, but results in a bulge near the pipe end where the thickness deviations are comparatively higher. Type 3 buckles the pipe in bulge shape at mid length, reduces the CER by 10.67%, and has no effects on the peak moment.

7.7 Parametric Study

The effects of the measured imperfections has been investigated for an NPS 42 inch pipe with 1067 mm nominal OD and 14.275 mm specified wall thickness. The sensitivity has also been investigated for these particular dimensions. Based on the sensitivity investigation, the OR deviation and wall thickness deviation models have been refined and simplified. OR deviation model 2 with Combination 3 of D_{max} and D_{min} has been identified as the best suited ovalization model. A symmetric thickness deviation model with $\theta_{neg\ dev} = 180$ degrees is seen to produce the same response as the measured wall thickness deviation model. The applicability of these two models for the buckling analysis of pipes with different dimensions is required to be investigated.

The parametric study is performed for three different D/t ratios of pipe: NPS 42 inch with 10.312 mm specified wall thickness ($D/t=103.47$), NPS 34 inch with 9.525 mm specified wall thickness ($D/t=90.71$), and NPS 42 inch with 14.275 mm specified wall thickness ($D/t=74.75$). Each pipe is analyzed in unpressurized and pressurized conditions. The pipes are first analyzed without any imperfections,

resulting in an ideal response. These responses are taken as the references for comparing the changes in behaviour of each pipe.

The OR deviation models corresponding to an ovalization of 0.015 demonstrated insignificant effects on the buckling response. The average ovalization in the UOE manufactured pipes were reported to be less than 0.01 in Chapter 4. Regardless, an ovalization of 0.01 is imposed through OR Deviation Model 2 – Combination 3 to all three pipe models in order to investigate its effect on pipes with higher D/t ratios.

The reduced thickness was observed in the NPS 42 inch pipe with 14.275 mm specified thickness. In order to investigate the effects of thickness reduction on pipes with higher D/t ratios, three symmetric cross sectional thickness deviation models with $\theta_{\text{neg dev}} = 180$ degrees are imposed on each pipe. The thickness deviation ranges are selected to be -5% to +10%, -10% to +20%, and -15% to +30% of the specified thickness.

A total of 30 FEA models are analyzed in the parametric study. The description of the legends in the M-R responses are as follows:

Ideal: No geometric imperfections

Constant Thickness: Ovalization imperfection present, thickness is constant

-“x”% to +”y”% Deviation: Ovalization imperfection present, thickness is varied between -x% to +y%

The results are presented in the following sections.

7.7.1 NPS 42 inch pipe with 10.312 mm specified wall thickness (D/t = 103.47)

The pipes are analyzed in unpressurized and pressurized conditions. For this D/t ratio, the internal pressure corresponding to 80% of SMYS is calculated to be 10.8 MPa.

The buckling responses of the unpressurized pipe are shown in Figure 7.42. It is observed that the ovalization of 0.01 has no effects on the buckling behaviour up to the peak moment, and the change in behaviour is in the post buckling stage. The imposed thickness deviations reduce the peak moment and CER of the pipe

with increasing deviation amplitudes. A 15% reduction of wall thickness results in a 22.8% reduction in CER.

The buckling responses of the pressurized pipe are shown in Figure 7.43. It is observed that the ovalization of 0.01 has no effects on the buckling behaviour up to and beyond the peak moment. The imposed thickness deviations reduce the peak moment and CER of the pipe with increasing deviation amplitudes except for the deviation range of -15% to +30%. A 15% reduction of wall thickness is seen to increase the CER by 3.58%. This increase is due to an additional bulge that formed at a location away from mid length, resulting in three bulges in the full length. The response does not represent the actual changes in behaviour.

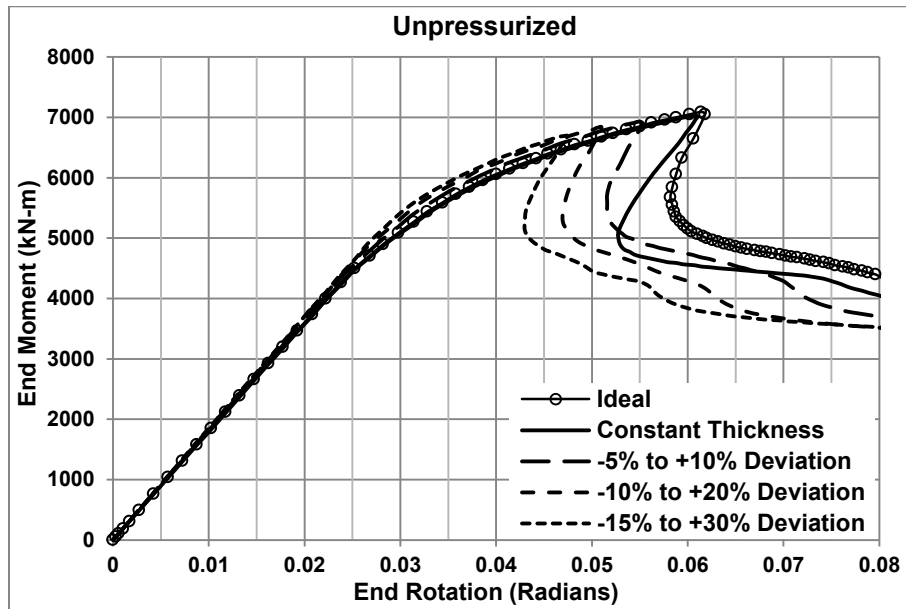


Figure 7.42 Moment-Rotation responses of unpressurized pipe with $D/t = 103.47$

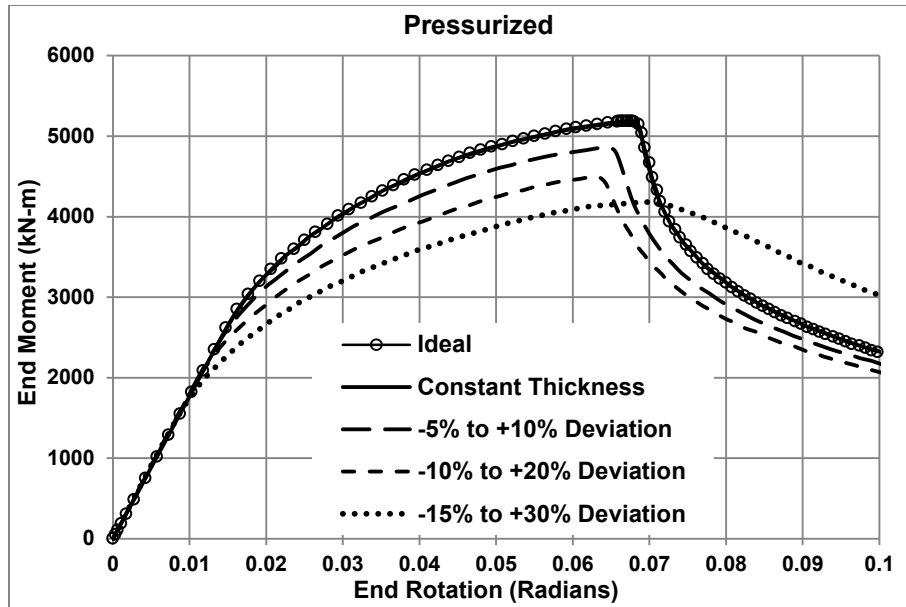


Figure 7.43 Moment-Rotation responses of pressurized pipe with $D/t = 103.47$. The formation of the additional bulge is due to the fact that a 15% reduction of a pipe with 103.47 D/t ratio is so excessive that the pipe wall is unable to withstand compression. In Figure 7.44 the longitudinal cross section of the buckled shape of this pipe with the thickness deviation ranges of -10% to +20% and -15% to +30% are shown. It is observed that up to a 10% reduction, the pipe wall is able to withstand the compressive stresses and buckles in the middle. For a 15% reduction, the pipe wall gets wrinkled with three bulges.

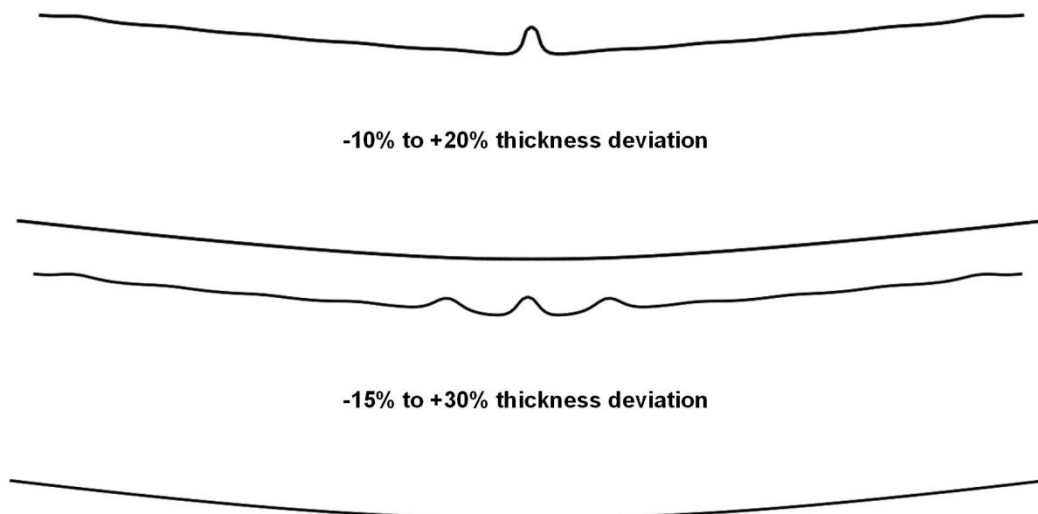


Figure 7.44 Longitudinal cross section of the buckled shape of pipes with the thickness deviation ranges of -10% to +20% and -15% to +30%

7.7.2 NPS 34 inch pipe with 9.525 mm specified wall thickness ($D/t = 90.71$)

The buckling responses of the unpressurized pipe are shown in Figure 7.45. It is observed that the ovalization of 0.01 has no effects on the buckling behaviour and the responses are identical in the pre and post buckling stages. The imposed thickness deviations reduce the peak moment and CER of the pipe with increasing deviation amplitudes. A 15% reduction of wall thickness results in a 29.11% reduction in CER.

For a D/t ratio of 90.71, the internal pressure corresponding to 80% of SMYS is calculated to be 12.31 MPa. The buckling responses of the pressurized pipe are shown in Figure 7.46. The responses are different from the typical response of pressurized pipes. The pipes are seen to buckle at a location away from the mid length, Due to the applied symmetry boundary condition, the deformed shapes show two bulges on either side, resulting in a higher than actual CER and a flatter response at peak moment. However, the same deformed shape is seen to appear in all pipe models with $D/t = 90.71$. Therefore, the comparison between them is deemed acceptable regardless of the high CER values.

It is observed that the ovalization of 0.01 has no effects on the buckling behaviour. The responses are identical in the pre and post buckling stages. The imposed thickness deviations reduce the peak moments of the pipe with increasing deviation amplitudes. A 15% reduction of wall thickness is seen to decrease the peak moment by 19.27%.

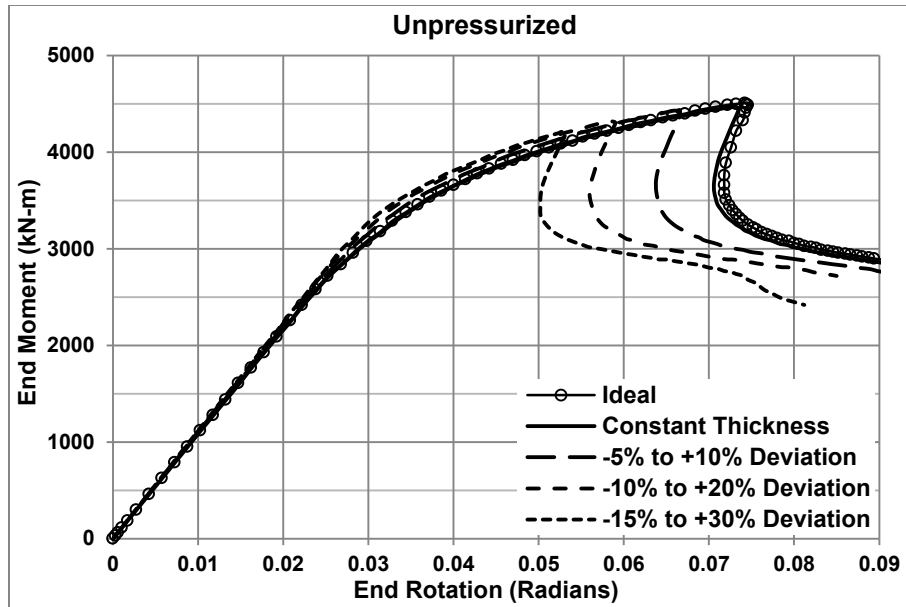


Figure 7.45 Moment-Rotation responses of unpressurized pipe with $D/t = 90.71$

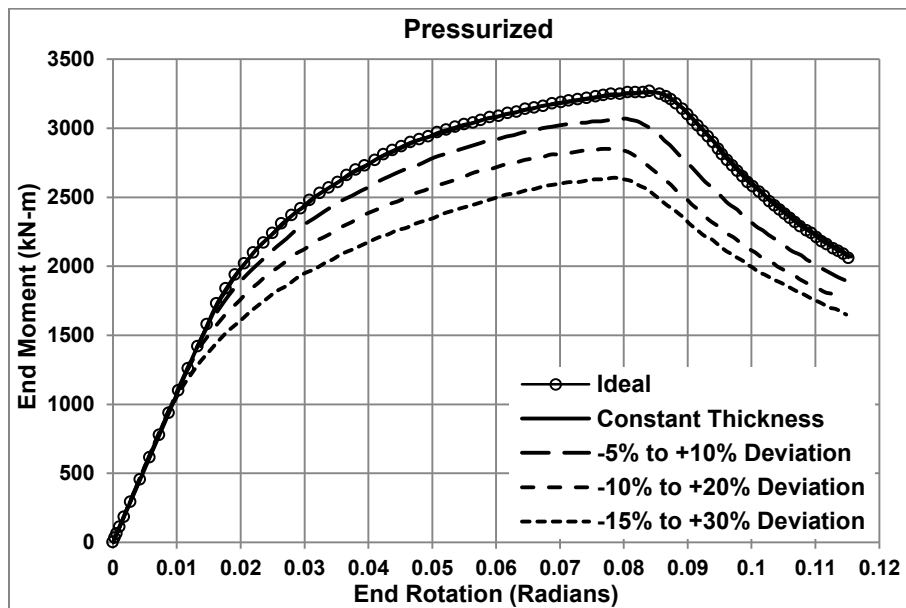


Figure 7.46 Moment-Rotation responses of pressurized pipe with $D/t = 90.71$

7.7.3 NPS 42 inch pipe with 14.275 mm specified wall thickness ($D/t = 74.75$)

The moment rotation responses for the unpressurized and pressurized conditions are shown in Figure 7.47 and Figure 7.48. The ovalization of 0.01 has insignificant effects on the buckling responses for the unpressurized condition.

The reduction of wall thickness consistently reduces both the peak moments and CER. A 15% wall thickness reduction reduces the CER by 27.51%.

For the pressurized condition, a 0.01 ovalization increases the CER by 1.41%. The wall thickness deviations cause the peak moment and CER to decrease consistently. A 15% wall thickness reduction reduces the peak moment by 18.6%.

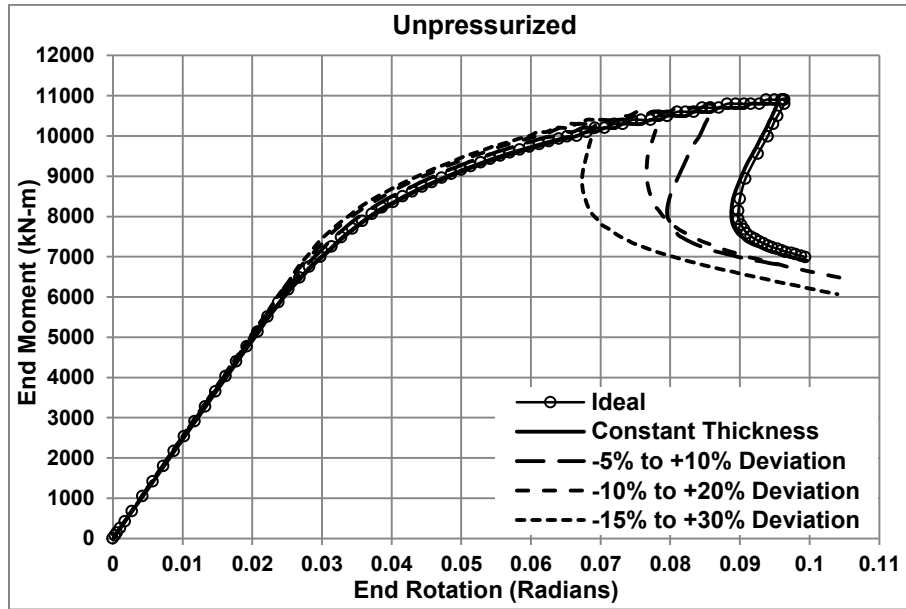


Figure 7.47 Moment-Rotation responses of unpressurized pipe with $D/t = 74.75$

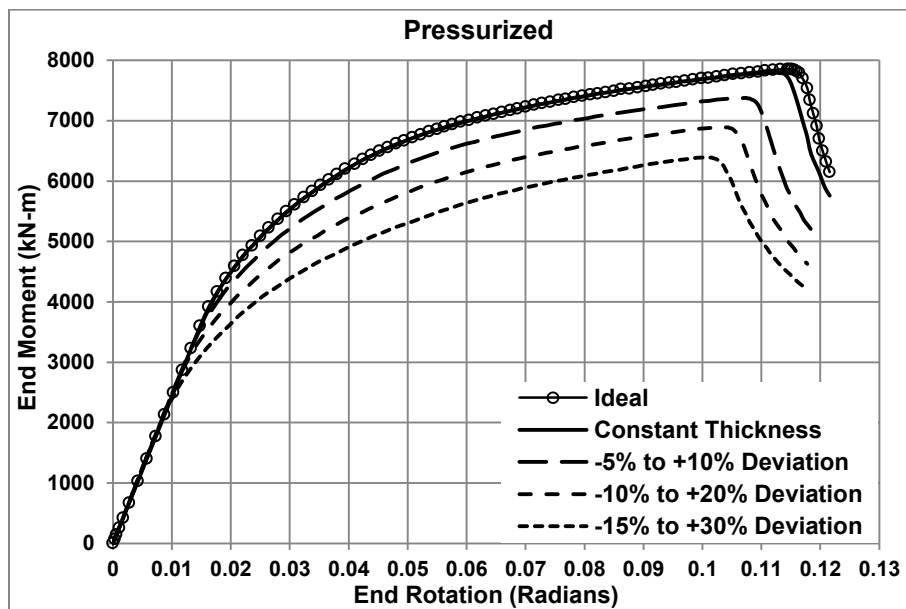


Figure 7.48 Moment-Rotation responses of pressurized pipe with $D/t = 74.75$

7.7.4 Summary of the parametric study

From the finite element analysis of the pipes with three different D/t ratios, it is observed that the 0.01 ovalization has insignificant effects on the buckling responses of unpressurized and pressurized pipes within this D/t ratio range. The thickness deviations have more prominent effects on the buckling responses for both unpressurized and pressurized conditions. The changes in peak moments and CER with increasing thickness deviation amplitudes are shown in Figure 7.49 and Figure 7.50. The thickness deviation amplitude in the horizontal axis of the plots is the difference between the maximum positive and negative deviations. Therefore, 15% deviation amplitude corresponds to a deviation of -5% to +10% and so on.

It is observed that the peak moments of the pipes with varying D/t ratios reduce consistently with increasing deviation amplitudes. The moment reductions in pressurized pipes are higher than in the unpressurized pipes.

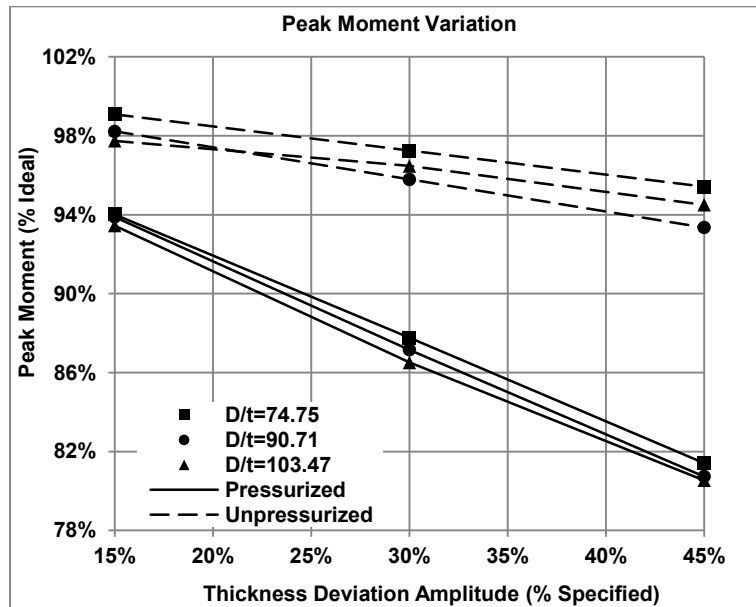


Figure 7.49 Changes in peak moments of unpressurized and pressurized pipes with increasing thickness deviation amplitudes

The CER also decreases with increasing deviation amplitudes for unpressurized pipes. For pressurized pipes with $D/t = 74.75$, the CER keeps decreasing

consistently up to a 45% deviation amplitude. For pipes with the two higher D/t ratios, the reduction in CER is observed up to a deviation amplitude of 30%, and then the CER increase towards a deviation amplitude of 45%. As mentioned previously, these are the cases where the pipe buckle does not appear in the middle, and the FEA results are affected by the applied symmetry boundary condition. For pressurized pipes, the transition of the FEA results towards the prediction of high CER with increasing D/t ratio is apparent from Figure 7.50. It should also be noted that a 15% reduction of wall thickness is very unlikely in a pipe with 10.312 mm and 9.525 mm specified thickness.

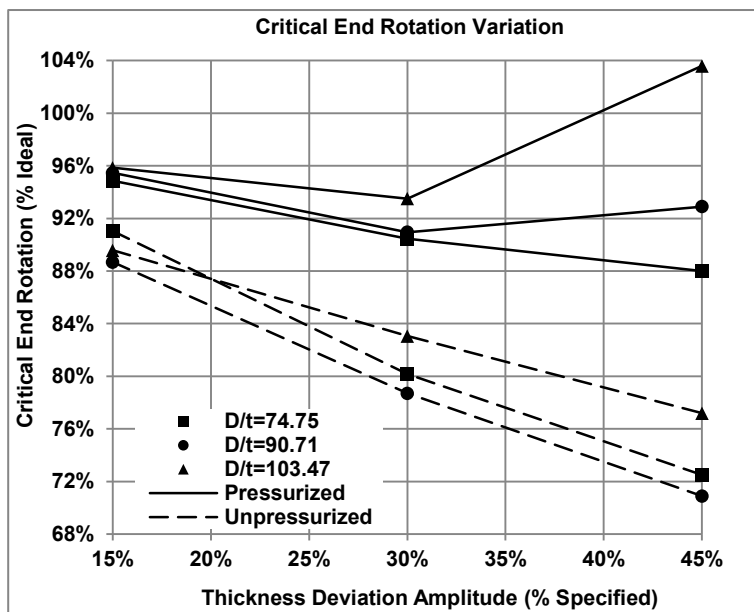


Figure 7.50 Changes in CER of unpressurized and pressurized pipes with increasing thickness deviation amplitudes

The OR and thickness deviation models were developed based on a D/t ratio of 74.75. The parametric study shows that these models are applicable to higher D/t ratios as well. It is possible that the errors in the CER values for higher D/t ratios with high thickness deviations are an effect of the mesh size and the imposed symmetry, which would be lost after the formation of the buckle. The mesh size was kept constant while the geometric properties of the pipes were varied. The optimum mesh size suggested in the literature is based solely on the pipe diameter. In this regard, it should be investigated whether the wall thickness deviation also needs to be considered while choosing an optimum mesh size.

The application of symmetry boundary conditions should be exercised cautiously for the buckling analysis of pipes with geometric imperfections.

Previously, experimental and numerical studies were carried out by Chen et al., (1993), DelCol et al., (1998), and Dorey et al., (2006), the results of which confirmed that the presence of geometric imperfections reduce the critical buckling capacity of pipes. From the parametric study, it is observed that irrespective of the D/t ratio, the ideal pipe with no geometric imperfections has a higher peak moment and CER compared to the pipes with geometric imperfections in both unpressurized and pressurized conditions. This parametric study concludes that the exclusion of the geometric imperfections in the buckling analysis of pipes will always lead to an over prediction of the critical buckling capacity, which agrees with the previous studies.

7.8 General Discussion on Initial Imperfections

The initial imperfections in linepipes have been characterized and modeled in various ways by previous researchers. Most of the studies focused on the deviation of the outside radii from a nominal or standard dimension. Chen et al., (1993) measured the OR deviation imperfection using physical measurements and incorporated them in their numerical model. They reported a maximum of 10% reduction in peak moment and 20% reduction in curvature corresponding to an assumed depression type imperfection of 15.4% of the wall thickness. Their model still over predicted the buckling capacities compared to the experimental results. Dorey et al., (2006) developed an assumed blister type imperfection model, which predicted a 6% (approximate) reduction in peak moment corresponding to an initial imperfection of 25% of the wall thickness of a pipe with $D/t = 92$. This model was in excellent agreement with the experimental results.

The UOE manufactured pipes are quite eccentric in geometry and material property compared to pipes from other manufacturing processes. The anisotropic behaviour has so far been the major focus of research in HSS UOE pipes. Tsuru et al., (2011) performed a numerical investigation on girth welded UOE pipes with plastic anisotropy and geometric imperfections. Their imperfection model was also based on radial deviation, the magnitude of which was maximum at the girth weld. Their study considered the difference in yield strength of the two pipe

segments on either side of the weld. They concluded that, while the addition of the geometric imperfections to the yield strength parameter decrease the critical buckling capacity, the effects of the strength parameter alone was more significant. Fathi et al., (2012) developed an anisotropic material model for HSS UOE pipes. In the absence of systematic initial imperfection measurements, he used the imperfection model developed by Dorey et al., (2006) to predict the results of full scale tests. Their FEA models showed good agreement with the experimental results, but over predicted the critical buckling capacity in most of the analyzed cases.

The FEA results of this study confirms that both the material property and the actual geometric imperfections present in the UOE manufactured pipes play important roles in predicting the critical buckling capacity. In an Ideal unpressurized pipe, the use of the longitudinal isotropic material over predicts the CER by 20% of the CER corresponding to the anisotropic material. Imposing the thickness deviation imperfection on the anisotropic model further reduces the CER by a maximum of 27%. This trend of CER reduction with increasing wall thickness deviation is evident within a D/t ratio range of 74 to 104. The ASTM A530/530M specified under tolerance of 12% of nominal wall thickness is, in this regard, far from being conservative. Within the studied ranges of D/t ratios, it is observed that a 10% reduction in wall thickness may reduce the peak moment by a maximum of 15% in pressurized pipes, while the CER in unpressurized pipes may reduce up to 20%. CSA Z662-11 specifies a resistance factor of 0.8 to be imposed on the ultimate compressive strain capacity of the pipe wall, which should be determined by "valid analysis methods", that accounts for initial imperfections in addition to other components. However, the qualification of initial imperfection in UOE pipes is not clear in the CSA code. Considering the resistance factor of 0.8, it can be assumed that the code accounts for a 20% reduction in critical buckling strain, which may not be conservative enough based on the observed reductions of CER in unpressurized pipes. Moreover, the codes do not address the reduction of the linear elastic range of buckling response of the pressurized pipes with wall thickness deviation.

7.9 Conclusion

The finite element analysis carried out in this chapter provides an insight into the possible changes in the buckling response of high strength steel pipes with the inclusion of initial geometric imperfections. The effects of two types of imperfections have been investigated individually and in combination. The OR deviation is seen to have insignificant effects on the buckling behaviour compared to an ideal pipe with a constant OR. The thickness deviation is seen to have major influences on the buckling response compared to the behaviour of an ideal pipe with constant thickness. The behaviours are also seen to be dependent on the direction of the applied rotation. The reduction in the buckling capacity was found corresponding to an applied rotation which induces compression to the pipe wall with reduced thickness. The combination of the two imperfections is seen to produce similar effects as the thickness deviation imperfection alone. The thickness deviation imperfection is therefore deemed the more important imperfection of the UOE manufactured pipes.

The geometric imperfections were further simplified through a sensitivity study. The simplified imperfection models are able to produce similar changes in the buckling behaviour compared to the more detailed models previously employed for the buckling analysis in this chapter. A parametric study was carried out using these simplified imperfections to investigate their applicability to the FEA models of pipes with higher D/t ratios. The imperfection models are observed to be quite robust within the parameter ranges of the parametric study. The study suggests that, while selecting an optimum mesh size for buckling analysis, the wall thickness deviation of the pipes in addition to its diameter may need to be considered. The study also confirms that the application of the symmetry boundary condition will result in a slight over prediction of the critical buckling strain in the cases where pipe buckle does not appear at the plane of symmetry. The symmetry boundary condition should be applied cautiously in such analyses.

A major limitation of this finite element study is the exclusion of the geometry and material properties of the longitudinal seam weld. The imperfection models indicated that the weakest buckling response can be expected when compressive strains develop near the location of the seam weld, where the wall thickness is less than specified and the OR is less than nominal. The inclusion of

the longitudinal seam weld in the FEA models can lead to a number of possible scenarios.

Regarding geometry, the higher thickness of the seam weld compared to the thickness of the pipe wall in its vicinity may prevent the pipe from buckling at low peak moment and CER. On the other hand, the abrupt changes in geometry at the seam weld location may contribute to stress concentrations and result in further decrease of the buckling capacity. In terms of material properties, the weld metal can be stronger than the pipe material itself and may contribute to an increase in the buckling capacity. On the other hand, the weld metal may be brittle and may fail to contribute at all to the overall buckling capacity. It would be unwise to speculate the effects of including the longitudinal seam weld geometry and its material property to the FEA models of the initial geometric imperfections on the buckling behaviour of high strength pipes. A more detailed analysis is required to come to a conclusion.

Buckling is governed by two aspects, material property and geometry. This study considered the effects of both material property and geometry on the buckling response of UOE manufactured pipes. Despite disregarding the longitudinal seam weld, the FEA results provide an understanding of the implications of the tolerances of outside radius and wall thickness of HSS UOE manufactured pipes.

CHAPTER 8: SUMMARY, CONCLUSIONS, AND RECOMMENDATIONS

8.1 Summary

High strength UOE manufactured steel pipes demonstrate plastic anisotropy in the longitudinal and circumferential directions, and the buckling resistance of such pipes weakens with the application of internal pressure. The presence of initial geometric imperfections in linepipes is proven to have detrimental effects on the buckling capacity. This research was carried out with the intent of expanding the knowledge of initial geometric imperfections in High Strength UOE manufactured steel pipes, and understanding the effects of such imperfections to the buckling capacity of line pipes subjected to bending.

A geometric imperfection measurement technique has been developed in this research that involves a high resolution 3D surface profiler for geometric data acquisition, and a 3D inspection and reverse engineering software for the geometric analysis of the acquired data. This measurement technique has been applied to the imperfection measurement of ten straight pipe segments and six protective pipe sleeves on straight pipes. This technique has resolved the difficulties in locating the axis of a pipe, which is rather challenging in a physical measurement setup. The technique has been further advanced to the measurement of five ninety degree pipe elbows. In addition to acquiring the outside surfaces of pipes, this technique is also able to acquire the inside surfaces relative to the outside. The measurement of pipe wall thickness on a very fine grid is therefore possible up to a certain length of a pipe from its end. In general, this imperfection measurement technique is very fast, produces a large amount of geometric information, and has acceptable accuracy compared to conventional physical measurement techniques.

The analysis of the acquired geometric data through the reverse engineering software has provided important information regarding imperfections in straight pipes, pipe sleeves and pipe elbows. It was found that the measured protective pipe sleeves do not conform to the dimensional specifications, which will lead to the development of high compressive strains in them after installation. The pipe elbows were found to have satisfactory geometric dimensions in terms of their

outside diameter and bend radius. The patterns of the wall thickness deviation of the measured elbows were seen to be symmetric about their horizontal planes of symmetry.

The geometric analysis results of the straight pipes showed that the initial geometric imperfections in such pipes follow distinct patterns in terms of outside radii and pipe wall thickness deviations from ideal dimensions. The magnitudes of these imperfections were seen to vary within certain ranges, but the patterns were seen to reappear along the length of a specimen and in different specimens. Eight of the ten pipes measured in this study were UOE manufactured, and the manufacturing information of the other two was unavailable. It was seen that the eight UOE manufactured pipes had similar imperfection patterns that were different from the patterns observed in the other two. These patterns were seen to appear consistently in all eight UOE manufactured pipes irrespective of their D/t ratios and manufacturer. This important finding led to the conclusion that the randomness of the initial geometric imperfections in UOE manufactured pipes is intrinsic to the imperfection magnitude, rather than their pattern. The characterization of the observed initial imperfection patterns confirmed that these imperfections are indeed the after effect of the UOE manufacturing process.

Initial geometric imperfection models have been developed that can capture the observed OR deviation and wall thickness deviation patterns in the UOE manufactured pipes. The effects of these imperfections on the buckling response of these pipes have been studied through finite element analysis. The study suggests that the observed wall thickness deviation imperfection has more influence on the buckling response compared to the observed OR deviation. The wall thickness imperfection can lead to an increase in the buckling capacity, or reduce the capacity detrimentally depending on the direction of the applied bending loads.

8.2 Conclusions

The following conclusions can be drawn from the imperfection measurement and the finite element analysis results:

3D surface profiling is a viable option for the inspection of linepipes. The eight UOE manufactured pipes measured in this research showed that the seam weld dimensions are consistent along their length. The outside radii have minor deviations from their corresponding nominal OR. The ovalization imperfections are very small and within the CSA Z662-11 specified tolerance. The wall thickness deviations are very high which ranges from -15% to +28% of the specified wall thickness. The ovalization imperfection, despite being very negligible, is seen to be comparatively higher in the pipes with higher D/t ratios. A correlation therefore exists between the ovalization and the D/t ratio of the UOE manufactured pipes.

The OR deviation pattern in the UOE manufactured pipes is a result of the expansion stage of the manufacturing process. The pattern is in the shape of waves that are consistent with the arrangement and number of expansion mandrels used in manufacturing. All of the eight UOE pipes studied in this research had twelve such waves around their perimeter which subtended an average angle of approximately 30 degrees to the centre, indicating the use of expansion mandrel with twelve segments in manufacturing these pipes. The overall shape of the imperfect pipe cross section can also be approximated in the shape of an ellipse with its minor axis oriented along the line connecting the centre of the pipe and the location of the longitudinal seam weld.

The thickness deviation pattern in the UOE manufactured pipes assumes a bell shaped curve when plotted against angles around the pipe perimeter. The thickness is lower in the vicinity of the longitudinal seam weld and higher at locations opposite to the seam weld in a pipe cross section.

The observed OR deviation and thickness deviation patterns appear consistently in the UOE manufactured pipes with different D/t ratios. The patterns are also independent of manufacturer. The patterns are the after effects of the manufacturing process itself. It is therefore concluded that the initial geometric imperfections in UOE manufactured pipes are not random. The randomness of

imperfection is in the imperfection magnitudes, while the imperfection pattern is consistent and recurring.

The wavy shape of the UOE manufactured pipe cross section does not have significant effects on their buckling capacity within the range of the imperfection magnitudes obtained from measurements. The elliptical cross section is a good approximation of the overall OR deviation within the range of measured imperfection magnitudes. In general, the levels of the OR deviation imperfection magnitudes obtained from measurements are seen to have negligible effects on the buckling behaviour through finite element analysis. However, a small reduction in buckling capacity was observed when bending was applied to a specific direction. This direction corresponds to the development of compressive strains near the location of the longitudinal seam weld.

The wall thickness deviation imperfection is found to have immense effects on the buckling capacity of the UOE manufactured pipes. The finite element study suggests that these effects depend on the level of the applied internal pressure, as well as the direction of the applied bending. In both the pressurized and unpressurized conditions, the lowest buckling capacity results when the applied bending induces compressive strains near the location of the longitudinal seam weld. The capacity improves significantly when the applied bending induces compressive strains in the location opposite to the seam weld. The application of internal pressure also affects the range of the linear portion of the buckling response. The linear range is found to be smaller corresponding to the development of compressive strains near the location of the longitudinal seam weld.

Both the OR deviation and the thickness deviation imperfections tend to reduce the buckling capacity of UOE manufactured pipes when the applied bending results in compressive strains near the location of the seam weld. The reduction in capacity due to thickness deviation is much higher than that due to OR deviation. The addition of the OR deviation imperfection to the thickness deviation imperfection does not result in any significant difference in buckling capacity compared to the buckling capacity obtained from the thickness deviation

alone. The thickness deviation imperfection is therefore considered to be more important in the study of buckling capacity of UOE manufactured pipes.

8.3 Recommendations

The results of this research provide a number of important information regarding the geometric imperfections and their effects on the buckling capacity of UOE manufactured pipes. However, the following areas require further attention and investigation:

The accuracy of the 3D scanner was verified against micrometer measurements and the improvement in the captured surface data was qualified by using a photogrammetry model. This was done in particular due to the unavailability of a cylindrical object that represents an ideal large diameter pipe with constant OD and wall thickness. The accuracy verification of the scanner can be carried out according to the guidelines provided by ISO 230-6 and ASME B5.54.

The research was limited to the studying of eight UOE manufactured pipes with D/t ratios of 74.75, 90.71, and 103.47. Further measurements need to be carried out on other D/t ratios in order to confirm the results of this study.

The initial imperfection measurement was carried out only on UOE manufactured pipes. The conclusion: "Initial imperfection patterns are not random" - should be confirmed by studying the initial geometric imperfections of pipes manufactured in other manufacturing processes.

The OR deviation or ovalization imperfection was observed to be consistent in magnitude in the measured pipes. Accordingly, the possibility of the variation of OR deviation along the pipe length was ignored in the finite element analysis. The effects of longitudinal variations of the OR deviation need to be studied.

The finite element analysis was carried out disregarding the geometry and material property of the longitudinal seam weld. The effects of the longitudinal seam weld geometry and material property on the buckling capacity of UOE manufactured pipes need to be studied in conjunction with the initial geometric imperfections to come to a conclusion regarding the detrimental effects of the initial imperfections presented in this research.

The effects of the geometric imperfections on the buckling response of pipes have been presented by comparing with the behaviour of an ideal pipe with no geometric imperfections. The buckling capacity of the pipes according to their designs was not considered. Therefore, the reductions in the buckling capacities of the pipes are not necessarily as large as was observed from the FEA results. The FEA results only implicate the importance of considering the initial geometric imperfections in the design of pipes against buckling.

REFERNCES

- Adeeb, S., Zhou, J., & Horsley, D. (2006). Investigating the Effect of UOE Forming Process on the Buckling of Line Pipes Using Finite Element Modeling. International Pipeline Conference. Calgary: ASME.
- Al-Showaiter, A., Taheri, F., & Kenny, S. (2008). Influence of Pipeline Misalignment on the Local Buckling Response. International Pipeline Conference. Calgary: ASME.
- Americal Society of Mechanical Engineers, 2012. B31.8-2012 Gas Transmission and Distribution Piping Systems. ASME.
- Americal Society of Mechanical Engineers, 2005. B5.54-2005 Methods for Performance Evaluation of Computer Numerically Controlled Machining Centers. ASME.
- American Society for Testing and Materials (ASTM) 2012. A381-12 Standard Specification for Metal-Arc-Welded Steel Pipe for Use with High Pressure Transmission Systems.
- American Society for Testing and Materials (ASTM) 2012. A530/A530M-12 Standard Specification for General Requirements for Specialized Carbon and Alloy Steel Pipe.
- Armstrong, P.J., Frederick, C. O. (1966). A Mathematical Representation of Multiaxial Bauschinger Effect. Report RD/B/N731, CEGB, Central Electricity Generating Board, Berkeley, UK.
- Bailey, R.W., & Kulak, G. L. (1984). Flexural and Shear Behaviour of Large Diameter Steel Tubes. University of Alberta: Department of Civil Engineering, Structural Engineering Report No. 119.
- Barrett, J., Kenny, S., & Phillips, R. (2009). Effects of Girth Weld on the Local Buckling Response of Conventional Grade Pipelines. ASME.
- Batterman, S. C. (1965). Plastic Buckling of the Axially Compressed Cylindrical Shells. AIAA J., 316-325.

- Bauschinger, J., (1886). Elastic limit, American Engineering.
- Borror, C. M., (2009). Certified Quality Engineer Handbook (3rd Edition). American Society for Quality (ASQ).
- Canadian Standards Association, 2011. Z662-11 Oil and Gas Pipeline Systems. Canadian Standards Association, Etobicoke, Ontario.
- Chen, Q., Elwi, A. E., & Kulak, G. L. (1993). Bending Strength of Longitudinally Stiffened Steel Cylinders. University of Alberta: Department of Civil Engineering, Structural Engineering Report No. 192.
- Chen, S., Li, W. F., Zhang, J., Wang, W. (2008). Active Sensor Planning for Multiview Vision Tasks. Springer.
- Chou Z., (2010). Health Monitoring of Buried Pipeline Buckling by Using Distributed Strain Sensory Systems. Ph.D. Dissertation, Department of Civil and Environmental Engineering, University of Alberta.
- Creaform Knowledge Base - Creaform Handyscan Manual
(www.creaform3d.com)
- Cumming, G., & Rathbone, A. (2010). Euler Buckling of Idealised Horizontal Pipeline Imperfections. International Conference on Ocean, Offshore and Arctic Engineering (pp. 1-8). Shanghai: ASME.
- Darmody, W. J. (1967). Elements of a Generalized Measuring System. In Handbook of Industrial Metrology. Englewood Cliffs.
- DelCol, P. R., Grondin, G. Y., Cheng, J. J. R., & Murray, D. (1998). Behaviour of Large Diameter Line Pipe Under Combined Loads. University of Alberta: Department of Civil Engineering, Structural Engineering Report No. 224.
- Dorey, A. B., Murray, D. W., & Cheng, J. J. R. (2006). Initial Imperfection Models for Segments of Line Pipe. Transactions of the ASME, 322-329.

Dorey, A. B., Cheng, J. J. R., & Murray, D. (2001). Critical Buckling Strains for Energy Pipelines. University of Alberta: Department of Civil Engineering, Structural Engineering Report No. 237.

Fathi, A., Cheng, J. J. R. (2012). A parametric Study on Buckling Response of High Strength Steel Pipes with Anisotropic Material Properties. International Pipeline Conference. Calgary: ASME.

Focke, E. S., Gresnigt, A. M., & Hilberink, A. (2011). Local Buckling of Tight Fit Liner Pipe. Pressure Vessel Technology, ASME.

Herynk, M. D., Kyriakides, S., Onoufriou, A., Yun, H. D. (2007). Effects of the UOE/UOC Pipe Manufacturing Processes on Pipe Collapse Pressure. International Journal of Mechanical Sciences, Volume 49, 533-553.

Hibbit, Karlsson & Sorenson, Inc. (2003). ABAQUS/STANDARD Theory Manual, Version 6.7.

Houliara, S., & Karamanos, S. A. (2011). Buckling of Thin-Walled Long Steel Cylinders Subjected to Bending. Pressure Vessel Technology, 1-9.

International Organization for Standardization, 2002. ISO 230-6:2002. Test Code for Machine Tools - Part 6: Determination of Positioning Accuracy on Body and Face Diagonals (Diagonal Displacement Tests)

Jahne, B., Haubecker, H. (2000). Computer Vision and Applications. Academic Press.

Jiao, R., & Kyriakides, S. (2009). Progressive Wrinkling and Collapse of Pipes Due to Axial Cycling. International Conference on Ocean, Offshore and Arctic Engineering (pp. 1-9). Honolulu: ASME.

Luzzi, L., & Marcello, V. D. (2011). Collapse of Nuclear Reactor SG Tubes Pressurized From Outside: The Influence of Imperfections. ASME.

Neupane, S., Adeeb, S., Cheng, R., Ferguson, J., Martens, M., (2012). Modeling the Deformation Response of High Strength Steel Pipelines. Transaction of the ASME, Journal of Applied Mechanics, September 2012.

Novozhilov, V. V. (1964). Theory of Thin Elastic Shells, 2nd Edition, P. Noordhoff, Groningen.

Obaia, K. H., Elwi, A. E., & Kulak, G. L. (1991). Inelastic Transverse Shear Capacity of Large Fabricated Steel Tubes.

Reed, C., Alastair, J., & Smart, D. (2004). Techniques for Monitoring Structural Behavior of Pipeline Systems. AWWA Research Foundation.

Sato, T., Yoshiki, M., Masahito, M., Nobuhisa, S., & Masao, T. (2008). Parametric Study on the Effect of Geometric Imperfections on the Bending Capacity of High-Strength Linepipes. 7th International Pipeline Conference (pp. 1-9). Calgary: ASME.

Shinohara, Y., Madi, Y., & Besson, J. (2010). A Combined Phenomenological Model for the Representation of Anisotropic Hardening Behavior in High Strength Steel Line Pipes. European Journal of Mechanics A/Solids, 917-927.

Simpson, J. A. (1981). Foundations of Metrology. Journal of Research of the National Bureau of Standards, Volume 86.

Souza, L., & Murray, D. W. (1999). Analysis for Wrinkling Behavior of Girth-Welded Line Pipe. ASME.

Stephens, M. J., Kulak, G. L., & Montgomery, C. J. (n.d.). Local Buckling of Thin-Walled Tubular Steel Members.

Suzuki, N., Kondo, J., Endo, S., Ishikawa, N., Okatsu, M., & Shimamura, J. (2006). Effects of Geometric Imperfections on Bending Capacity of X80 Linepipe. 6th International Pipeline Conference (pp. 1-9). Calgary: ASME.

Tianfeng, Z., Menglan, D., Xiaodong, P., & Xianhong, F. (2010). Lateral Buckling of Non-Trenched High Temperature Pipelines with Pipelay Imperfections. Petroleum Science, 123-131.

Torselletti, E., Vitali, L., & Bruschi, R. (2005). Bending Capacity of Girth-Welded Pipes. ASME.

Varady, T., Martin, R. R., Cox, J. (1997). Reverse Engineering of Geometric Models-An Introduction. *Computer-Aided Design*, 255-268.

Veerappan, A., Shanmugam, S., & Soundrapandian, S. (2010). The Accepting of Pipe Bends With Ovality and Thinning Using Finite Element Method. *Pressure Vessel Technology*, 1-9.

Villarraga, J. A., Rodriguez, J. F., & Martinez, C. (2004). Buried Pipe Modeling with Internal Imperfections. *Journal of Pressure Vessel Technology*, 250-257.

Wang, C. (2003). Definitions and Correlations of 3D Volumetric Positioning Errors of CNC Machining Centers. *Proceedings of the IMTS 2004 Manufacturing Conference*, Chicago, IL, September 8-10, 2004.

Yang, Z., Kumar, S. B., & Tronskar, J. P. (2008). Fitness-For-Service Assessment of the Pipelines with Localized Geometric Imperfections such as Buckles and Wrinkles. *Key Engineering Materials*, 173-176.

Yatabe, H., Fukuda, N., Musuda, T., & Toyoda, M. (2004). Analytical Study of Appropriate Design for High-Grade Induction Bend Pipes Subjected to Large Ground Deformation. *Journal of Offshore Mechanics and Arctic Engineering*, 376-383.

Yoosef-ghodsi, N., Kulak, G., & Murray, D. (1994). Behaviour of Girth Welded Line Pipe. *University of Alberta*.